GeologyInvestigating the structural and mechanical properties involved in catastrophic volcanic collapse

Investigating the structural and mechanical properties involved in catastrophic volcanic collapse

Lily Moore
PhD thesis
Birkbeck, University of London

I declare that this thesis has been composed solely by myself and that it has not been submitted, in whole or in part, in any previous application for a degree.

Lily Moore

Acknowledgements
I would like to acknowledge here those who have supported me throughout this PhD, without whom this project would not have been possible. Firstly, I would like to thank my funders for this studentship, the NERC London Doctoral Training Partnership. I am extremely grateful to my supervisors Professor Tom Mitchell and Professor Hilary Downes for their support and guidance throughout the PhD. Tom, for his consistent advice and encouragement, as well as his training and assistance with lab work. Hilary, for her support with organising fieldwork, providing valuable feedback and helping me to stay on track. I would like to thank Dr Simon Day for his expert advice and for sharing datasets and samples, which enabled me to carry out the work on Ritter. I would also like to acknowledge Dr Sebastian Watt for his advice and sharing of datasets. I would like to recognise all those who previously collected datasets and researched on this topic, referenced within this thesis. Thank you to my brilliant field assistants: Ashley, Karin and Bob. Finally, I could not have undertaken this journey without the love and support of my friends and family. Special thanks to my parents, Mike and Fiona, and my sister, Abigail for always being around to proofread or give advice. I would like to thank my partner, Peter for being by my side and supporting me through the whole experience.

Abstract

Volcanic collapses occur globally across a range of volcanic settings with an occurrence rate of five events per century. Collapse events are extremely destructive and can be tsunamigenic. The 2018 collapse and tsunami involving Anak Krakatau highlights the potential impacts of these events. Studying volcanic collapse scars with evidence of tsunamis is critical to further understanding the possible causes of instability. This thesis studies two examples of tsunamigenic volcanic collapse of different scales and volcanic setting: Ritter Island (Papua New Guinea) and Fogo (Cape Verde).

Drone surveys and structure from motion (SfM) modelling is used to create high resolution 3D models of both these collapse scars. These datasets provide improved detail about the island's structure. Samples from these collapse scars have been measured to determine the range of mechanical and hydraulic properties of the rocks making up the edifice including porosity, permeability and uniaxial compressive strengths. These properties are then discussed with the geomorphological analysis to examine how the pre-collapse volcano may have developed instabilities contributing to collapse.

Results include an updated estimate on the collapsed volume for Ritter Island of 3.7 km^3. At Ritter, compressive strengths were 50% lower in lava samples affected by alteration identifying this as a possible weakening mechanism. At Fogo, pyroclastic layers have been identified as weakest material within the edifice. Dyke orientation analysis at both volcanoes has highlighted similar trends in intrusions perpendicular to the direction of collapse. This similarity in the intrusion pattern across the two edifices suggests this could be a common weakening mechanism. These results are important in the field of hazard assessment and monitoring. Improved pre-collapse reconstructions and volumes directly impact on tsunami modelling. Also, monitoring of the type and extent of alteration as well as intrusion emplacement orientation and flank movement can help identify unstable edifices.

Table of Contents

Table of figures

Table of tables

Table of equations

1 Introduction and literature review

1.1 Introduction

Volcanic edifices are inherently unstable structures for several reasons and can collapse catastrophically forming highly destructive hazards. Periods of growth and collapse are intrinsic to a volcano's life cycle. They occur across a wide range of volcanic settings and in varying states of volcanic quiescence. Their global occurrence rate is 5 events per century (Dufresne et al., 2021). Catastrophic volcanic collapses have only been relatively recently identified as a major volcanic process and hazard (McGuire, 1996). Research in this area is essential as they can be extremely devastating events and are difficult to predict or mitigate against.

Precursory signals are not well defined for catastrophic volcanic collapses and the hazard is not widely understood or recognised. As a result, identifying an emergency situation at a volcano at risk of flank collapse is difficult. In addition, to mitigate the risk for vulnerable communities, this hazard must be communicated effectively in order to inform or evacuate residents. This would prove difficult as events of this type are infrequent with only a small number having occurred in recent history, meaning that our experience is limited.

The physical properties of the rocks and processes within a volcano controls instabilities developing in the edifice and triggering mechanisms will determine collapse frequency. Instabilities arise from a variety of factors such as weak basement rocks or layers, alteration, steep edifices, seismicity and intrusions (Romero et al., 2021, Heap et al., 2021a, Heap et al., 2021b, Zernack and Procter, 2021). Triggering mechanisms include pore fluid pressurisation, magmatic activity, seismicity or environmental factors (McGuire, 1996, Reid, 2004, Vidal and Merle, 2000, McMurtry et al., 2004). It has also been suggested that prehistoric collapse events tended to coincide with the onset of warmer interglacial periods (McMurtry et al., 2004). With our current warming climate, it is particularly important understanding the processes that lead to collapse and identify possible precursors to improve prediction and warning systems.

In order to improve risk and hazard assessment for volcanic collapses, it is important to reconstruct elements of previous collapse scars. For tsunami modelling, the most important factors that control the size and distribution of the waves are the volume of material and the speed of disintegration. Volume can be estimated from the remnants of these collapses by reconstructing the pre-collapse edifice. A more accurate volume calculation gives better tsunami modelling scenarios and therefore an improved insight into evaluation of the extent

of damage from historic events. This would help to estimate volumes of material that are at risk of collapsing for assessing future hazards. In addition, reconstructing the pre-collapse edifice gives insight into the internal structure of a volcano. This can help identify internal weaknesses within the pre-collapse edifice. This is useful to identify any precursory activity that may indicate that a flank is vulnerable to collapse.

Evidence of catastrophic volcanic collapse globally suggests that the historical examples are mostly in island-arc settings and involve relatively small collapse volumes compared to intraplate ocean island examples. Despite this, the repercussions of smaller-size events can be devastating, involving extensive damage and fatalities. Recent examples of this include the collapse of Ritter Island in 1888 and, more recently, Anak Krakatau in 2018. Evidence of much larger collapses, with the potential to be much more destructive, is seen in ocean island settings. It is important, therefore, to investigate these recent smaller examples, alongside much larger collapses. This may help to determine any scale-independent similarities between the structure or properties of each scenario. Using the smaller, more recent examples which we know more about will help in assessing the hazard of these much larger collapse events which we have yet to experience in recent history. Therefore, subduction-related Ritter Island (Papua New Guinea) and intraplate Fogo Island (Cape Verde) are the two study volcanoes selected for this project.

Ritter Island is a well-studied benchmark within this area of research as it is the site of the largest collapse and subsequent tsunami in recent history. In 1888, a collapse event reduced its 750 m conical edifice to a 120 m island. The collapsed material disintegrated to the west and generated a tsunami with wave run-ups up to 15 m on nearby coasts (Ward and Day, 2003). Hydrothermal activity may have preceded the event up to a week before and the collapse was followed by reports of eruptive activity (Watt et al., 2019). Past work on this event have calculated collapse volumes that vary between 2.4 km^3 (Karstens et al., 2019) and 4.2 km^3 (Day et al., 2015).

Fogo is an ocean-island volcano with an average diameter of 25 km. Its morphology is characterised by an eastward-opening depression surrounded by the 20 km horseshoe-shaped Bordeira cliff, up to 1000 m high, with slope angles between 60°and 90° produced by one or more major volcanic collapses (Day et al., 1999, Martínez-Moreno et al., 2018). The depression, called Chã das Calderas, is covered in post-collapse lavas and lahar deposits and contains a younger stratovolcanic cone, Pico do Fogo. The collapse, dated at 73 ka, reduced

an estimated 3500 m edifice to its current elevation of 2700 m (Worsley, 2015), with an estimated volume of 150-200 km^3 (Day et al., 1999). Evidence of a megatsunami resulting from the collapse has been found on neighbouring islands at elevations of 270 m (Ramalho et al., 2015).

1.1.1 Aims and objectives

Aims

The overarching aim of the thesis is to characterise volcanic collapse and assess how instabilities may develop within volcanic edifices which eventually lead to collapse. Two historic collapse events will be investigated using "Structure from Motion" (SfM) technology to reconstruct pre-collapse topographies. From these reconstructions, collapse dimensions and volumes will be estimated and internal edifice structure will be examined and structures mapped. Samples from collapsed edifices will be measured for mechanical and hydraulic properties of the rocks and compared with the reconstructed edifice to highlight any weaker layers.

Fogo and Ritter Island share a history in major volcanic collapse and, although they differ in tectonic setting and size, they have a similar post-collapse morphology. Therefore, a second aim is to characterise the similarities between the two collapses and to determine what, if any, instabilities they had in common before collapsing. This will help identify any scale-independent instabilities that could be commonly observed at unstable flanks and will therefore useful for monitoring and hazard assessment.

Objectives

- A major objective of this project is to use "Structure from Motion" (SfM) modelling from drone imagery of both volcanic collapse scars to create improved datasets for the areas to generate many avenues of analysis from the resultant models. This wealth of data from these models will highlight the value of using SfM modelling when assessing volcanic collapse scars, particularly in remote regions. A developed workflow for this method will be explored and discussed.
- Using a previously collected dataset from Ritter Island (as outlined in section 2.3.1), a SfM 3D model will be generated of the subaerial island. This will be used to generate

a detailed geological and morphological map, for geospatial analysis and to reconstruct the pre-collapse cone.

- Experimental work to determine the mechanical and hydraulic properties of the rock samples will characterise the rocks that made up the edifice indicating any weaker layers or weakening processes. This includes the porosity, permeability, uniaxial compressive strength and Young's modulus. This work, alongside the geological map, will allow an investigation of the probable structure and instabilities within the pre-collapse Ritter edifice.
- A field trip to Fogo, Cape Verde will be carried out to collect rock samples and perform a drone survey of the Bordeira cliff collapse scar.
- An SfM model will be made of the Borderia cliff from which the trends of the cross-cutting intrusions can be identified and mapped. These will be used to speculate on the pre-collapse structure of Fogo.
- Determination of the mechanical properties of the rock samples will yield a range of properties that made up the edifice. These new aspects of research of Fogo will postulate possible avenues of instability within the edifice as well as investigate previous suggestions from the literature (Day et al., 1999).
- The two collapse edifices will then be discussed in comparison to evaluate the possible sources of instability within the pre-collapse volcanoes. This will highlight key similarities and differences and help identify significant instability parameters that may coincide in ocean island and arc volcanoes.

1.2 Volcanic collapse: literature review

Volcanoes have been a key area of study for many years in terms of eruptive and magmatic processes, however attention has been paid to volcanic lateral collapse only in the last few decades. Volcanic edifices grow very rapidly and therefore are inherently unstable structures and, when a number of controls reach a critical state, can collapse. Collapse events are very destructive and have several secondary hazards, in particular the generation of tsunamis which extend their destructive reach. The key focus of research in this field to date has been identifying historic collapses and what factors lead to instability and the triggering of collapse.

1.2.1 Global distribution and frequency

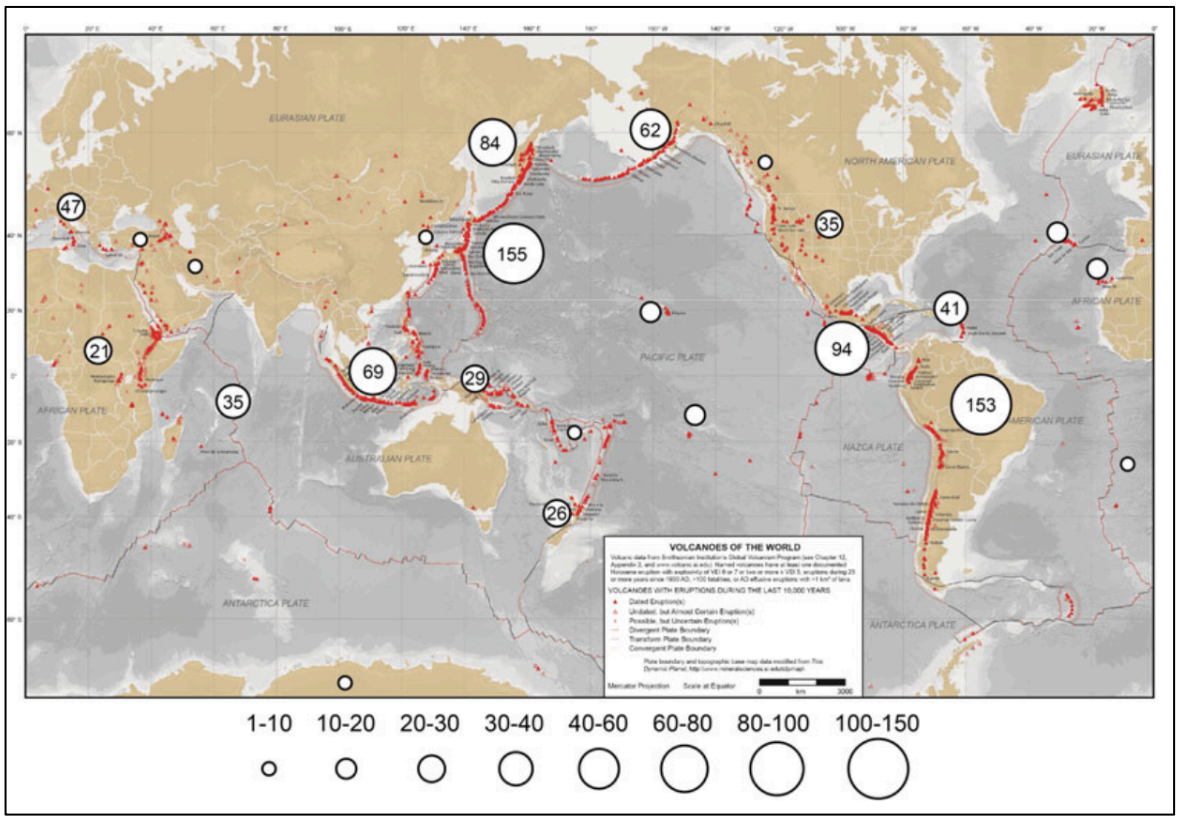

Figure 1.1: Figure from Dufresne et al., 2021 showing a map of global locations of volcanoes (in red) and the distribution of volcanic debris avalanche deposits.

The eruption and subsequent collapse of Mt St Helens in 1980 led to the recognition of volcanic debris avalanches as a major process and hazard (McGuire et al., 1997). Key characteristic morphological features on a volcanic edifice and within collapse deposits were then identified at known collapses and have been used to identify others globally and even on other planetary bodies (McGuire et al., 1997, Watt et al., 2021). These events were not well understood because the evidence of many landslides has been obscured by erosion and

renewed volcanic activity (Watt et al., 2021). As a result of this, the ages of most known volcanic landslides fall within the last 0.5 Ma, with many older events yet to be discovered (Blahůt et al., 2019). There are > 1000 volcanic debris avalanche deposits identified at 594 volcanoes globally, according to a database by Dufresne et al. (2021). Twenty eight collapses > 0.1 km^3 have occurred since 1500 AD, implying that ca. 5 volcanic landslides occur per century on average (Dufresne et al., 2021). Volcanic collapse is globally distributed and ubiquitous across all volcanic settings. There is evidence of collapse in continental subduction settings, as in the case of Mt St Helens, at island-arc subduction settings, such as the Bismark Arc, and at intraplate ocean-islands for example at Hawaii, the Canary Islands or Cape Verde. Figure 1.1 from Dufresne et al. (2021) shows their database of volcanic debris avalanches globally, in which around half of the examples are located in Japan, the Americas and Russia. Blahůt et al. (2019) collated a database of 182 giant volcanic landslides at volcanic islands, 32 of which were in the Cape Verde Islands and 12 in the Bismark Arc.

Submarine volcanic collapse deposits have been mapped at over sixty islands (Watt et al., 2021). Multiple collapses are deduced to have come from single edifices, indicating that episodes of growth and collapse are part of the development cycle of many volcanoes. Figure 1.2 shows the global distribution of 150 islands where volcanic debris-avalanche deposits have been mapped. Volume estimates from this dataset indicate that intraplate ocean-island settings have the capability of producing larger flank collapse events compared to island arc settings.

The distribution of known volcanic collapse sites may also be biased towards countries or groups of islands that are more affluent, or spatially biased towards volcanoes that have been recently active (Blahůt et al., 2019, Watt et al., 2021). For example, in Figure 1.2, 92% of the island arc deposits mapped are from three arcs, the Aleutian, Bismark and Lesser Antilles, and from the Island of Stromboli (Watt et al., 2021). It is therefore likely that further collapse scars and deposits may be identified elsewhere in the future as exploration continues. Some populations have an increased vulnerability to this hazard due to a lack of knowledge and surveying, for example in small island developing states (Clare et al., 2018). These groups of islands also tend to have disproportionately high vulnerability to these hazards due to their remote nature, poorer economies and often having highly populated areas near sea level (Clare et al., 2018). Witham (2005) collected a database of the human impacts of volcanic events during the 20th century and found that 741 fatalities occurred as a result of volcanic

collapse with many more injured, homeless or evacuated. There is therefore continued need to pursue research into volcanic collapse.

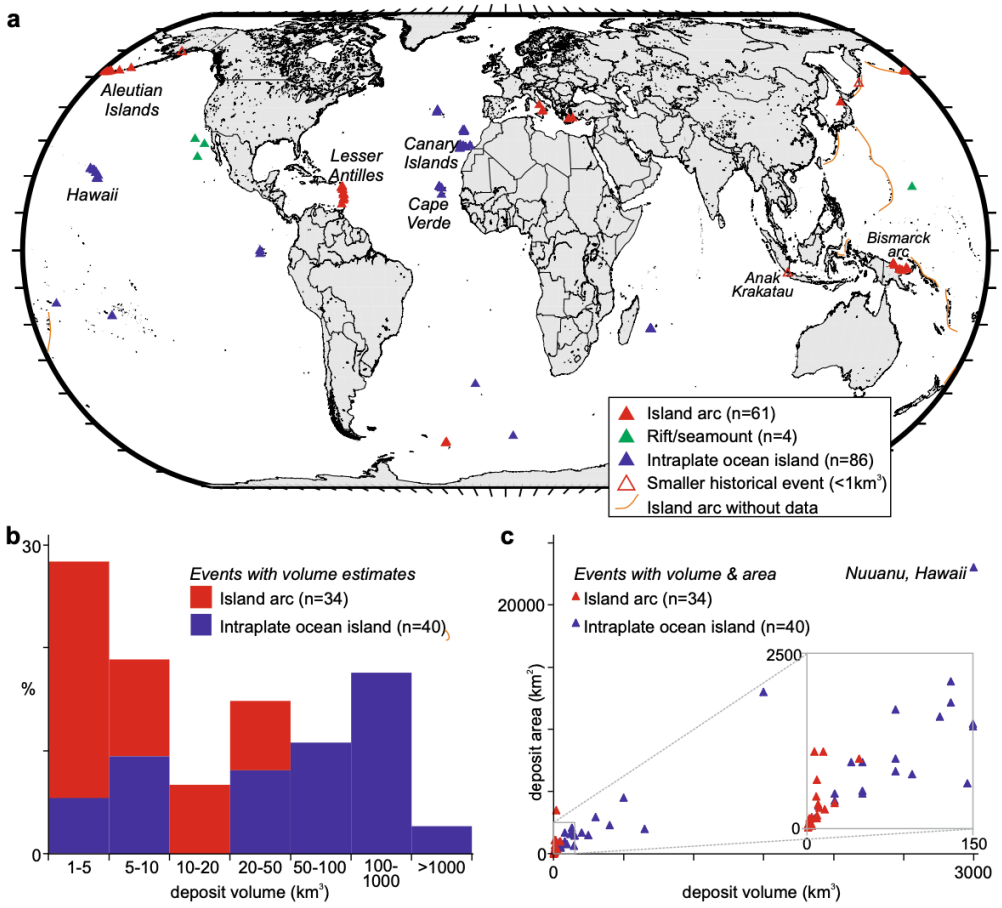

Figure 1.2: a) Global distribution of volcanic islands with debris avalanche deposits mapped distinguishing tectonic setting. b) distribution of deposit volumes and c) area vs volume of deposits (Watt et al., 2021)

There are several crucial case studies to acknowledge which have furthered the research in this area, these being Mt St Helens, the Hawaiian island chain and Anak Krakatau.

1.2.1.1 Mt St Helens case study

The collapse and eruption of Mt St Helens in 1980 was the first photographed and well documented example of flank collapse (Figure 1.3). This was summarised by Voight et al. (1981) and Glicken (1996) using photographs, eye-witness accounts and fresh deposit analysis. A magnitude 5.1 earthquake on May 18th 1980 triggered the collapse of a cryptodome on the northern flank which had grown in the weeks preceding this event (Figure 1.3) (Glicken, 1996, Voight et al., 1981). This became a debris avalanche (Figure 1.3a) that slid along a basal décollement and deposited a hummocky block facies and matrix facies as the flow scoured and mixed with the bedrock (Glicken, 1996). This slide led to a sudden

depressurisation of the magma beneath the edifice and caused a lateral blast which flowed over and deposited material on top of the debris avalanche deposit (Figure 1.3d). A Plinian eruption then followed, producing tephra that formed a widespread deposit (Glicken, 1996). This illustrated how destructive an event such as this can prompt extensive research into catastrophic volcanic collapses to create a benchmark to which other flank collapses can be compared (Voight et al., 1981).

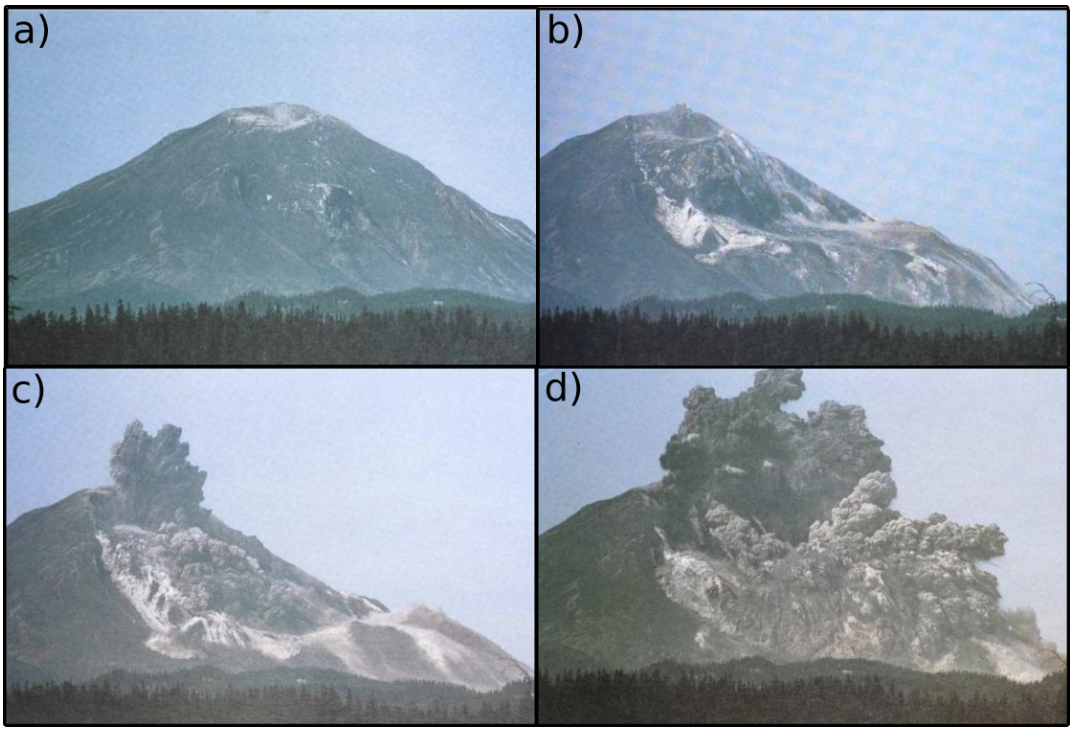

Figure 1.3: Series of images from Voight et al. (1981) displaying the stages of the catastrophic collapse and lateral blast of Mt St Helens in 1980.

1.2.1.2 Hawaiian Islands case study

Following the Mt St Helens collapse in 1980, the study of volcanic collapses increased in importance, with more prehistoric collapses being recognised. The Hawaiian Islands, a chain of volcanoes associated with hotspot magnetism in the Pacific Ocean, show many examples of flank failure. This case study showed how flank growth and collapse is a key part of a volcano's life cycle.

Initially thought to be due to erosion, the typical amphitheatre collapse scars on the Hawaiian islands were re-interpreted as the head scarps of mass failures. Moore et al. (1989) used sonar surveys along 700 km of the Hawaiian ridge to reveal > 100, 000 km^2 of exposed debris avalanche and slump deposits. These included 17 well defined landslides, as well as evidence of several older ones beneath, showing that failures occur throughout a volcano's

lifecycle (Figure 1.4)(Moore et al., 1989). Based on this evidence, it was proposed that large-scale collapses occur most often toward the end of the shield-building stage when the volcanoes are 2-4 km above sea level and the slopes are at their steepest, but at a lower rate post-dormancy (Moore et al., 1989, Iverson, 1995). Submarine surveys showed that the high velocity landslides travelled into and up the other side of the Hawaiian deep, indicating they had high enough velocities to be able to move uphill (Moore et al., 1989).

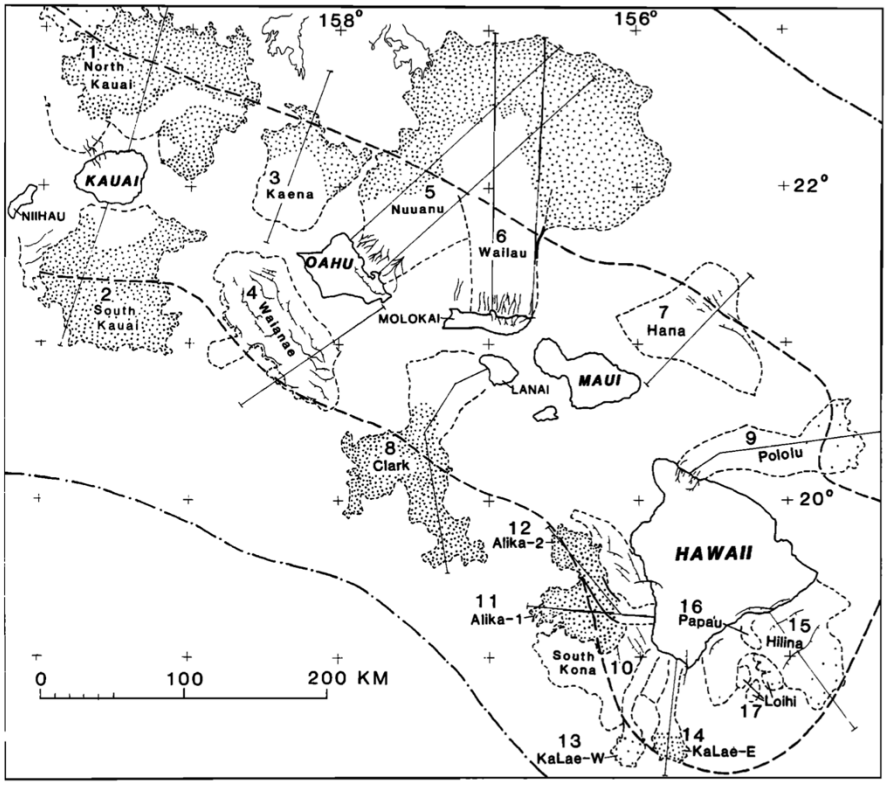

Figure 1.4: The 17 well defined landslides identified at the Hawaiian Islands, from Moore et al. (1989)

Moore and Moore (1988) found gravel deposits high on Hawaiian coasts that had been originally considered as uplifted shorelines and hypothesised that these were tsunami deposits generated from these giant volcanic landslides. One deposit, the Hulopoe Gravel, consists of three coarse units containing clasts of basalt and limestone of varying size, deposited by strong waves estimated to have been up to 375 m high from the elevation of the deposits (Moore and Moore, 1988). This event occurred 105 ka ago, based on U-series dating (Moore and Moore, 1988).

1.2.1.3 Anak Krakatau

Until the collapse of Anak Krakatau, the only volcanic-island collapse-generated tsunami with detailed observations on wave arrival times was from Ritter Island. Therefore, this event is key to understanding failure and tsunami generation processes in more detail.

On the 22nd of December 2018 Anak Krakatau experienced a major collapse which removed 50% of its subaerial volume into the Sunda Strait (Figure 1.5) (Grilli et al., 2019). This produced a tsunami with runups of 13 m in nearby populated coastal regions in as little as 30 minutes, causing at least 437 fatalities (Grilli et al., 2019). Estimations of the landslide volume range between 0.22 and 0.3 km^3 (Grilli et al., 2019).

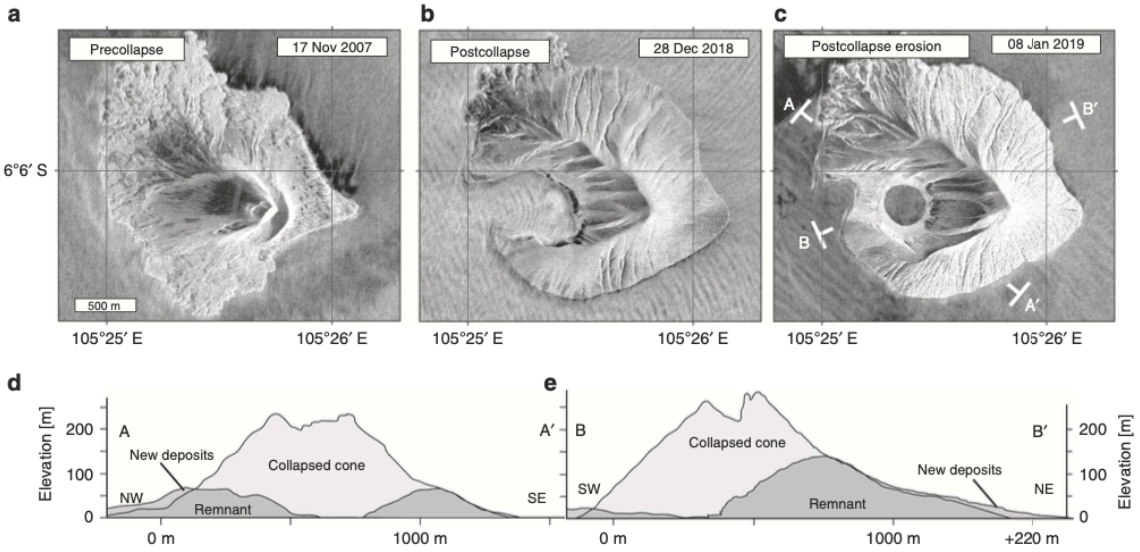

Figure 1.5: Changes in morphology following the collapse of Anak Krakatau in satellite radar imagery where a) shows the island pre-collapse, b) shows it immediately following collapse and c) shows the island after post-collapse erosion had occurred. d) and e) show the cross-sections through the island before and after collapse. Taken from Walter et al., 2019)

An early warning system for tsunamis had been installed in the region but, as it was designed for earthquake-generated events, it did not provide a warning (Zorn et al., 2023). This highlights a major issue with warning systems for such events and how monitoring flank stability is key to preventing loss of life (Watt et al., 2021, Zorn et al., 2023).

InSAR data from the years preceding the event showed how the flank was already moving before the collapse in December 2018 (Zorn et al., 2023). Accelerations in this movement were linked with two intrusion events in 2017 and 2018 (Zorn et al., 2023). The activity that began in June 2018 continued until the collapse and is likely to have contributed to the instability of the edifice due to accumulation of new material (Walter et al., 2019). The slip is suggested to have been accommodated by a décollement (Zorn et al., 2023). The single

wave train that the tsunami produced suggests failure occurred in a rapid single phase of movement (Grilli et al., 2019).

Following the collapse, extensive phreatic explosions occurred followed by volcanism which buried the landslide scar within days (Grilli et al., 2019, Walter et al., 2019). It is unclear if eruptive activity triggered the collapse of the edifice or if it was a consequence of collapse, similar to the case of Ritter Island.

This event was not only a new benchmark of flank collapse and tsunami generation but also it shows how a relatively small event, compared to other prehistoric collapse evidence, can produce devastating repercussions.

1.2.2 Hazards and impact

Collapses are usually considered to be almost instantaneous, as in the case of Mt St Helens where seismic activity was followed within seconds by the catastrophic collapse. However, in some cases, deformation may occur over a long period of time, as in the case of Etna where a section of the flank has become detached and has been sliding seawards for thousands of years (McGuire, 1996). Slumping and avalanching can be seen as end-members of emplacement mechanisms with respect to large-scale volcanic mass wasting (McGuire, 1996).

Volcanic collapses can involve the disintegration of large volumes of material and can therefore be a highly destructive hazard. A debris avalanche is where a mass detaches and moves downhill under gravity (McGuire et al., 1997). They are highly mobile, unsorted masses of rock and soil that have the potential to increase in speed and volume, therefore they can run over topography and are extremely destructive (McGuire, 1996). Clast size reduces with distance as the mass disintegrates. The avalanche tends to entrain increasing amounts of sediments and water and transitions into a debris flow (McGuire et al., 1997). They are highly scouring and destructive adjacent to the edifice and can continue at high velocities in the direction of flow (McGuire et al., 1997).

There are several secondary hazards associated with edifice collapse, which can pose an even larger risk to the surrounding area both locally and distally. Occasionally, as in Mt St Helens, a collapse will be accompanied by a lateral blast. These can be attributed to a rapid reduction in pressure as material is removed from the edifice. Magmatic eruptions can occur alongside collapse and be a triggering mechanism (McGuire et al., 1997). This can be

accompanied by other secondary hazards such as ash fall, lava flows, pyroclastic density currents or ballistics.

If a volcano is near a body of water, for example in an ocean-island or arc setting, a major secondary hazard associated with collapse is the generation of tsunamis by displacement of large volumes of water. These can be highly damaging and extends the destructive reach of the event across bodies of water and can severely affect coastal areas, as demonstrated by Anak Krakatau in 2018 (Grilli et al., 2019).

These hazardous events also have large socio-economic impacts due to their size, destructiveness and unpredictability. As these events are so destructive locally and also distally with the additional tsunami hazard, the threat to property, infrastructure and livelihood is high in areas proximal to the volcano or to the coast. There are also significant environmental impacts that occur as a result of collapse due to the dramatic way they modify the landscape, such as changes to local and distal drainage systems and patterns of erosion over long timescales (Tost et al., 2015).

Experience of the identification and monitoring of this hazard at volcanoes is minimal due to the lack recent example events and therefore there is little understanding on the complex processes that can trigger collapse. Even if a flank is identified as hazardous, then it is still difficult to determine at what point the situation becomes critical. Also, there are additional unknowns on the timing, size or direction of collapse as well as what, if any, secondary hazards may occur. This can increase the risk of this hazard to local communities if there is little or no warning preceding an event. Currently, the global tsunami warning system uses automated processing of seismic data and is therefore adept at dealing with earthquake-generated tsunamis but not volcanic-generated waves (Fan et al., 2024). The complexity of the generation mechanisms that could cause a volcanic tsunami mean that it is more difficult to interpret tsunami signals within the data (Fan et al., 2024). In addition, many potential tsunamigenic volcanoes are isolated ocean island volcanoes, often in Small Island Developing Nations. Their remote nature and probable weaker economies mean that establishing monitoring networks could also prove challenging (Fan et al., 2024, Clare et al., 2018).

This lack of or difficulty in monitoring or implementing warning systems reduces the ability to create accurate hazard maps or to issue evacuations for populations at risk. With no warning or evacuation from these highly destructive events, the threat to life is high. For example, at Anak Krakatau, there was no local warning of the collapse event that occurred. In

addition, the resultant tsunami also was not detected on tsunami warning systems, resulting in many fatalities. Following this event, there have been cases of tsunami warning from erupting volcanoes with the potential to collapse. For example, Mount Ruang, Indonesia, erupted explosively in April 2024 leading to Indonesia's national volcanology agency to predict that the volcano would collapse and cause a tsunami (Magramo, 2024). Hundreds of citizens were evacuated in this event but no tsunami occurred. This is an important advance in this hazard awareness but, in this case and many others, these warnings and evacuations were issued during an eruption. However, as seen in many cases, collapse can occur independently of any eruption and are much more difficult to monitor, predict and mitigate against.

Because of their lack of frequency, the awareness of volcanic collapse and their associated hazards is still relatively low. This means that communities are more exposed to the hazard where it is not well understood, particularly when it has never been experienced before. To convince communities to evacuate in these circumstances may also be difficult. In particular, as evacuations are issued, it is essential to have open communications between scientists, governing bodies and communities to maintain a level of trust.

In summary, the potential impact of volcanic collapse events is large, involving significant damage to infrastructure, the environment and economies as well as a threat to life. It is therefore essential to develop our understanding of these events and how instabilities develop and can potentially be monitored and hence mitigated against.

1.2.3 Collapse Morphology and deposits

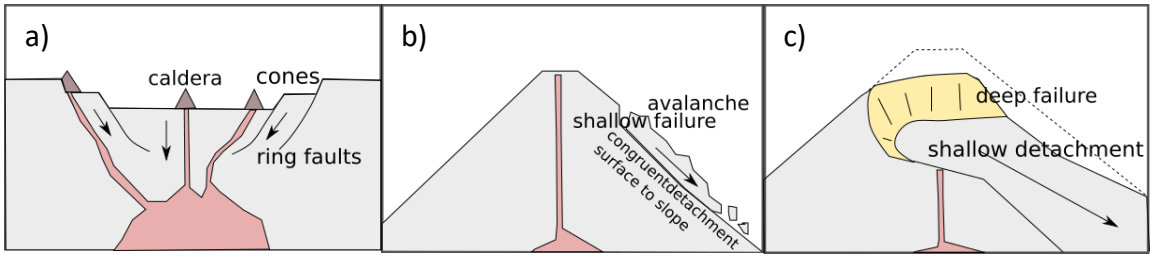

Figure 1.6: Diagrams displaying the different methods of mobilising material on volcanic flanks; a) caldera collapse; b) shallow failure; c) deep-seated failure

Several processes occur on volcanic edifices that can result in the rapid failure of large amounts of material on various scales. Caldera collapse (Figure 1.6a) occurs when material collapses into an emptying shallow magma chamber aided by ring faults surrounding the collapse. These events can also have tsunamigenic potential, for example at Santorini and Krakatau (Sigurdsson et al., 2006, Latter, 1981). Gravitational adjustments of an unstable

volcanic edifice leads to either slow spreading causing deformation at the base or to rapid flank failure (Siebert, 1984). There is evidence that edifices can transition from slow creeping deformation and accelerate into rapid avalanches (Day et al., 1997).

Flank collapse movement starts with slip on a discrete shear zone or fault zone and can result in varying scales and types of collapse (Day, 1996). Figure 1.7 from McGuire (1996) displays the range of scales and frequency of volcanic collapses. Bernard et al. (2021) defines *'the initiation phase of volcanic landslides as the translation, rapid and mostly horizontal, of one (or more) portion(s) composed of multiple volcanic units over a slide surface produced by a failure in the volcanic edifice'*.

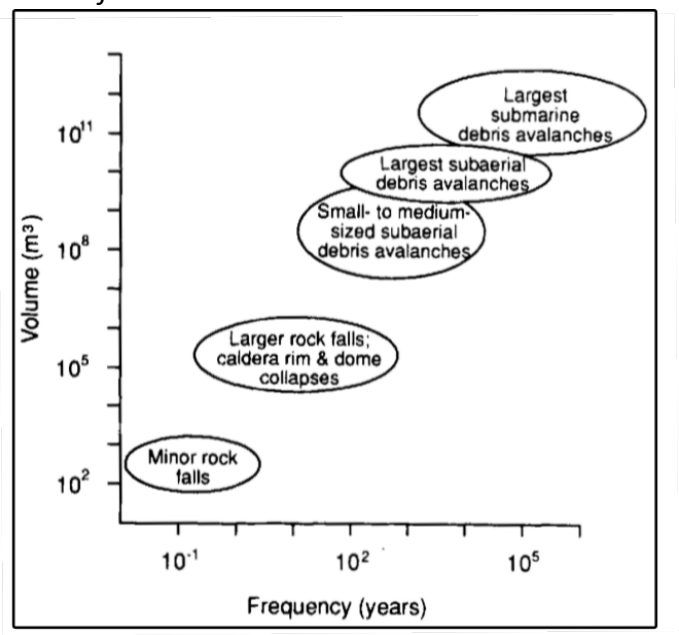

Figure 1.7: Frequency and volume of collapse events from McGuire (1996).

There are two main types of volcanic landslide: rock avalanches and volcanic debris avalanches which vary with the volume of material excavated from the source edifice (Dufresne et al., 2021). Shallow flank failure (Figure 1.6b) where failure planes are congruent to the dip of the edifice, can result in smaller rock avalanches or falls (Elsworth and Voight, 1996). Thin-skinned events, for example on Stromboli, occur more frequently than larger ones and are often associated with external triggers such as intense rainfall episodes or seismicity that can loosen material (Elsworth and Voight, 1996). These have the potential for a long run-out and may pose a small threat of tsunami generation. Lateral collapses have deep-seated failure scarps (Figure 1.6c) that produce larger volume volcanic debris avalanches and have higher tsunamigenic potential (Dufresne et al., 2021). These can have more complex and

multifaceted destabilising factors and triggering processes and are associated with deeper processes.

With respect to larger failures, Siebert (1984) used findings from Holocene collapse events to divide collapses into three main types in relation to their association with eruptive activity: Bezymianny-type, Bandai-type and Unzen-type.

- Bezymianny-type are collapses that are associated with magmatic and phreatic activity from a pre-collapse intrusion. Mt St Helens is an example of this.
- Bandai-type are collapses associated with phreatic eruptions and hydrothermal discharges but no pre-collapse intrusion
- Unzen-type are collapses involving hydrothermal discharge but no explosive activity or pre-collapse intrusion.

However, it is challenging to classify older collapses in terms of these types because the involvement of magmatic activity is often difficult to determine.

The volcanic landslide scar is the depression formed during a volcanic landslide. Siebert (1984) used studies of various deep-seated collapses worldwide to describe characteristic morphologies of flanks that have experienced collapse. Bernard et al. (2021) later proposed a descriptive scheme based on these features to describe the quantitative parameters of the collapse scar and the shape of the scar.

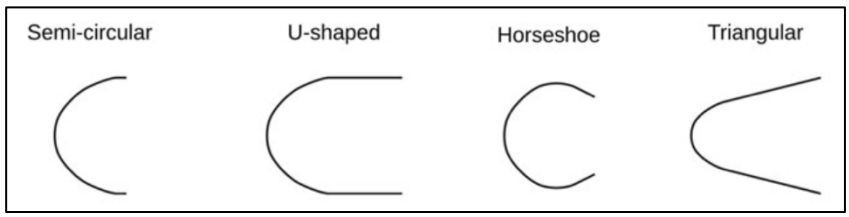

Figure 1.8: Plan view of common shapes of volcanic landslide scar from Bernard et al. (2021)

Scars are usually 'amphitheatre' shaped, lengthening in the direction of landslide emplacement. The depressions are often deeper than they are wide, have high sidewalls, gently sloping floors and a sharp break in profile marking the headwall of the scarp (Siebert, 1984). Bernard et al. (2021) suggests four possible descriptive terms for the scape of the scar: semi-circular, U-shaped, horseshoe and triangular (Figure 1.8). A semi-circular scar has a width twice as long as its length. A U-shaped scar has a semi-circular headwall with parallel side walls with a longer length than width. Horseshoe-shaped scars have a smaller aperture than

their maximum width and triangular scars have divergent linear side walls (Bernard et al., 2021).

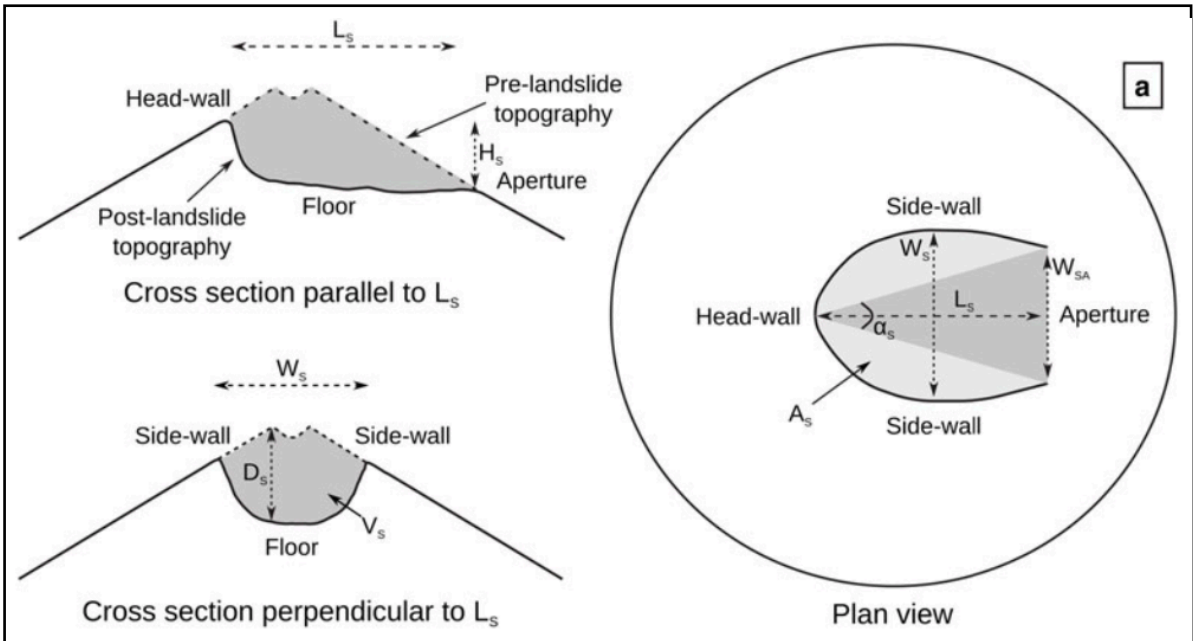

Acronym	Descriptive parameter	Definition
L_S	Scar length	Distance from the head-wall to the middle of the aperture
W_S	Scar width	Maximum distance between the side-walls, orthogonal to the length
W_{SA}	Scar aperture width	Distance between the side-walls at the aperture
H_S	Scar height	Height between the top of the head-wall and the aperture
α_S	Scar aperture angle	Angle between the lines drawn from the head-wall to the side-walls extremity
β_S	Scar slope	Slope between the top of the head-wall and the aperture (β_S = atan H_S/L_S)
γ_S	Scar azimuth	Azimuth of L_S
A_S	Scar area	Surface of the scar in plan view
D_S[a]	Scar depth	Maximum depth of the scar between the pre and post-landslide topography
V_S[a]	Scar volume	Volume difference before and after the landslide
T_S[a]	Scar thickness	Average thickness ($T_S = V_S/A_S$)
AR_S	Scar aspect ratio	Ratio between the average thickness and the radius of a circle of equal area ($AR_S = T_S/\sqrt{(A_S/\pi)}$)
EF_S	Elongation factor	Ratio between the scar length and width ($EF_S = L_S/W_S$)
CF_S	Closure factor	Ratio between the scar aperture width and the scar width ($CF_S = W_{SA}/W_S$)

[a]Parameters with a large error if pre- or post-landslide topographies are poorly known

Figure 1.9: Geometrical parameters defined on cross sections and plan view of a typical scar (above). Table (below) defining these quantitative parameters. By Bernard et al. 2021.

Bernard et al. (2021) described the three main morphological features of a volcanic landslide scar as the 'wall' (the steep portion of the scarp), the 'floor' (the flat interior of the depression), and the 'aperture' which measures the region between the lowermost points of the wall. The walls can be separated into the headwall and sidewalls, the sidewalls being

parallel to the direction of the landslide. The parameters indicated in Figure 1.9 provide a good basis on which to compare different volcanic landslides.

The position of a collapse scar within a volcanic edifice probably depends on the local and regional stress regimes. Typically, volcanoes that experience these regional stresses have a three-armed morphology, roughly 120° apart due to upward loading (Fiske and Jackson, 1972). These are expressed in swarms of dykes, fissures and parasitic cones parallel to maximum compression (Siebert, 1984, Foeken et al., 2009). Intrusions along these zones creates oversteepening, loading effects and differential stress under a volcano and, when these reach a threshold value, large-scale collapse can occur. The axis of the collapse scar therefore tends to be perpendicular to these stress regimes between branches, although this may also be influenced other elements, for example by topography or pre-existing structures (Siebert, 1984). Figure 1.10 depicts this typical relationship between the triple-armed morphology and location of collapse scars seen at many island volcanoes.

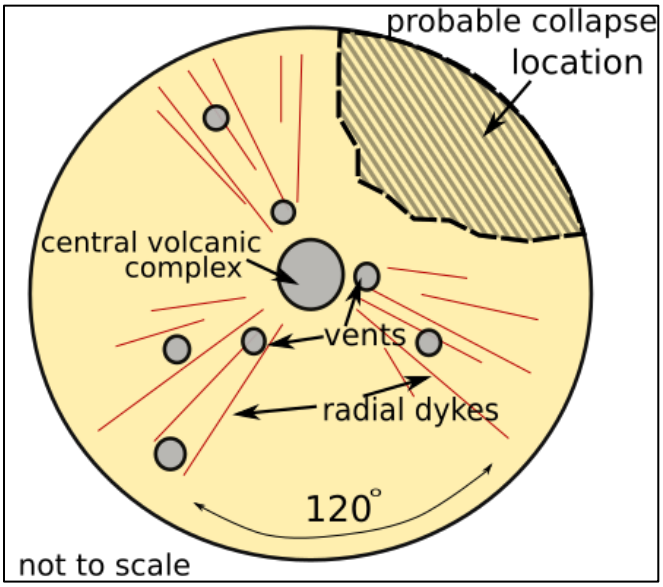

Figure 1.10: Diagram showing typical triple-armed morphology of volcano expressing regional stresses and area of likely collapse.

A description of the transport phase of the flow is defined by Bernard et al. (2021) as '*a rapid water-unsaturated gravity driven mass movement of multiple volcanic units'.* At the base of the scar, whether it is subaerial or submarine, there tends to be a hummocky terrain composed of the deposited material. This often contains mega-clasts and usually forms a lobate deposit (Siebert, 1984). A volcanic debris avalanche deposit is composed of epiclastic, unsorted, heterogenous and heterometric breccias derived from the original edifice as well as entrained material from the transport path (Bernard et al., 2021, Siebert, 1984).

Bernard et al. (2021) has defined the different facies within a volcanic debris avalanche deposit (VDAD). These facies include, from proximal to distal, the edifice block facies (EBF), the substratum block facies (SBF) and the mixed facies (MF). A typical feature seen in these deposits are jigsaw cracks, a chaotic fracture network observed at all scales and in seen all of the facies (Bernard et al., 2021). The deposit forms a hummocky topography which is a widespread area of hills and depressions (Siebert, 1984). Torevas are intact sections of the edifice that have moved a short distance from the source with some rotation (Bernard et al., 2021). The volume of the primary failure is that of the material excavated from the edifice. However, the volume of the deposit includes the entire mass that was deformed or mobilised resulting from the initial failed mass, and can therefore be much greater (Watt et al., 2021).

1.2.4 Controls on stability

Volcanoes can become unstable due to a number of factors and a triggering mechanism can cause mobilisation of the unstable mass by weakening frictional forces (McGuire et al., 1997). The structure of an edifice, and the way in which it grew, can be a source of instability that may lead to collapse. This can include the properties of the basal layer on which the volcano is built, layers of weaker rock, hydrothermally altered regions, intrusions and faults (Romero et al., 2021, Heap et al., 2021a, Heap et al., 2021b, Zernack and Procter, 2021, Bakker et al., 2015). Edifice stability also responds to external factors such as seismicity or erosion.

A volcanic edifice can become unstable due to a several different processes operating over varying timescales. During a volcano's lifecycle, it may have one or more phases of collapse. Multiple collapses are known to have occurred on a single edifice, with evidence of up to 19 collapses at a single volcano (Dufresne et al., 2021).

A trigger mechanism will cause mobilisation of a previously developed instability by weakening frictional forces, allowing material to accelerate downslope. A slope fails as a result of shear stresses acting parallel to the surface on shear planes, generating shear strain deformation. The resistance to the shear strain is the shear strength, which is dependent on the ratio of a number of different characteristics according to the Mohr-Coulomb failure criterion (Coulomb, 1776). Equation 1.1 defines the shear strength of a fault, T_f, where C refers to the cohesion of a material, μ is the frictional coefficient, σ_n, the normal stress (MPa) and the p_f, pore fluid pressure (MPa).

Equation 1.1: Shear strength of a rock according to Mohr-Coulomb failure criterion

$$T_f = C + \mu(\sigma_n - p_f)$$

There are several different forces in place on an edifice including gravitational, lithostatic, hydrostatic, magmastatic and frictional (Figure 1.11). The main causes of destabilisation include seismicity, magmatic activity, hydrothermal alteration or gravitational spreading when these forces are forced into an imbalance (Andrade and de Vries, 2010). The mechanical properties of the rocks making up the edifice are key factors in the stability of the volcano and can be influenced by many processes. The type and direction of collapse is controlled by the edifice morphology including the structural setting and presence of any weak layers (Acocella, 2005). Figure 1.12 provides an overview on how the structure of an edifice can affect the instability of its flanks and shows various methods of triggering that will be further discussed.

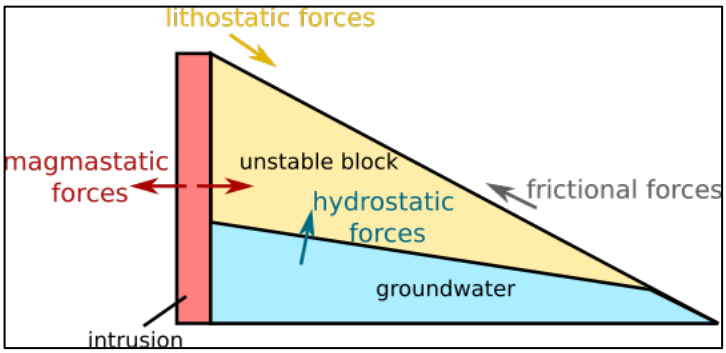

Figure 1.11: Diagram showing different types of forces acting to destabilise a block in a volcanic edifice (adapted from Ray, 2017).

The main factors leading towards instability in volcanic edifices are:

1. The frequency of intrusion emplacement
2. Presence of weak basement
3. Hydrothermal alteration
4. Steep edifices with a slope near the critical angle
5. Fault systems
6. The mechanical properties of the volcanic rock
7. Susceptibility to external forces including climate change.

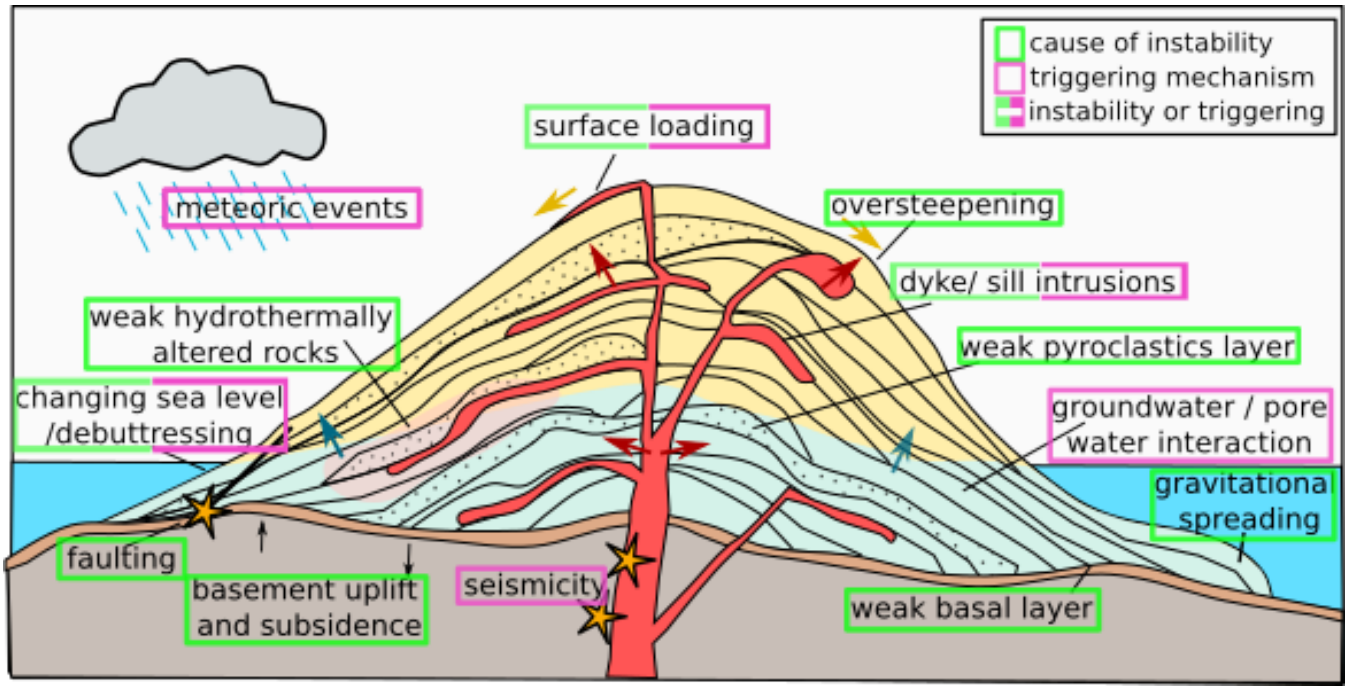

Figure 1.12: Diagram showing structure of volcanic edifice with factors leading towards instability and highlighting various triggering mechanisms. Adapted from McGuire (1996).

1.2.4.1 Intrusion emplacement

In polygenetic mafic systems, basaltic dykes are common and, when they reach the surface, they can feed central vent, flank or fissure eruptions (Romero et al., 2021). This can be in the form of radial dykes or sub-parallel sills. The geometry of dyke intrusions and fractures react to the heterogeneities in the flank, load and interactions between other dykes and faults (Gonzalez-Santana et al., 2023). Dyke emplacement is usually perpendicular to the minimum principle compressive stress and reflect the regional stress regimes. Because of this preferential emplacement orientation, continued dyke intrusion and volcanism along a particular axis over time leads to an imbalanced build-up of material. Magmatic and hydrothermal pressures increase with the emplacement of dykes, pushing the flanks outward (Elsworth and Voight, 1996). For example, during dyke emplacement within the edifice at Etna in 2001, instability developed within the flank as a result (Battaglia et al., 2011). This was suggested to be due to the induced lateral forces, and hydrothermal weakening was minimal and therefore may work over a longer timescale (Battaglia et al., 2011).

Intrusions into volcanic edifices cause slopes to deform and over-steepen, as well as causing localised seismicity up to magnitude 7 (McGuire, 1996, Romero et al., 2021). Dykes can also be emplaced along pre-existing faults within the edifice. Additionally, lateral forces

applied from growing magma chambers can increase shear stress on flank faults, which can push them closer to failure (McGuire, 1996). Intrusions also produce large amounts of thermal energy within the flanks and influence pore fluid pressures and thus the strength of the surrounding rocks. The rocks making up the edifice also vary in strength in response to prolonged loading and unloading, suggesting that they can accumulate damage from repeated dyke intrusions (Romero et al., 2021).

Before an edifice collapses, it may show some signs of instability by creeping seaward. This creates extensional forces along an axis which can lead to significant changes in dyke architecture (Walter and Troll, 2003). Swarms and rift zones can propagate as a result, the axis of which may be determined by the stress field in the edifice and is an alternative suggestion to how triple-arm junctions are formed (Walter and Troll, 2003).

Gonzalez-Santana et al. (2023) used numerical models to suggest that shallow intrusions tend to facilitate slip on shallow-dipping faults whereas deeper intrusions favour slip in steep edifices on steep faults. Volcanoes with higher rates of magmatism generally show increased instability and flank slip. Intrusion and earthquake events can increase this rate of slip (Poland et al., 2017, Zorn et al., 2023). The flank collapse of Anak Krakatau in 2018 was preceded by gravitational movement on the flank facilitated by a décollement (Zorn et al., 2023). This movement was accelerated by the emplacement of magma within the flank during periods in 2014 and 2018 (Zorn et al., 2023). In total, the south-western flank moved 1.1 m over a four year period (Zorn et al., 2023).

1.2.4.2 Hydrothermal alteration

Complex geothermal systems develop in volcanic areas due to the interaction between magmatic gases and groundwater (López and Williams, 1993). By studying altered 'halos' surrounding intrusions, Engvik et al. (2005) suggested that volatile-rich melts can propagate hydraulic fractures during emplacement. Fluids are emplaced from the tip of the main fracture, creating alteration halos surrounding the intruding rock. This means that the emplacement of intrusive rocks may locally increase permeability in their host rocks.

Hydrothermal fluids cause different types of alteration which can play a major role in changing the strength of the rocks and increasing susceptibility to failure. Equation 1.2 is a derivative of an equation by Hubbert and Rubey (1959), given by Day (1996). It expresses how the critical angle of inclination (degrees), θ_c, depends on pore pressure (MPa) (as a fraction of

lithostatic load), λ, and the frictional coefficient, μ, assuming the cohesive strength on a slide surface is zero.

Equation 1.2: Critical angle depending on pore fluid pressure and friction

$$\boldsymbol{tan\theta_c = (1-\lambda)\mu}$$

The critical angle describes the maximum angle at which a slope can stand unsupported. From Equation 1.2, an increased pore pressure will decrease the critical slope angle, making it more likely to fail. This relationship can be dictated by the permeability and porosity of the rock type by allowing fluid pressure to build up or dissipate. This critical angle should be monitored closely when assessing hazardous volcano collapse scenarios.

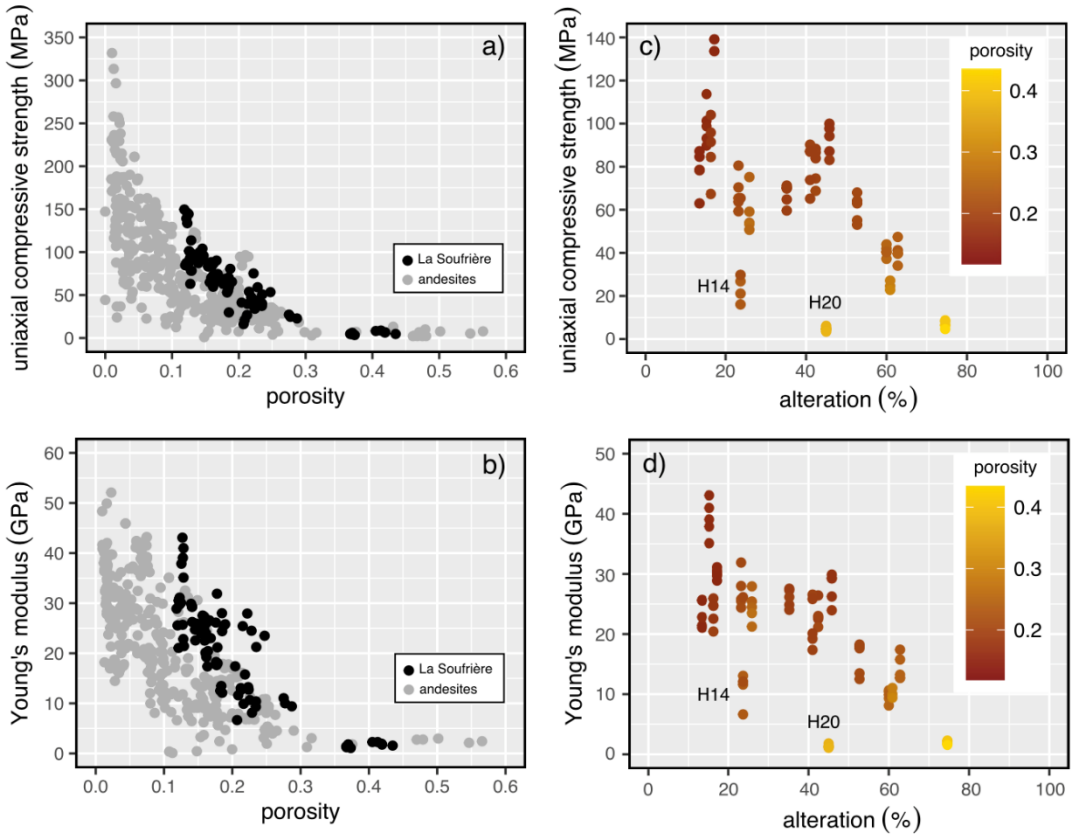

Figure 1.13: From Heap et al. (2021) showing a) uniaxial compressive strength and b) Young's modulus against porosity of Andesites from La Soufrière and other andesites. c) uniaxial compressive strength and d) Young's modulus as a function of alteration indicating porosity.

Some types of alteration can reduce permeability of rocks due to mineral precipitation in pores and microfractures (Heap et al., 2019). Laboratory samples showed decreasing permeability by four orders of magnitude (Heap et al., 2019). This can lead to the build-up of pore fluid pressure in volcanoes to the extent that it could cause fragmentation of dome materials and stimulate explosive eruptions, as well as promote spreading and lead to flank

collapse (Heap et al., 2019). Heap et al. (2021a) used measured rock properties in numerical models and found that high pore fluid pressure zones increase flank deformation.

Other types of alteration can increase dissolution and cause an increase in permeability and thus a decrease in strength. This can be caused by acid-sulphate leaching increasing the amount of clay minerals (del Potro and Hürlimann, 2009). Hydrothermal alteration can reduce the frictional coefficient of a volcanic edifice by increasing the proportion of clay minerals (Day, 1996, Romero et al., 2021). Following Equation 1.1, this reduction in friction coefficient will reduce the shear strength of a rock and, in turn, from Equation 1.2, reduce the critical angle of a slope, making it more likely to fail. Clay-rich units resulting from hydrothermal argillic alteration can be some of the weakest materials within an edifice (del Potro and Hürlimann, 2009).

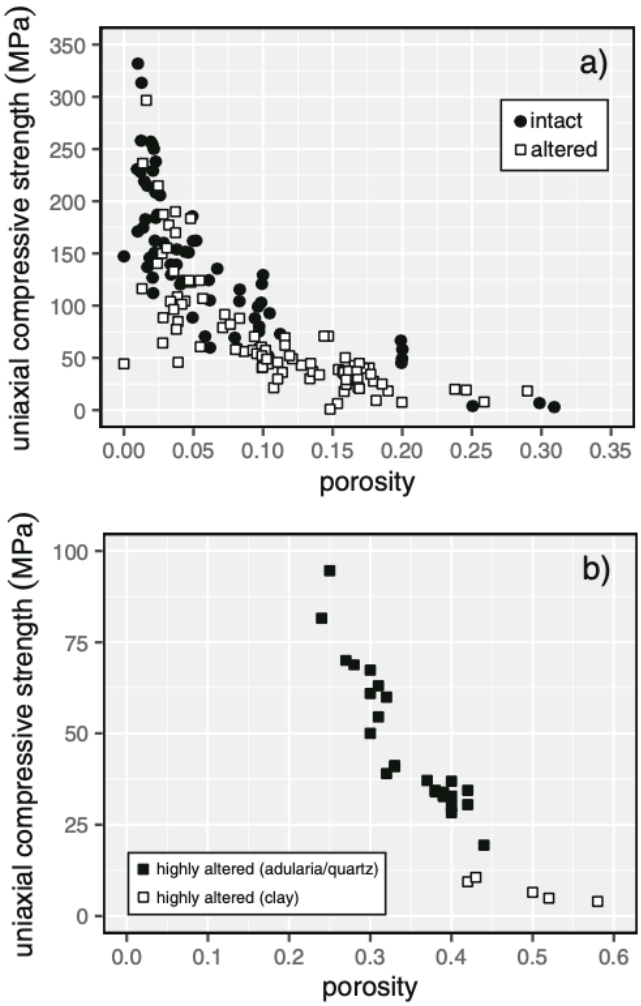

Figure 1.14: Uniaxial compressive strength as a function of porosity comparing a) intact and altered rock and b) the type of alteration. From Heap and Violay, (2021).

As a basalt weathers, there is a rapid loss of CaO and MgO concentrations which can lead to a significant loss in strength of up to 43% of bearing capacity (Romero et al., 2021).

Heap et al. (2021b) analysed altered and non-altered rocks from La Soufrère de Guadeloupe. They found that the advanced argillic alteration reduced uniaxial compressive strength, Young's modulus and cohesion significantly (Figure 1.13). Using these values with numerical modelling, it was concluded that this, in turn, affects the volcano stability and promotes volcano spreading and increases the likelihood of collapse (Heap et al., 2021b).

The presence of alteration can largely affect the mechanical response of the rock. Depending of the alteration type, it can either increase or decrease porosity (Figure 1.14b). This clear relationship between alteration and the stability of an edifice means that it should be monitored at volcanoes with risk of collapse.

1.2.4.3 Edifice steepening and gravitational loading

Continued extrusive volcanism on flanks leads to increased surface loading from the deposition of additional material as well as creating steeper slopes. Polygenetic edifices are often constructed in rapid eruptive stages, forming unstable slopes with steep upper flanks (Zernack and Procter, 2021). Material that builds up can include lava domes or flows, tephra fall and pyroclastic density currents, ash layers, lahars and debris flow deposits (Zernack and Procter, 2021). Continued extrusion and intrusion cause steepening to near the critical angle of roughly 30–40°. Over long periods, where edifice construction rates overtakes erosions rates, edifices can approach their natural stability (Zernack and Procter, 2021). A large collapse will therefore restore forces back to an equilibrium in response to a triggering mechanism. Strato-volcanoes rarely reach heights greater than 3000 m (Zernack and Procter, 2021). A feedback cycle can occur where persistent flank slip facilitates more dyke intrusions and eruptions, hence increasing gravitational loading causing more slip (Gonzalez-Santana et al., 2023, Poland et al., 2017).

The type of substrate on which a volcano is built is also important, as gravitational spreading occur on weaker or sloping basements to accommodate sliding, hence creating instability through an edifice (McGuire, 1996, Gonzalez-Santana et al., 2023, Poland et al., 2017). There are many examples of volcanic spreading at a variety of scales. For example, at Etna, it has been proposed that the slow spreading of its Eastern flank is accommodated by ductile flow of carbonate basement units (Bakker et al., 2015, Castagna et al., 2018). Borgia (1994) identified and described five different stages of growth an edifice may experience leading to spreading. Gravitational spreading occurs when there is a layer of unconsolidated

material within the substrate, for example pumice-rich pyroclastic sequences. This layer may show ductile deformation under the weight of the overlying volcano and therefore slowly flows outward. This can occur radially or in a single direction (Andrade and de Vries, 2010, Borgia, 1994). From this, a variety of structures develop within an edifice to accommodate this movement including intersecting grabens dividing the edifice into segments, and fold and thrust belts at the base of flanks (Andrade and de Vries, 2010). Typically, a volcano spreads to flatten the edifice as a natural response to prevent collapse. However, there are occasions where spreading leads to destabilisation and ultimately collapse (Andrade and de Vries, 2010). Andrade and de Vries (2010) propose that gravitational spreading acts as a destabilising factor that enhances the probability of catastrophic collapse during early stages of volcanic growth where segments are established and flanks are still steep. Mt Etna is an example of a volcano that is slowly spreading. The frequency of these growth and collapse cycles are suggested to be controlled by the edifice growth rate, the eruptive style of the volcano, instabilities within the edifice and the scale of any preceding collapses (Zernack and Procter, 2021).

Over long periods, gravitational spreading is often the driving force behind why many volcanic flanks are slipping seaward, however magmatic activity can play a larger role in this movement in some flanks (Figure 1.15) (Poland et al., 2017).

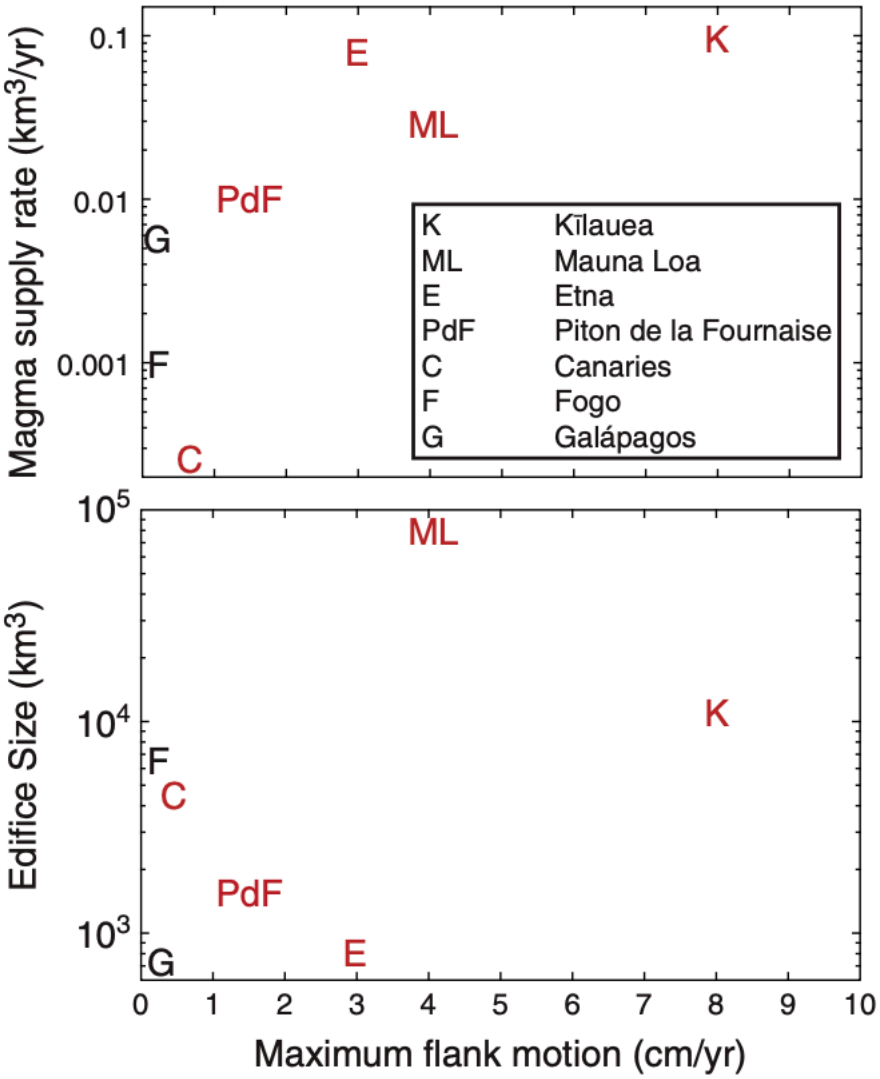

Figure 1.15: Comparing flank motion to magma supply (top) and edifice size (bottom) from Poland et al., 2017.

1.2.4.4 Mechanical properties of volcanic rocks

Assessing the mechanical properties of rocks that make up these unstable edifices is essential to understand how and why they might deform. The mechanical behaviour of volcanic rocks varies due to differences in microstructure and mineralogy (Heap and Violay, 2021). This includes varying porosity, pore geometry, crystal content and geometry, glass content, extent of microcracking or level of alteration (Heap and Violay, 2021). The array of mechanical and

hydraulic properties can create different failure modes in an edifice that may be triggered depending on prevailing conditions.

Porosity is important in assessing volcanic rock properties, as it strongly influences the permeability and the strength of a rock. Volcanic rocks have wide ranges of porosity as a result of complex compositions, magma ascent and emplacement (Heap et al., 2014, Shea et al., 2010). The type and geometry of pore spaces are also important in determining the strength and permeability and manner of deformation (Figure 1.16) (Heap et al., 2018, Heap et al., 2021b). In volcanic products, porosity is determined by the vesicularity of the rock and any micro- or macro-fractures that may be present. The size, shape, quantity and distribution of the vesicles depend on physical processes that control magma ascent and eruptions (Shea et al., 2010). Vesicle nucleation is determined by the magma properties including viscosity and volatile content and their growth depends on degassing during ascent (Shea et al., 2010). In low viscosity melts, lower vesicularity can form as a result of coalescing and outgassing. Higher rates of magma ascent can result in a larger number of vesicles (Lautze and Houghton, 2007). Therefore, low viscosities, more likely in more mature melts, with high ascent rate often forms the most bubble-rich melts.

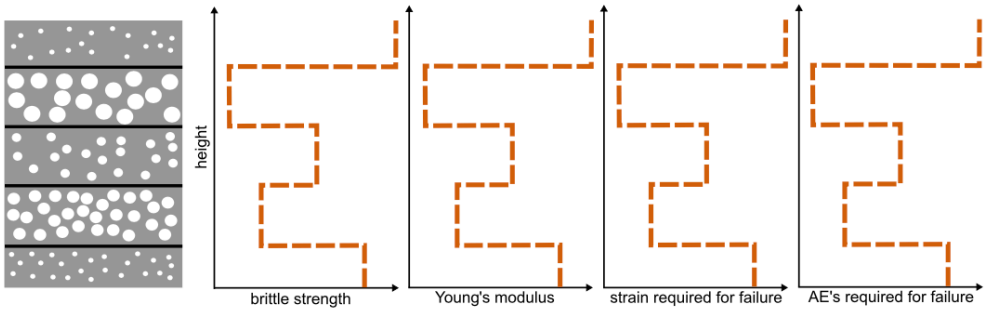

Figure 1.16: The change of strength, Young's modulus, strain at failure and acoustic emissions required for failure in lava strata containing variable porosity and vesicle sizes from Heap et al. (2014).

An increase of porosity and vesicle diameter result in a reduction of strength, for example an increase of porosity from 0 to 40% results in a reduction of uniaxial compressive strength by a factor of 5 (Heap et al., 2014). This is attributed to the presence of vesicles locally amplifying stress within groundmass and promoting the nucleation of microcracks that, with increasing stress, coalesce resulting in macroscopic failure (Heap et al., 2014). This means that edifices built from explosive activity, i.e., with high volatile content and porosity are more likely to form unstable layers and create unstable structures whereas effusive eruptions i.e. low volatile porosity content, may form stronger edifices (Heap et al., 2014). Tuffs tend to deform by distributed cataclastic pore collapse whereas extrusive porous rocks are more likely

to form localised compaction bands where pores are connected by microcracking (Heap and Violay, 2021, Heap et al., 2015). More porous rocks may also allow increased hydrothermal fluids into the rock and thus influence the level of alteration.

Permeability is important within a volcano as it dictates the distribution of fluids and of pore fluid pressure within the flanks (Heap et al., 2018, Heap et al., 2021b). The porosity, including pore size, shape and tortuosity of pathways as well as the presence of fractures, control the permeability of a rock and therefore volcanic rocks can have wide ranging permeabilities (Figure 1.17) (Wright et al., 2009, Eggertsson et al., 2020). Low permeability layers prevent dissipation of fluids and can lead to an increase of pore fluid pressures. The build-up of pore fluid pressure can promote explosive volcanism and instabilities leading to flank collapse. Permeability tends to increase as a function of porosity in volcanic rocks with some variation as a result of the presence of pore connectivity and micro-fractures (Figure 1.17) (Eggertsson et al., 2020). Alteration can either increase permeability through dissolution (Heap et al., 2021b), or decrease it through precipitation (Heap et al., 2021a). Increasing confining pressure at depth can reduce permeability due to crack closure, if present. During loading and unloading, these cracks may not recover fully resulting in permanent changes in permeability (Eggertsson et al., 2020).

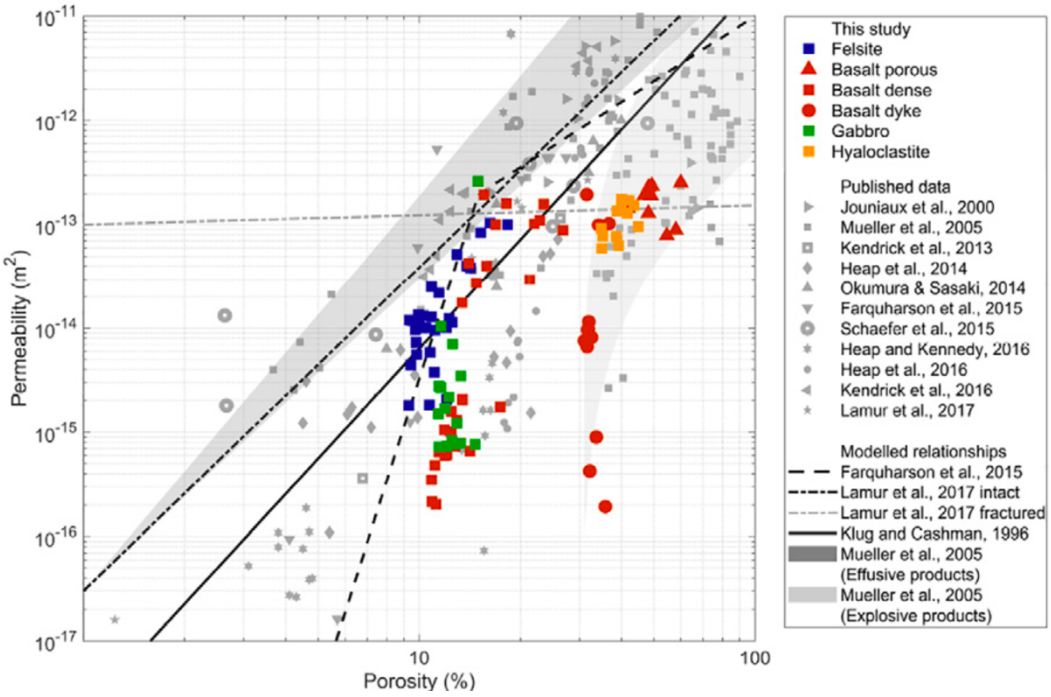

Figure 1.17: Permeability as a function of porosity for previously published datasets from Eggertsson et al. (2020)

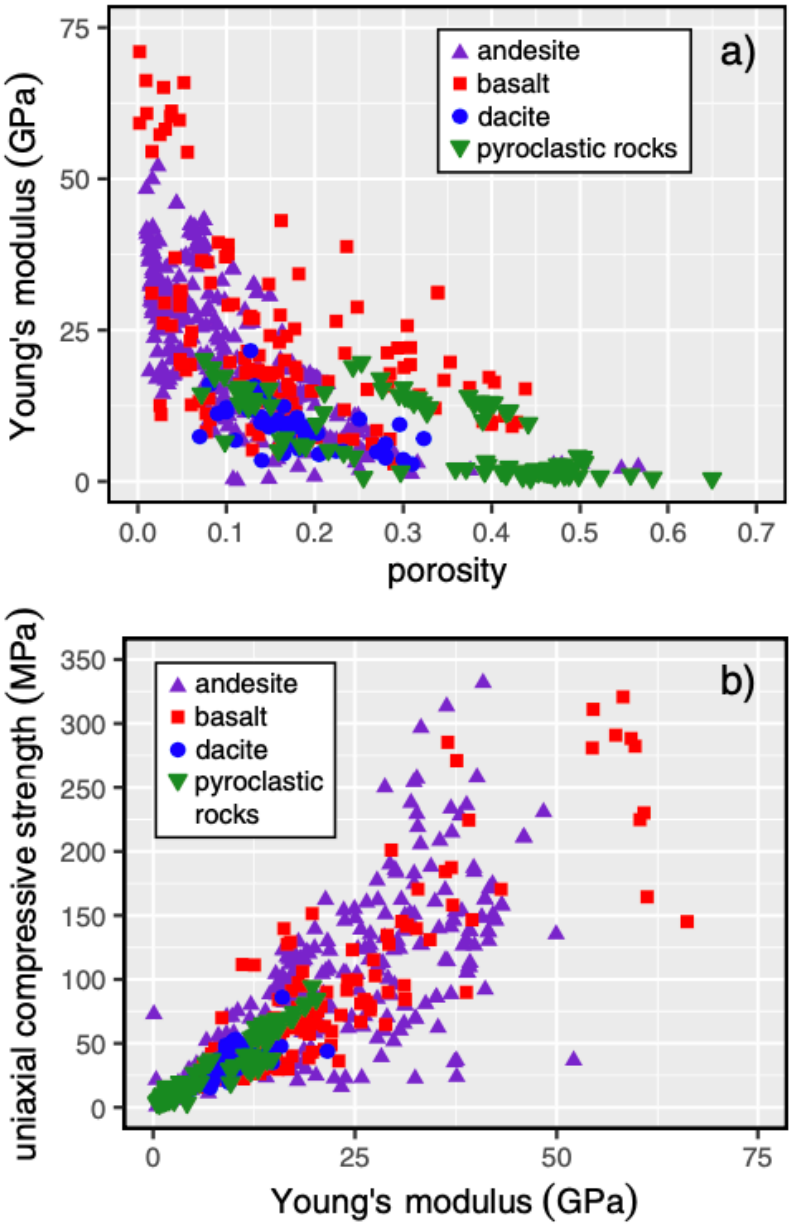

Figure 1.18: From Heap and Violay, 2021. a) Young's modulus as a function of porosity. b) UCS as a function of Young's modulus for a variety of volcanic rocks.

The uniaxial compressive stress (UCS) of volcanic rocks has been studied to assess variations in the strength of rocks in these settings. The UCS has been shown to decrease as a function of porosity (Figure 1.18). Figure 1.18a suggests that the UCS decreases nonlinearly with increasing porosity and there is some scatter in the data with a larger range of possible strengths at low porosities and a smaller range at high porosities (Heap and Violay, 2021). Figure 1.18a shows that pyroclastic rocks have a range of porosities but low UCS compared to basalts and andesites which have a wider range of porosity and strength. Basalt shows more scattered data compared to andesites. This scatter may be because of the variety of characteristics that can occur. The presence of phenocrysts and microlites may create weaker

rocks due to the presence of microcracking that may act as foci for stress concentration (Heap and Violay, 2021). Rock strength is also suggested to decrease as a function of pore size (Heap and Violay, 2021).

The Young's modulus represents the stiffness of a rock and describes the relationship between stress and strain. This is useful to determine how rocks will behave when deformed. Figure 1.18b suggests that the UCS increases as a function of Young's modulus for all volcanic rocks. The plot shows a better defined trend at < 10 MPa and more scatter at > 10 MPa due to the range in characteristics (Heap and Violay, 2021). Pyroclastic rocks are characterised by low Young's modulus and UCS, whereas there is a wider range for basalts and andesites (Heap and Violay, 2021).

The mechanical behaviour of volcanic rocks is variable and these differences can have huge effect on the stability of volcanic edifices (summarised in Figure 1.19). Therefore, further parameterisation of mechanical properties of volcanic rocks generally and more specified for different volcanoes will improve mitigation power (Schaefer et al., 2015).

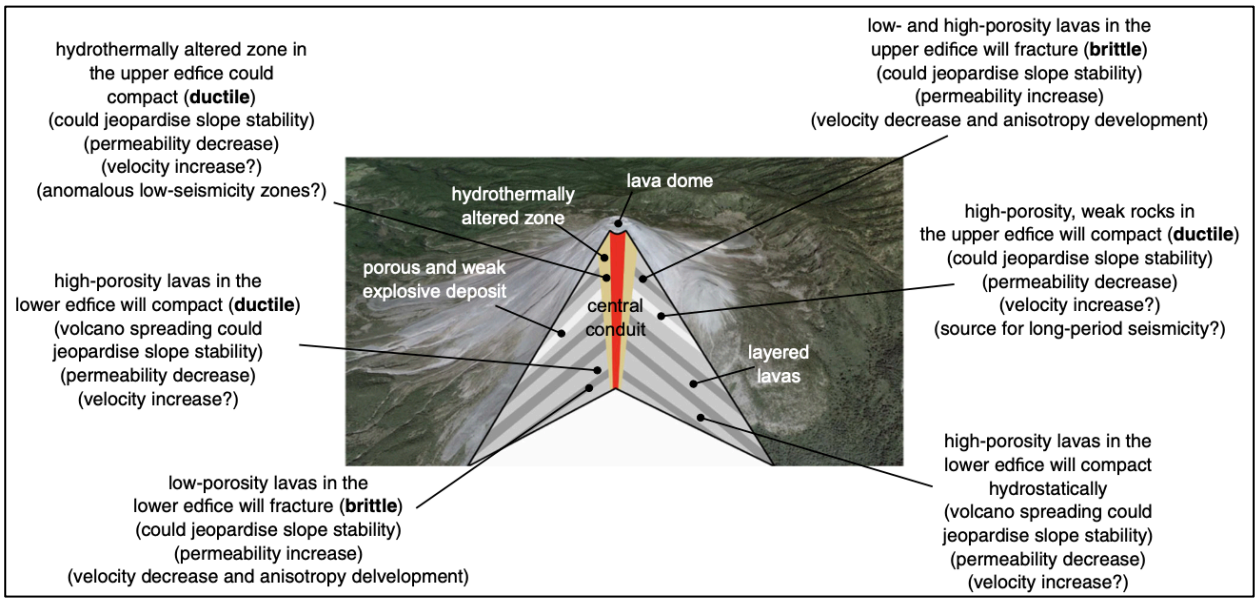

Figure 1.19: Diagram of a typical structure of a stratovolcano highlighting behaviour and failure process for volcanic rocks from Heap and Violay, 2021.

1.2.5 Triggering mechanisms

Several triggering mechanisms have been proposed to be the cause the collapse of an unstable edifice. A triggering mechanism will create an imbalance of forces which will overcome the frictional forces holding a block in place. The triggering mechanism of catastrophic collapse is geologically instantaneous (Vidal and Merle, 2000, Andrade and de Vries, 2010). Triggers can include exogenic causes such as removal of a buttress that had been

providing lateral support, increasing load on slopes, meteoric events. Endogenic causes involve the change in pore fluid pressures such as dyke emplacement, seismicity or eruptive activity (Andrade and de Vries, 2010). It is likely that several factors working together may be responsible for the weakening and triggering of an edifice collapse (McGuire et al., 1997).

Many triggers for past volcanic collapses have been related to magmatism (Bezymianny-type collapses). In these cases, triggers may include magma reservoir replenishment, the filling of magma conduits, and dyke emplacement (McGuire, 1996). Seismicity can also be a trigger for collapse by weakening frictional properties in a rock as regional or local seismicity are common in volcanic areas. Reactivation of basement faults can also trigger a lateral collapse (Vidal and Merle, 2000).

For collapse events with no clear magmatic association, i.e., Bandai- or Unzen-type collapses, it is more difficult to find an associated triggering mechanism. Evidence for triggers includes phreatic explosions or presence of hydrothermal alteration has shown that fluids also play an important role in the mechanical failure of flanks (McGuire, 1996).

The effect of pore fluid in a fault system can reduce shear strength by increasing pore fluid pressure according to Equation 1.1 (if P_f *increases,* T_f decreases) and therefore reduce the critical angle of inclination of a slope (Equation 1.2). Fluid pressure will therefore weaken materials so they can deform under lower differential stresses that would otherwise be insufficient for failure (Fossen, 2016). In theory, pressurisation can increase hydrostatic pressure (the pressure from a given weight of water) over lithostatic pressure (the pressure imparted from a given thickness of rock overburden) if fluids are unable to dissipate fast enough. If high enough, forces can switch from compressional to tensional forces within the pore spaces or fractures of a rock. These scenarios may occur in extreme circumstances where magmatic intrusions induce pressurisation within impermeable host rocks where fluid cannot migrate away quickly. The shear strength of the basal failure plane can be reduced through mechanical or thermal induced pore fluid pressurisation (Elsworth and Voight, 1996).

Water-saturated volcanoes are vulnerable to the weakening effect of hydrothermal pressurisation. However, the resultant instability can be difficult to determine as it also depends on a variety of other factors including temperature distributions, porosity, permeability and rheology of rocks and any fault geometries (Day, 1996). Material properties of a volcanic edifice, such as permeability and pore dilation behaviour, govern the predisposition to collapse and are key factors in controlling the extent of pore fluid

pressurisation (Lachenbruch, 1980). For example, the strength will determine how the volcano will deform under stress and whether it will experience slip hardening in self-limiting small movements, or slip weakening as catastrophic failure (Day, 1996). In low permeability rocks, pore fluid pressures will be sensitive to changes in heat of the host rock and from compaction, however the transfer of these higher pressures to surrounding rocks will be slow and therefore pore pressures are elevated near the intrusion. In high permeability rocks, pore fluid pressurisation will be buffered by rapid fluid dissipation to surrounding rocks and

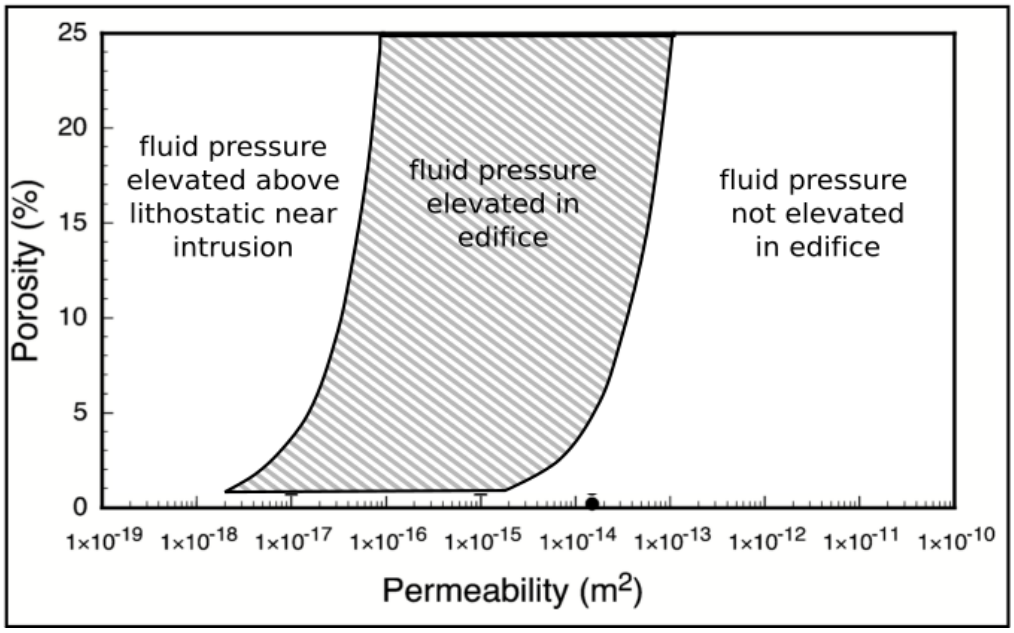

Figure 1.20: Relationship between porosity, permeability and the response fluid pressure from intrusions at depth from Reid (2004).

therefore minimal disturbance is felt at the surface (Day, 1996). Permeabilities between these two end-points will allow fluid pressure to elevate to the edifice. Figure 1.20 shows this relationship as described by Reid (2004).

Such pressurisation can occur by compaction of the rock, where pores and fractures with trapped fluid decrease in volume, and if this fluid cannot escape, then pressure increases. Fluid pressure can also be increased by volcanic intrusions intruding into the water-saturated rock mass and heating the trapped fluids. If the fluids cannot escape, the pressure will increase due to adiabatic heating. For example, when confined water is heated, the pressure can increases rapidly by over 1 MPa (Lachenbruch, 1980). The effect of this within the edifice would be a sharp reduction of effective normal stress and dynamic friction along a potential failure plane (Elsworth and Voight, 1996). Mechanical pressurisation can occur over hours to

days, whereas thermal pressurisation occurs more slowly from days to weeks and is more enduring and widespread (Elsworth and Voight, 1996).

Changes in pore fluid pressure can be rapid in a volcanic edifice and can result from emplacement of intrusions within the edifice, heating from intrusions at depth or changes in heat transfer in hydrothermal systems. This can have severe consequences on the volcano's strength and is therefore an important triggering mechanism (Day, 1996). Pore fluid pressurisation can occur from degassing of volatiles from crystallising intrusions due to the increased volume of fluid, heating from magmatic fluids and the ascent of highly pressurised fluids released at depth (Day, 1996). It can also be as a result of deformation where pores can collapse, increasing pore fluid pressures and reducing permeability. However brittle deformation may increase permeability through fracturing. Thermal deformation can also affect permeability, although it is more likely to have higher impacts on lower porosity rocks (Day, 1996). Delaney (1982) used numerical solutions simulating pressurisation, expansion and flow of fluids in a saturated intact host rock experiencing sudden heating. This showed that pore fluid pressure increased most significantly when the intrusion is emplaced rapidly and is in contact with impermeable materials with high thermal diffusivities and porosities. Day (1996) calculated that hydrothermal pressurisation will be more effective in volcanic settings where a high thermal gradient is present. Interaction of magma and fault systems can result in fault pressurisation and rapid heating. Movement on such faults may cause weakening of the whole edifice (Day, 1996).

Reid (2004) suggested this relationship between pore fluid pressures and edifice stability was crucial and that deeper intrusions may be a significant trigger. Numerical modelling was used to show that remote intrusions can temporarily elevate pore fluid pressures which can propagate to the shallow edifice and modify effective stresses. This would mean that hydrothermal pressurisation from deeper sources can threaten the mechanical stability of volcanic edifices (Reid, 2004).

Water quantities may also play a role in how the flank will collapse, either in a collapse abortion, as a debris avalanche or slump (McGuire, 1996). Once a landslide has been triggered and begins to slip, at higher velocities over 1 m/s, depending on the material properties, the friction coefficient can be reduced abruptly by 10-20% of its initial value and can reach almost zero (Wibberley et al., 2008). This is called dynamic weakening, and can serve to increase the velocity of a landslide even further.

External environmental factors can be important in triggering collapse, for example heavy rainfall in the short term or changing sea level in the long term can both affect pore pressure levels in the edifice (McGuire, 1996). McMurtry et al. (2004) made links between the timing of the large landslides on the Hawaiian Islands with the onset of interglacial periods over the last 5 Ma. They showed that nearly all the landslides occurred during the onset of warm interglacial periods. This may be due to the region being wetter and warmer during these periods, which could have increased water retention in porous volcanoes and caused a rise in frequency and intensity of tropical storms. This might increase interaction between groundwater and magma, causing a rise in pore fluid pressures and phreatomagmatic activity acting as a triggering agent for landslides (McMurtry et al., 2004). This relationship suggests that this hazard may become increasingly common in a warmer climate.

1.2.6 Effects of unloading

Growing basaltic volcanoes such as those at the Hawaiian ridge experience subsidence due to the gravitational load from the weight of the growing edifice on the oceanic crust (Smith and Wessel, 2000). However, some processes, including gradual erosion, reduce this subsidence and compression. Giant landslides result in a large redistribution of mass which, like melting glaciers, results in isostatic consequences on the underlying crust (Smith and Wessel, 2000). This 'landslide rebound' effect at ocean islands occurs on a much faster timescale and affects a more local area compared to glacial rebound, with suggested rates of twice as much being suggested due to the speed of the event, a thinner oceanic lithosphere and a less viscous asthenosphere (Smith and Wessel, 2000). The consequences of this process may include crustal earthquakes and reactivation of fault lines, changing volcanic activity rates and compositions of erupted lavas, as well as changing the volcano's internal stress distribution and hence the pathways for magma propagation (Smith and Wessel, 2000, Carracedo et al., 1997, Le Corvec and McGovern, 2018, Watt, 2019).

In some cases, after a large flank collapse occurs, a reorganisation of the volcano plumbing system leads to the migration of the conduit and main vent (Romero et al., 2021). The location of the post-collapse vent tends to be toward the direction of collapse within the collapse scar by altering the pathways of the intrusions (Romero et al., 2021). This is suggested to be in the order of a few hundred meters up to kilometres (Romero et al., 2021).

Large collapses in both arc and intraplate settings have shown evidence of being followed by large volume and compositionally anomalous eruptions, although not in all cases indicating this phenomenon depends on the presence of eruptible magma in a crustal reservoir (Watt, 2019). Such examples show more mafic compositions indicating a much deeper source from the ascending magmas, suggesting that this could be the effect of surface unloading from major collapse events (Watt, 2019). This redistribution of mass is also suggested to cause the reorganisation of magma plumbing systems following a collapse event without a large-scale eruptions (Watt, 2019). Ritter island is an example of this effect, as post-collapse eruptive products show a bimodal felsic and mafic phase eruption, distinct from any other eruption at Ritter (Watt, 2019).

1.3 Summary

In summary, understanding catastrophic volcanic collapse is still a relatively new field of science and the current knowledge, outlined in this chapter, indicates that the processes that control flank collapse are complex and are affected by a number of factors. Volcanoes can become unstable from the influence of intrusions, hydrothermal alteration, edifice steepening and weaker layers. Collapse can be triggered by magmatic intrusions, eruptive activity, pore fluid pressurisation and seismicity. The way in which the edifice responds is governed by the morphology and the mechanical and hydraulic properties of the edifice. Understanding these aspects further at collapse scars will help assess weakening mechanisms.

2 Ritter Island: Geology and geomorphology and pre-collapse reconstruction

2.1 Introduction

Ritter Island is the remnants of a conical island-arc volcano in Papua New Guinea. It's collapse and tsunami in 1888 has become a notable case study in the field of volcanic collapse. Its pre-collapse activity and morphology and accounts of the tsunami was described in local records. The Ritter Island collapse event is the largest volcanic collapse and tsunami in historic times and it therefore pertinent to know more about the structure and morphology of the island that eventually collapsed.

This chapter reviews published literature on Ritter Island including descriptions of the island's geology and various estimations of the pre-collapse morphology and collapsed volumes. Collapse volumes are particularly key and directly used in modelling tsunami generation and is therefore vital to be well-constrained.

Previous research excursions to Ritter Island have amounted collections of data which was used in this project. This includes detailed bathymetric surveys, a number of rock samples from the island and its submarine collapse scar and a set of drone imagery of Ritter Island.

In this chapter, this imagery was used in structure from motion (SfM) modelling to create a 3D model, elevation data and a high resolution orthomosaic of the island where this was previously poorly constrained. This model and images were used to geologically map the island and describe its morphology in detail. The subaerial island was then analysed alongside the bathymetry of the surrounding seafloor to collect measurements of the scar and ultimately reconstruct the pre-collapse island and calculate an improved collapsed volume estimate.

This work then allows for a discussion of the geomorphology of the pre-collapse island highlighting possible mechanisms for instabilities to form which led to its eventual collapse.

2.2 Ritter Island Literature review

2.2.1 Introduction

The crescent-shaped Ritter Island lies on the eastern end of the West Bismarck island arc, northwest of mainland Papua New Guinea at 5°31'S 148°07'E, between the larger islands of Sakar, Umboi and New Britain (Figure 2.1).

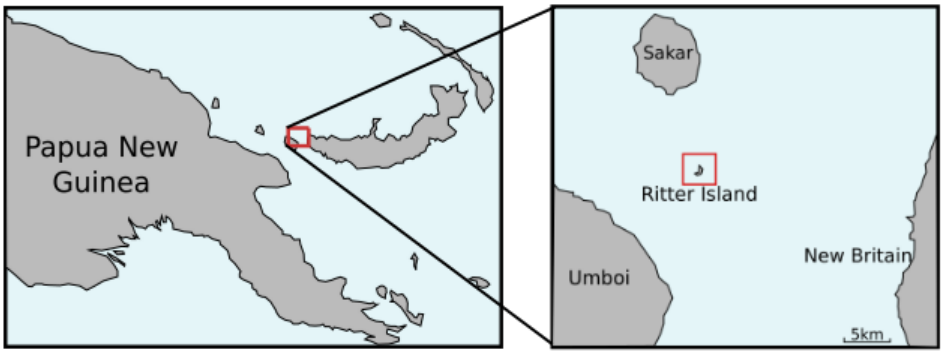

Figure 2.1: Maps showing the location of Ritter Island, Papua New Guinea.

Ritter Island has been the focus of study due to its well-documented catastrophic collapse in 1888, making it a benchmark for other ocean island volcanic collapses (Ward and Day, 2003). Collapses of a similar size to the Ritter 1888 event are estimated have a global recurrence time of 100 years (Day et al., 2015). This island and its collapse are particularly significant because of the historical accounts before and after the 1888 event. The uninhabited island was well known and used by passing ships as a reference point and therefore detailed descriptions of it exists.

2.2.2 Geological background

The region of Papua New Guinea has a complex geological setting associated with a zone of microplates formed from the oblique convergence of the Australian and Pacific plates (Figure 2.1).

The New Guinea region has evolved as a result of an oblique and rapid convergence of the Pacific plate, moving to the west-southwest, and the Australian plate moving northward (Baldwin et al., 2012). The plates are converging at approximately 110 mm/yr toward the northeast (Benz et al., 2011). The Australia-Pacific plate boundary extends over 4000 km and is dominated by the general motion of northward subduction or collision of the Australian plate (Benz et al., 2011). This convergence had developed dynamic variation in a complex zone of microplates along the strike of the boundary between the Australian and Pacific plates. This involves areas of subduction, seafloor spreading, collisional orogenesis and strike slip faulting.

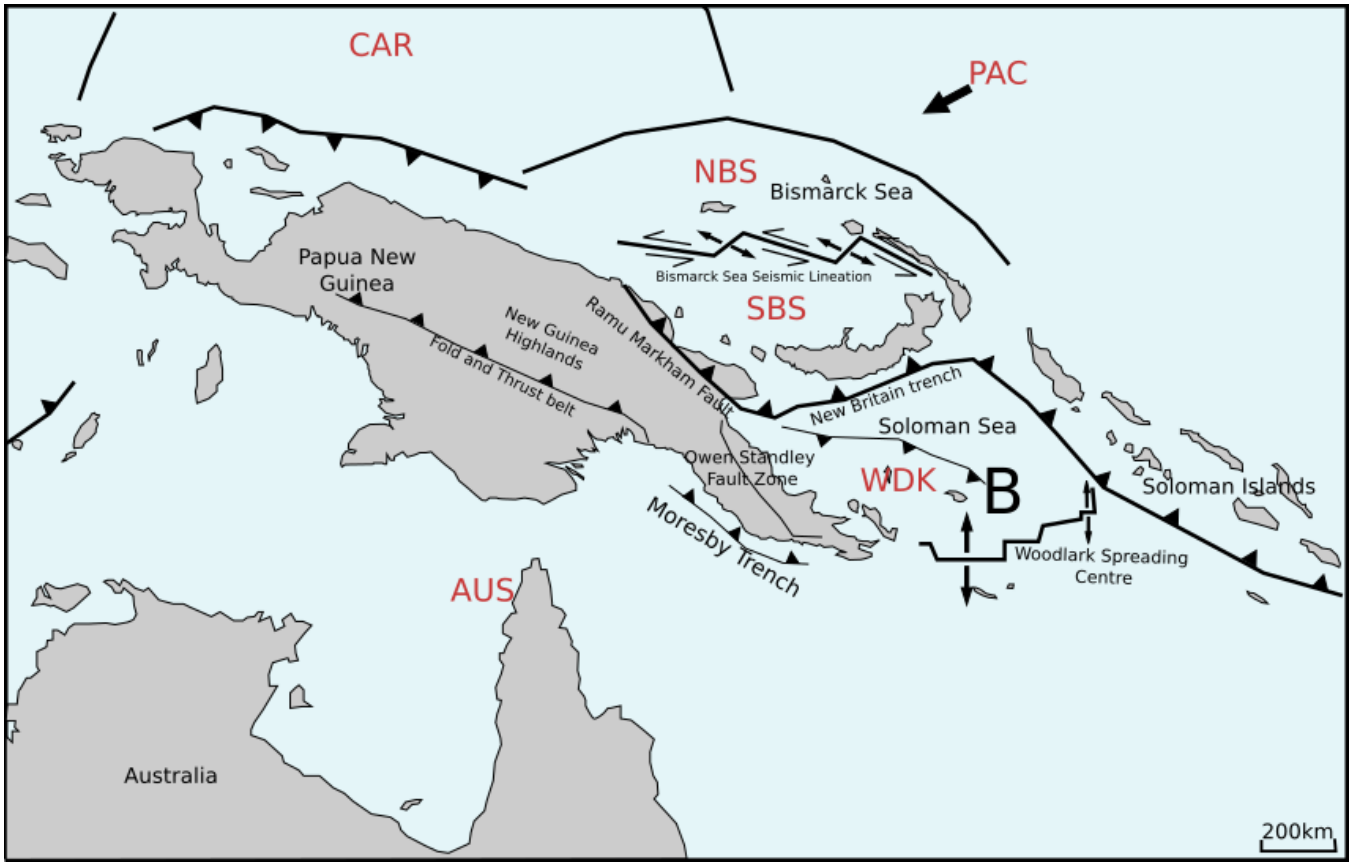

Figure 2.2: The tectonic setting of the Papua New Guinea region. Plate abbreviations refer to AUS as Australian, WDK as Woodlark, SBS as South Bismark, NBS as North Bismark, PAC as Pacific and CAR as Caroline plate.

The major active fault systems relating to plate boundaries include the New Britain Trench, Woodlark Spreading Centre, the Owen Stanley Fault Zone, the Bismarck Sea Seismic Lineation and the Ramu-Markham Fault (Figure 2.2)(Wallace et al., 2004). Seismicity is therefore common in the New Guinea region with ≥ 22 M7.5 recorded earthquakes since 1900 (Benz et al., 2011). The number of microplates are controversial but the major plates and microplates discussed include the Australian, Pacific, North Bismarck, South Bismarck, Woodlark and the New Guinea Highlands fold and thrust belt (Wallace et al., 2004).

In the Cenozoic, New Guinea was on the northern edge of the northward-moving Australian Plate. As it progressed it collided with and created island arcs and microplates (Baldwin et al., 2012). It is assumed that initially the Pacific plate was being subducted beneath the Australian creating the Solomon Sea as the associated back-arc basin. During the late Miocene, the southwest boundary of the Pacific plate known as the Ontong Java Plateau collided with the Solomon arc, resulting in a subduction reversal (Baldwin et al., 2012). Therefore since 3.5 Ma, the Solomon Sea has been subducting at the New Britain Trench, forming the Bismarck Sea as the back-arc basin (Figure 2.2) (Baldwin et al., 2012). The

Bismarck volcanic arc lies at this boundary. This is where Ritter Island is situated, hence, the volcanism on Ritter is subduction-related.

To the west of New Britain, along the length of the boundary known as the Western Bismarck Arc, there is convergence between the Australian and South Bismarck plates as arc-continent collision (Woodhead et al., 2010). The movement here is accommodated by the Ramu-Markham fault (Figure 2.2). Collision has been oblique and therefore has progressed along the arc from west to east. The rate of subduction is higher in the eastern section of the arc (Wallace et al., 2004).

The differences in the sources of magmatism means that the lavas erupted in the west and east parts of the Bismark arc differ from each other in composition (Tollan et al., 2017, Woodhead et al., 2010). Overall this has led to magmatism in the East Bismarck Arc on New Britain from subduction of the Solomon/Woodlark plate at the New Britain and South Solomon Trenches (Woodhead et al., 2010). Seismic data reveals a steeply dipping subducting slab decoupled from the overlying lithosphere (Woodhead et al., 2010).

In the West Bismarck Arc there is also subduction-related magmatism from an oblique collision which spread eastward since 3-3.5 Ma so that volcanism at Ritter began within the last million years (Tollan et al., 2017). The West Bismarck Arc, including Ritter Island, spans a broad range of compositions from basalts to rhyolites due to varying degrees of crustal contamination from sediments on the subducting slab into the magmas ascent to the surface (Tollan et al., 2017, Woodhead et al., 2010). The eastern part of the arc has more primitive magmas due to decreasing levels of partial melting westwards due to the influence from arc-continent collision (Tollan et al., 2017, Woodhead et al., 2010). Seismic data shows evidence of this south-dipping limb but becomes increasingly dismembered and diffuse to the west (Woodhead et al., 2010). Chemical variations across the West Bismarck arc are due to the oblique conversion whereas in the west, the components from the subducting slab have been melted out, in the centre there is an enhanced subduction signature and in the east the system is still in a ‘pre-collisional state’ (Woodhead et al., 2010).

Earthquakes and tsunamis are not uncommon in the area due to its tectonic complexity. For example a M7.1 earthquake that triggered a submarine landslide created a tsunami killing over 2000 people in 1998 (Tappin et al., 2001). Additionally, a M7.8 megathrust earthquake in 2007 to the west of the boundary generated a tsunami killing at least 40 people (Benz et al., 2011).

The Ritter Island collapse event was not unique in the area, as Silver et al. (2009) mapped 12 debris avalanches around the Bismarck Volcanic arc. This study used multibeam and side scan sonar study to identify characteristic collapse deposits around 11 different volcanoes. The Ritter Island event and evidence of further collapses shows that there is significant risk for future volcanogenic tsunamis in this area.

2.2.3 Accounts of Ritter Island

2.2.3.1 Pre-collapse records

The first European explorers to reach Papua New Guinea were the Portuguese in the 1500s. The first record of Ritter Island was by William Dampier in 1700 who discovered the Dampier Straight where Ritter lies. Since then, Ritter Island was a prominent landmark in the Bismarck Sea for sailors passing through the area (Ward and Day, 2003). For this reason, there are a number of accounts and sketches of the island before the catastrophic collapse in 1883 (Figure 2.3). This helps interpret the pre-collapse morphology and categorise the nature of the island and its eruptions.

There are eye-witness accounts of the tsunami that followed the collapse event in 1883, but none for the collapse itself. Due to the German populations witnessing the waves arriving at the shoreline of missions on the coast, the wave was accurately timed using pocket watches. This has allowed reconstruction of the event (Ward and Day, 2003). Since 1883 there have been intermittent observations at Ritter Island. Presently, Ritter Island is not monitored but individual accounts are provided using bulletin reports from Rabaul Volcano Observatory (Ray, 2017). Ray (2017) used 37 primary and secondary reports including navigational logs administrative communications, personal communication, journalistic texts and scientific texts to interpret and recreate a chronological account of Ritter as summarised in appendix 1 and displayed in a timeline in Figure 2.4.

These reports describe numerous strombolian type eruptions from the pre-collapse island which was described and sketched as having a steep conical morphology (Figure 2.3)

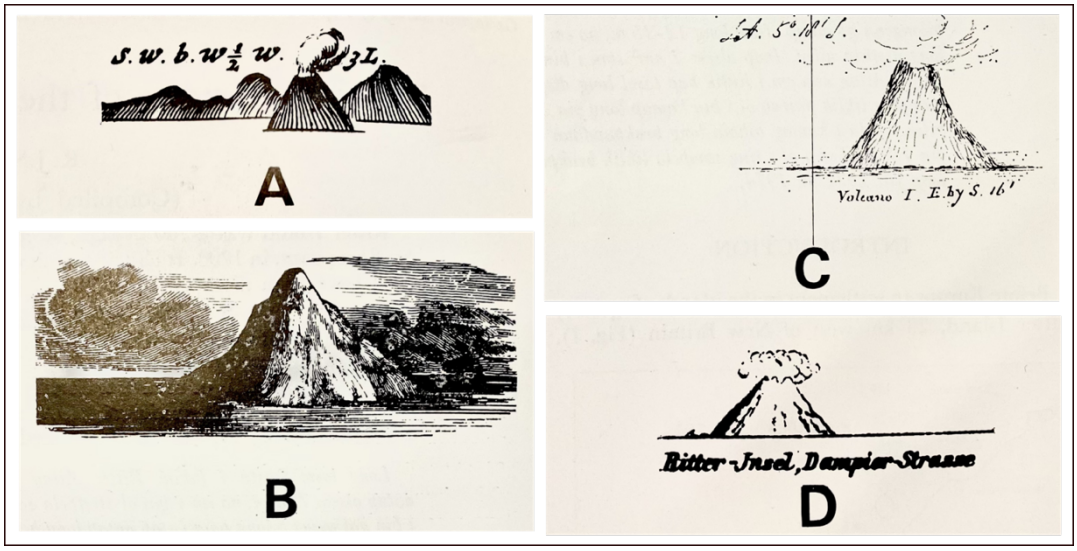

Figure 2.3: Sketches of Ritter Island from the 18th and 19th century. A. Ritter in 1700 B. A sketch of Ritter Island made in 1834. C. sketch from 1842-46. D. Ritter in 1887. From Cook (1981) and references therein.

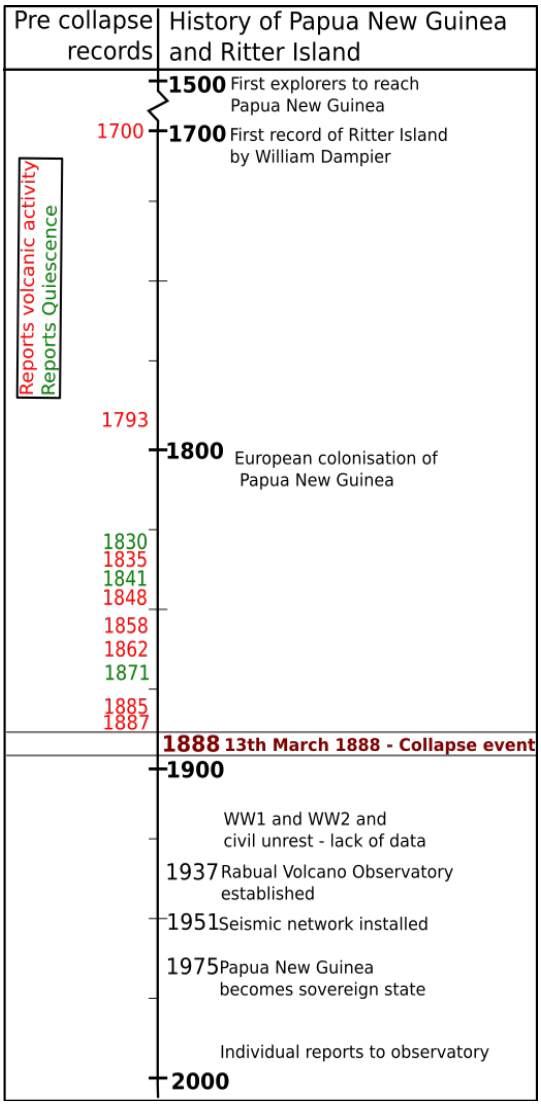

Figure 2.4: Timeline showing history of Papua New Guinea and Ritter Island including the nature of the pre-collapse reports in terms of volcanic activity based on report by Ray (2017)

2.2.3.2 13th March 1888 event

The event which occurred in March 1888 was significant, producing a tsunami that affected coastlines locally and distally. There are numerous records of both the event and aftermath which helps piece together an idea of the sequence of events. Ray (2017) reviewed these accounts with the main information as follows:

- Freiherr von Schlenitz had described the island before the event as *'an almost regular cone with a crater edge on the peak from all sides producing steam constantly'*. He described the event as an *'explosion'* of the island devastating the western coast of New Britain. After the event he reported *'it no longer has its regular form, but appeared to have collapsed and had irregularities along the side and base that had not been there before'.*
- Captain Schneider described the island soon after collapse as *'a small jagged crater edge'* open to the west and described the rocks as including red and black tuffs and lavas. They described it as loose and rubbly.
- Robert Steinhauser wrote an article describing the tsunami at Finschhafen and his rescue expedition to the coast of New Britain. From his position at 6.30am on March 13th 1888 he was able to see the harbour and the arrival of the tsunami waves. He described *'A dull thunder-like noise that lasted probably around ten seconds'.* He then saw the sea retreat exposing a coral reef followed by a wave *'the water, suddenly rising, broke against the coast with a terrible vengeance'* describing it rise by approximately 3 m. He reported that this repeated itself several times and that he could see three tsunamis approaching the New Guinea coastline from the east. He states the time between wave arrivals was four to five minutes and that the wave speed was 10 mph roughly equalling 4.47 m/s or 16 km/h (Ray, 2017).
- On March 16th 1888, a captain of a steamboat described how he found the shape of the coast so changed that they found orientation difficult. '*Entire flat areas of land have disappeared; the entire coast up to the mountains destroyed'.* He reported that the native survivors they found described a '*big water'* throwing them into the trees where they held on until the water retreated.

- Steinhauser, on his rescue mission the following day, described the destruction of the low-lying areas of the coastline with a thick layer of mud, fallen trees, boulders of coral reefs washed up by the waves and decaying fish.
- An anonymous report describes the tsunami arriving at a colonial settlement, Hatzfeldhafen, at 6.40am stating that it rose 2 m above the highest flood mark. Peter Hansen describes a roaring of the ocean at 5.50am and the rise in turbulent water, and continued to describe multiple waves arriving. Another anonymous report states that the first four of twenty waves were the largest to reach the shore, stating the waves arrived every 3 minutes and lasted for an hour.
- Oral traditions of the event from resident communities were recorded by Sister Mona Sackley in 1974. From this, a story from Gabriel Alsapo's father who lived in northwest New Britain at the time of collapse was translated. He states that the pre-collapse island morphology of Ritter was a '*high mountain and long'.* Another report suggested that there was an eruption before the collapse and tsunami, but it does not suggest how long before. It does describe the island after collapse as '*a low rock was all that remained*'.
- The only sketches of the island soon after collapse are by an anonymous artist in 1891 (Figure 2.5). These indicate that the island as had a jagged and sharp relief, due to lack of erosion (Ray, 2017). We can compare this to present-day images to see how the island has changed. We can draw similarities between crescent shape of the island, the high point to the south, the layers of lava exposed and the islet to the south.

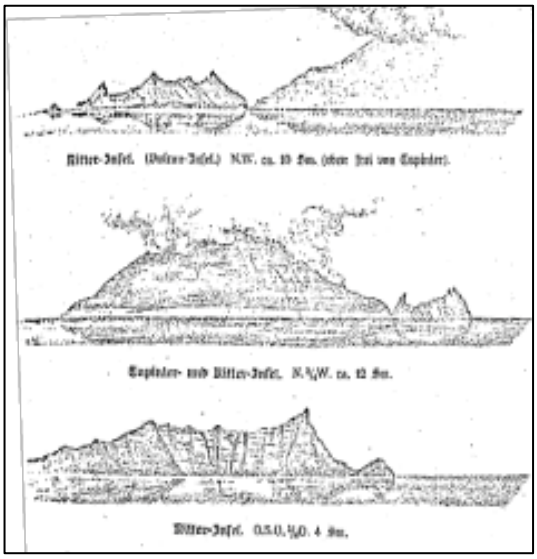

Figure 2.5: Sketches of Ritter Island; the first sketch showing Sakar to the east, the second showing Ritter to the South of Sakar and the third a sketch of the collapse scar by an anonymous artist in 1891.

2.2.3.3 Post-Collapse Activity

Since the catastrophic collapse, there are only limited reports of any activity of Ritter Island. The first known activity was in October 1972 where earthquakes were recorded and felt up to 35 km away (Saunders and Kuduon, 2009). Hydrothermal vents were seen producing black and white clouds close to the island and rumbling was heard at the local coastlines (Saunders and Kuduon, 2009). A similar pattern of earthquakes were recorded in 1974 and steam plumes were reported to erupt 700 m to the west of Ritter and rock falls were seen on the island (Saunders and Kuduon, 2009). Further possible activity was recorded in 1996 and 1997. In 2006, small earthquakes were felt and ash clouds reported possibly due to rock slides on the island and, in 2007, three large explosions were heard and steam was observed followed by a number of waves (Saunders and Kuduon, 2009). This activity at the island has two inferred sources, either the rise of fresh magma at the site of the new submarine cone development to the west of Ritter, or hydrothermal activity from water coming into contact with hot rocks from slope instability close to the shores of Ritter (Saunders and Kuduon, 2009).

2.2.3.4 Collapse Event Interpretation

Villagers on New Britain who survived the tsunami did not report any noise, explosion, eruption column or earthquakes (Cooke, 1981). In addition, reports from local communities on Umboi state that explosions were heard and seismic activity was felt but no eruption

occurred. Numerous fumaroles suggest hydrothermal activity so possibly a phreatic eruption occurred, indicating a Bandai-type collapse. The event created a single wave-train, based on eyewitness accounts, suggesting a single failure motion or rapid succession of retrogressive failures (Watt et al., 2019, Day et al., 2015). It reduced the 750 m cone to a small crescent-shaped island and left a large collapse scar with a 2 km headwall, 5 km long and 4.4 km wide (Day et al., 2015, Paris et al., 2014, Siebert and Roverato, 2021). Johnson (1987) initially estimated that the slope failure volume was 4-5 km^3. The volume of collapsed material was later re-estimated as 2.4 km^3 ± 0.2 km^3 which represents 20% of the affected sediments as evidenced from seafloor surveys (Karstens et al., 2019, Watt et al., 2019).

The landslide created a tsunami that had over 15 m elevation on the nearby coasts of Sakar and Umboi with short wave periods (Ward and Day, 2003). These waves reached as far as 540 km away at Rabaul harbour (Paris et al., 2014). The high elevation of the waves suggest high velocities, with an estimated wave speed of 40 m/s from modelling (Ward and Day, 2003). This study used a reconstruction based on a 1985 sonar survey using a landslide volume of 4.6 km^3 and the simulations were compared to historical observations (Ward and Day, 2003). The number of tsunami related fatalities is estimated to be 500 – 3000 (Paris et al., 2014).

Watt et al. (2019) suggests that the primary landslide mass disintegrated rapidly due to the weak material making up the edifice. The material was deposited in the proximal basin and distally as turbidites with the mid-region made up of debris flow deposits.

Residents of surrounded islands noted sounds of possible eruptive activity and there were also reports of ash fall (Cooke, 1981). This could be interpreted as magmatic activity or phreatic activity due to depressurisation of a hydrothermal system (Johnson, 1987).The initial landslide is suggested to have triggered a magmatic eruption which followed the event, producing a distinctive evolved basaltic magma composition (Watt et al., 2019). This eruption is suggested to have produced pumiceous deposits, consistent with reports of volcanic deposits observed to the west of Ritter (Watt et al., 2019). There is a possibility that this magma ascent could have destabilised the edifice triggering the collapse or the collapse may have caused depressurisation triggering the eruption (Watt et al., 2019).

The single wave-train from the tsunami that was produced by this event indicates that the catastrophic collapse was the principle wave generation mechanism and a submarine eruption was not significant (Watt et al., 2019). This initial single stage of tsunamigenic collapse is inferred to have been followed by multiple stages and flow transformation, based

on morphological features and erosional patterns amongst the seafloor deposits (Watt et al., 2019).

An alternative interpretation from Karstens et al. (2019) is that the collapse occurred over two phases. This is suggested to be a deep-seated gradual spreading interpreted from possible evidence of compressional deformation within the edifice and the surrounding seafloor followed by the rapid catastrophic failure removing 2.4 km^3 of the edifice (Karstens et al., 2019).

2.2.4 Ritter Island Morphology

2.2.4.1 Pre-collapse morphology

The information gathered from eyewitness reports and descriptions of Ritter Island before the collapse event in 1888 provide insight of what the volcano looked like and how it behaved. Various accounts of eruptive activity suggest that Ritter was intermittently active showing strombolian style activity, including lava fountains, lava flows and small ash columns (Ray, 2017). The lack of reports of significant ash fall suggests the column height would not have been significant enough for dispersal. Often the eruptions described suggest that more than one cone was active, indicating the presence of dyke-fed eruptions, fissures or parasitic cones. The present-day morphology shows a cross-section of the island showing numerous cross-cutting dykes throughout the edifice. Where there were reports of vegetation, we can infer that the island would have been quiescence, allowing vegetation to thrive (Ray, 2017). Seismic events have been recorded within these reports, larger ones may be attributed a regional event due to the complex tectonic region, they would have likely experienced thrust earthquakes. Smaller events as described in 1862 are likely to be caused by degassing events at Ritter, or other volcanoes in the region (Ray, 2017).

Overall, we can infer that Ritter was an active volcano throughout the 1800s, mainly characterised by strombolian eruptions. The morphology of the volcano was described similarly and therefore we can infer relatively unchanged through the 200 years of descriptions. It has been described as a steep-sided conical island with little or no vegetation in most observations. Eruptions have appeared to have mainly occurred at a central vent at its summit, giving it a visible crater described by witnesses on many passing ships.

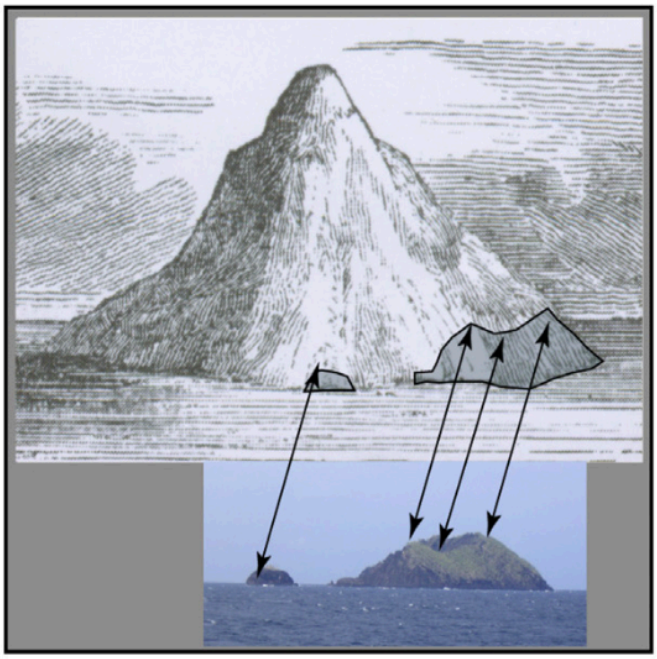

Figure 2.6: Sketch of Ritter Island from 1835 with photograph of current morphology estimating scale of island from Day et al. (2015).

Sketches and reports of the island, for example in Figure 2.6, show how steep the island was perceived to be. Durmont d'Urville's calculations suggested the sides to be over 50° and other sketches indicate slopes to have a steepness 60° (Johnson, 1987). These are likely to be exaggerated accounts as the current subaerial morphology have slopes of 44° which is likely to be more representative (Johnson, 1987). Figure 2.6 shows the interpretation of pre- and post-collapse morphology from Day et al. (2015). The accepted estimate of the height of the original island based on eyewitness accounts is 750 m above sea level and an east-west width of 1.5 km (Day et al., 2015, Ward and Day, 2003, Cooke, 1981). The current north-south length of the island is roughly 1.9 km so it may have been elongated in this direction (Day et al., 2015).

2.2.4.2 Present-day subaerial morphology

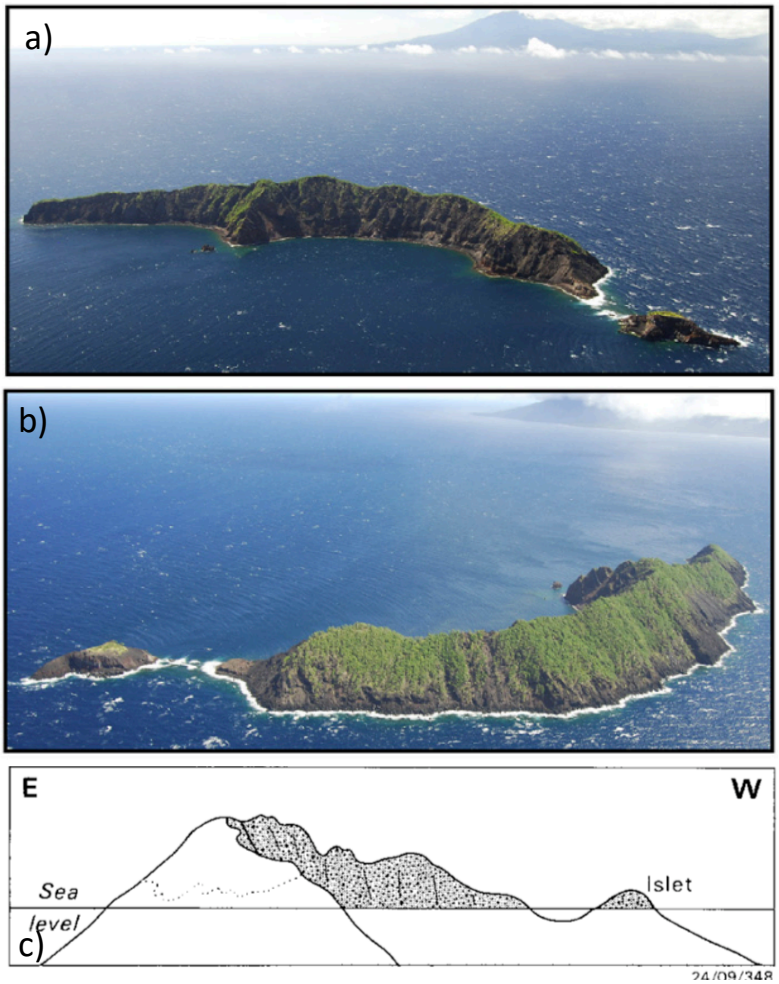

Figure 2.7: Photographs of Ritter Island from the a) southwest and b) southeast (Day et al., 2015) and c) Ritter island sketch adapted from a photograph from the north (Johnson, 1987).

Today, the morphology of Ritter remains largely unchanged since collapse. Figure 2.7 shows aerial images of the current morphology of the eastern and western sides of the island. The island extends 1.9 km in length and is 140 m at its highest (Johnson, 1987, Day et al., 2015). Its morphology is dominated by the top of the horseshoe-shaped collapse scar which extends across the western side island. The eastern side of the island represents the original pre-collapse edifice which has an average angle of 44° (Johnson, 1987). There is also a small islet to the south of the island as depicted in Figure 2.7c (Johnson, 1987).

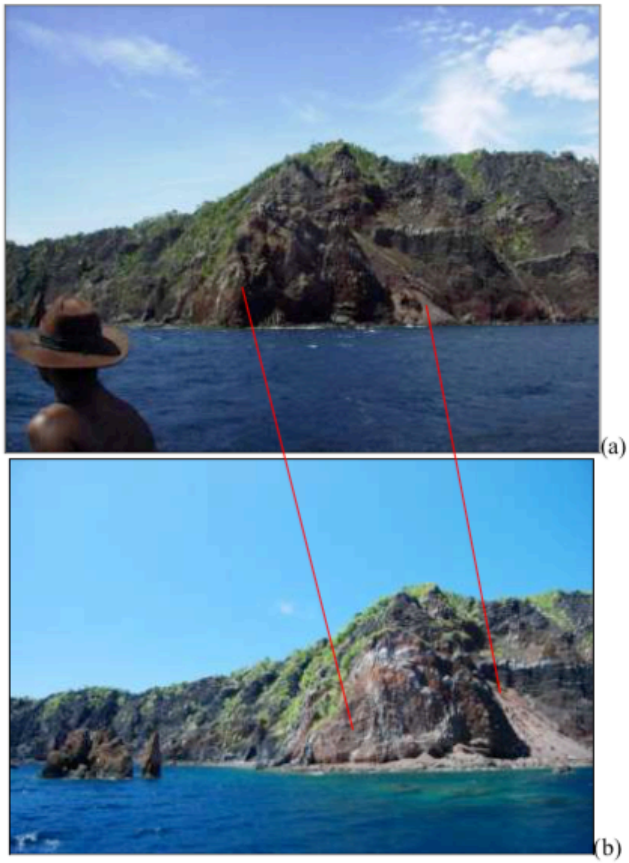

Figure 2.8: Images taken from (a) 2007 and (b) 2009 visits to Ritter Island of the central portion highlighting the differences caused by erosion (Saunders and Kuduon, 2009).

The eastern remains of the island show that the edifice was dominated by poorly consolidated coarse volcaniclastic units including rubbly and spatter-fed lavas, some massive flow cores and fine scoria (Watt et al., 2019, Day et al., 2015). The oldest remaining subaerial layers are tuffs and thin scoria beds (Day et al., 2015). These layers are bedded on a metre scale and all dip steeply to the east (Day et al., 2015). The southern islet of Ritter has on a slightly different form with a massive lava layer with a rubbly top extending at least 70 m depth (Saunders and Kuduon, 2009). N-S striking dikes and intrusions cross-cut these rocks throughout the sequence and can be seen outcropping underwater also (Saunders and Kuduon, 2009, Day et al., 2015). Alteration is visible at the base of subaerial sequence (Day et al., 2015). Gullies are presently incising the exposed scar from post-collapse erosion. There is no evidence of large collapse prior to the 1888 event. The west of the island has a marine erosional platform extending 20-100 m from the island. It deepens from the shoreline at 20° before a break in slope 15-30 m deep where it steepens to 45° (Saunders and Kuduon, 2009). The platform consists of 0.5-2 m angular blocks and scoria.

The rocks that make up this island and therefore the landslide failure mass are relatively weak and likely to have rapidly disintegrated (Watt et al., 2019). Visits to Ritter since the 1970s have revealed that the island is eroding rapidly due to its 'steep sides, the depth of the surrounding sea, weak lithology and exposed position' (Saunders and Kuduon, 2009). The notable difference between the island then and more recently is that areas of hydrothermally altered rock have been newly exposed. It is suggested that the island experiences large mass movement on all sides, differences in photographs taken in 2007 and 2009 of the central cusp of the island show major slabs have been removed and talus aprons developed, see Figure 2.8 (Saunders and Kuduon, 2009).

During the dives in 2007 and 2009, a spring was identified at the southern cove, indicating hydrothermal activity is ongoing on the island (Saunders and Kuduon, 2009). Additionally a baked soil horizon was identified at 12 m depth, showing the island has a history of subsidence (Saunders and Kuduon, 2009).

2.2.4.3 Submarine morphology

The first bathymetric survey using single beam bathymetry was carried out surrounding the island in 1985 (Johnson, 1987). Originally, the Ritter collapse event was likened to the Krakatau eruption and tsunami in 1883 and therefore perceived as a caldera-forming event (Johnson, 1987). Following this seafloor survey however, it was first suggested that this was actually a catastrophic slope failure (Johnson, 1987). Although the instrument used was limited to 1000 m depths, the survey illustrated the nature of the seafloor. This survey revealed a west northwest facing amphitheatre-shaped avalanche scar extending from the island (Johnson, 1987).

The scar showed a maximum diameter of 4.4 km, width of 3.5 km and area of 13 km^2, allowing Johnson (1987) to estimate the volume of collapse to be 4-5 km^3. The scar is U-shaped with the southern limb being longer than the northern one (Johnson, 1987). The seafloor is interpreted to have a hummocky topography as in other cases of catastrophic collapse and there are two large mounds interpreted as coherent blocks of slumped material or 'torevas' (Johnson, 1987). Possible other conical vents were also identified and the pre-collapse steepness of the eastern side was interpreted to be steeper than the western flank which failed (Johnson, 1987).

The depth from the pre-collapse profile show a 500-600 m difference at its maximum extent at the scar (Ward and Day, 2003). A 500 m thickness is also indicated by the height of the toreva blocks (Ward and Day, 2003).

Further seafloor mapping by Day et al. (2015) using multibeam bathymetry, sonar, seismic reflection surveys and photographs of the sea floor gave additional insight into the submarine morphology surrounding Ritter (Figure 2.9). This showed the scar has a 2 km north to south orientated headwall extended to the western foot at 900 m depth, where it is 4 km wide with an arc of 60° (Day et al., 2015). The walls of the scar limbs are 100-200 m high above the post-collapse volcanism and fill the shape of which indicated a single movement of failure (Day et al., 2015). The scar has been partially filled by post-collapse volcanic cones, the largest being 500 m high with a 250 m wide crater (Day et al., 2015, Watt et al., 2019). This was the location of eruptive plumes recorded in 1972 and 1974 (Day et al., 2015). Samples show the cones surface is made of loose scoriaceous gravel composed of abundant clinopyroxenes and plagioclase with some orthopyroxene and olivine (Watt et al., 2019). The location of this post-collapse volcanism is postulated to be in the scar as rising magmas will tend to take advantage of the weakened collapse structure and the reduction in confining stress (Day et al., 2015).

From this survey, the landslide deposit is seen to extend at least 70 km from the headwall of the collapse scar (Day et al., 2015). Based on the Glicken (1996) characterisations of the Mt St Helens deposit, Day et al. (2015) described the facies seen in the submarine deposits at Ritter Island (Figure 2.9). The deposit has been split into three distinct morphological facies; the large block avalanche facies, the matrix-rich debris avalanche facies and the distal debris flow facies (Day et al., 2015). These are distinct due to the clear stages of rheological transformations during the movement and of the landslide and the geometry and associated erosional features it left behind after emplacement (Day et al., 2015). A further survey involving 3D seismic data, bathymetric and backscatter data was taken in 2016 and discussed in Watt et al. (2019) (Figure 2.10).

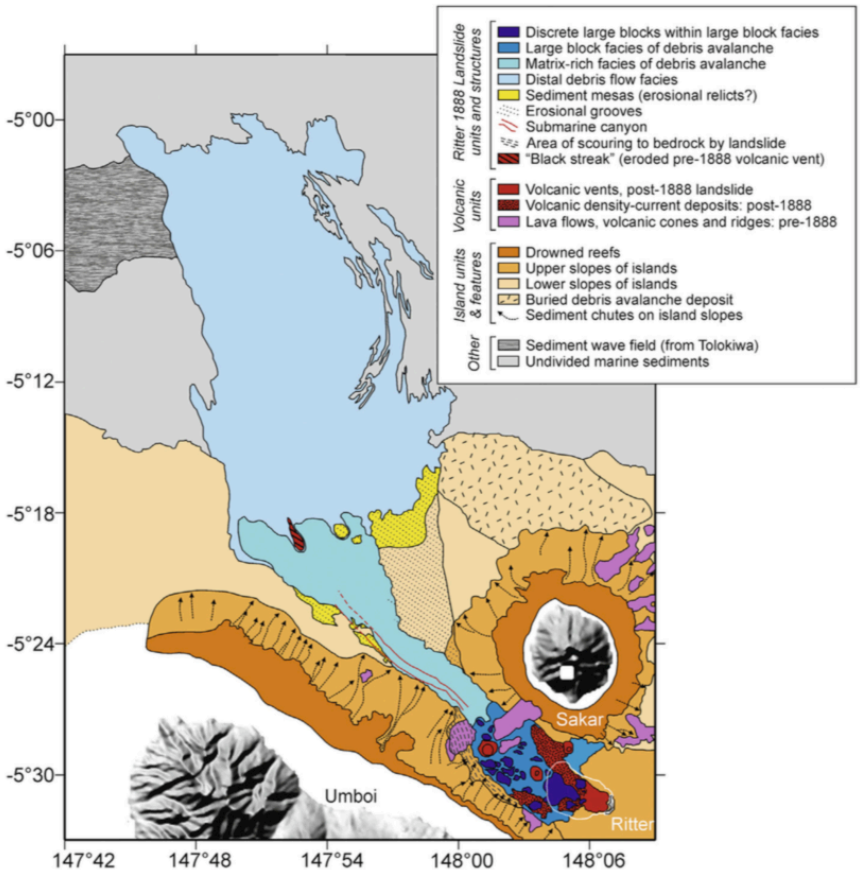

Figure 2.9: The morphological interpretation of the bathymetry around Ritter Island (Day et al., 2015).

The large block debris avalanche facies is the portion of the deposit closest to the scar. It extends 12 km from the headwall of the scar and lies between two submarine volcanic ridges (Day et al., 2015, Watt et al., 2019). It lies at depths of 900-1240 m further to the west with an average slope angle of roughly 2.1° (Day et al., 2015). The deposit may have ponded before the constriction of the other islands, much like seen at other collapse blocky facies (Day et al., 2015). This deposit has a blocky or hummocky morphology, the largest block being at the mouth of the scar, as previously described by Johnson (1987) as a toreva block, also interpreted as a back-rotated coherent block showing well-developed seismic reflections representing an intact segment of the edifice (Day et al., 2015, Watt et al., 2019). Other large blocks are concentrated on the southern and western margins (Day et al., 2015). More recent seismic surveys have shown, however, this region is underlain by bedded sediment which has been folded and thrust faulted, which may the explain of the presence of these mounds (Watt et al., 2019, Karstens et al., 2019). This folding reflects some in-situ seafloor deformation (Karstens et al., 2019, Watt et al., 2019). The area containing the mounds is incised by a series

of channels which deepen to the southwest inferred as erosion driven by the disintegration of the mass flow (Watt et al., 2019).

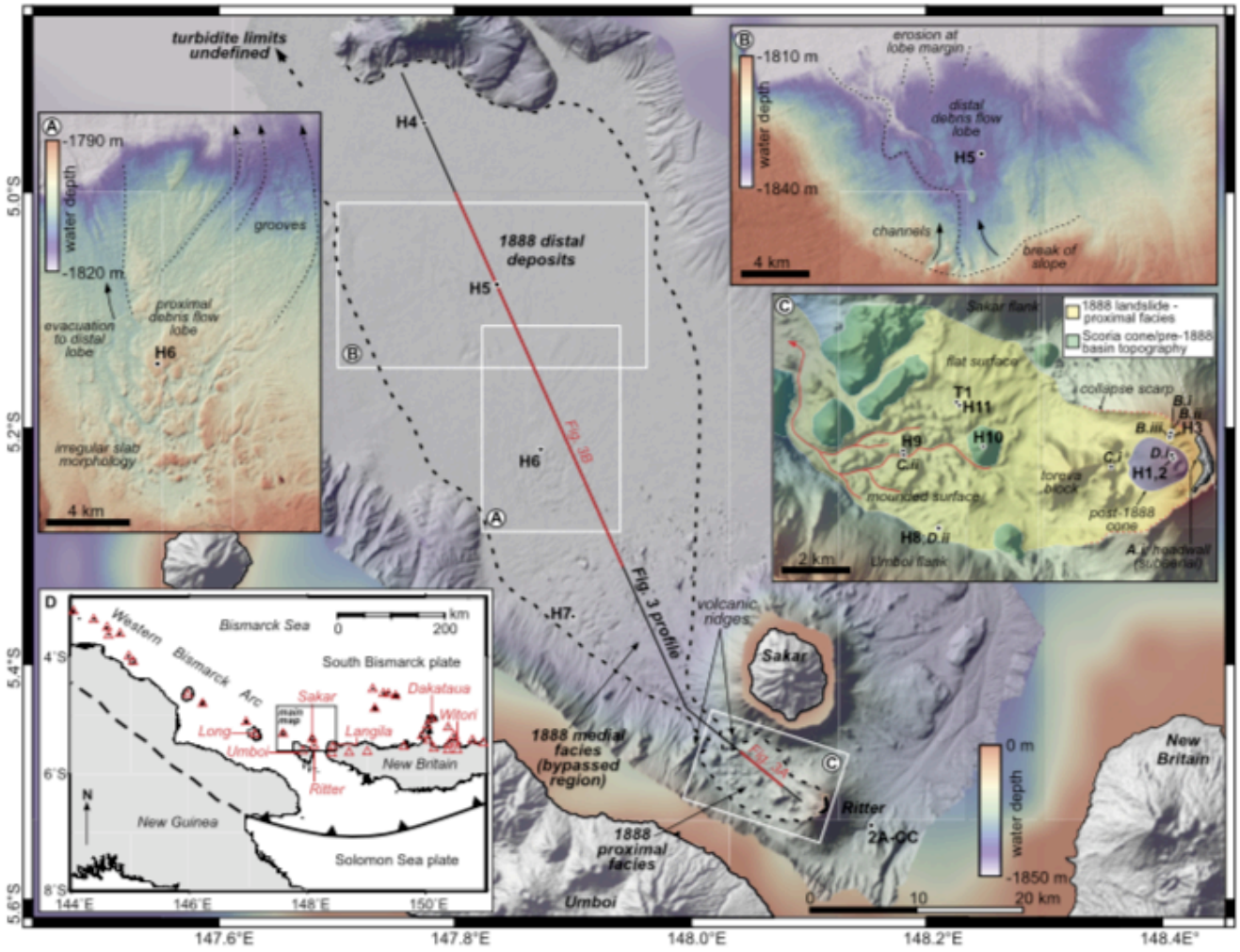

Figure 2.10: Bathymetry around Ritter Island highlighting morphological features where A and B show areas of the distal deposit, C showing the landslide scar area and D showing the regional Bismark Arc (Watt et al., 2019).

The transition from the blocky facies into matrix-rich debris avalanche facies is located in the constriction of ridges between Umboi and Sakar (Day et al., 2015). The backscattered survey showed this area as a mottled pattern and the seismic data as a coarse blocky and non-stratified mass (Day et al., 2015). Smaller mounds 100-300 m across of high intensity backscatter are interpreted as smaller angular clasts of the Ritter edifice (Day et al., 2015). The lower end of the matrix facies are a series of lobes partially covered by bioturbated marine sediment with mounds representing further clasts of edifice material (Day et al., 2015).

The transition into the distal flow deposit appears sharp in the backscatter survey. The presence of blocks decrease to leave a flat seabed in the distal deposit (Day et al., 2015). Here the deposit consists of a laterally extensive sheet with poorly defined margins and an average

slope of 0.11° (Day et al., 2015). Where the base of the deposit could be seen on seismic reflection surveys, the thickness is 5-10 m (Day et al., 2015). Images of the deposit showed extensive bioturbation indicating the soft nature of the material, and areas of rounded clasts orientated SW to NE on the seabed (Day et al., 2015). The matrix deposit is estimated to have a minimum volume of 6.4 km^3 due to entrainment of sediment bulking the deposit (Day et al., 2015). Watt et al. (2019) describes this deposit as a lobe 15 km wide and up to 16 m in thickness, thinning downslope toward a break in slope. This lies above an inferred buried margin of a large landslide deposit, suggested to have an origin from Sakar or Umboi; beyond this point a second lobe of similar dimensions is identified. The surface of this distal deposit has an erosional fabric including grooves extending to the northeast and meandering channels in the secondary lobe. This is inferred to be the final stage of movement from the Ritter collapse deposits (Watt et al., 2019). Samples from this area suggest that remobilised existing seafloor material makes up a lot of this region of the 1888 deposit (Watt et al., 2019). The most distal part of the deposit has a smooth surface and is sheet-like and has been interpreted as turbidites derived from the 1888 collapse event (Karstens et al., 2019). Figure 2.11 shows a summary of the processes involved in the emplacement of the collapsed Ritter material (Watt et al., 2019).

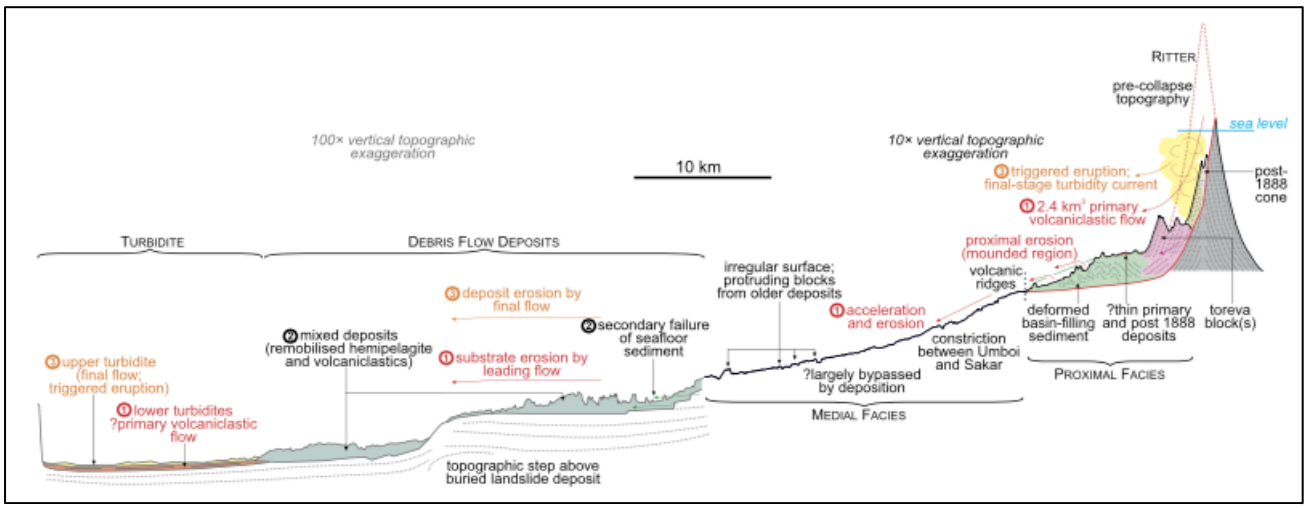

Figure 2.11: Summary of processes involved in the emplacement of the Ritter deposits (Watt et al., 2019).

Day et al. (2015) estimated the volume of the collapse by subtracting a grid of the present topography from a grid of the reconstructed estimated pre-collapse surface to obtain a value of 4.2 km^3. This estimation used a reconstruction of the pre-collapse island using an elevation of 750 m and slope of ~45° with steeper western sides and a N-S length of 2 km.

Dilation of collapse material can occur during emplacement due to sediment entrainment and an estimated 75% of the original material makes up the large block facies (Day et al., 2015). The total volume involved in this event as estimated by Watt et al. (2019) is up to 13 km^3 where deposits are distributed within the proximal basin and in the distal turbidite. This is much larger than the initial failure volume from a variety of interactions, flows, erosion and secondary failure of the seafloor (Watt et al., 2019).

Karstens et al. (2020) simulated tsunami waves from a shallow and deep slide plane which had volume estimates of 2.59 km^3 and 7.34 km^3 respectively. Here volumes were also calculated by reconstructing a pre-collapse surface based on geophysical data and historic accounts of the island. This was done by removing the slide scarp from present-day bathymetry and extracting contour lines at 50 m intervals between 450 m and 800 m depths (Karstens et al., 2020). Ellipsoids were fitted to fill the gaps in bathymetry and at shallower depths, the ellipsoid from 450 m was used at a constant slope. Their study concluded that it is likely that the catastrophic collapse of the volcanic cone was responsible for the magnitude of the tsunami. Slide volume, velocity and the geometry of the scar are directly used in the resultant tsunami modelling.

2.2.5 Petrology

Samples of post-collapse cones show that these rocks are compositionally distinct from the pre-collapse rocks (Watt et al., 2019). Samples representing pre-collapse submarine Ritter are dominated by equant clinopyroxenes with variable compositions of olivine and plagioclase (Watt et al., 2019). Samples representing post-1888 volcanism show differences to the pre-collapse rocks in both glass and mineral composition of the mafic components and are seen to be more evolved (Watt et al., 2019). Ongoing eruptions and extrusion of magma show more evolved melts than the pre-collapse melts (Watt et al., 2019).

2.2.6 Cause/Trigger

A number of different mechanisms have been proposed as causes of destabilisation of a volcanic edifice. Most suggest that a flank can become destabilised over a long period of time either via tectonics, magnetism or material weakening and that triggering mechanisms

can cause the unstable flank to disintegrate relatively instantaneously via various processes (McGuire, 1996).

Johnson (1987) suggested how continued volcanic activity on Ritter Island accumulated material on the edifice to the point where the critical angle of repose was exceeded causing the failure of the edifice. Siebert (1984) previously suggested that a typical critical angle of failure for a volcanic slope is 20°, supporting the idea that the slope of pre-collapse Ritter was unstable.

Day et al. (2015) suggested that, due to the lack of evidence for tectonic triggers, external environmental triggers or obvious magmatism, that the probable cause of collapse is associated with phreatic activity and pore fluid pressurisation from a deep magmatic intrusion below the edifice. A suggested failure surface is that of a compacted deep marine sediment creating a weak low-permeability base on which the edifice was built (Day et al., 2015). Later suggestions from Watt et al. (2019) suggests that magmatic activity may have been more prevalent from the evidence of post-collapse volcanism.

2.2.7 Summary

The 1888 collapse event at Ritter Island has been well studied. This work has included analysis of the collapsed material using bathymetric and seismic studies, highlighting distinct depositional facies to understand processes involved in the emplacement of the slide (Watt et al., 2019, Karstens et al., 2019). There has also been some work describing the subaerial lithologies, however, to date, there has been no detailed geological map of the island (Watt et al., 2019, Saunders and Kuduon, 2009). Previous collapse volume estimates have also been made by reconstructing the bathymetry data and using assumptions on for the pre-collapse morphology of the island including the slope and height (Karstens et al., 2020, Day et al., 2015). These estimates cover a wide range of volumes and are therefore not well constrained. It is essential to improve estimates to be able to provide more accurate tsunami modelling. Previous tsunami simulations were based on previous volumes (Karstens et al., 2020, Ward and Day, 2003).

Although work on the submarine datasets of Ritter Island have helped build a clearer picture of the collapse event, little work has been done on the subaerial island due to the lack of quality data of elevation and maps. In addition, despite this being a major collapse event, no work has previously been done on the mechanical properties on the rocks that

make up the edifice. This chapter will address these factors to develop the sub-arial island dataset, improve pre-collapse island reconstruction and assign the lithologies mechanical properties.

2.3 Methods

2.3.1 Data collection

Much of the work on Ritter Island was achieved by using the previous work and datasets collected by others. I would like to acknowledge and thank them for their work here:

- Drone imagery taken in 2016 on the SO252 (RV Sonne) cruise collected by Berndt et al. (2017). This dataset contains a series of drone videos containing arial imagery of Ritter Island with a resolution of 72 dpi.
- Rock samples collected in 2005 by Simon Day – referred to as 'SD' sample set as used by the collector.
- Rock samples collected in 2009 by Saunders and Kuduon (2009) – referred to as 'Rit' sample set as used by the collector.
- Submarine rock samples collected by Berndt et al. (2017) – referred to as 'H' sample set as used by the collector.
- Bathymetry data collected by Berndt et al. (2017) – A 5 m/px dataset containing the area to West of Ritter of the scar and deposits and a 25 m/px dataset containing a much wider area containing the Eastern flank of Ritter and the distal deposits (Figure 2.12)
- Previous work and thin sections of SD and Rit samples by Ray (2017) – this contains work on records providing descriptions of the island before and after collapse and accounts of the tsunami in the surrounding regions and detailed petrological work on Rit and SD samples.

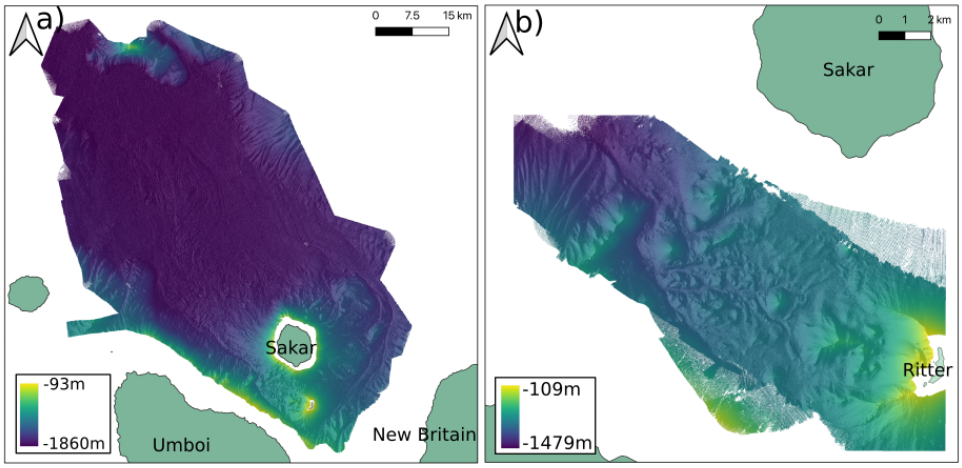

Figure 2.12: Bathymetric datasets collected by Berndt et al. (2017) a) 25 m/px resolution and b) 5 m/px resolution.

It should be noted that the intention for the sample collection for each of these sample sets for Ritter Island for was petrological analysis. This means that these samples were selected to be fresh and intact rather than weathered or altered. Therefore, any mechanical property investigation based on these samples will have this bias. Therefore, the values produced will likely to be end-members for the true spread of rock properties whereas the more weathered rocks, which can be identified on the sub-aerial island imagery, may prove weaker but are not represented in this sample set.

2.3.2 SfM modelling

Structure from motion (SfM) photogrammetry is the process of generating three-dimensional (3D) surfaces and structures from a series of images of an object or area from different viewpoints (Schonberger and Frahm, 2016). The technique of SfM has been used in research since the 1980s however the progressive improvement of technology mean its utility can be applied in many different fields (Eltner and Sofia, 2020). The different aspects of technological advancements affecting the progression of this method include the camera quality, UAVs (Unmanned Aircraft Vehicles), GNSS (Global Navigation Satellite System) and computer intelligence. High resolution topographic datasets can be produced which is often fundamental in modern geoscience.

A number of advantages are associated with using UAVs alongside SfM to produce DEMs (digital elevation models) and orthomosaics. Often, results can be produced that are of a much higher resolution and cheaper than alternative sources such as satellite imagery or LIDAR (Light Detection and Ranging) (Eltner and Sofia, 2020). In addition, results can have good spatial accuracy as well as being able to produce results quickly and easily, dependant on the size and quality of raw data. The resolution can be determined by planned flight routes at specific heights. Temporal frequency can also be easily controlled and fulfilled at frequent intervals (Eltner and Sofia, 2020). This method can also image and model vertical features, which has been essential in this project as the scarp of volcanic collapse are often vertical or near-vertical features.

The method for generating a model from images involves feature detection and matching across overlapping images. Positioning of the cameras are detected and the points are given values in 3-dimensional space to create a sparse point cloud of the intended object (Eltner and Sofia, 2020). The workflow of producing a SfM model using UAV imagery must be

considered carefully. The method includes multiple stages including planning, indoor preparation, for example battery charging and data back-up, flight execution and data processing (De Beni et al., 2019). This is outlined in the check list in Figure 2.13 and discussed below. In this discussion, the object or area that is intended to modelled will be referred to as the “target feature”.

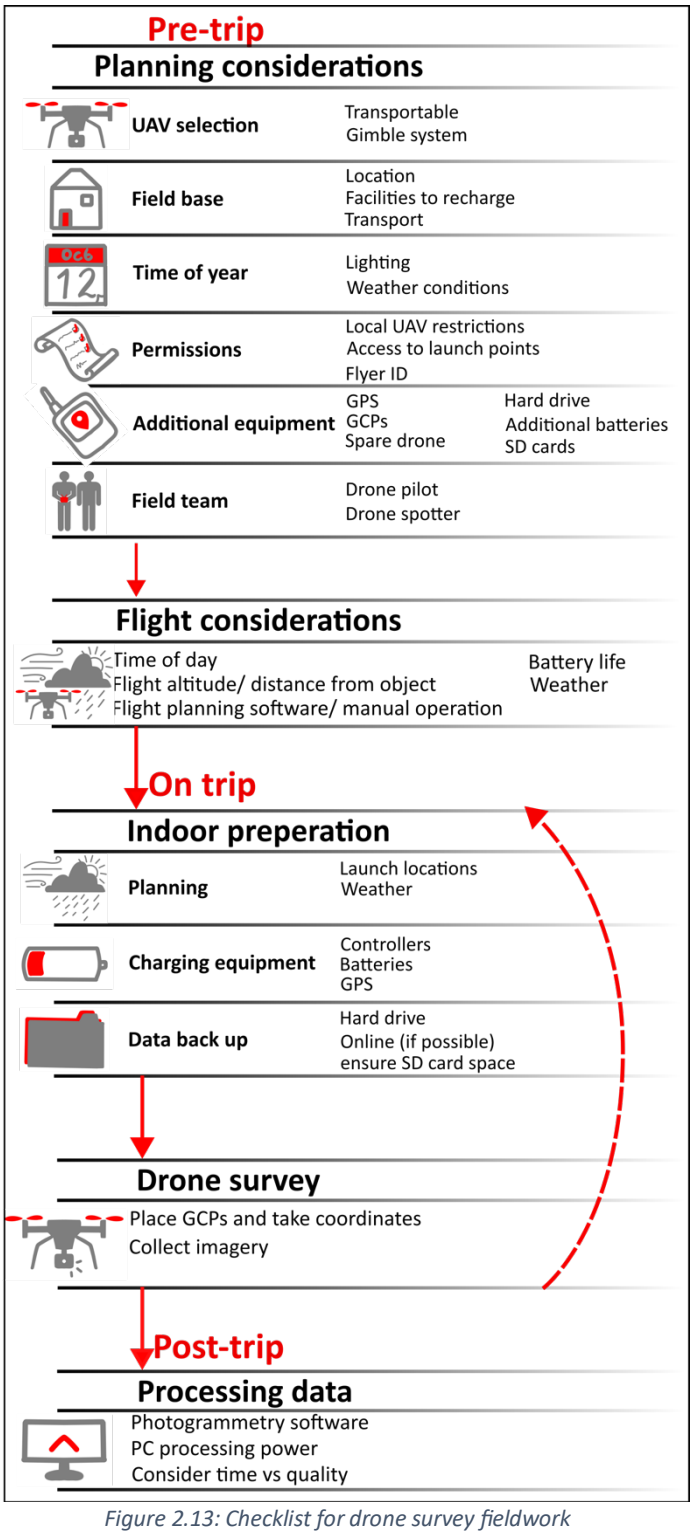

Figure 2.13: Checklist for drone survey fieldwork

Planning considerations

SfM models requires fieldwork to be undertaken to collect UAV image datasets of the target feature. Planning this fieldwork includes careful consideration once the location and the target feature has been identified.

- **UAV selection**
    - Where some field sites, including in this project, may have been less accessible and require hiking, the UAV must be transportable, easy to assemble and disassemble and able to take off from slightly uneven ground or from hand take-offs (De Beni et al., 2019).
    - The UAV should have appropriate gimble stabilisation to be able to capture sharp frames needed for ease of data processing (De Beni et al., 2019, Eltner and Sofia, 2020).
- **Field base**
    - Location of field base would ideally be close to target feature to allow easy transport for drone surveys, particularly if battery charging needs to be done within the day for further surveys.
    - Base must have ability to charge equipment to maintain efficiency for data collection
    - Transport to drone survey site must be accessible from base for example by car, hiking, public transport etc.
- **Time of year**
    - An optimal time of year to undertake a survey is when weather conditions are likely to be fair with minimal precipitation and low wind speeds to allow drone flights to take place
    - In addition, the time of year when data is collected will affect the lighting of the target feature. For example, a summer's day will allow more light in the day for imagery to take place and for the target object to be best lit.
- **Permissions**
    - Research local UAV permissions in area of drone survey to find if any flight restrictions are in place or if any permissions are needed. Maximum flight altitude may restrict imagery of target feature (Bonali et al., 2019).

- Ensure safe and legal access to intended drone launch sites
- Ensure Civil Aviation Authority (CAA) Flyer ID is obtained before survey, if UAV is more than 250 g.

- **Additional equipment**
  - In addition to the drone, it is essential to consider other equipment needed for fieldwork, some are suggested here.
  - Ground control points (GCPs) can improve the accuracy of the model or provide a reference to calculate the error of the geolocation, even if the UAV has accurate GNSS capabilities (Eltner and Sofia, 2020).
  - A GPS is useful for recording locations of GCPs
  - A spare drone could be considered, if possible, for insurance if there is a fault with the first. Ideally, they would be of the same specification to ensure consistency across image datasets. In addition, spare propellers and SD cards should be taken.
  - Additional batteries should be taken to increase possible survey time before recharge is needed.
  - A hard drive, preferably a rugged one, should be taken in order to safely back up drone survey data.
- **Field team**
  - As well as a drone pilot, a drone spotter is needed to maintain sight of the UAV for safety.

Flight considerations

When planning the drone survey flights there are also many things to consider.

- The changing daylight also will affect the exposure and shadows of the images captured. Depending on the reason for data collection, having shadows in the resultant model may not have any effect, however, if the purpose of the SfM model is to analyse the texture of the target feature, then shadows may obscure some details. Ideally, when the sun is facing directly towards the target feature, then shadows will be minimal. At more oblique angles, the shadows are longer. In addition, if the survey is taken over a number of days, the time of day should be kept as similar as possible for image matching purposes.

- The weather affects many aspects of drone surveys. Most importantly, conditions that are too windy or rainy can restrict flight progress. The weather must be monitored daily to assess whether safe launches can be made. In addition, changing cloud levels will change the lighting and this may affect image matching. The air temperature will also have an effect of battery life where too hot or cold conditions will reduce battery flight times.
- The battery life time must be considered when planning flight lengths. Additional batteries and convenient charging facilities will maximise drone flight time per day (Bonali et al., 2019).
- When flying the drone manually to collect imagery (as opposed to automated flight plan software), there are considerations:
    - Include image overlap throughout the survey to improve image matching during processing (Mosbrucker et al., 2017).
    - Ideally, the drone should be kept at a constant height relative to the ground surface to create a constant resolution model; this is much more difficult when the terrain is steep (De Beni et al., 2019).
    - Images should be captured of the target object from various angles to improve coverage of the structure to build a more accurate 3D model. Collecting images of oblique angles to the ground surface produces a more accurate model with limited 'doming effects' (Bonali et al., 2019).

Indoor Preparation

During the trip, before and after surveys take place, indoor preparation must also be considered and actioned to maximise efficiency.

Planning

- Before entering the field and beginning surveying, it is important to plan the day according to lighting and weather. For example, checking the weather forecast for any rain or high winds allows planning of timing of flights. More extreme weather will also determine battery life when considering planned flight times.
- It is also useful to plan launch sites, if for example imaging a long steep feature such as a cliff, to ensure good image coverage is collected at reasonable intervals along the area.

Charging

- Equipment should be fully charged before entering the field. For example, drone controllers, portable mobile phone devices, drone batteries, GPSs, portable chargers. When field base is proximal to drone survey, a recharge during the day may be possible to maximise flight time. Everything should also be recharged before the following field day.

Data back-up

- Following a day of data collection, it is paramount to back up this data as soon as possible for security. If possible, this should be done on a physical hard drive and online if internet access is available.
- The drone SD cards should then be cleared and replaced ready for the next data collection.

Processing Data

- The photogrammetry software can be selected due to its capability, preferred operating system and price. The software used in this project was Agisoft Metashape.
- The computer processing power must be adequate to process large datasets.
    - The RAM (Random Access Memory) of the system will limit the size of the project. Therefore, an increased RAM is preferable for a project with large datasets needing higher quality processing. As recommended by the software manual, advanced processing would be achievable with a 32-128 RAM
    - The recommended CPU (central processing unit) for using this software to enable processing of complex geometries has 6+ cores with 3.0+ Ghz
    - The GPU (graphics processing unit) is recommendation for using software such as Agisoft is 1 - 2 NVIDIA or AMD GPUs with 1920+ unified shaders
- When processing the data, the time and quality of the resultant model generation needs to be considered as prioritising one over the other will result in a trade-off. The highest level of processing for example in image matching, tie point and surface generation require more time and processing power. However, if the result is needed in an urgent scenario, for example in the context of hazard monitoring, then the quality of this processing would need to be sacrificed to produce the model more quickly.

Within the scope of this project, SfM modelling was used to generate 3D models of the collapse scars at the two field locations at Ritter Island and Fogo Island. In the case of Ritter Island, the imagery had already been collected and provided from a previous excursion (Berndt et al., 2017). For Fogo, a field trip was planned and executed based on these parameters discussed in section 4.3.2.2. The drone imagery was performed 6 years apart, which meant that drone technology had moved on between the two field campaigns. The Ritter imagery was taken over the ocean, with only three flights, whereas the Fogo imagery was taken on land, with vastly more flights and 15 launch points. Therefore, slightly varying techniques were used to process the data. The main steps followed for both locations and more specifically for Ritter Island are discussed here.

2.3.2.1 Agisoft software

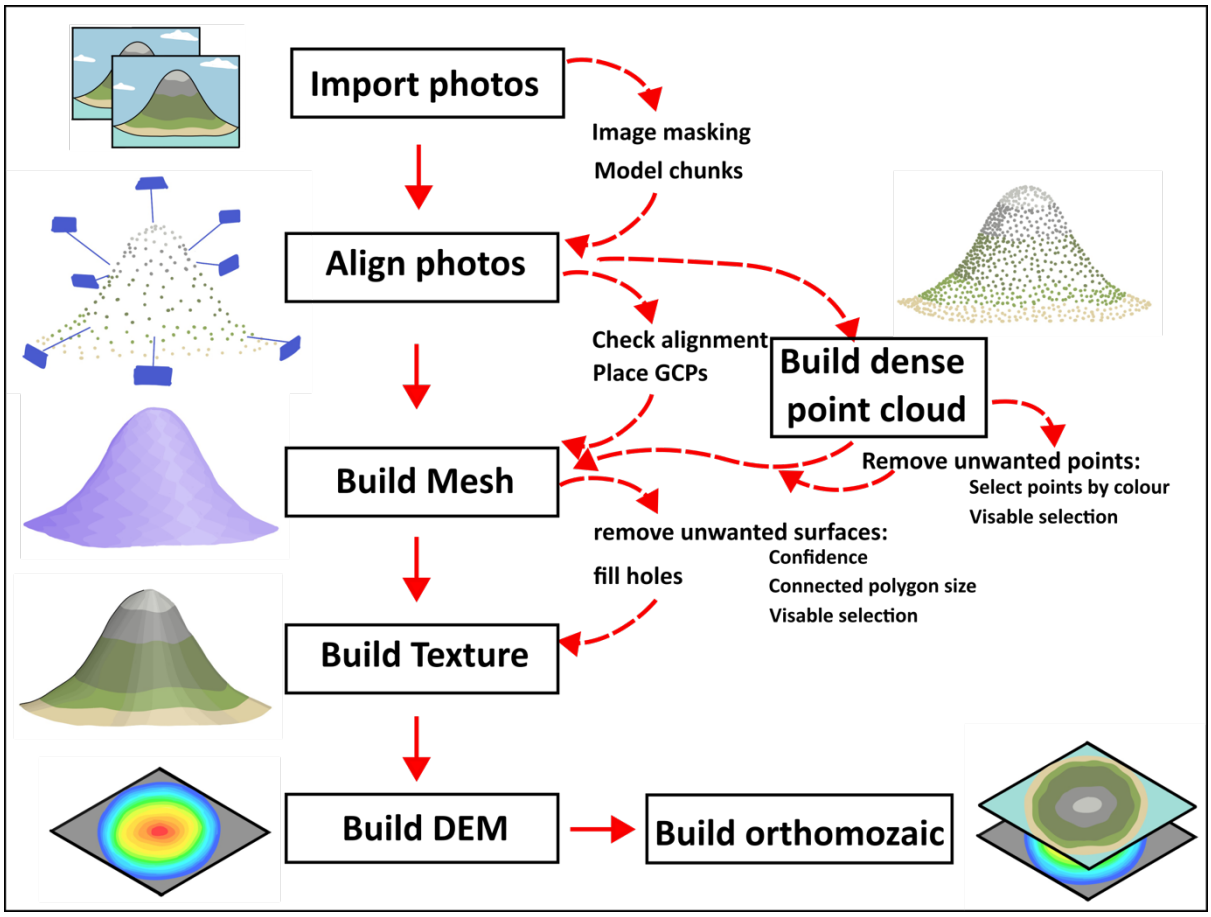

Figure 2.14: Agisoft process for building 3D model from drone imagery

The SfM modelling technique was used in this project for both study locations to generate 3D models of the collapse scars at Ritter Island and Fogo. Data processing was achieved using Agisoft Metashape software, which uses photogrammetric processing of photographs to create 3D spatial data that can be used within GIS software. This method aligns images to create a tie point cloud and depth maps of a surface. From this a dense point cloud and mesh can be generated. Textures can be generated from the original images and the resultant outputs are DEMs and orthomosaics. Figure 2.14 outlines this process with the main stages:

- **Import images.** All images from the drone survey are imported into Agisoft workspace.
    - In some cases, masks can be used on individual photographs to remove the sky, ocean or other unwanted features from the process to improve model quality.
    - To improve image alignment and processing speed, the images can also be separated into 'chunks' to be processed independently and merged later.

The photos can be grouped into chunks based on the area in the images displayed. Some areas of overlap between the chunks should be included by using the same images, which means that the chunks can accurately be merged at a later stage.

- **Align photos.** After the images are masked, they are aligned against one another to generate a point cloud of tie points. The Agisoft photo aligning process creates 'tie points' where the images are matched and estimated photo locations are displayed (Figure 2.15A). Depth maps are created during this stage (Figure 2.15C),
    - In an ideal scenario, drone image data will have geolocated metadata associated with each image. Agisoft software is able to read this source data and locate where the images were taken from and at what angle. Hence the software will more easily line up the images and produce a model that is accurately georeferenced. For Ritter Island, the images were not geotagged and, as a result, the model had to be georeferenced manually afterwards using satellite data as a reference. For Fogo, the images were geotagged and also GCPs (ground control points) were used, so the resultant model could be more easily geolocated. GCPs can be imported and placed on the images at this stage to aid alignment.
    - Within each chunk, the alignment process can be run several times while keeping the correctly aligned photos at each iteration to improve the alignment of the remaining images. This is a key stage if the images are not geotagged.
- **Build dense point cloud –** A dense cloud can then be generated from tie points (Figure 2.15B).
    - Unwanted points are then selected and removed. This can be done by visibly selecting and deleting the points or by using the 'select points by colour' tool. This is useful if selecting a feature of a distinct colour that is unwanted for example areas of sky or ocean.
- **Build mesh** - From this dense cloud data or from the depth map data, a polygonal mesh is created for each chunk (Figure 2.15D). Agisoft software recommends generating the mesh from the depth maps as opposed to using the dense point

cloud. Using the depth maps means the resultant mesh would be more detailed and uses less RAM.

  - Unwanted faces are removed at this point. This can be done by visibly selecting unwanted regions and removing them**.** In addition, the gradual selection tool can be used to select and remove polygons based on their relative model confidence. Here areas less than 10% are removed. The smallest connected polygon size can also be selected to remove floating areas of inaccurate model.
  - Any areas where there are holes in the model due to a lack of image cover are filled using the 'fill holes' function. This function only works where the 'hole' is surrounded by areas of mesh. These are also areas where the model is more uncertain due to reduced coverage from the drone imagery. This model uncertainty can be visualised in Agisoft in terms of relative accuracy based on point cloud coverage, which is useful to identify the areas which may involve the greatest error (Figure 2.15D.iii).

- **Build texture** – A texture can be generated using the original images to improve viewing the 3D model. The texture size can be increased for a more detailed model but it increases the size of the file. This mesh model can be viewed as shaded or a texture can be generated from the original images (Figure 2.15D.i), or it can be viewed as a solid model (Figure 2.15D.ii) which can be useful to visualise the structures within the model. At this point the chunks are aligned and merged to generate the whole model.
- **Build DEM -** Once the mesh has been generated successfully, Agisoft can then be used to generate the model in tiff formats that can be used in GIS software. Digital Elevation Models (DEMs) represent elevation data in raster format where each pixel represents an elevation value. Agisoft can generate a DEM from the depth maps or the mesh model and exports it as a raster file type. Using the depth maps can produce a more accurate model, however using the mesh removes some of the noise which is preferable for slope analysis. In generating this file, the projection and resolution can be selected. The Coordinate Reference System (CRS) that can be selected so that it can be imported geolocated into GIS for further use and analysis. The quality of the DEM increases with the drone survey coverage;

however, higher resolution models will produce a much larger file size which can be difficult to manipulate.

- **Build orthomosaic –** Orthomosaics are another raster file type that can be produced and exported from Agisoft using the DEM as the surface. These are datasets where images are stitched together as a mosaic using the original images and texture produced to create a continuous planar image. These can be useful to observe features in higher resolution than satellite imagery. In addition to map view orthomosaics, these datasets can be generated in any orientation in Agisoft. For the purpose of this project, a map view orthomosaic was generated as well as a lateral view of the cliff face for both islands, so that patterns and structure can be observed from each perspective.

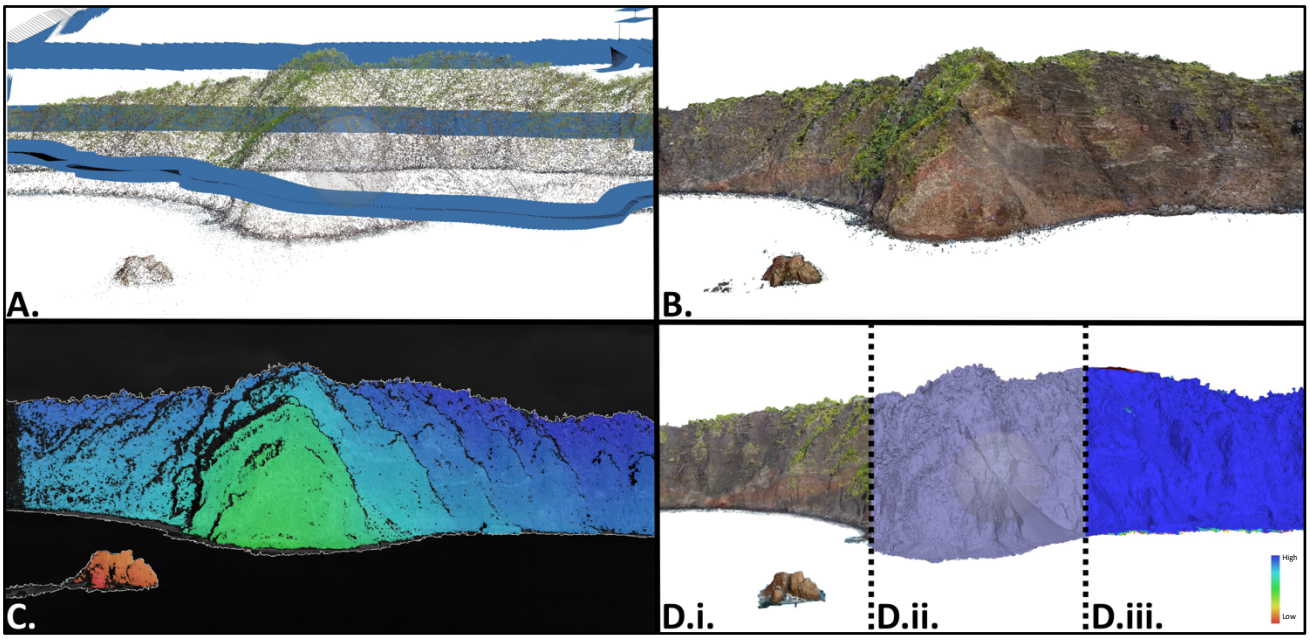

Figure 2.15: Stages of processing in Agisoft software using Ritter Island as an example. A. Tie point cloud generated from camera alignment displaying the estimated location of the cameras in blue. B. Dense point cloud generated from depth maps. C. An image with depth map overlayed. D. Mesh generated from depth maps displayed as i. textured, ii. Solid and iii. Relative confidence.

For the purpose of this project, the drone survey and resultant model did not have a time pressure on model production. Therefore, there was time to process models at the highest possible quality to get the best model resolution based on the collected data. This is needed to map and measure the collapse scars. In addition, processing was carried out following the data collection and on computers with high quality specifications. To improve the speed of processing of the large data volumes, three machines were used in parallel to

produce the models. The specifications of the machines used had an Intel i7-9700 processer with 3GHz, 128 GB of RAM and a NVIDIA GeForce GPU. Where structure from motion modelling is being used increasingly for monitoring and emergency response purposes in geohazard assessment, this is important to consider (Bonali et al., 2019). Often, for emergency investigations, processing must be carried out rapidly. Where internet access may not be ideal in remote locations, processing must be achieved in the field using portable computers and require quick processing. This may affect the accuracy of the model (Huang et al., 2017).

In this thesis, 3D models that have been generated for the collapse scars can be viewed using the links to Sketchfab. The models and links are listed in appendix 2 and referred to throughout the thesis. The models are password protected where the Ritter model's password is 'ritter' and the Fogo models password is 'fogo'.

2.3.2.2 Ritter Island imagery processing in Agisoft

The series of drone videos taken in 2016 was used within Adobe Premiere video editing software to extract image frames at 1 second intervals at the highest resolution possible at 72dpi. These photos were then imported into Agisoft. As the photos used to create this model were extracted from a video, individual geotags could not be attributed to the image files. This meant that images are less easily aligned and the final model had to be georeferenced manually.

There were three iterations of the model where each subsequent attempt had various aspects improved. The first iteration was generated without the use of masking images; this introduced some uncertainty when generating point clouds. Therefore, the second iteration used the masking tool in Agisoft which involved tracing and deselecting the unwanted sections of each image, for example areas of sky and ocean. The final iteration of the model also used this masking method, as well as using the 72 dpi images extracted from the original drone videos and at more regular intervals to create a high resolution model.

The images were grouped into two chunks, highlighted as shown in Figure 2.16: east and west. As the drone surveys were not taken at the same time, there are some differences in the quality of image taken. For this reason, and the lack of georeferencing, these two sets of images could not be automatically cross aligned in the software, despite having overlapping areas of the island.

Each of the images were individually masked within Agisoft. This process involved selection of areas in each image that displayed ocean and sky to remove these regions from the process of alignment to reduce error in generating point clouds. Each chunk was then processed separately generating separate meshes. As these images were not georeferenced, alignment was run a number of times where errors occurred within the tie point cloud. Where some images were incorrectly aligned, they were reset and the process was run again whilst aligning them to the correctly aligned images.

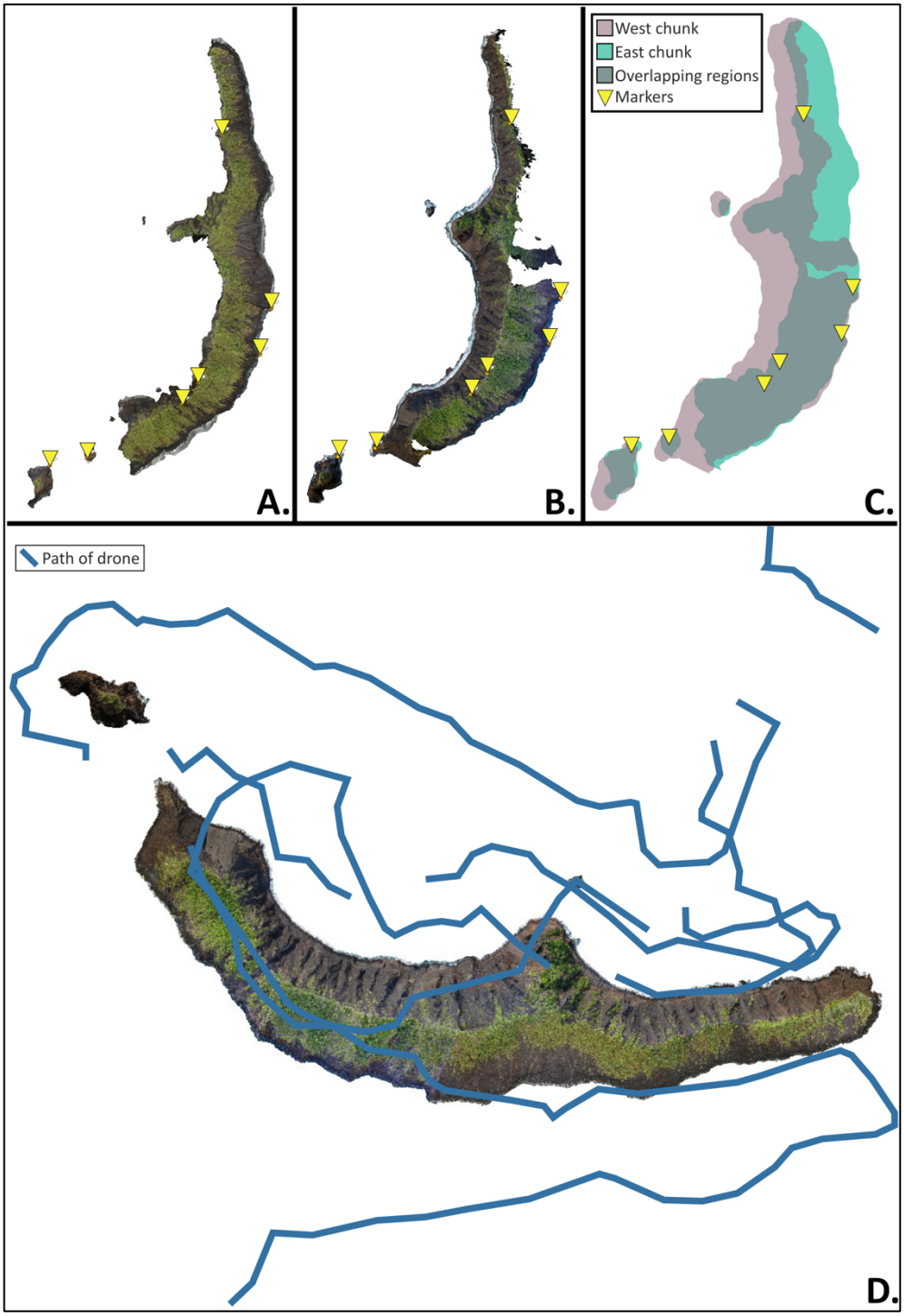

Figure 2.16: Construction of Ritter Island 3D model in Agisoft using chunks. A. Displaying the east chunk with markers. B. Displaying the west chunk with markers. C. Showing how the east and west chunks lined up using the markers to construct the whole island model including areas of overlap. D. Final combined model showing the trace of the inferred drone path over Ritter Island.

The eastern chunk had fewer images of lower quality, had less coverage and had poorer lighting conditions, so more error is present in the resultant model compared to the western side. In total, 343 images were masked aligned for this eastern chunk. The western

chunk had more images, were of higher quality and had good coverage in most areas. 2956 images were masked and aligned for this chunk.

To align the separate chunks, key identifiable features that can be seen in the overlapping areas of the model are marked as 'markers' on the chunks. Here 7 markers were identified across the east and west chunks (Figure 2.16). These were chosen as the most identifiable points across both chunks distributed across most of the model. These points were then used to align the separate chunks and subsequently to merge them. The mesh was reprocessed from the amalgamated depth maps and a mesh model was generated of the whole island. There were fewer points identified in the north of the island and therefore the model alignment may be less inaccurate in this region.

Figure 2.16D shows the merged chunks and the whole inferred path of the drone. This drone path shows where the coverage across the island is lacking, for example on the northern tip, the south eastern tip and the east side of the island. The level of uncertainty in this model can be viewed using an Agisoft feature that allows the mesh to be viewed in terms of relative 'model confidence'(Figure 2.15 D.iii). This relative confidence is a software feature that uses the density of tie points to estimate accuracy of the model. Selection using this confidence criteria was used to select the least confident areas to be removed. Anything below 10%

confidence was removed from the mesh. These include areas with little coverage and also areas of ocean at the base which were included in the mesh.

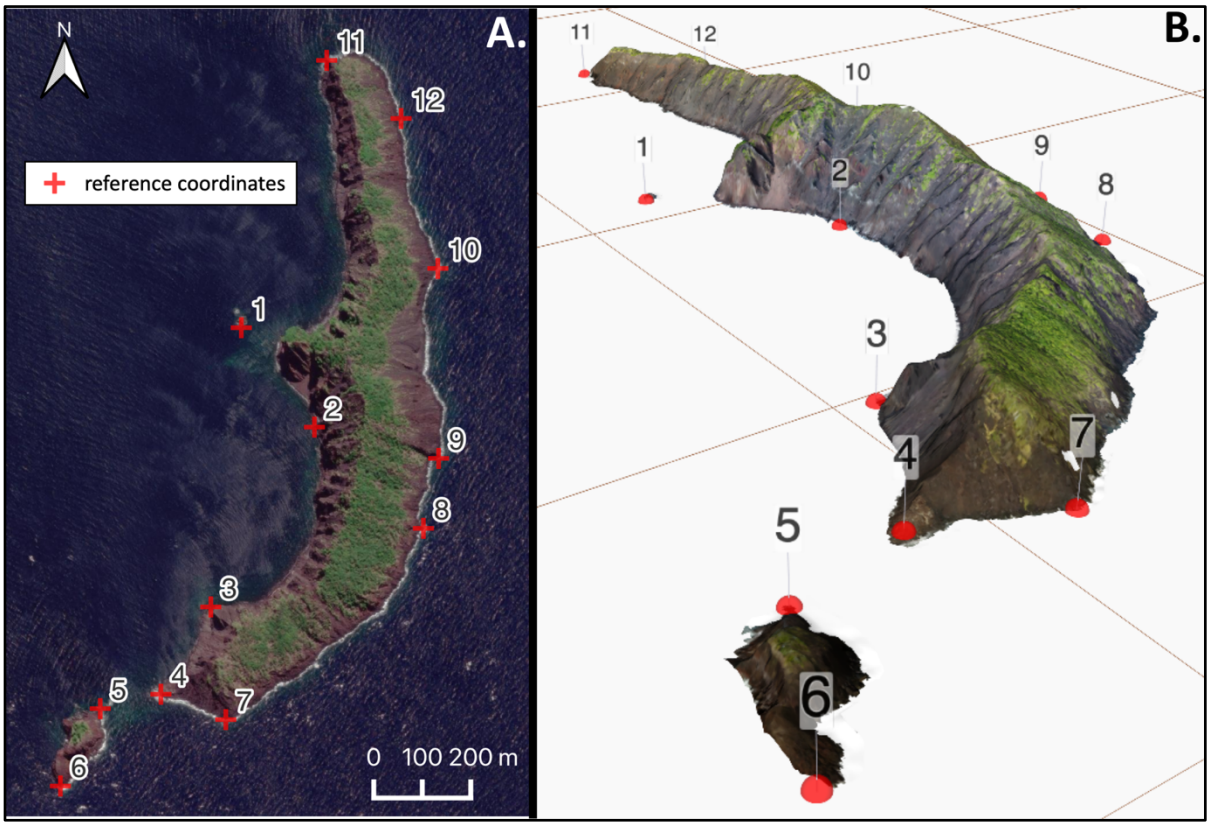

Figure 2.17: Georeferencing process for Ritter Island. A. displays 12 reference points on ESRI satellite image. B. The same 12 points on 3D model of Ritter Island.

As this model was not georeferenced, it had to be manually geolocated using a reference satellite image from ESRI. On QGIS, 12 points were created as a point shapefile using ESRI satellite imagery of the island as a reference where an identifiable feature of the coast of the island could be seen (Figure 2.17A). The WGS84 latitude and longitude were extracted using the QGIS function 'Add X/Y fields to layer'. The altitude is assumed to be 0 m as the points are at sea level and there is no reliable elevation data available for the island. This assumption may introduce some error as this value may be slightly different due to the tidal range at the coast. Reference points higher up on the slopes of the island could not be used as available elevation data for this island was poor. These points were then imported into Agisoft as reference points. Each point was then identified and marked on the 3D model (Figure 2.17B). The model was then transformed to match these coordinates and the was therefore georeferenced in the coordinate reference system (CRS) WGS84.

2.3.3 GIS analysis of Ritter Model

2.3.3.1 GIS project settings

The local CRS (Coordinate Reference System) used for Papua New Guinea area is UTM zone 55S ID: EPSG: 32755. Due to the georeferencing process outlined in section 2.3.2.2, the model outputs from Agisoft are geolocated in WGS84. Where some datasets used were originally projected in WGS84 or other, they were reprojected into UTM for consistency. An island shape polygon was made using the orthomosaic as a guide to clip the DEM raster down to show only the island data. The other major raster datasets used includes the two sets of bathymetry data collected by Berndt et al. (2017).

2.3.3.2 Placing sample locations

The set of samples provided were taken from Ritter Island in 2006 and 2009 and a submarine set from 2016 as described in section 2.3.1. The 2006 SD sample set was provided with coordinates taken at the time of collection. Figure 2.18A shows these coordinate locations; however, these do not line up with the island orthomosaic, possibly due to poor satellite quality affecting the coordinate readings. Using the descriptions and images from the field notes, the sample locations can be more accurately identified using the model (Figure 2.18C) and orthomosaic, therefore the positioning was corrected (Figure 2.18B). There may be some inaccuracy here due to the rapid erosion of the island where some sample sites may have been weathered or covered by scree in between the time of collection and the time of the drone survey. The 2009 samples were given locations by a field sketch and a labelled image from Saunders and Kuduon (2009) and therefore the image can be matched with the 3D model based on this to define the sample locations and add them to the GIS software as point shapefiles (**Error! Reference source not found.**). The 2016 submarine set of samples were provided with GPS locations from the time taken and are assumed to be accurate and no changes were made (Figure 2.19)(Berndt et al., 2017).

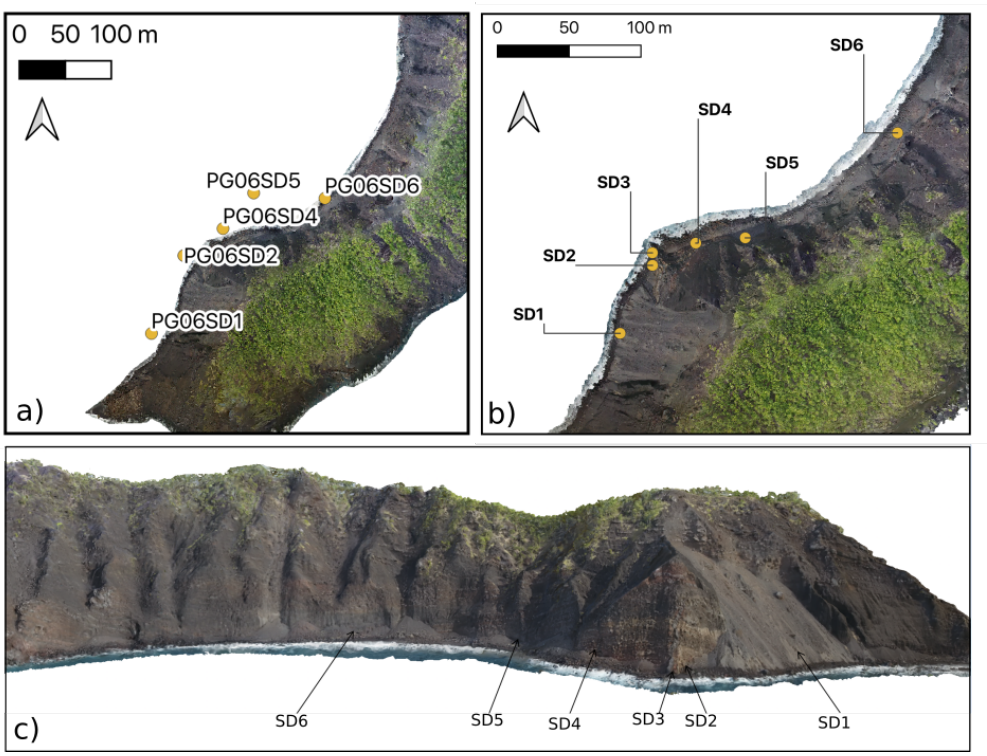

Figure 2.18: SD sample location positioning process using QGIS and structure from motion model; a) coordinates from original 2005 collection, b) placed sample locations using orthomosaic and model, c) Agisoft screenshot of structure from motion model used for placing SD samples.

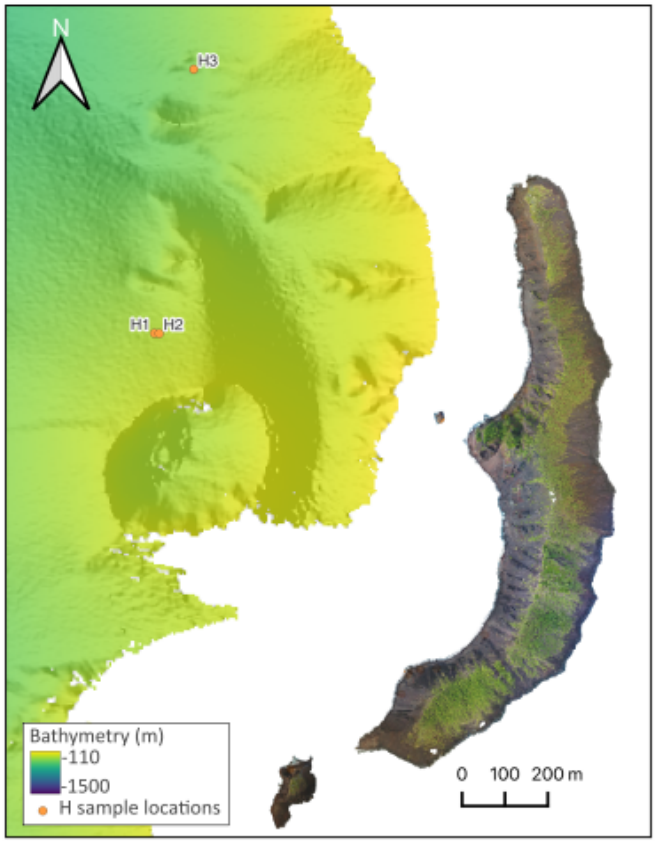

Figure 2.19: Locations of submarine 'H' samples collected in 2016.

2.3.3.3 Orthomosaic analysis

The orthomosaic of Ritter Island is an excellent resource for mapping the surface of the island. When analysing both the aerial and side-view orthomosaics, areas of higher uncertainty can be identified as gaps or blurred sections where the area of the island had less drone coverage. Different features can be identified on this orthomosaic such as vegetation, areas of red alteration and geological features.

Figure 2.20: Images showing example of highlighting areas of 'red' alteration using Adobe photoshop; a) the original image of the central cusp of Ritter Island, b) using saturation and colour filters to highlight these areas and c) using the colour range selection.

Areas of alteration were identified using the original drone imagery using Adobe photoshop software. Images showing areas, identified by a red tinge, can be enhanced or edited to highlight them further. One way of highlighting these areas is to increase the saturation of the image and increase the selective colour effect to further enhance the 'red' altered areas (Figure 2.20b). An alternate method is to emphasise these areas of alteration by selecting the colour range from the image and to highlight this as saturated colour whilst the rest of the image is unsaturated (Figure 2.20c). This process can then be used on images across the island to help identify these areas and match them to the model to be then mapped as polygons. This same process of saturating and extracting the altered areas can also be applied to the orthomosaics.

The Photoshop process was used on the orthomosaic to highlight areas with a more reddish hue, in order to map areas of alteration or weathering. This method was also used to highlight green hues to map the vegetation cover.

Where vegetation covers the island, an undulating relief is produced in the DEM output of the model. The vegetation cover area was used to discount areas of undulating slope terrain when calculating the slopes of the island. After the orthomosaics were edited in Photoshop to highlight these zones, they were georeferenced and brought into QGIS. The raster calculator was used to isolate the coloured areas using the colour bands. This was

achieved by a formula removing the greyscale areas where Band 1 = Band 2 = Band 3. The remaining raster displayed the isolated coloured areas as a value of 1 and the rest of the area as 0. This was then polygonised and saved as a new shapefile layer. This layer was then manually edited where there were areas of error or to simplify the shapefile by removing vertices or shapes with a small area. This process created precise polygons with a high number of nodes compared to the relatively simpler polygons produced by manually mapping. The areas mapped using this method represented areas of alteration and areas of vegetation (Figure 2.21). The area of these polygons can be calculated to estimate vegetation cover and area affected by alteration over the whole island or different regions.

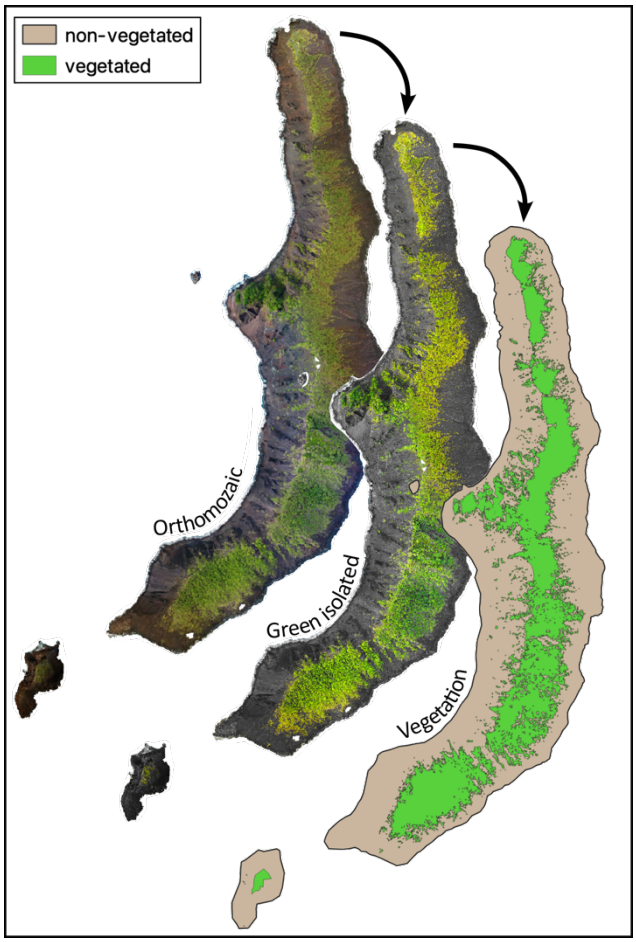

Figure 2.21: GIS process on defining vegetation cover as a polygon at Ritter Island from the orthomosaic

2.3.3.4 DEM analysis

QGIS software has various spatial analysis tools which can yield measurements from the constructed DEM, including slope and aspect analysis. Volume, area and dimensions can also be calculated.

Base map

A Ritter Island base map was generated using the DEM data by creating a 'hill shade layer', based on the aspect of the island, and 10 m contour lines based on the elevation. This forms the base map of the geological map.

Interpolating 'no data'

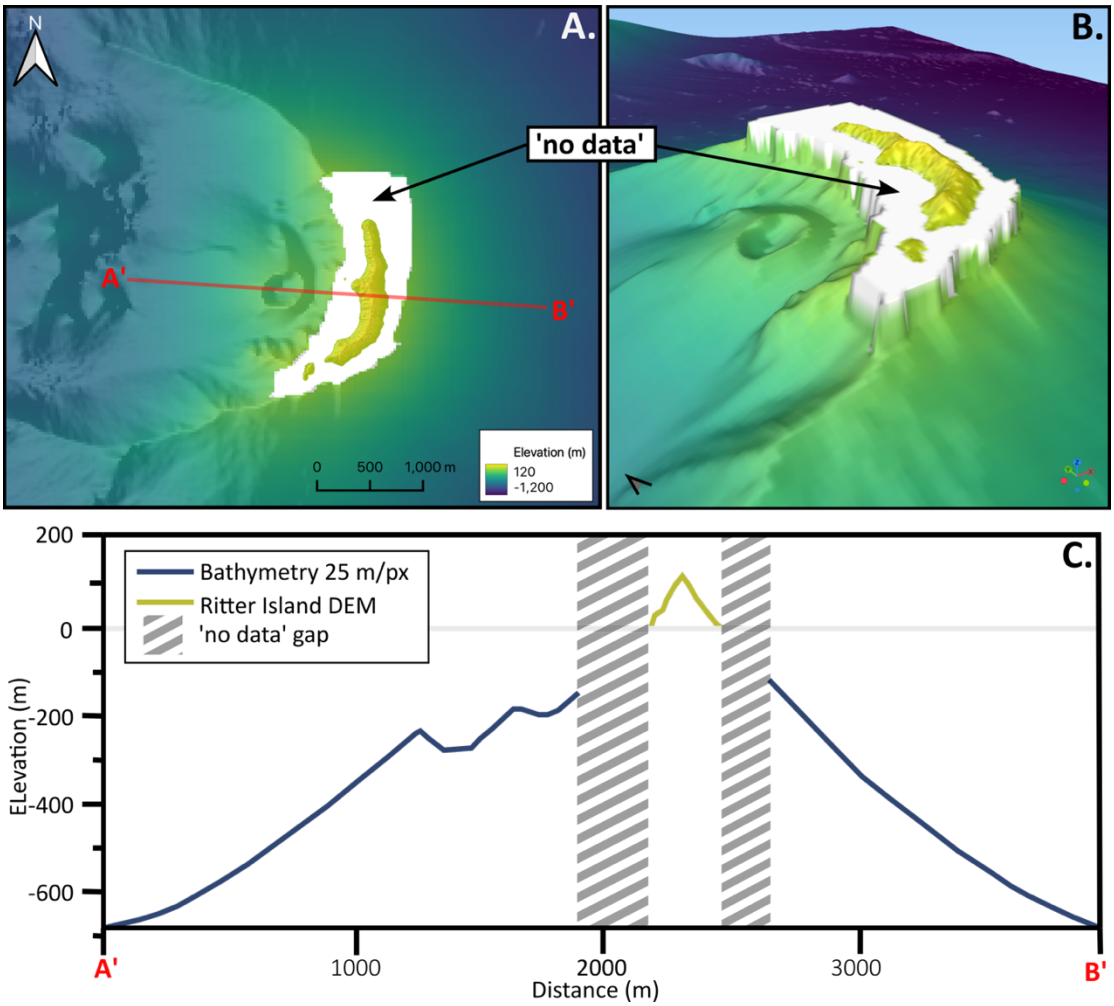

Figure 2.22: A. Bathymetry (25m/px) alongside Ritter Island DEM showing 'no data' gap in A. map view with cross-section line and B. 3D view. C. cross-section across bathymetry and DEM showing 'no data' gap.

Figure 2.22 shows the Ritter DEM alongside the 25 m/px resolution bathymetry. The bathymetry survey does not cover the shallower areas proximal to land, roughly between -

300 m and 0 m elevation, and therefore there is a gap in this data. QGIS interpolation methods can be used to approximate elevation data between the 25 m/px bathymetry data and island elevation. This can be achieved this by merging the two raster files at the lowest resolution of the two which is 25 m/px. The data gap was assigned as 'no data' represented by the value -9999. The 'Fill No Data' tool can then be used within the QGIS software, which calculates the missing 'no data' pixel values by using inverse distance weighting from the surrounding pixel values and smoothing the result. The maximum number of pixels used to search out for values to interpolate was 20 and one smoothing iteration was run after interpolation to get results which best fit the existing surfaces.

There are some limitations using this method as there is an assumption of continuous smooth surface between the gaps and may miss out any finer detail or undulations in the bathymetry that may be present in reality. On completing this process, the infilled gap raster file was converted into contour lines and observed in 3D to help identify any obvious issues with the output (Figure 2.23). Here, a section to the north of the island looked as if it would be inaccurate due to a flat portion where the northern limb of the scarp would continue. In addition, due to the lower resolution, the small western islet was not included in the interpolation, therefore the western submarine slope was projected closer to the main coast of Ritter then we know is possible due of the presence of the islet. To help resolve these

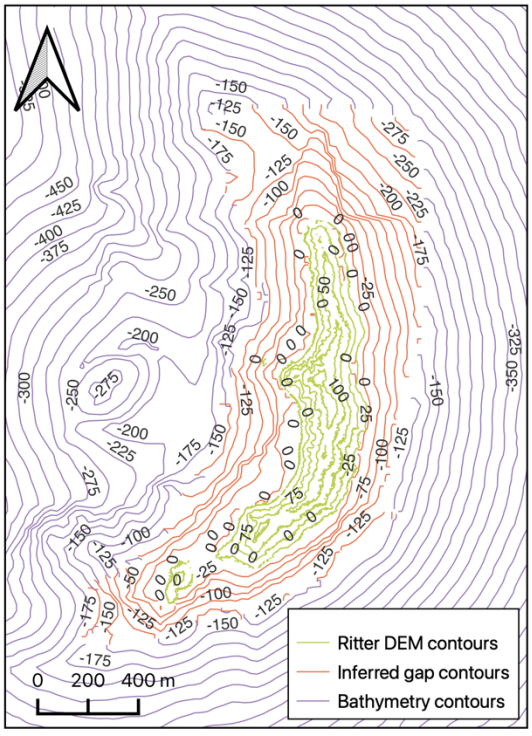

Figure 2.23: Contour lines of bathymetry and Ritter DEM and the infilled 'no data' gap.

inferred inaccuracies, the 25 m contour lines had their vertices edited to represent a more realistic pattern. These edited contour lines were then interpolated into a surface raster as the final 'no data' gap and merged alongside the bathymetry and the island.

Slope analysis

Slope measurements are useful for Ritter Island as they can be used to compare the steepness of the western side of the island which represents the top of the collapse scarp, and the eastern side which represents the original pre-collapse slopes. This can be used to reconstruct the pre-collapse cone.

Initial analysis of the slopes of Ritter was made through a series of seven E-W trending cross-sections through the DEM. These were done using the 'qProf' plugin for QGIS software that generates height and slope profiles from DEMS to produce topographic and geological profiles. For each profile, a CSV output can be produced containing the elevation data as well as the slope with distance along the section. This data then required some processing which involved splitting the information between the east and western slope. The eastern slope value outputs were negative due to the direction of the slope, so these were converted to positive values. Small values < 1 and negative values were then removed to compare only seaward-dipping portions of the profile and finally the values were rounded up to whole numbers.

The slope of the island can also be analysed using GIS statistical analysis over raster data created from the DEM. A smoothed version of the DEM was used to reduce some of the noise from the higher resolution version to produce a better average of the slopes. The 'slope' algorithm on QGIS calculates the angle of inclination of the terrain in degrees from the input DEM raster. The output of this produced a raster layer where pixel values represented the angle of slope.

This slope layer was used to identify the areas of deposited eroded material in scree slopes and blocky deposits at the base of the cliff on the western side. These areas have much shallower slopes compared the cliff and therefore the sharp change from steep to shallow slopes bounds the edges of these deposits and can be mapped. This mapped deposit can also be compared to the orthomosaic to verify the accuracy.

The slope layer can also be used to gain a whole raster analysis or compare separate areas. Ritter Island was split into different areas based on the slope direction to compare the east and west sides and also the vegetation cover. These were represented by polygon

shapefiles. Vegetation on large portions of the eastern side and some of the western part had an effect on the angle of the slope due to the undulating relief it produced. The main island was separated into east and west by using the 'aspect' algorithm on QGIS. This tool calculated the aspect of the DEM, expressing each pixel as a compass direction between 0 and 360°. This resultant aspect raster image was then manipulated to display 0-180° as one colour and 180-360° as a second colour. These groupings were selected as the resultant effect on the DEM created the clearest difference between the two sides. The island shape polygon was then split manually following the path of this clear partition to create west and east shapefiles (Figure 2.24). The vegetation polygon generated using the method in section 2.3.3.3 was used to clip these shapefiles to create a polygon for each side covering only areas with no vegetation using the 'difference' tool in QGIS (Figure 2.24). The 'zonal statistics' tool was then used which calculates the statistics of a raster layer for overlapping polygon layers. This was done for the east and west polygons both with and without vegetation to see the impact that inclusion of vegetation made. This was also done with and without the influence of the post-collapse deposits area. The aspect tool was also used upon the DEM and visualised for the direction of slope facing NW, NE, SE and SW to visualise the gullies that incise the island. Gullies were mapped on the western side where there was a sharp change from NW and SW or from NW to NE where the general trend of the slope was to the north at the central cusp or to the south (Figure 2.25).

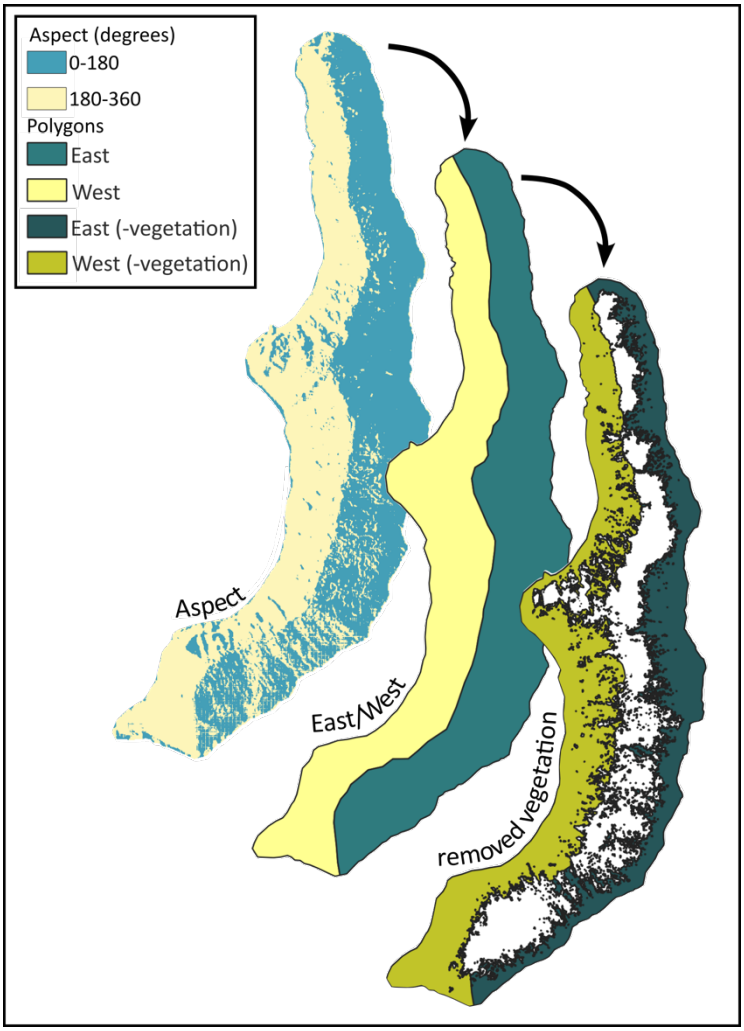

Figure 2.24: GIS process of separating the east and west of Ritter Island from the DEM 'aspect' and removing the vegetation cover to create polygons representing this area for slope analysis.

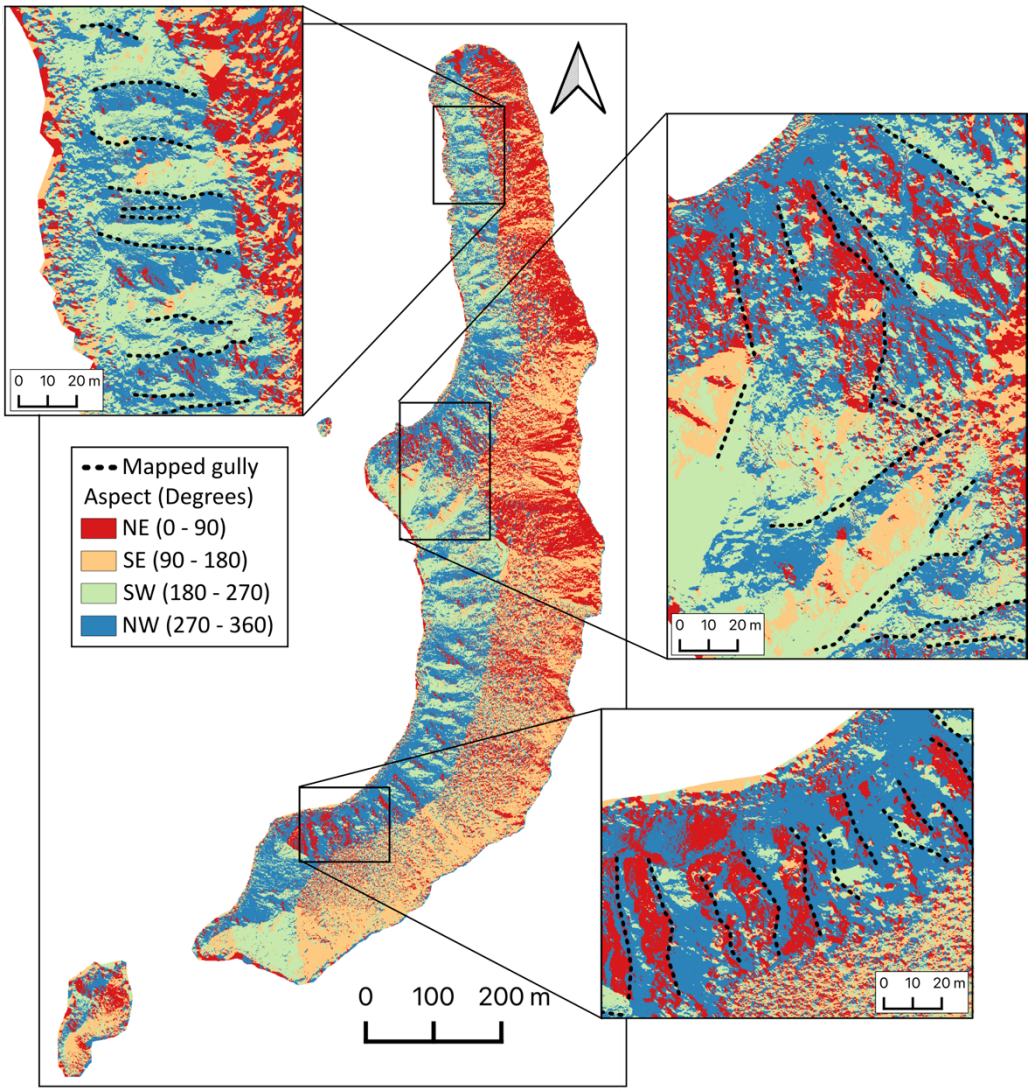

Figure 2.25: Ritter Island DEM represented by slope aspect used for mapping erosional gullies.

Island and collapse measurements

Various measurements can be taken from the new DEM and also from the DEM alongside the bathymetry and interpolated data. Bernard et al. (2021) suggests a comprehensive set of measurements to describe the shape of a volcanic collapse scar their methods are followed in this section applied to Ritter Island. Some additional measurements are also made of Ritter Island and the scar.

2.3.3.5 DEM measurements

A number of measurements can be obtained upon analysing the DEM raster in isolation. The maximum elevation is taken as the maximum pixel value directly from the elevation raster. The length of the island was measured from the northern extent to the southern extent and

along the curve of the island. The width of the island was also measured at its maximum by the central cusp. Raster volume analysis also provides information on the surface area and the volume of the subaerial island.

Recreating the pre- and post-collapse cone

In order to use this new DEM data to calculate a volume of collapse, the original pre-collapse cone first needed to be constructed from the available DEM and bathymetry data. In addition a scar surface beneath any deposits must also be constructed similar to the methods used in Day et al. (2015) and Karstens et al. (2019). Day et al. (2015) used the previously estimated slope angle of 45° to reconstruct the pre-collapse island with assumptions that the island was slightly elongate to the N-S and that the western slope was steeper. Karstens et al. (2019) used an average slope and island shape based on the -450 contour.

The following method generated a pre-collapse cone based on several assumptions. The first is that the island is perfectly conical. This is unlikely to true, however most observations of the island described the shape as conical so this provides a good estimation. In addition, the peak is assumed to be pointed, also based on sketches of the Island as opposed to having a crater. The second assumption is that the pre-collapse peak elevation was 750 m above sea level as used in methods by Day et al. (2015). Additionally, the slope of the subaerial cone is assumed to have a constant angle. The average angle calculated from the raster analysis of the eastern portion of the present-day cone was 38.4°.

Two end-members of the angle of slope were also tested here to determine the range of error in calculated volumes. A higher angle of 44° as suggested by Johnson (1987) was used and a lower angle of 29° was used from the lowest average slope from the profile analysis.

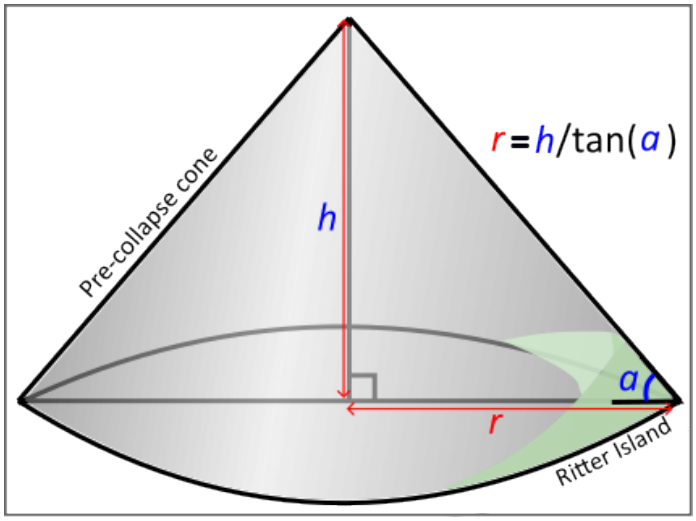

Figure 2.26: Trigonometic parameters used to calculate the radius of the pre-collapse island cone.

Assuming the subaerial island was originally conical, the radius of its base could be calculated using trigonometry, where *h* is the height of the pre-collapse cone, assumed as 750 m, and *a* is the average angle of slope (Figure 2.26). A point shapefile was made creating 10 m spaced points along the eastern edge of the present-day island. A buffer using the radius of the island was generated around each point. Where the buffer lines intersect with one another was assumed to be the most likely location for the central peak of the island. This location was verified by making another point shapefile along the peak of present-day Ritter Island. The DEM value was extracted from each of these points and a new field was created to calculate the distance to the peak from each point using trigonometry. A secondary buffer was generated around these points using these point values. The intersection of all these buffers was used to find the peak of the island. A Kernal Density Estimation 'heat map' was created from all of the line intersection points to the east of the island. The maximum clustering value was taken to be the central peak and a point shapefile was generated at this point to represent this (Figure 2.28).

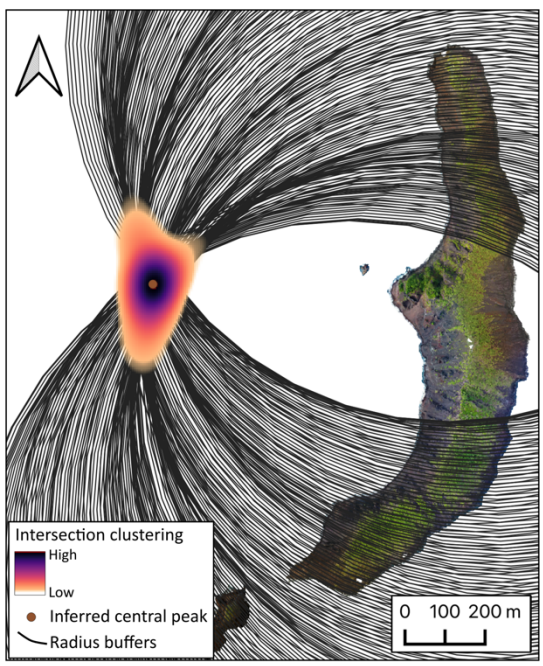

Figure 2.28: Process of using radius buffers to find the likely peak of the pre-collapse volcano.

The 'multiring buffer' tool was used to create 15 equally spaced lines to represent 50 m contours (750 m / 50 m =15) using the island radius divided by 15 to calculate the spacing of the contours (Figure 2.27A). Each of the line shapefiles was given an elevation attribute from 0 m to 750 m. The TIN (Triangulated Irregular Network) interpolation tool was used with these contours to interpolate the elevation attribute to create an elevation raster representing a cone from each of the angles at 10 m/px (Figure 2.27B and C).

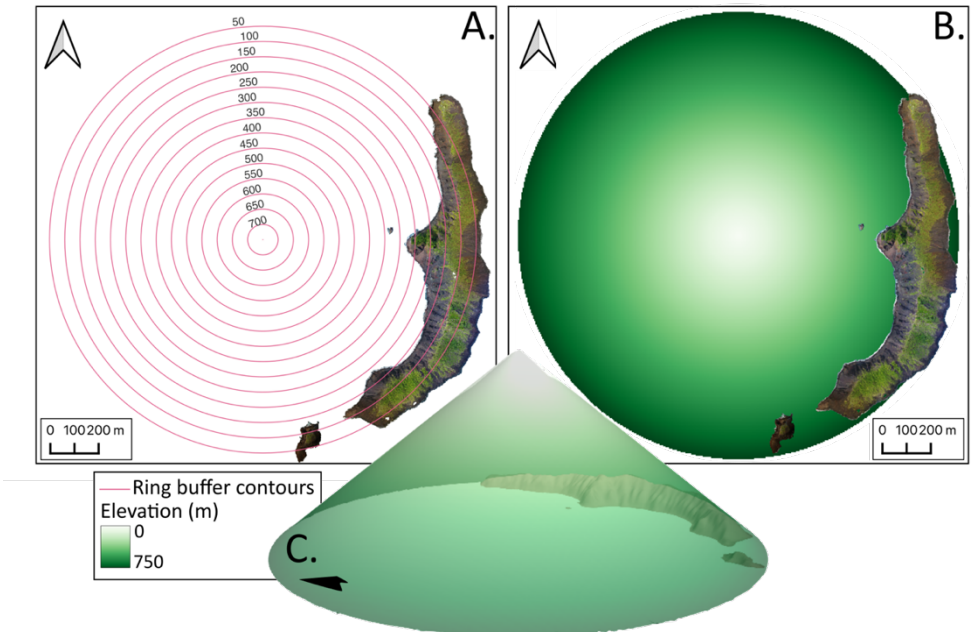

Figure 2.27: The process of building the inferred pre-collapse cone using A. ring buffer contours to interpolate the B. Conical raster surface. C. Reconstructed cone displayed in 3D alongside Ritter Island.

An additional method was used to create the 38.4° cone to include the current eastern slope of the island topography. The 38.4° slope was extended from the peak of the island as opposed to the base of the island. From the peak shapefile point layer, a new field was made to calculate the contour spacing from each elevation to the 750 m peak. Points were generated at these intervals assigned with their respective elevation value. These elevation points replaced the points from a symmetrical cone of the same angle and a surface was generated using TIN interpolation. This surface was then merged with the eastern DEM of the present-day island to include it in the surface calculations. This produced a result which did not significantly differ from the original method. It produced a slightly smaller volume. In addition, this method assumed that the current slope topography was the exact same at the time of collapse, however mapped shallow collapses may not have happened pre-collapse. Therefore, the first method extending slopes from the base was used and replicated for the other slope variations.

The bathymetry also needed to be reconstructed in order to perform volume calculations. To do this, the bathymetry raster data first needed to be converted into 50 m contour line shapefiles. The 25 m/px bathymetry was used as it had spatial coverage on all sides of the island. The portion of the bathymetry that represents the collapse scar was clipped out of the contours, leaving a gap to reconstruct. It is assumed from the remaining bathymetry that the collapsed portion was likely to have continued on this circular trend. Therefore, new curved ellipsoidal contours were made to fill in this gap joining the two edges of the original bathymetry with the same elevation value assigned. This was continued to where the base of the original edifice extends to.

This base is difficult to infer as the edifice had grown on a saddle between the larger islands of Sakar to the north and Umboi to the south (Figure 2.29). To the east, the edifice seems to extend deeper as the bathymetry deepens. However, to the west the edifice has grown on this shallower saddle (Figure 2.29). Figure 2.29 shows the interpretation for the influence of the Ritter edifice on the contours of the bathymetry, aided by the interpretation of the geological map from Day et al. (2015). To the west, the edifice is inferred to extend to a depth of between -850 and -900 m. Therefore, the contours for reconstruction were inferred to a depth of -850 m and also to -900 m to provide different end-members for the volume estimates. -850 m was chosen as this is where the conical shape of the bathymetry ends and the visible scarp extends to (Figure 2.30). -900 m was chosen as this may have been where

the sidewall may have extended beneath the deposits to the base of Sakar slopes. The reconstructed bathymetry and subaerial island contours were then merged and interpolated into the reconstructed DEMs also at 10m/px (Figure 2.30). -900 m estimates will give a maximum volume estimate to values and the -850 contributes to a minimum though this also depends on the inferred scarp surface.

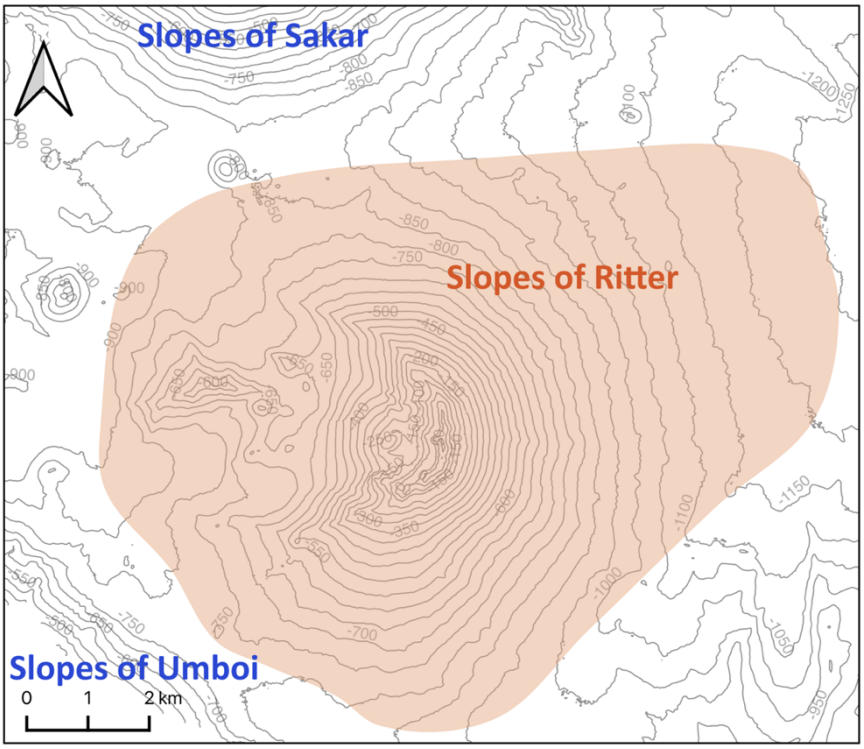

Figure 2.29: Contour map of Ritter Island and the surrounding bathymetry (including data gap and new Island elevations) highlighting where the Ritter Volcano slopes extend to based on this bathymetry and a geological map from Day et al. (2015).

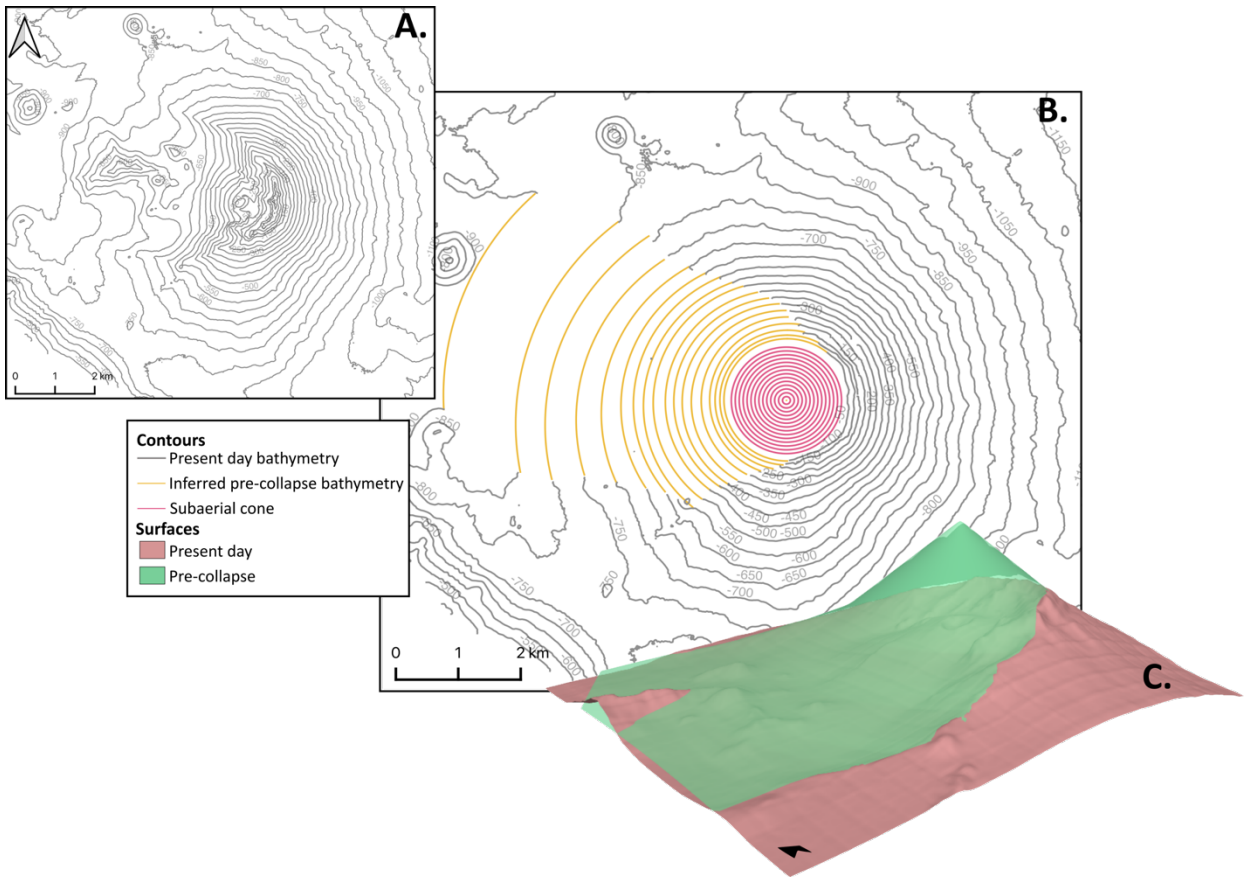

Figure 2.30: The process for reconstructing pre-collapse surfaces A. The present-day bathymetry represented as contour lines. B. The ellipsoidal inferred contour lines for the pre-collapse bathymetry as well as the inferred subaerial cone. C. Displays the surface of the present-day topography overlain by the inferred pre-collapse cone in 3D.

A new surface to represent the slide plane was also created to use for the calculations of the volume of excavated material, by removing any post-collapse volcanism and collapse deposits. To do this the bathymetry contours were cut at the base of the collapse scarp and new contours were assumed in the gap. These were assumed to continue the concave shape from the upper slope, interpreted to be part of the original scarp (Figure 2.31B). TIN interpolation was used to create this surface at 10 m/px (Figure 2.31C). A way to improve this method is to calculate the depth of the scarp using seismic profiles, however this is complicated due to the different materials making up the seafloor.

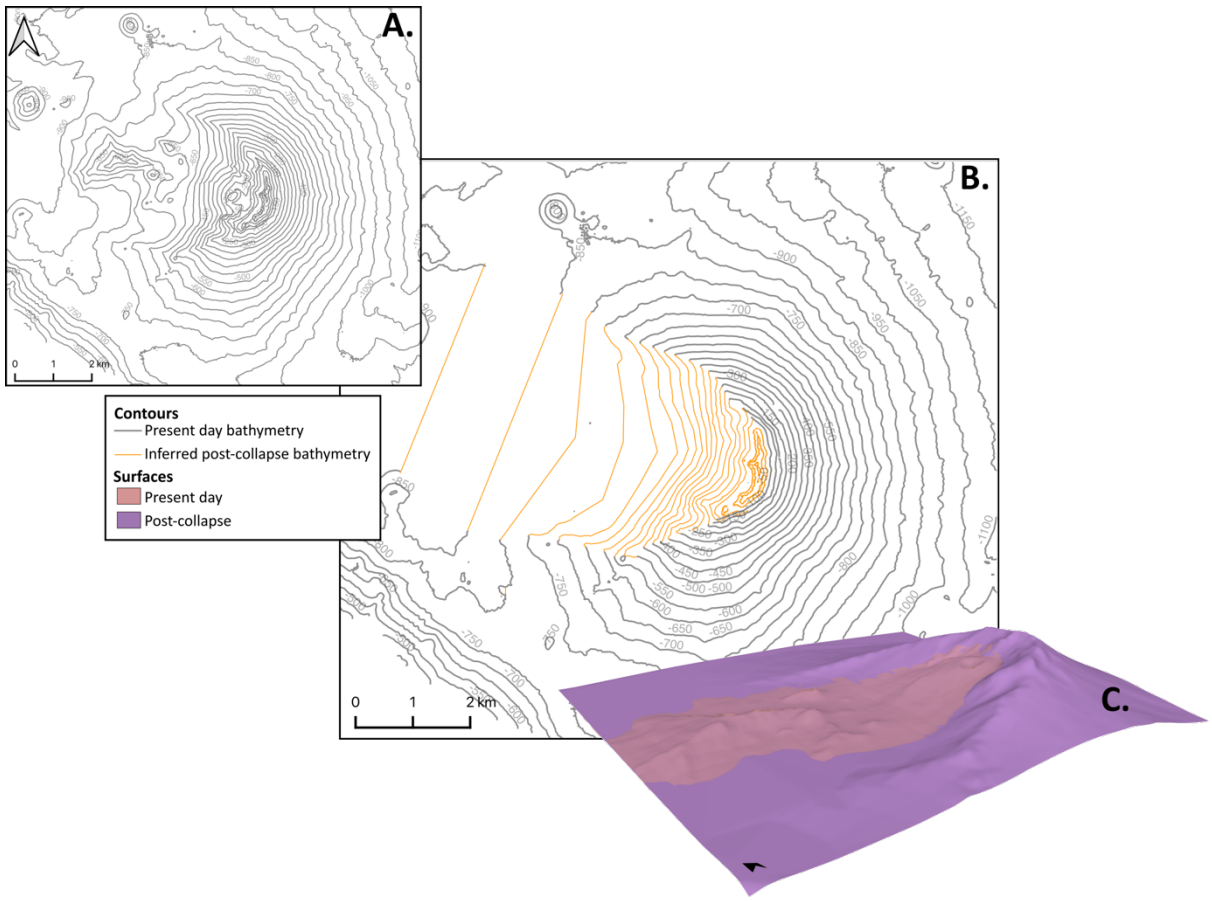

Figure 2.31: Interpretation of the post-collapse bathymetry. A. The present-day bathymetry represented as contour lines. B. Inferred contour lines for the post-collapse bathymetry. C. Displays the surface of the present-day topography overlain by the inferred post-collapse surface in 3D.

Volcanic Scar metrics

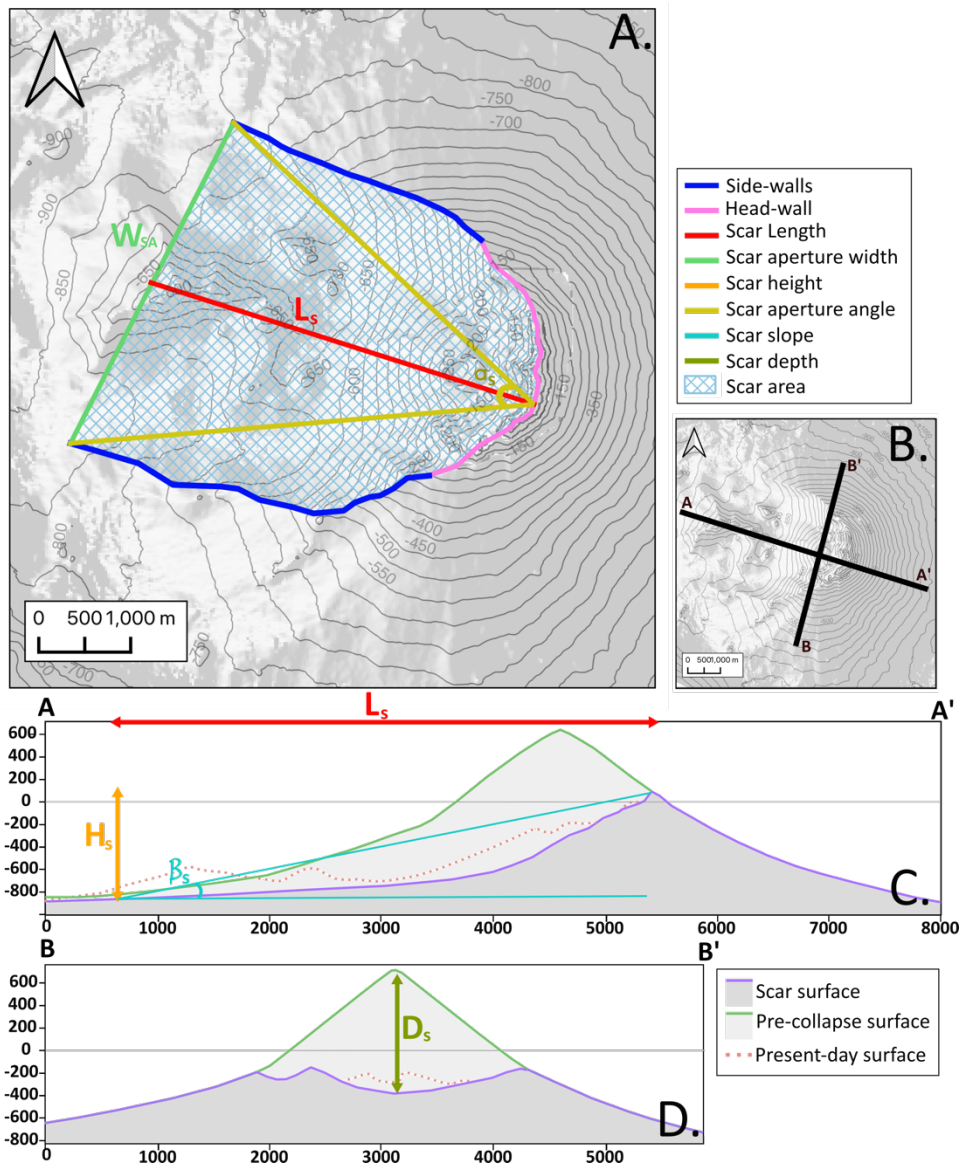

Figure 2.32: Identifying measured parameters defined by Bernard et al. (2021). A. Map view of Ritter Island highlighting measured parameters. B. Map showing cross sections A and B. C. Cross-section through Ritter lengthways showing the inferred scar surface and pre-collapse surface as well as present-day bathymetry highlighting measured parameters. D. Cross-section through Ritter widthways highlighting measured parameters.

Bernard et al. (2021) described a series of morphological metrics by which a volcanic collapse scar can be measured and therefore compared to other scars. These measurements can be measured from the new DEM of Ritter Island alongside the bathymetry and inferred surfaces. The list of parameters measured here were defined by Bernard et al. (2021) (Table 2.1). These measurements can primarily be calculated using GIS. Initially the 'head-wall', 'side-walls' and 'aperture' were identified from the dataset with line shapefiles drawn for each of these (Figure 2.32A). These parts of the wall differ as the head-wall is usually facing the aperture whereas the side-walls are more parallel to the direction of the landslide emplacement. The observed

sidewalls were identified but these may extend beneath overflowing deposits to the east. The aperture is the section between the side-walls lowest points (Bernard et al., 2021).

Table 2.1: Definitions of scar measurements from Bernard et al., 2021.

Acronym	Parameter	Description	Measured
L_s	Scar length	Measures the distance from the head-wall to the middle of the observed aperture.	In QGIS, the centre of the aperture line was found and a new line drawn to the central point of the headwall which was then measured in meters (Figure 2.31).
W_s	Scar width	Measures the maximum distance between the side walls.	In this case, this distance is the same as the scar aperture width (W_{sa}) due to the shape of the scar (Figure 2.32A). The aperture line was measured in meters.
H_s	Scar height	Measures the elevation difference between the top of the headwall and the aperture.	The aperture elevation is taken at the midpoint of the aperture of the interpreted surface for the post-collapse pre-infill surface. The top of the headwall is taken as the peak of the DEM for Ritter Island. The difference between these gives the scar height (Figure 2.32C).
α_s	Scar aperture angle	The angle of the lines drawn from the headwall to the base of the side-walls	Angle measured using QGIS
β_σ	Scar slope	Measures the slope from the top of the head-wall and the aperture (Figure 2.30C)	This can be calculated using trigonometry with the equation: $\beta_s = \tan^{-1}(Hs / L_s)$.
γ_σ	Scar azimuth	Measures the azimuth of the line of the scar length	Calculated by measuring its bearing in QGIS.
A_s	Scar area	Measures the area of the scar in plan view.	This was calculated by creating a polygon shapefile bounded by the head-wall, side-walls and aperture and calculating its area (Figure 2.32A).

D_s	Scar depth	Measures the maximum depth of the scar between the pre- and post-collapse topography (Figure 2.32D).	This is measured using the raster calculator to subtract the inferred post-collapse pre-infill surface from the inferred pre-collapse island surface. The maximum value on the resultant raster file is the scar depth in metres.
V_s	Scar volume	The volume difference between the pre- and post-landslide topographies	The volume of material excavated from the collapse, not including any entrained sediment from the resultant flow, was estimated using the surfaces generated using methods in the previous section. A polygon shapefile was drawn covering the area of collapse which was bounded by the current peak of Ritter Island, the top of the collapse scarps and the -850 m contour. Each raster surface was clipped to this extent (Figure 2.33). The QGIS algorithm 'Raster surface volume' calculates the volume beneath a raster grid's surface as well as outputting the total area and the number of pixels analysed. This was used to analyse the Ritter DEM. The raster calculator was used for each slope angle reconstruction to subtract the present-day bathymetry from the reconstructed pre-collapse cone and also to subtract the interpreted post-collapse scar from the pre-collapse cone. This produced a raster layer from which area and volume calculations could be made from the pixels > 0. The areas < 0 are where the seafloor has increased due to deposits, so it was discounted. The interpretation of the original edifice and the scar plane based on the present-day topography involves a large possibility for error associated with any measurements taken from these surfaces. The Toreva blocks seen at the base of the scar were included as material excavated.
T_s	Scar thickness	Measures the average thickness of the excavated portion of the edifice	This is calculated by: $T_s = V_s/A_s$.
AR_s	Scar aspect ratio	Describes the ratio between the average thickness and the radius of a circle of equal area	Calculated by: $AR_s = T_s/ \sqrt{(A_s/ \pi)}$.

EF_s	Elongation Factor	Describes ratio between scar length and width	Calculated by $EF_s=L_s/W_s$
CFs_s	Closure factor	Describes the ratio between the scar aperture and scar width	Calculated by: $CF_s= W_{sa}/W_s$.

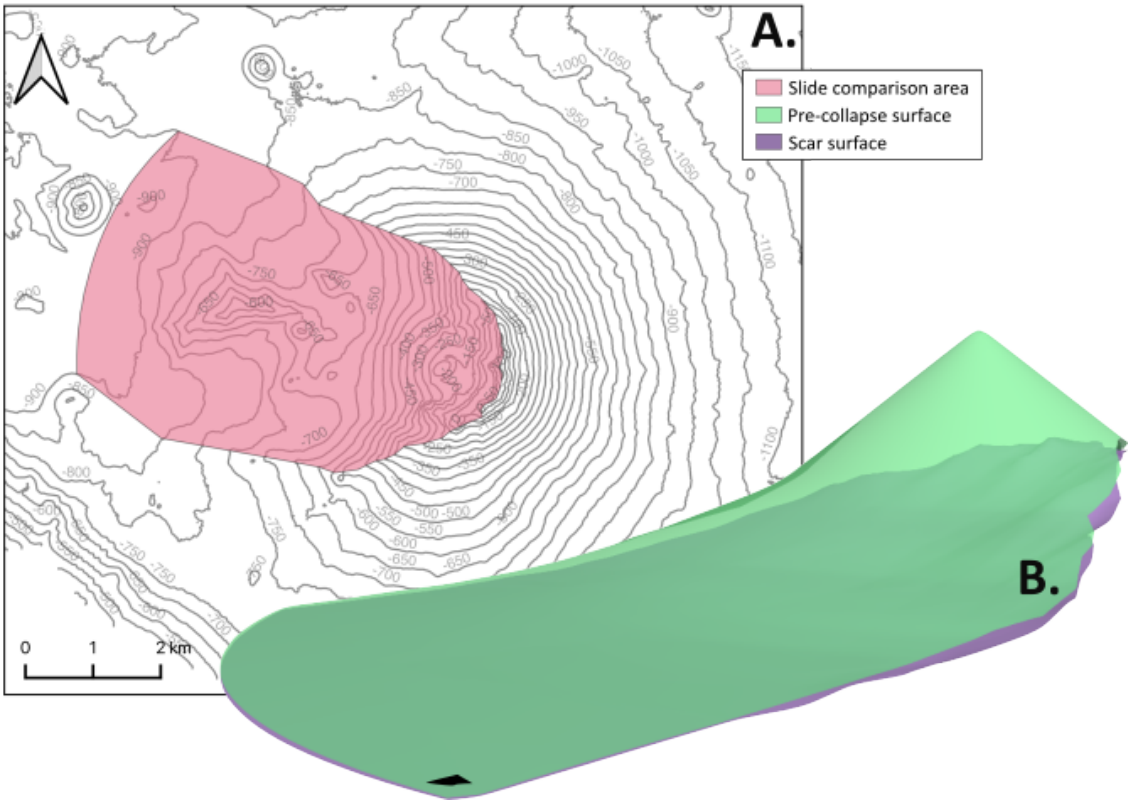

Figure 2.33: A. The comparison layer for each inferred surface. B. 3D surfaces of the pre-collapse surface and scar surface used to calculate thicknesses and volumes.

As suggested by Bernard et al. (2021), any measurements using the reconstructed pre- and post-collapse topography surfaces generated using these GIS method may have large errors associated with them but can be useful to compare to other estimates and other volcanic collapse scars.

Error considerations

As well as the variation in volume generated by differing dips explored using the two end-members for the angle of the subaerial cone, there are other decisions where error may be induced into the scar measurements shown above. Two of the main sources of error are the length of the sidewalls which affects the length of the scar, the aperture width, the angle of the scar, and the scar height. The sidewalls are estimated to end around the -850 contour, but the scar could extend further towards the -900 contour and be buried beneath the deposits

of the collapse or could be shorter than estimated. The maximum and minimum length of sidewall were used to calculate maximum and minimum values which were average and used to express the variance of the result.

In addition, the surface estimates as the base of the scar, originally drawn using contours which continued the curved shape of the observed upper scarp and then flattened at the base of the scarp affect the scar depth calculations. A more exaggerated scar was therefore drawn to represent the deepest extent and a less curved contoured scar was drawn to represent the shallowest extent to calculate the variance of this measurement.

2.3.4 Digital mapping

Move is a GIS-based software used for digital geological and structural modelling, interpreting data and creating geological cross-sections. A combination of Move, Agisoft and QGIS software was used to map geology and geomorphology on Ritter Island and Fogo with a particular focus on flank stability and collapse. This process includes identifying mappable units and features on the model, tracing their extents, creating line and polygons shape files and represent them two dimensionally as a map view or in three dimensions as surfaces. From this, strike and dip data can be estimated and cross-sections can be inferred.

As this field site was not visited in person, all rock types had to be inferred based on their appearance from the model and original imagery. The only ground-truthed rocks here are the locations where samples have been taken by previous excursions. These can be identified on the model but are grouped at the base of the cliff. A mapping log was kept during this process to collect further detail on the island with sketches and observations (Figure 2.34)

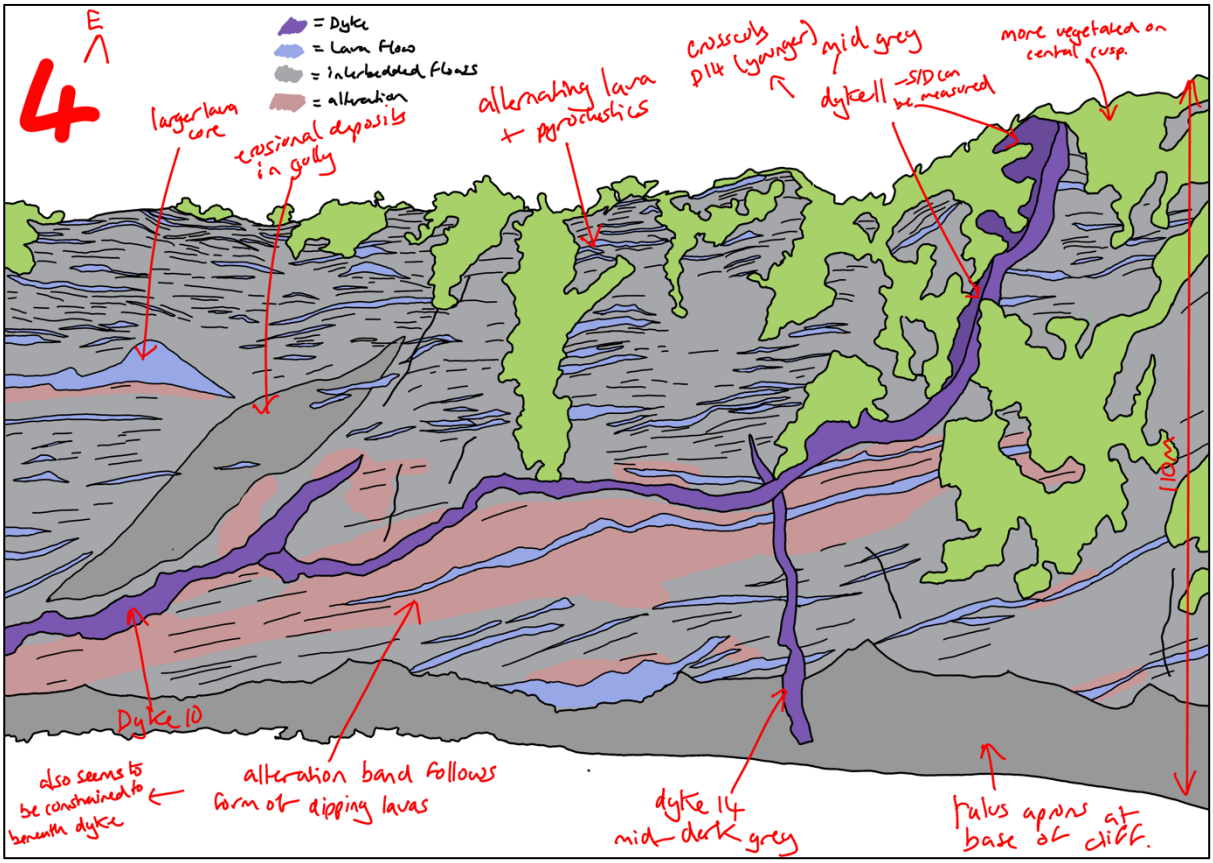

Figure 2.34:Example of sketches and observations made for Ritter Island highlighting the main mapped features

The major geological units mapped were the dipping layered host rock units, the cross-cutting intrusions and the reddish altered areas. These units were chosen based on information from literature. Day et al. (2015) described the islands units as volcaniclastic units including spatter-fed lavas, massive flow cores and fine scoria. The dipping layers units mapped are likely to be the flow cores but the spatter-fed lavas and scoria are harder to identify using this model, so it is assumed they make up areas between the mapped 'layered host rock' units. The mappable layered units may also be sills following the dip of the lava flows but at this stage it is difficult to discern and hence they may have been grouped together. Day et al. (2015) also described the cross-cutting steeply dipping dykes trending roughly north-south, the largest of which are easily identified and mapped. Day et al. (2015) also described the presence of altered reddish rocks which can also be identified using this model.

Intrusions that were distinguishable on the high-resolution texture of the model were mapped in Agisoft in 3D. These were mainly cross-cutting dykes, however some of the 'horizontal' units mapped as dipping lava flows may have been misidentified sill features but at this resolution it is difficult to confirm this. The software allowed ease of the movement of the model and combined overlays with the original images (Figure 2.35).

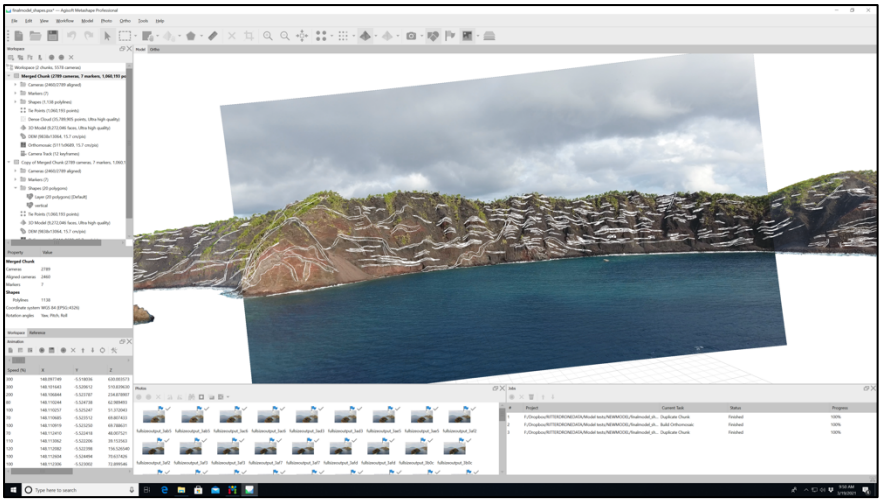

Figure 2.35: Screenshot from Agisoft software showing method of mapping rock horizons using the model alongside the original drone images.

Each of the interpreted dykes were then measured in terms of their thickness, measured at different points along their extent, their length, their elevation range within the cliff and distance north along the cliff. The dykes were also described in terms of their colour and sinuosity. Using the 'filter by point' function on Agisoft allowed the set of drone photos to be filtered by a chosen point on the model to allow further detail of each dyke to be observed. Descriptions and measurements were collected for each dyke inferred (appendix 3).

The cross-cutting dykes varied in colour on the model, possibly representing differing ages, composition or grain size. These were recorded and mapped as different units, assuming that dykes of a similar colour were emplaced at the same time. The categories of the cross-cutting dykes were mapped as were as a range of light grey to dark grey as well as brown-, green- and yellow-coloured units (Figure 2.36). This method of classification is qualitative and may not distinguish between more detailed changes in the rock types. It is also relatively subjective and may be affected by the on the lighting of the image or shadows. The relative ages of the groups of dykes could, in areas, be assumed where the intrusions cross-cut one another.

Figure 2.36: The colour classification used to map cross-cutting intrusions at Ritter Island. The colours represent the average colour range for each classification with examples of each from drone imagery.

The dipping layered units are inferred to be alternating dipping lavas and pyroclastics deposited by repeated eruptions (Watt et al., 2019, Day et al., 2015). Throughout most of the island section, these alternating layers were not laterally continuous and they were relatively thin and difficult to map en masse. They were mapped as 'form lines' in order to gain the bigger picture structure of the host rock. This was also done in Agisoft as a separate shapefile to the dykes (Figure 2.37). The paler, more distinct layers in these successions are inferred to be lavas and the darker ones as pyroclastic units. In appropriate sections, a log of the alternating lavas and pyroclastic flow deposits was measured in terms of their relative thicknesses.

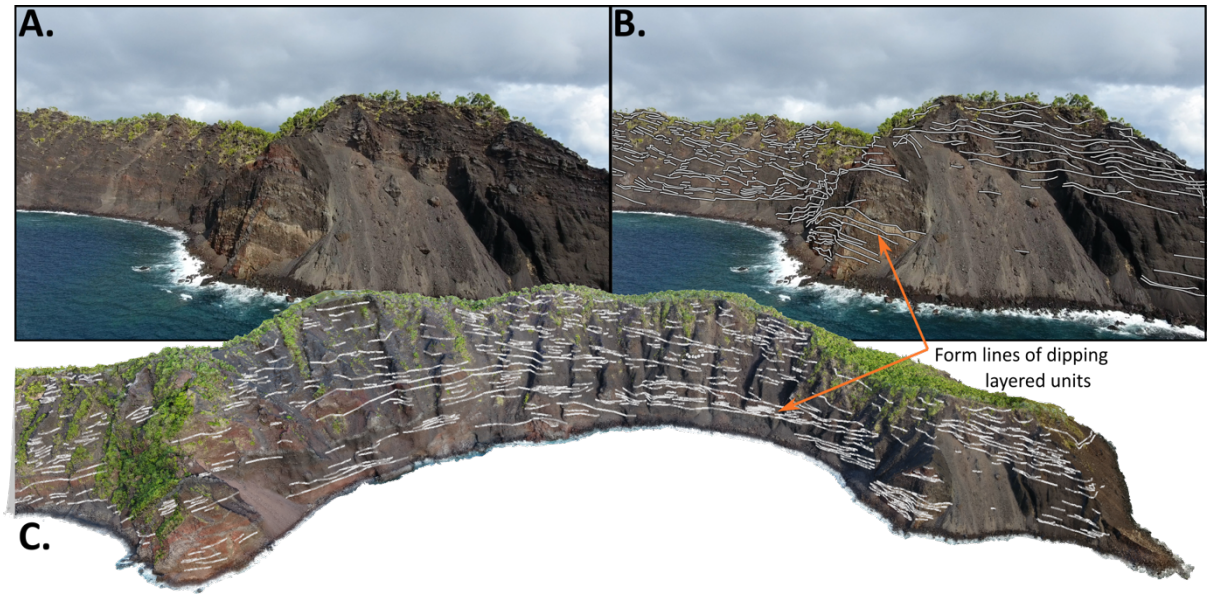

Figure 2.37: Form line mapping for dipping layered units. A. Original drone image of Ritter Island. B. overlain form lines onto image in Agisoft. C. 3D model of ritter with form lines as 3D line shapes on Agisoft.

The altered areas of host rocks were also mapped using the process in section 2.3.3.3. They were mapped as an overlapping layer onto the form lines.

The mapped features were then exported from Agisoft as line shapefiles in the local coordinate system and imported into the Move software. The DEM and orthomosaic made can also be imported into Move software as raster data and the orthomosaic is overlain on the DEM. Due to the large file size of the orthomosaic and DEM, the island was split into different chunks to allow smooth use of the software. An additional decimated DEM layer was also generated and imported to allow for coarser observations.

Move allows the model view to be switched easily between map, 3D and cross-sectional views. Polygons can be drawn between the mapped lines of the dykes to create the units in map view, and can then be projected onto the DEM to be viewed in 3D. Some issues arose

from this process as where cliffs were steep or overhanging the polygons were too thin to be projected onto the DEM therefore some of the polygons had to be extended to be able to be observed in map view

Where the features create a flat plane on the surface of the model, a strike and dip measurement could be accurately measured. Strike and dips could also be estimated where the linear feature interacted with the topography. These measurements were taken by manually rotating a disk representing the plane of each unit on the software until it lined up with the trend of the unit (Figure 2.38). Some error is introduced into the map by using this method and some units were unable to be measured as dips were unknown based on the extent of the outcrop. Where possible, multiple strike and dip measurements were taken from dykes as some were sinuous and changed direction so this would allow an overall trend to be observed.

Move has various functions that allows analysis of measurement data in various forms. For example, the direction of the dyke intrusions can be plotted using rose plots and stereonets. In addition, analysis of these trends against change with distance east, north or vertically can be viewed. These volcanic islands were originally assumed to be conical with one or more central vents creating radial trends from the flows and intrusions. Analysing these trends allowed investigation on the radial trends, or otherwise at Ritter Island.

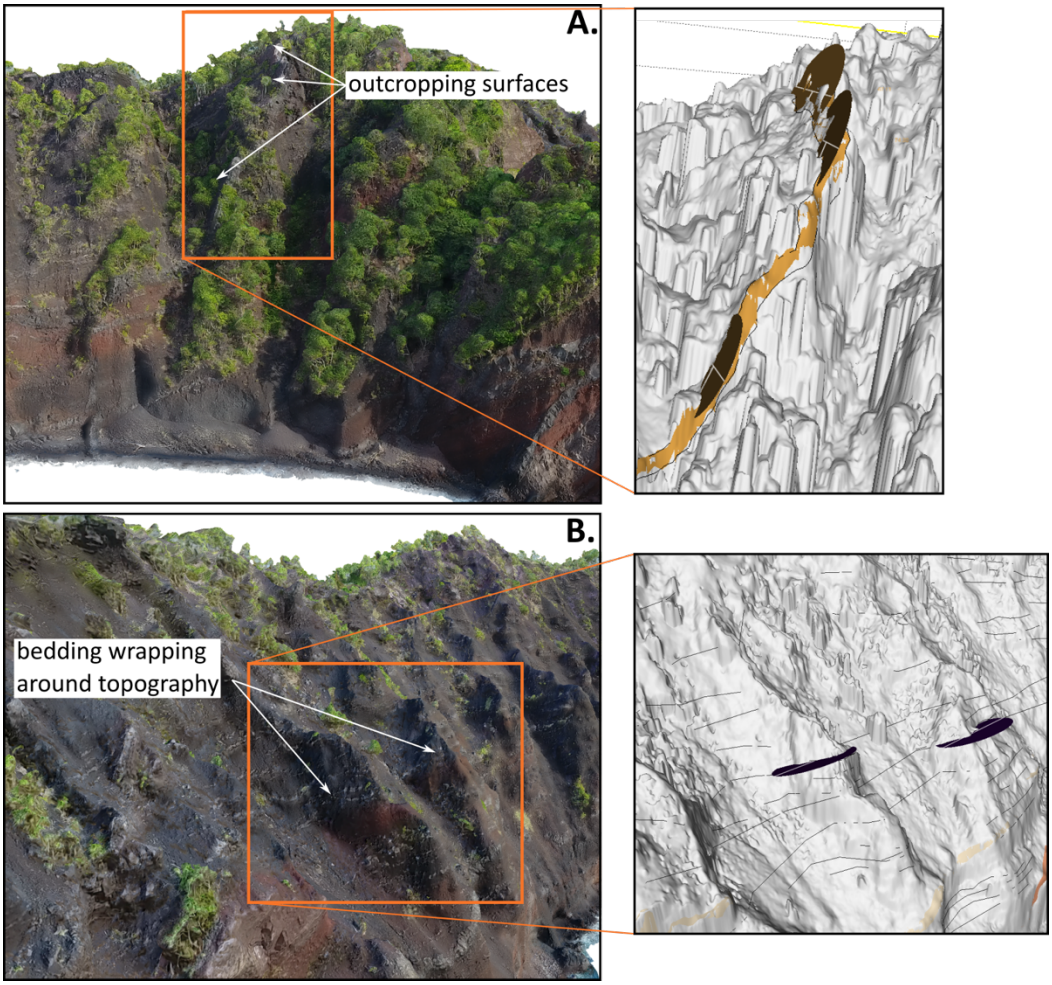

Figure 2.38: Measuring strike and dip. A. where a feature outcrops as a plane for example a dyke of Ritter Island, this surface can directly be measured on Move. B. Where a planer feature interacts with topography, for example these dipping beds at Ritter Island wrapping around gullies so a 'disk' can be fitted to measure strike and dip in Move.

When the units and measurements have been mapped, cross-sections can be constructed through the model projecting these mapped features onto section profile. East to west radially trending sections were made through the island and cross-sections were inferred from the outcrops and estimated dips to represent the dipping host rocks, cross-cutting dykes and bands of alteration. These were made radially as the assumption of the original edifice is that it was conical and therefore this would produce sections towards the centre of the island.

Dips are collected within an area of the cross-section trace (Figure 2.39a). The model profile is generated (Figure 2.39b) and the apparent dips and where the trace intersects with the polygons are projected onto the section (Figure 2.39c). From these projections the rest of the cross-section can be interpreted.

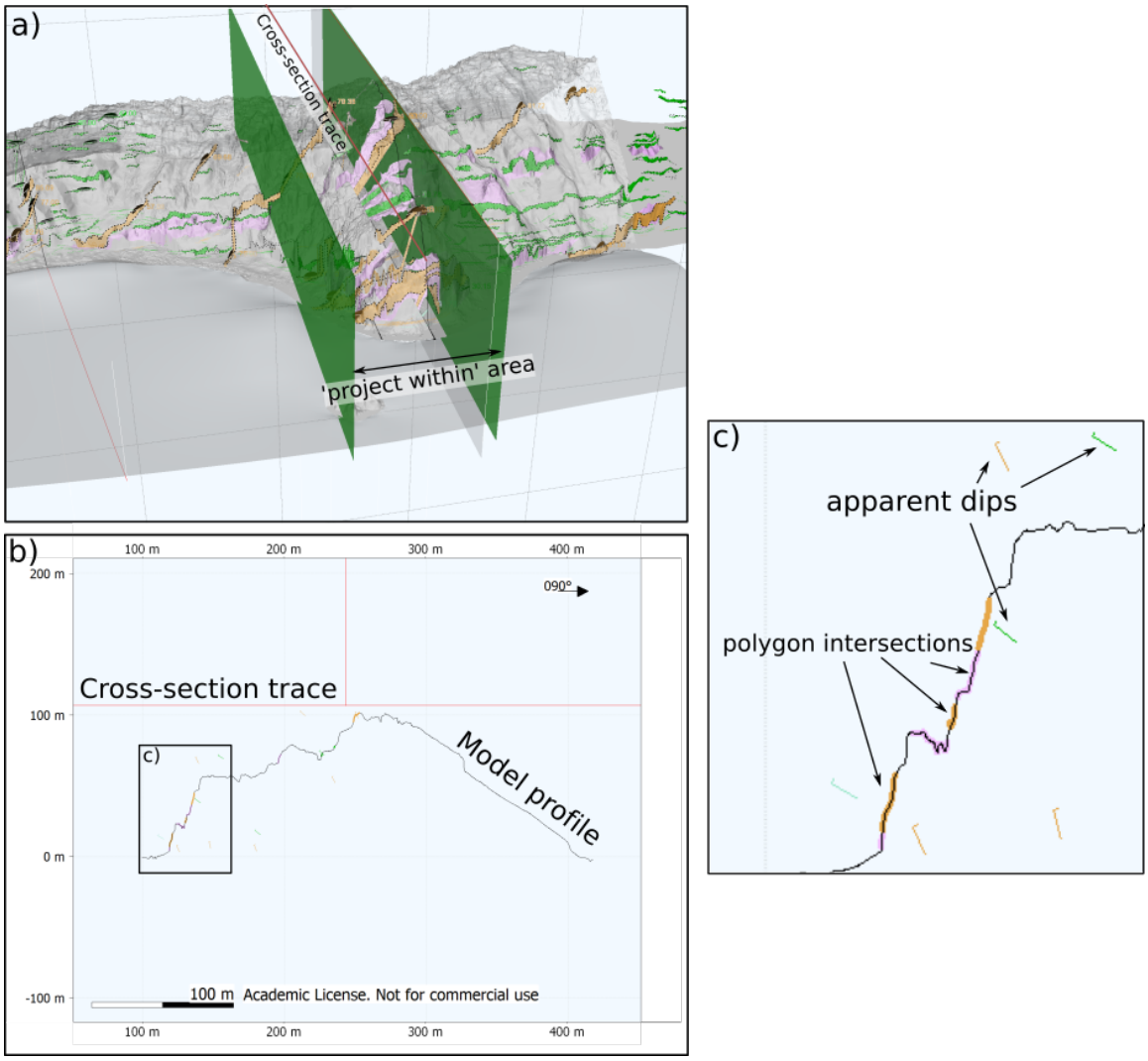

Figure 2.39: Cross-section construction process on Move software a) a 3D view of the model highlighting the area where data points are collected within b) the cross-section trace showing the model profile and projections highlighted in c) showing a close-up section of the model profile with projected apparent dips and polygon intersections.

This was all mapped in 3D and in 2D as a map view and then later converted into an east-facing view of the side of the island to best display this inferred map.

2.4 Results

2.4.1 Model results

Using the process described in section 2.3.2, a high-resolution structure from motion model of the island was produced. This model can be viewed at (https://sketchfab.com/3d-models/ritter-island-3-701e10c7a2a144eaa9fd6214e7288bfa). The main model outputs are:

- an orthomosaic aerial view of the island with a resolution of 5.53 cm/px (Figure 2.40B),
- an orthomosaic side view of the island with a resolution of 7.43 cm/px (Figure 2.40D)
- a DEM with a resolution of 7.33 cm/px (Figure 2.40A)
- a base map generated from the DEM data (Figure 2.40C).

Much information can be gathered about the island and collapse scar from these outputs. The orthomosaic provides a very high-resolution visual aerial representation of the island, allowing rock horizons to be identified and used in geological mapping (Figure 2.40B). Due to the steepness of the cliff face, some of the trends in the geology are less easily traced as an aerial view. Therefore, a lateral orthomosaic was also generated to observe the west of the island which allows further detail of the sequence of lavas and crosscutting dykes to be mapped (Figure 2.40D). The DEM was used within GIS analysis for a variety of measurements on its own and alongside the bathymetry data. The base map is used as a base for the geological map.

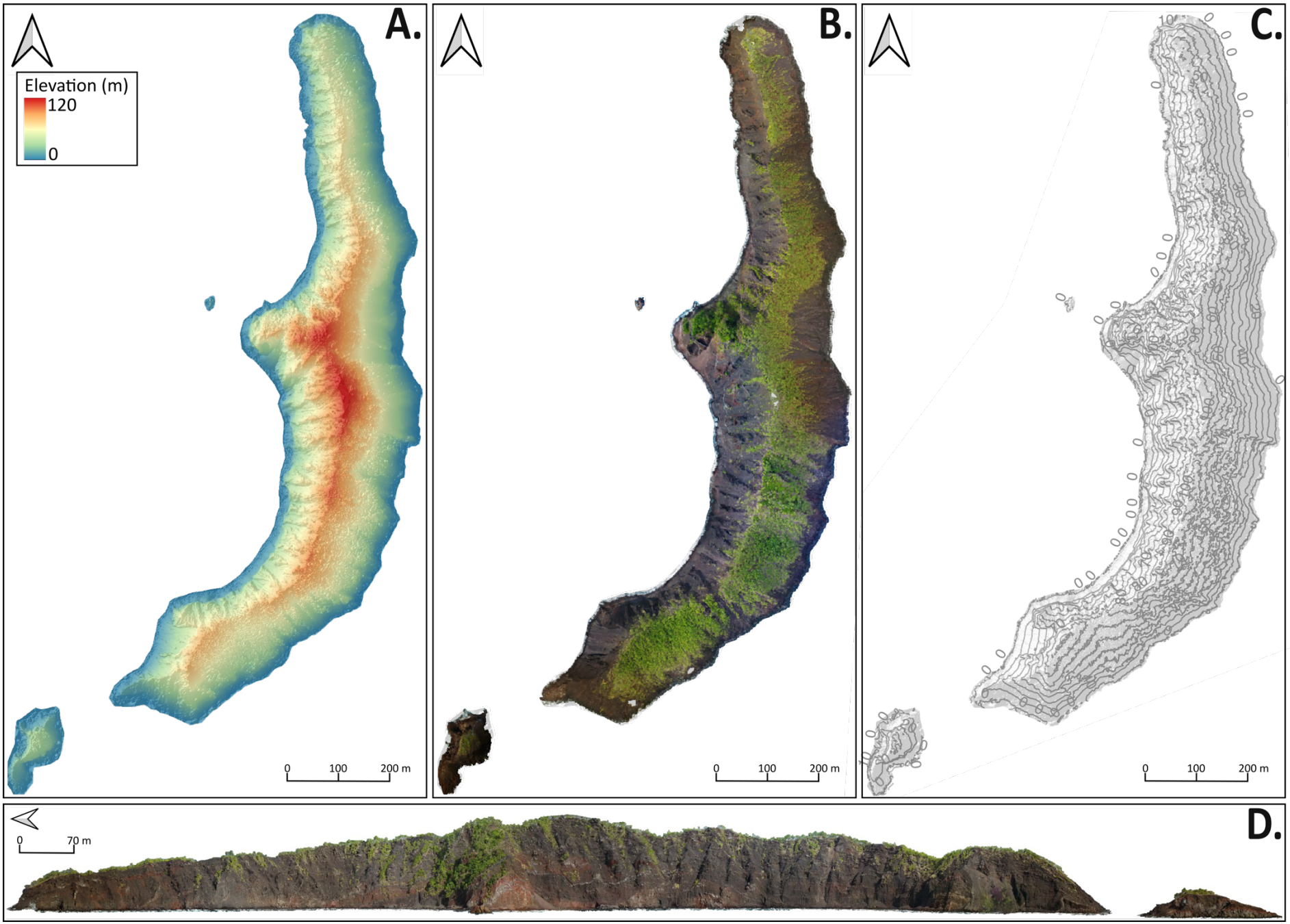

Figure 2.40: SfM modelling results for Ritter Island. A. DEM B. Orthomosaic, plan view C. Base map D. Orthomosaic, side view.

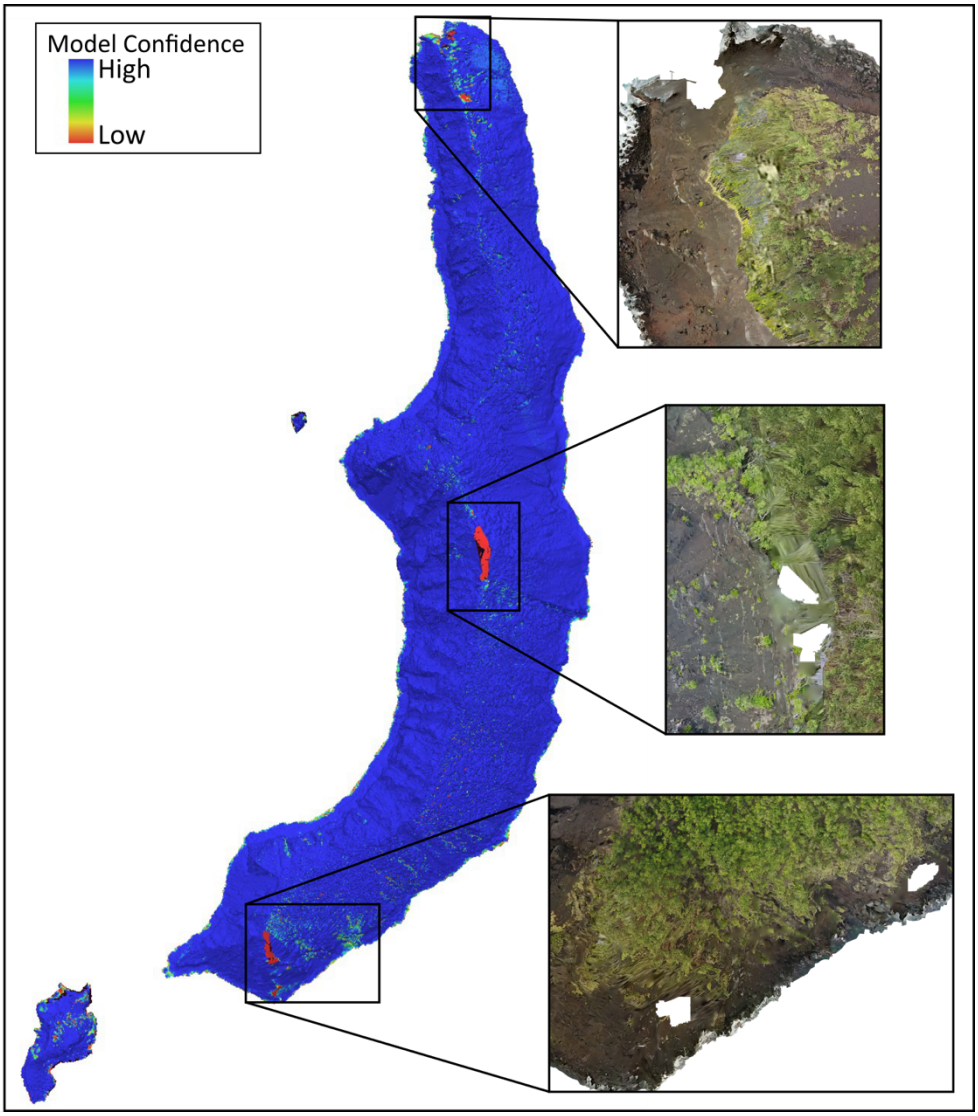

Figure 2.41: 3D model confidence of Ritter Island with areas of low confidence highlighted and effects of orthomosaic image shown.

The model can be viewed in terms of relative 'confidence' in Agisoft software, based on number of tie points from the model process (Figure 2.41). As shown in Figure 2.41, most of the island appears as 'high confidence', reflecting the good image coverage and therefore tie point density in these areas. Using this software tool, it is difficult to compare between these areas of apparent high density. This tool is most useful to identify the areas of lowest confidence derived from low image coverage and low tie point density. Areas of lower confidence and therefore possible inaccuracy can be identified. This low level of relative confidence is often due to the lack of image coverage over an area. This means that the resultant point cloud created from image alignment is sparser in these locations and thus the surface generated involved more error. These areas of low confidence affect how the DEM and orthomosaic results look. It is particularly apparent in the orthomosaics where these

areas are represented as gaps or the image appears more 'blurred' as the Agisoft software has estimated the arial view from other images. Figure 2.41 highlights these low confidence areas. These include low confidence on the northern tip, the central peak and the southern edge of the island as a result of little or no image coverage.

2.4.2 GIS analysis results

2.4.2.1 Orthomosaic analysis

The aerial orthomosaic shows that the eastern side of the island, which is assumed to be representative of the original outer slope of the pre-collapse volcano, is more vegetated compared to the western side (Figure 2.42). The vegetated area of the whole island and comparing the two sides was calculated by methods described in section 2.3.3. The vegetation cover area is 0.11 km^2 representing 33.93% of the whole island, including the islets. The vegetation cover is 49.88% for the eastern side and 17.18 % for the western side, not including the islets.

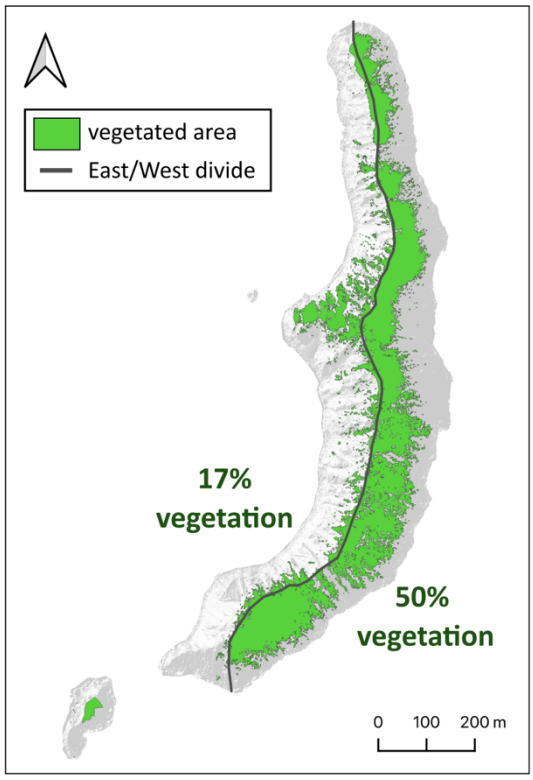

Figure 2.42: Vegetation cover at Ritter Island, comparing the percentage coverage for east and west slopes.

The orthomosaic shows the more exposed western side of the main island which represents a cross-section of the original edifice showing dipping lava bodies, cross-cutting dykes and areas of red alteration. This section of the island is mapped in detail in section 2.4.3.

2.4.2.2 DEM analysis

'No data' gap

The 'no data' gap in the area between the edge of the new Ritter Island DEM and the 25m bathymetry was inferred and infilled using the method in section 2.3.3.4. This gap is from mainly -150 m to sea level though reaching slightly deeper to the north east of the island at -300 m. There is some error associated with this area inferred due to the assumptions and manual aspect of this method. Figure 2.43 shows this filled in data gap in 3D and along a cross-section. In cross-section and 3D, the angle of the filled data gap seems to continue from the bathymetry data and therefore the probability for error is low.

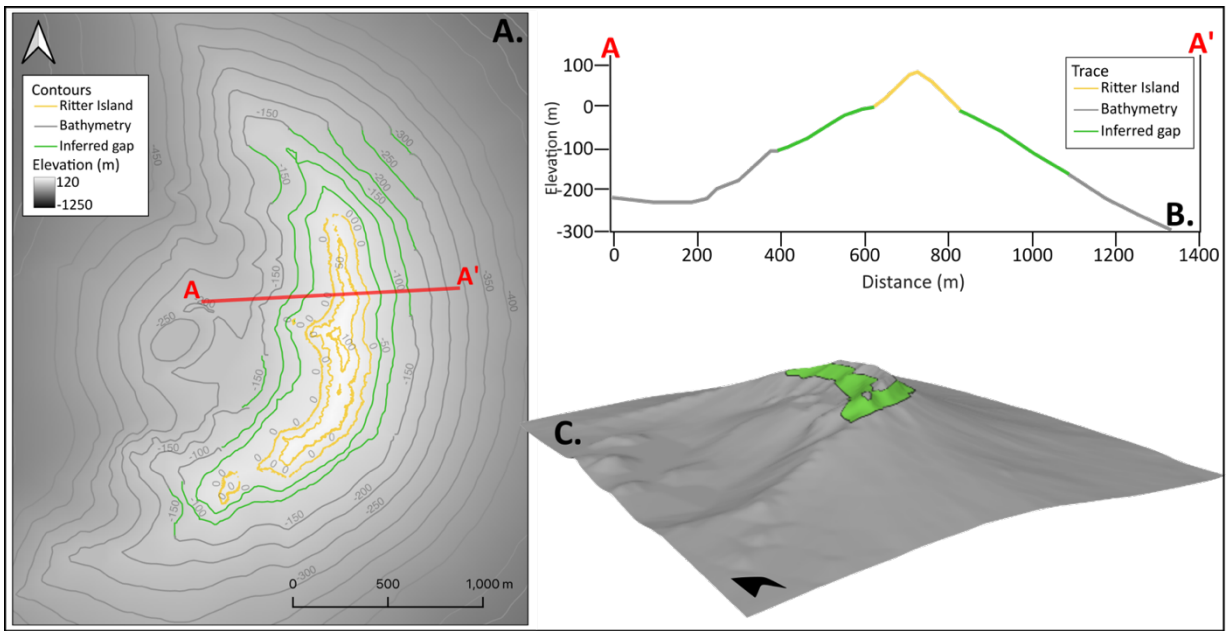

Figure 2.43: Inferred data gap between Ritter Island and the bathymetry data seen in A. map view showing the trace for the B. cross-section through the area and C. highlighting the inferred area in 3D – the model of this can be seen at (https://sketchfab.com/3d-models/ritter-island-inferred-data-gap-9d36bf4cb6c84e17bad51a8368644b7d)

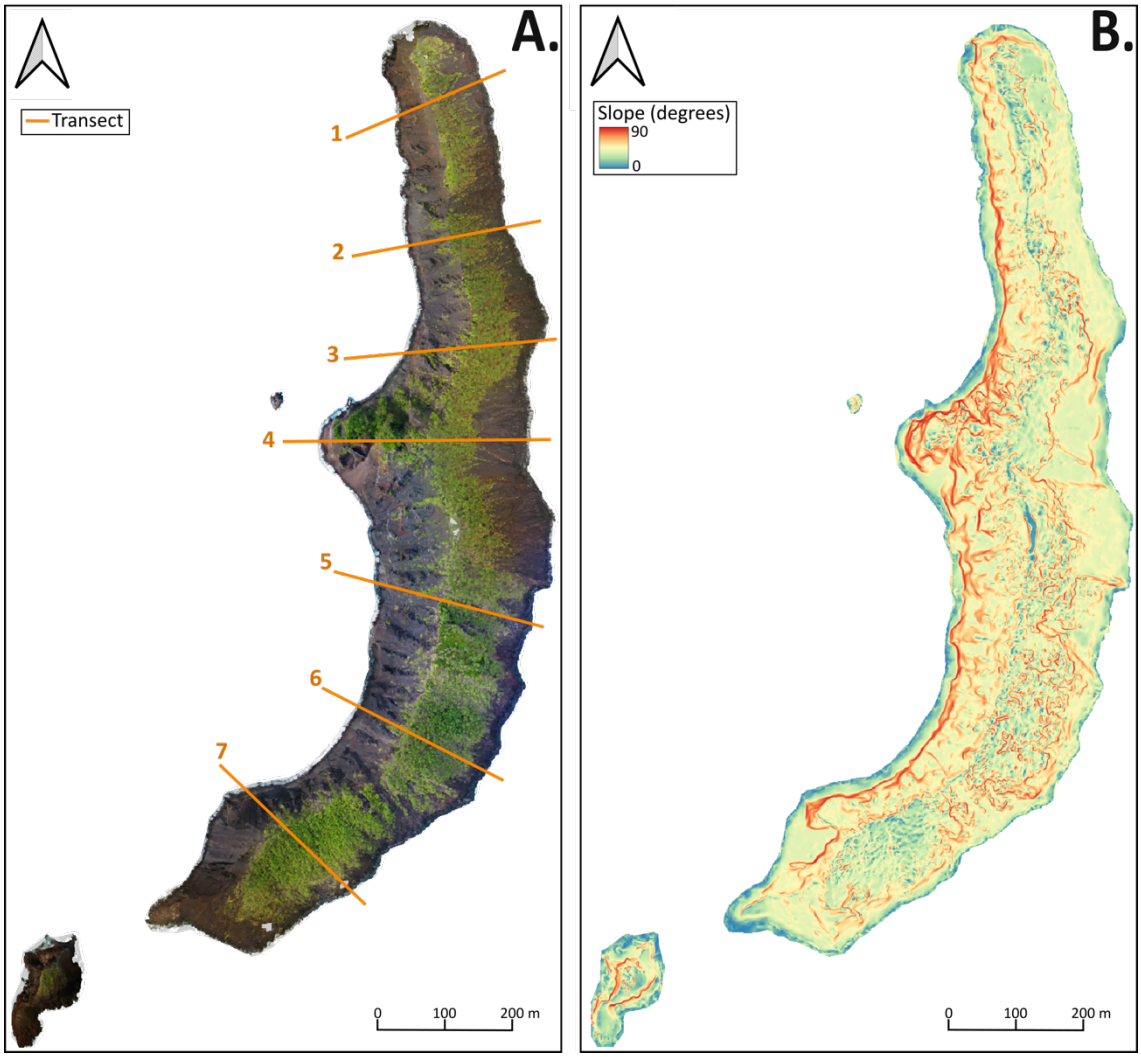

Figure 2.44: A. Ritter Island with slope analysis transects 1-7. B. Ritter Island DEM represented as slope angle – also can be viewed in 3D (https://sketchfab.com/3d-models/ritter-island-slope-analysis-806e48eb476c44a3a2ba4732e3694eea)

Slope analysis

The DEM is a useful dataset for Ritter Island as the eastern slope is representative of the pre-collapse edifice and is used in the reconstruction of this surface. The western cliff without the erosional deposits will be representative of the angle of the collapse fault and therefore is also important to constrain.

The results from the seven E-W trending profiles assessing the slope angle of the DEM shown in Figure 2.44A are shown in Table 2.3. From these we see that the average slope for the east is 34.3°. The average slope for the west is similar at 35.4°.

Table 2.2: Results of the transects 1-7 slope analysis on the east of Ritter Island (degrees).

Transect	1	2	3	4	5	6	7	Average
mean	28.97	33.92	33.12	32.28	37.78	38.15	35.28	34.3
median	26	33	31	31	37	38	32	32.0
mode	29	46	33	30	49	44	29	
1st quartile	16	19	19	20	22	22	19	19.0
3rd quartile	37	47	44	42	52	52	51	47.0

Table 2.3: Results of the transects 1-7 slope analysis on the west of Ritter Island (degrees).

Transect	1	2	3	4	5	6	7	Average
mean	33.23	34.74	33.00	33.00	37.74	37.40	38.08	35.4
median	32	33	28	28	36	37	36	33.0
mode	16	36	6	6	28	36	21	
1st quartile	17	18	15	15	22	25	21	19.0
3rd quartile	47	47	49	49	52	49	53	50.0

The results from the slope analysis from the whole DEM are stated in Table 2.4 (Figure 2.44). Here the eastern and western sides are compared both including the influence of the overlying vegetation and without. The western side is also analysed without the area inferred as the post-collapse erosional deposits including the scree slopes at the base of the cliff. These results give higher averages than the transect method on both sides. Both sets of results show that the eastern side of the island has a more consistent dip of 38.4°, whereas the western side varies more with a steeper average of 48.49°. This can be seen in the visual representation of the slope analysis (Figure 2.44). The western side is very gullied with shallower portions at the base and very steep trend along the lower extent of the cliff.

Table 2.4: Results from slope analysis of the DEM (degrees)

name	mean	median	Standard deviation
WEST	42.04	41.83	16.50
WEST - veg	41.83	41.53	16.37
WEST – veg – erosional deposits	48.49	46.44	12.87
EAST	38.79	38.14	13.49
EAST - veg	38.40	38.42	11.99

Island DEM measurements

A number of measurements can be taken from the new DEM of the Island. The maximum elevation of the island is above the central cusp and measures 117.46 m. At this point, the

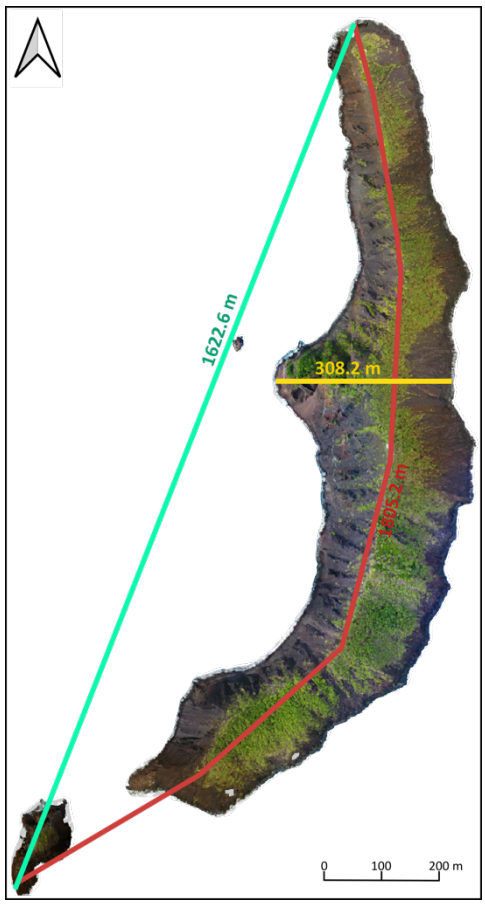

Figure 2.45: Ritter Island dimensions measured. Tip-tip length (blue), curved length (red) and maximum width (yellow).

sea level from the reference satellite image was assumed as '0 m'. Tidal changes in this region are minimal (< 1 m) so this assumption does not introduce much error.

The dimensions of the island were also measured (Figure 2.45). The northern extent to southern extent as 1622.6 m. Following the curve of the island, the measurement was 1805.2 m. The width of the island was measured at 308.2 m. The island surface area is 0.31 km^2 and the volume is 0.01 km^3.

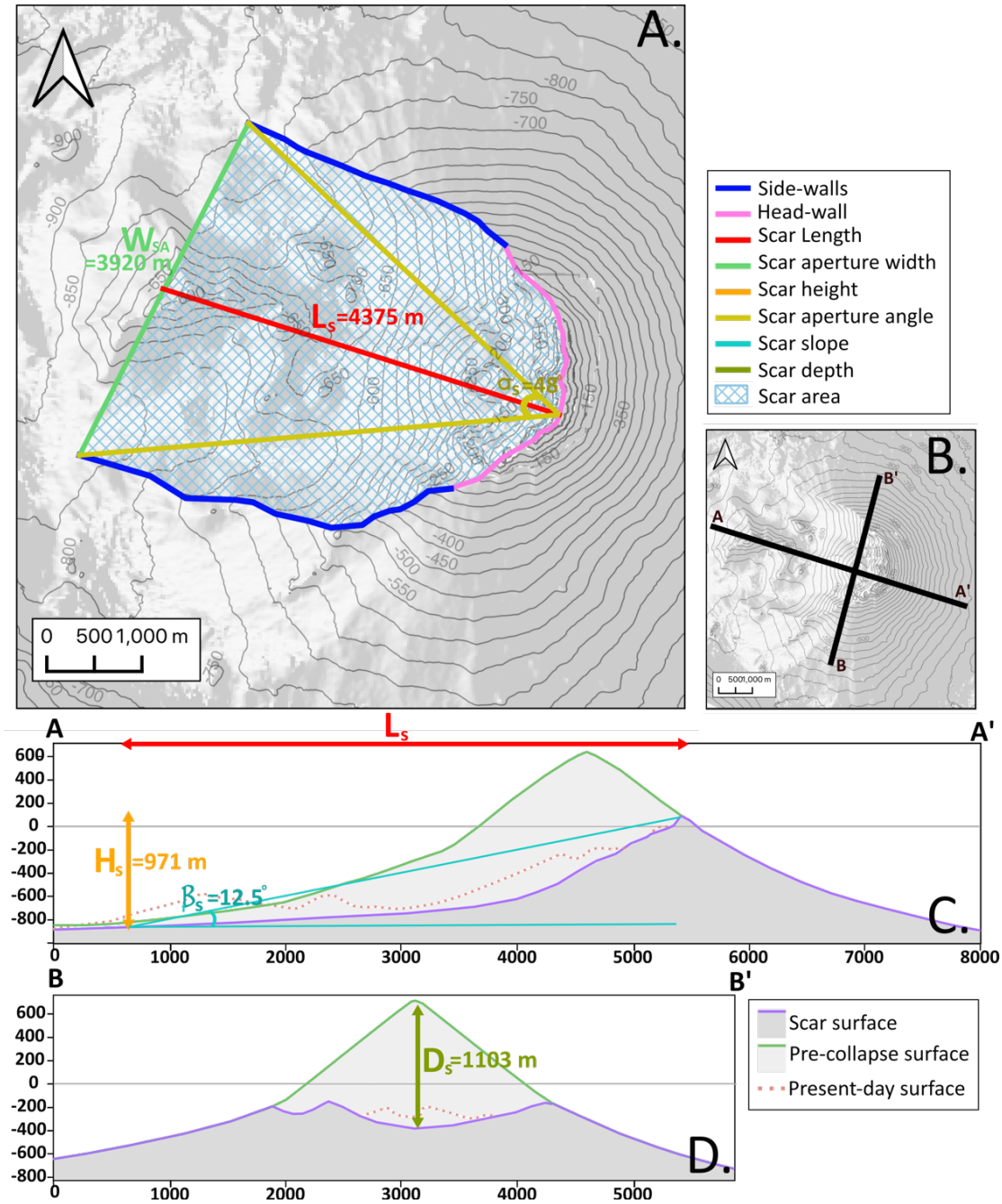

Figure 2.46: Results of scar measurements A. map view B. showing where cross-sections are drawn. C. cross-section through section A, D. cross-section through section B.

Volcano Scar metrics

The Ritter Island DEM was combined with the no data gap and the bathymetry in order to measure the parameters suggested by Bernard et al. (2021). Table 2.5 summarises these measurements and are displayed in Figure 2.46. Bernard et al. (2021) also categorised a number of descriptive terms when describing scar shape. As the side-walls are almost parallel in places but gradually divergent, this scar shape could be described as U-shaped to triangular.

Table 2.5: Measurements taken from the combined DEM and bathymetry in Figure 5 using parameters set out by Bernard et al. (2021). Volume measurement error here based on base of scar.

Parameter Acronym	Parameter description	Results	Variance
Ls	Scar length subaerial (m)	4374.8	±630
Ws	Scar width (m)	3919.6	±17
Wsa	Scar aperture width (m)	3919.6	±93
Hs	Scar height (m)	970.6	±48
as	Scar aperture angle (°)	48.0	±6
Bs	Scar slope (°)	12.5	±1
ys	Scar azimuth (°)	287.5	±0.6
As	Scar area (km^2)	13. 8	±2
Dsa	Scar depth (m)	1102.5	±93
Vsa	Scar volume (km^3)	3. 7	±0.4
Tsa	Scar thickness (m)	266.5	±17
Ars	Scar aspect ratio	0.13	±0.02
Efs	Elongation factor	0.31	±0.16
CFs	Closure Factor	1	±0.02

Volume calculations

The volume of the excavated material for the landslide was measured by calculating the difference in inferred surfaces. These were made by using the average slope attained from DEM slope analysis at 38.4°. In addition, surfaces were created for two end-members to compare the effect of this slope angle. The upper end-member was taken by the suggested angle of slope from by Johnson (1987) at 44°and the lowest was from the shallowest slope value found from the section slope analysis at 29°. An additional method was trialled for a 38.4° slope to include the detail of the present-day undulations of the eastern slope. These surfaces were compared to the present-day seafloor and the inferred scar surface. The results from these calculations are displayed in

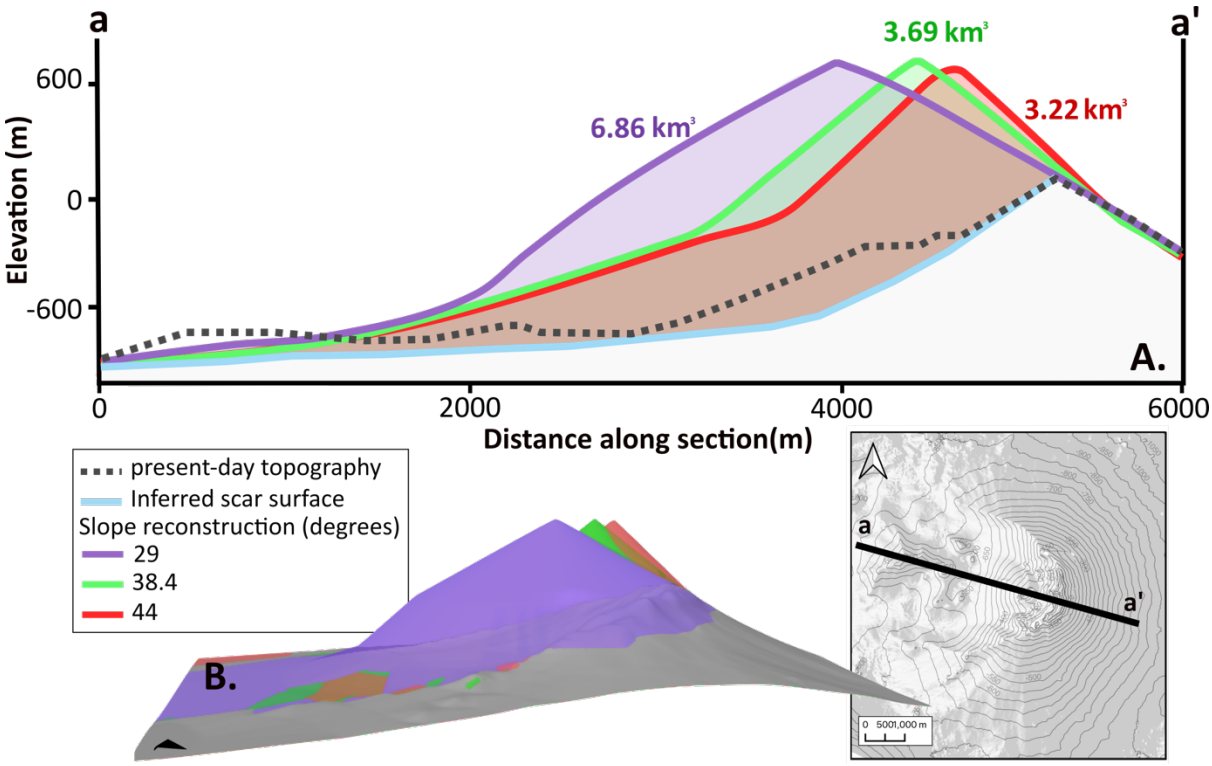

Figure 2.47: Volume calculations of collapsed material using reconstructed surfaces of different angles A. in cross section and B. in 3D – this can also be viewed at (https://sketchfab.com/3d-models/collapsed-materail-volumes-0f3124beb49344419d2c2edbf0242a21)

Table 2.6 using the reconstruction down to 900 m depth. The values calculated from using the depths to 850 m were on average 0.06 km^3 lower (Figure 2.47). From these results, it was clear that the 'detailed' surface creation method had small effect on the resultant volumes calculated. The difference between the values taken using the current day bathymetry and the scar surface is on average 0.55 km^3. The reconstructed cones for 44°, 38.4° and 29° had diameters of 1554 m, 1892 m and 2706 m respectively. By analysing the surfaces in relation

to the present-day topography, it can be observed that some surfaces fit better into the space and contours (Figure 2.47). The wider base of the cone from the shallower slope also seemed to not fit the reconstructed bathymetry whereas the base of the 38.4° cone fits within the inferred contours of the reconstructed bathymetry. The volume of collapsed material on the best fit cone is 3.7 km^3.

Table 2.6: Results from volume calculations for various slope angles at Ritter Island. In the method column, the words are referring to the inferred surfaces created. 'cone' is the reconstructed cone generated from the angle of the slope, 'present' refers to the present-day morphology surface, 'scar' refers to the inferred scar surface and the addition of 'detail' included the method where the present-day subaerial island is included on the cone.

Angle of slope (degrees)	Source	Raster calculation method	Volume (km^3)
38.4	slope analysis average	= cone - present	**3.3**
38.4		= cone - scar	**3.7**
38.4		= cone (detail) - present	**3.3**
38.4		= cone (detail) - scar	**3.7**
44	Johnson (1987)	= cone - present	**2.8**
44		= cone - scar	**3.2**
29	minimum from qprof analysis	= cone - present	**5.1**
29		= cone - scar	**5.5**

The best-fit cone, using the slope angle of 38.4°, is analysed alongside the present-day bathymetry (Figure 2.48). From this, it can be observed that the post-collapse cone is in line with the summit of the reconstructed cone. The location of the inferred conduit feeding the activity at Ritter Island can therefore be assumed not to have moved following collapse.

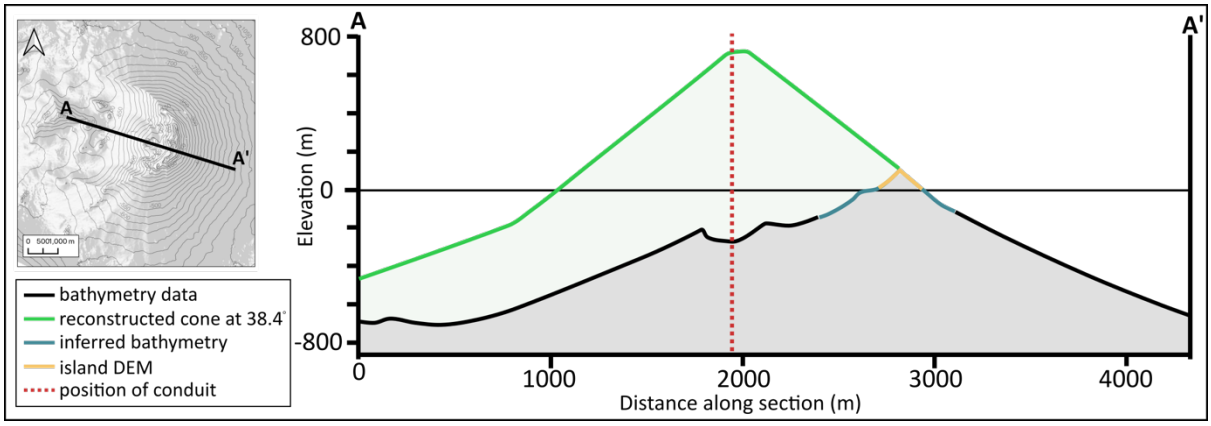

Figure 2.48: Cross-section through Ritter Island and the surrounding bathymetry and the reconstructed cone, highlighting the inferred location of the present-day conduit.

2.4.3 Ritter Island Geology

Figure 2.49 displayed the geological map and cross-sections inferred for Ritter Island following methods described in section 2.3.4. It also shows some erosional features such as gullies, deposits and evidence of shallow collapse. Please see the map insert which displays the full version of geological map. This shows the mappable geological features including the dipping layered units, the cross-cutting intrusions and areas of alteration.

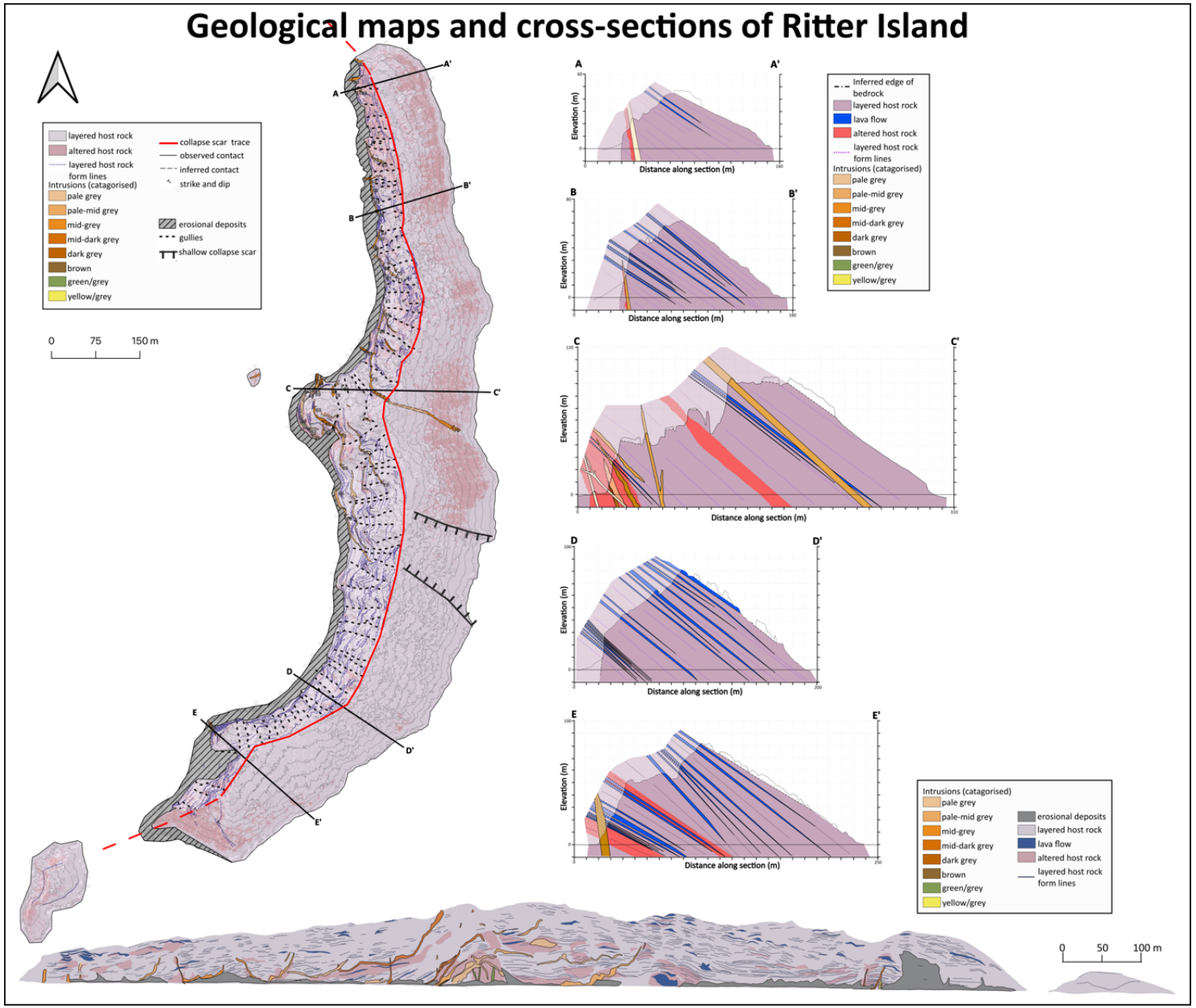

Figure 2.49: Geological map of Ritter Island with cross sections and a side view of the island. More detailed version of this figure can be seen in separate insert.

2.4.3.1 Dipping Layered Unit

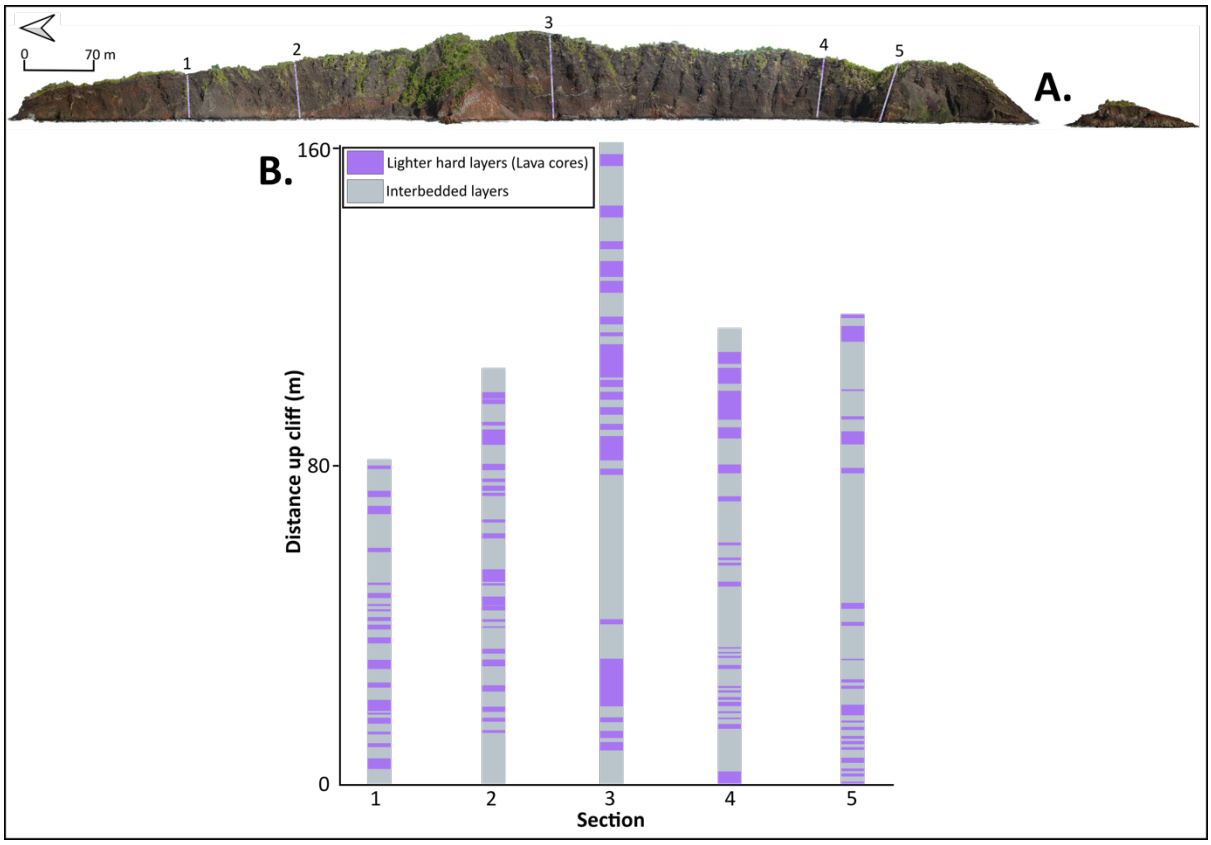

Figure 2.50: A. Side-view orthomosaic of Ritter Island highlighting locations of sections. B. Sections of layered unit host rock shown as thicknesses.

The majority of the subaerial Ritter Island consists of the dipping layered units as the host rock. These are bedded at a meter scale and alternate between lighter material and darker rubbly material. This is inferred to be the layers described in previous literature as interbedded lavas and scoria (Day et al., 2015). The lighter material tends to protrude from the cliff face more and is therefore inferred as harder lava flows. Figure 2.50 shows the measured thicknesses of the mappable layers at different sections though the cliff, measured at the angle of the exposure. This shows that the inferred lava flows appear consistently across the island with an average thickness of 1.8 m and ranging between 0.4 and 8.5 m. Some units may be smaller than this but too small to identify or map at this resolution. Of the mapped sections from the cliff, 24.58% of it was the lighter lava core layers. These layers are normally relatively thin and lens shaped, tapering towards the edges, with the sporadic appearance of some

thicker lavas often appearing less uniform in shape possibly inferred as channel filling lavas. The interbedded rubbly layers appear to be much thicker on average.

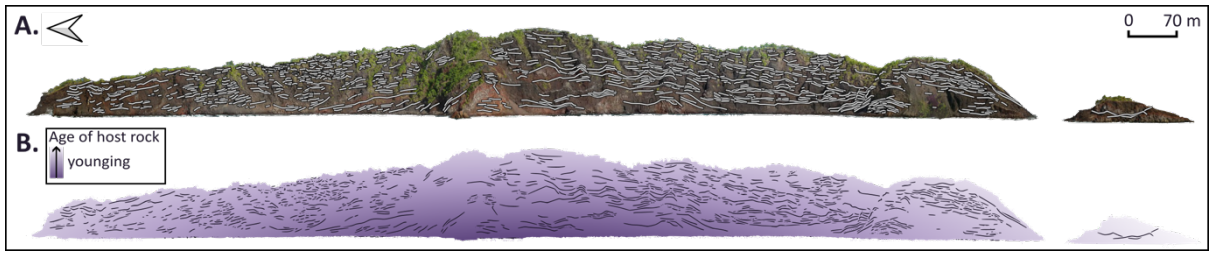

Figure 2.51: Form lines of the layered host rock unit on A. the side-view orthomosaic and B. inferred relative age based on these form lines.

Figure 2.51 shows the 886 mapped form lines of this unit across Ritter Island, also highlighting how laterally extensive the layered unit is. The average lateral extent of these layers is 17.7 m with maximum lateral extent being mapped up to 257 m. These form lines also indicate how the layers built up over time. There is no evidence of overturned structures and way up indicators such as the rubbly lava tops, suggesting that the layers are younging upwards. Towards the central cusp, the form lines seem to angle upwards suggesting the central region has older rocks at its base than the rocks at the same elevation laterally (Figure 2.51B).

Figure 2.52A shows the structural measurement data collected from the dipping layered units where possible from the model. 30 measurements were taken in total across most of the island and at varying elevations. These measurements show that the general trend of these beds is N-S striking (Figure 2.52B). Figure 2.52B highlights how the strikes to the north trend more toward NNW-SSE and the strikes in the south trend more towards NE-SW. When assessing these measurements relative to the assumed centre, these dipping units are generally striking perpendicular to the central point.

The dipping layers are not laterally continuous and therefore cannot be assumed as continuous throughout the volcanic edifice as features such as flow channels and levees would have been present during emplacement of the lava flows. For example, Figure 2.52 shows the strike and dip measurements for the layered unit depending on the dip value. From this it is clear that the beds are not completely consistent. However, it can be inferred that the general

angle of dip for all of these layers is dipping outward and at an average of 32.9°. This general trend is represented as this on the cross-sections where there was no direct measurement.

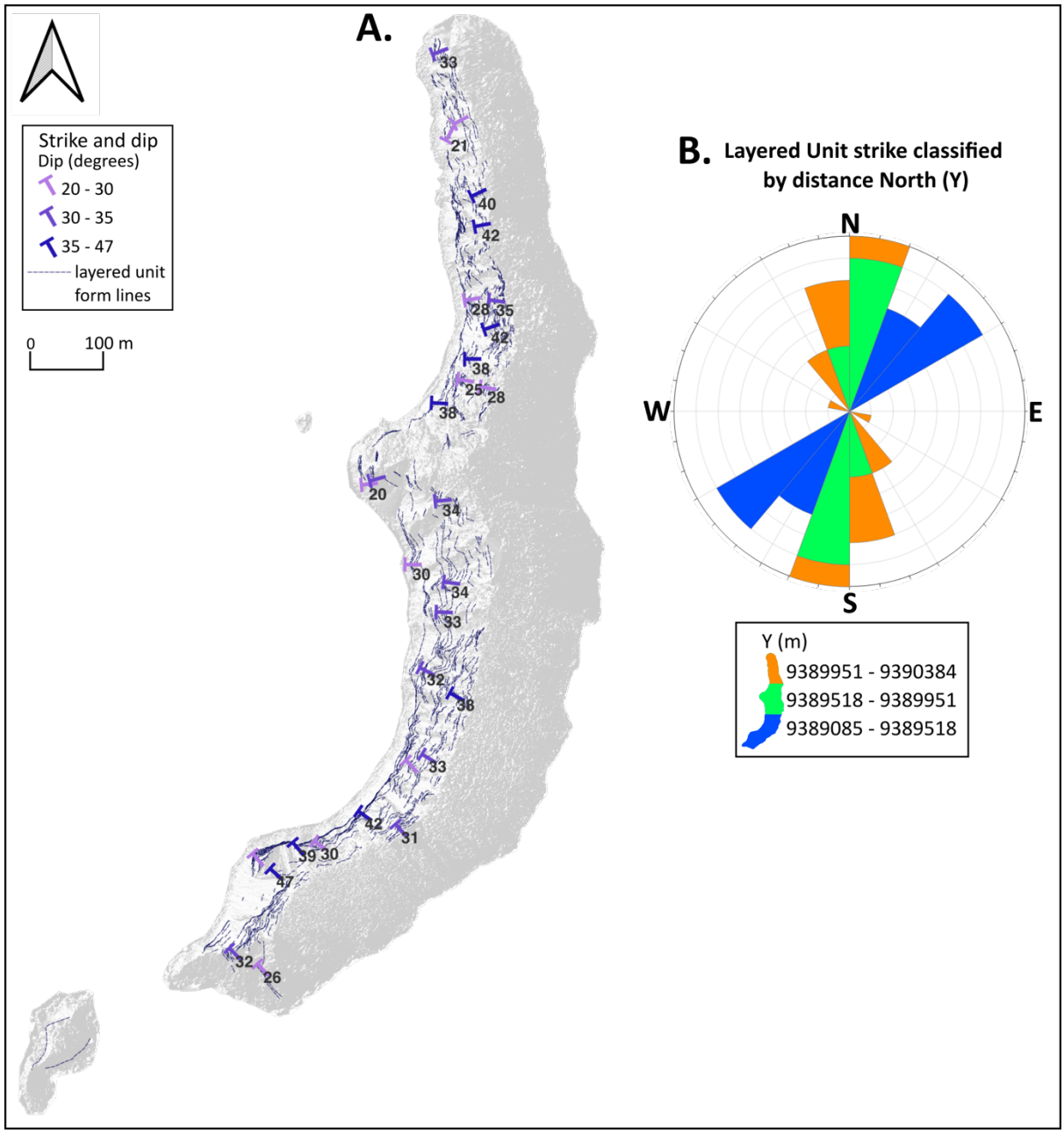

Figure 2.52: A. Dipping layered units on Ritter Island with measured strike and dips classified by angle of dip. B. Rose plot of strike orientations of the layered units classified by distance north (Y). C. Cross plot showing angle of dips of layered unit against elevation of the measurement (Z).

2.4.3.2 Cross-cutting intrusions

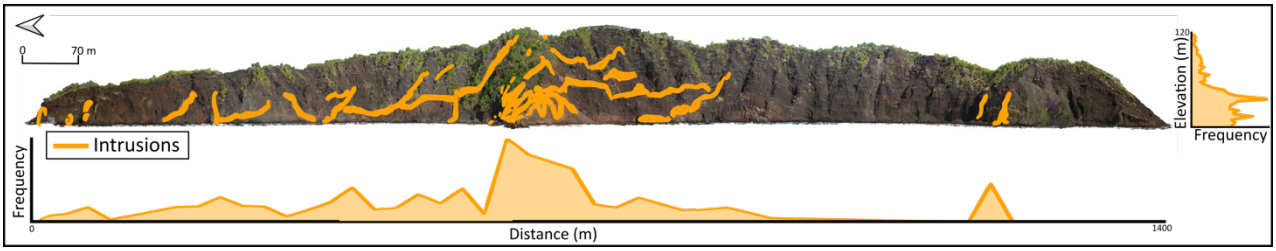

Figure 2.53: Ritter Island side orthomosaic displaying the mapped intrusive unit and the frequency of intrusions across the length of the island and vertically.

39 intrusions were identified and mapped onto the 3D model of Ritter Island. Figure 2.53 shows how the intrusions are distributed both horizontally north (Y) and vertically (Z) across the cliff. Here we see that density of dykes lowers as the elevation increases. The outcrops of the dykes here will not be a true representation on the extent of the intrusion as this cliff represents a cross-section through planes at oblique angles and therefore there is an observational bias. Only one dyke appears to reach the top edge of the cliff whereas the average limit to the dykes is at 42 m elevation. The horizontal distribution along the Y axis shows that there is a cluster of dykes in the central cusp and very few in the southern cove. The dip of the host rock trend dips down in the southern cove also so the reason for the absence of dykes here may be due to the younger succession of rocks here.

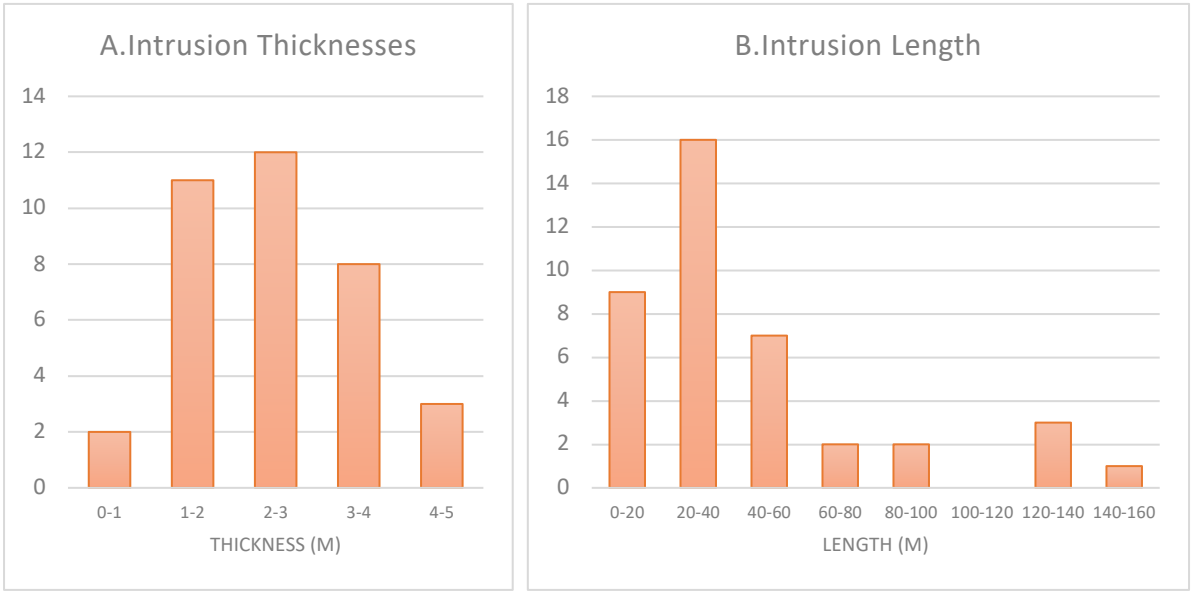

Figure 2.54: Histograms showing distribution of measurements taken from intrusions at Ritter Island including A. The thickness, B. The length.

Figure 2.54 shows the distribution of measurements across all of the mapped dykes. The thicknesses of the intrusions ranged between 0.9 m and 4.85 m and had an average of 2.49 m. Most of the dykes had a thickness of < 3.1 m (Figure 2.54 A). The average length of

dykes seen in the cliff is 43 m but the majority are < 40m due to there being a number of longer dykes measured with lengths over 120 m (Figure 2.54 B). In 8 of the intrusions mapped the tip of the dyke was seen and few dykes extended vertically higher than 60 m.

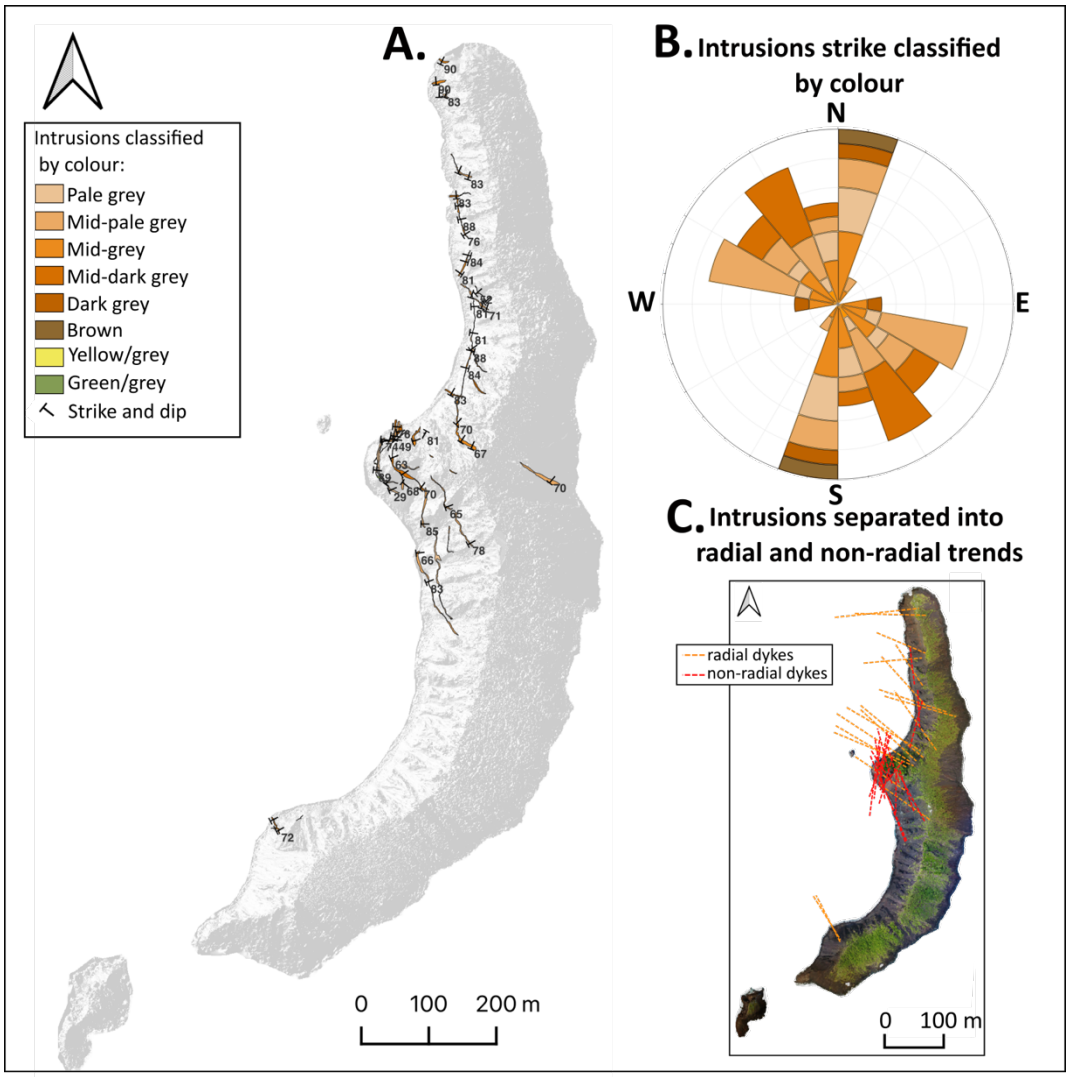

Figure 2.55: A. Mapped intrusions on Ritter Island classified by colour, B. Rose plots of the structural measurements of intrusions, C. dyke trends separated into radial and non-radial.

51 structural measurements were made of the cross-cutting dykes (Figure 2.55). The average dip of the mapped intrusion measurements is 73.6°. The measured dips range between 29° and vertical. Some of the mapped dykes could not be measured.

Mostly throughout this cliff section, intrusions are solitary and therefore it is difficult to determine the age relationship between other intrusions. Where some dykes cross-cut one another, a relative age can be established. As the similarly coloured dykes are assumed to be of the same age of emplacement, we can infer this relative age across the rest of the island.

In this section, intrusions will be referred to by the allocated number denoted in appendix 3, In the northern cove, the dark grey dyke 5 cross-cuts the mid grey dyke 6. In the

central cusp, mid-dark grey dyke 17 cross-cuts mid-pale grey dyke 20. To the north of the central cusp, pale grey sill 42 is cross-cut by mid-dark grey dyke 14 which is cross-cut by mid grey dyke 11. Dyke 11 also extends the complete elevation of the cliff making it definitely younger than all of the host rocks. Some of the dykes that do not extend as far up the succession may be post-dated by the younger flows of the host rock. From these relationships, it seems that generally, the darker dykes tend to be younger than the paler dykes.

By observing the succession of layered units and cross-cutting dykes, there does not appear to be any large-scale faults offsetting the rocks within the cliff. Smaller offsets and faults may not be able to be observed at this resolution. Some linear features are apparent at the central cusp, striking N-S, where the cliff steps down and gullies are incised. However, as these do not appear to offset the succession of host rocks, this may be the presence of a dyke that has been preferentially eroded. This would fit with the trend of N-S dykes in this region of the central cusp.

2.4.3.3 Alteration

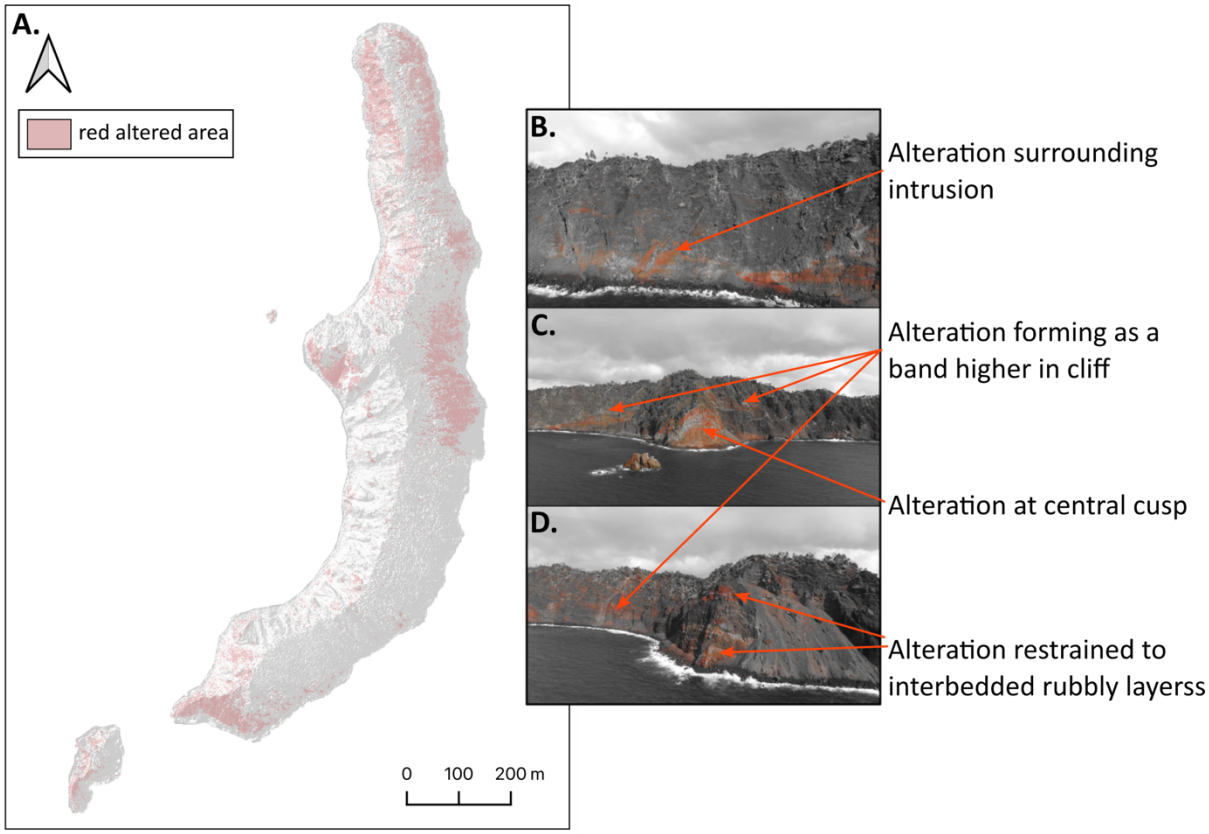

Figure 2.56: A. Alteration mapped on Ritter Island. B. alteration highlighted at north of cliff. C. Alteration highlighted at central cusp. D. Alteration highlighted to the south of cliff.

The inferred altered areas which have a reddish colour were mapped as 15.75% of the whole island from the orthomosaic. This includes areas which represent erosional deposits or surface weathering. The western side the island has 12.89% showing this red alteration. Other than the erosional deposits, it appears that only the host rock of dipping layered unit is altered and mainly within the rubbly interbedded layer and less within the lava flows (Figure 2.56D). The areas of alteration are concentrated at the base of the cliff on the western side on the near vertical faces (Figure 2.56A). This may indicate that alteration was present parallel to the slip plane of the collapse event. There are some bands of alteration appearing as layers in the cliff at a higher elevation near to the central cusp often coinciding with the thicker lava or intrusion layers (Figure 2.56B and C). Nearly all the central cusp host rock appears to have this red alteration (Figure 2.56C).

2.4.3.4 Erosion

By analysing the DEM of Ritter Island, some patterns and erosional structures can be identified. Using the slope aspect method described in section 2.3.3.4, a series of 85 gullies

were mapped incising the western slope (Figure 2.57). They are present through the whole length of the cliff and are often infilled with scree composed of the eroded material. Scree and blocky eroded deposits are present along the base of the cliff and in places extend higher in the cliff, particularly in the south and on the central cusp (Figure 2.57).

Any gullies on the eastern side are less incised, however there are some sharp features which cut inwards from the general trend of the eastern slope. These are inferred to represent evidence of shallow flank collapse possibly pre-dating the major collapse event (Figure 2.57).

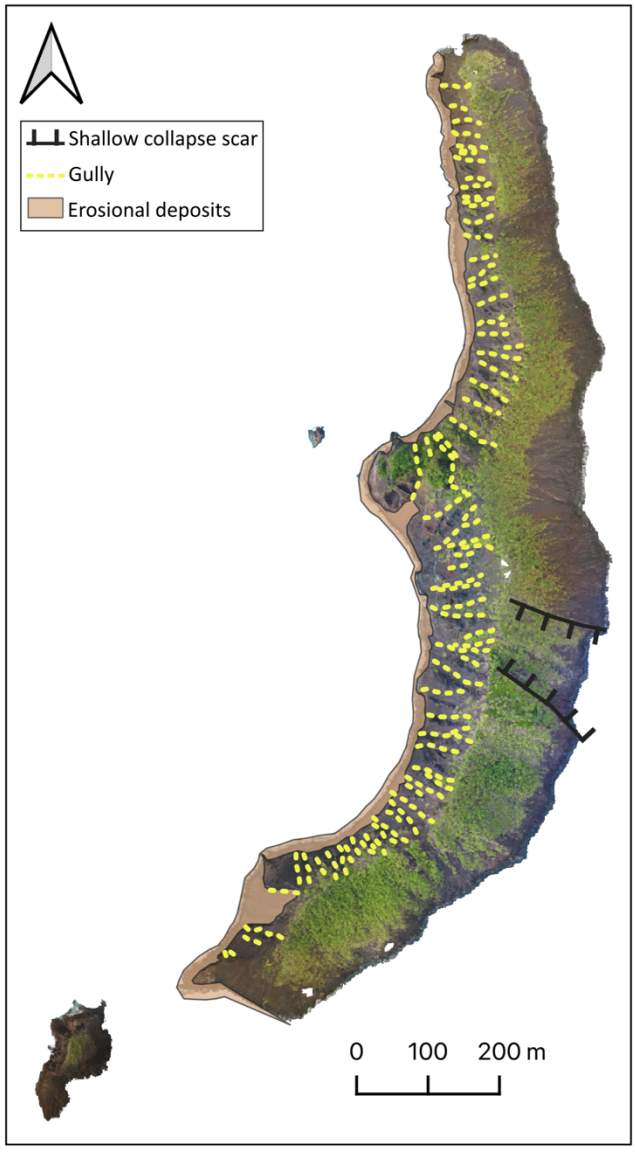

Figure 2.57: Orthomosaic of Ritter Island with mapped erosional features.

2.5 Ritter Island geology and structure summary

The new high-resolution model, DEM and orthomosaics produced for Ritter Island has allowed a detailed study on the geology and structure of the island and its relation to the collapse scar formed by its catastrophic collapse. This has allowed for some speculation on the evolution of Ritter Island pre- and post-collapse as discussed here (Figure 2.58).

- Measurements of the island and bathymetry deduced that this U-shaped to triangular-shaped collapse scar had a minimum length of 4375 m, a width of 3920 m and a height of 971 m. It has an inferred depth of 1103 m and an average thickness of 267 m.
- Slope analysis over the DEM estimated an average eastern slope of 38.4°. We can use this angle to assume that this was the average slope of the conical pre-collapse island. This is shallower than the previous estimates of the island slopes of 44° based on historic sketches (Johnson, 1987).
- This angle was used to reconstruct the pre-collapse cone. This, and the assumed surface of the collapse scar, provided an estimated collapsed volume of 3.7 km^3. This is 0.5 km^3 lower than the estimate from Day et al. (2015) of 4.2 km^3. This value is more than the shallow slide plane volume estimated by Karstens et al. (2020) of 2.59 km^3. Day et al. (2015) used this previously suggested slope value and an assumed more elongated volcano to calculate the volume. Karstens et al. (2020) used the shape and angle of the – 450 m contour for their estimations. The result from this research is between these two estimates and the difference may have largely resulted from the differences in the inferred collapse scar plane as well as the differences in slopes used for the pre-collapse island. However, the new assumption that the cone had slopes of 34.8°, using a high-resolution elevation model of the subaerial island where there was previously none, has introduced a more precise estimate for the subaerial portion of this volume estimate. The volume of the island is important to constrain due to its implications of tsunami modelling at this volcano as it directly feeds into modelling scenarios. The 12% reduction or the 42% increase from previous estimates will have a large impact on the size of the modelled tsunami.
- The reconstructed cone has a summit that lies above the post-collapse cone that is growing in the scar. The summit can be assumed as the main vent and hence the

location of the conduit feeding the eruptions pre-collapse. This suggests that the conduit did not shift in position following the collapse in 1888.

- The layered extrusive unit that makes up the host rock of Ritter Island is described as poorly consolidated coarse volcaniclastic units including rubbly and spatter-fed lavas, some massive flow cores and fine scoria (Watt et al., 2019, Day et al., 2015). Mapping of this unit shows that the flow cores have an average thickness of 1.8 m and represent 25% of this unit. These layers where generally thin and not laterally continuous but sometimes appeared as thicker channel-filling flows. Structural measurements of this unit indicate they dip between 20 and 47°, perpendicular to the assumed central peak. This cooperates with the idea that there was a central main vent on pre-collapse island.
- This host rock is cross-cut by a series of intrusions which can be seen clustered in the central cusp, sporadic in the northern cove and sparse in the southern cove. The extent of these intrusions is mainly seen in the lower elevations of the island, rarely extending higher than 60 m. The intrusions have an average thickness of 3.1 m and an average length of 38 m. The presence of this clustering in the centre may be due to the fact that this section of the cliff is wider and therefore reaching closer toward the centre of the volcano. It may also imply the age of the host rock where the younger host rocks may have had less time to be intruded hence suggesting the youngest host rocks may lie in the southern cove. This fits with the undulating trend of the host rocks. The presence of the dyke cluster in the centre protruding further than the rest of the cliff suggesting that it may be as a result of stronger rocks from the presence of the dykes.
- The intrusions generally trend N-S across the length of the island with some evidence of radial dykes trending toward the centre of the pre-collapse island. When assessing this trend relative to an assumed centre of a cone, these dykes trend perpendicular to the azimuth of the slide scar. This may represent dykes intruding along a preferred weakness along this plane. This weakness may have been caused by the beginnings of creep westward of the edifice due to some underlying weak layer corroborating previous suggestions of gradual spreading from Karstens et al. (2019). The intrusion of these dykes at this orientation may have increased E-W trending magmatic pressure contributing to the instability and the eventual collapse to the west (Figure 2.58).

- The varying colours of these intrusions may have some suggestion of composition and age. Relative ageing from the cross-cutting relationship of the intrusions suggest that the darker dykes tend to be younger than the paler dykes. The paler colours may be as a result of varying compositions but more likely because of differing extents of weathering. This inference is further evidenced by the cross-cutting relationships. The N-S trending dykes are of varying colours and hence inferred ages suggesting the preferred dyke orientation may have been present in the edifice over a long period.
- Some of the host rocks are discoloured by red alteration. The western cliff has 13% of its area discoloured with this alteration. This seems to be concentrated at the base of the cliff in steeper sections or surrounding intrusions. This alteration may be associated with hydrothermal processes as they seem to surround the intrusive units (Figure 2.58). This alteration on the steeper portions of the cliff may also suggest that this alteration was present along regions of the slip plane of the collapse event indicating this may have been a contributing factor to the instabilities in the cliff (Figure 2.58).
- Observing erosional patterns show that gullies incise the cliff throughout the western face. This, and presence of multiple scree slopes and blocky deposits at the base of the cliff, emphasises how extensive post-collapse erosion is. This further highlights the weakness of the materials making up the island.
- Evidence of shallow collapse can also be inferred in the eastern slope, possibly pre-dating the major collapse event, again highlighting the precariousness of the slopes of the pre-collapse cone.
- Further investigations into the mechanical and hydraulic properties of the rocks at Ritter in the context of the geomorphology of the present-day and pre-collapse volcano discussed in this chapter will help to highlight any further sources of instability.

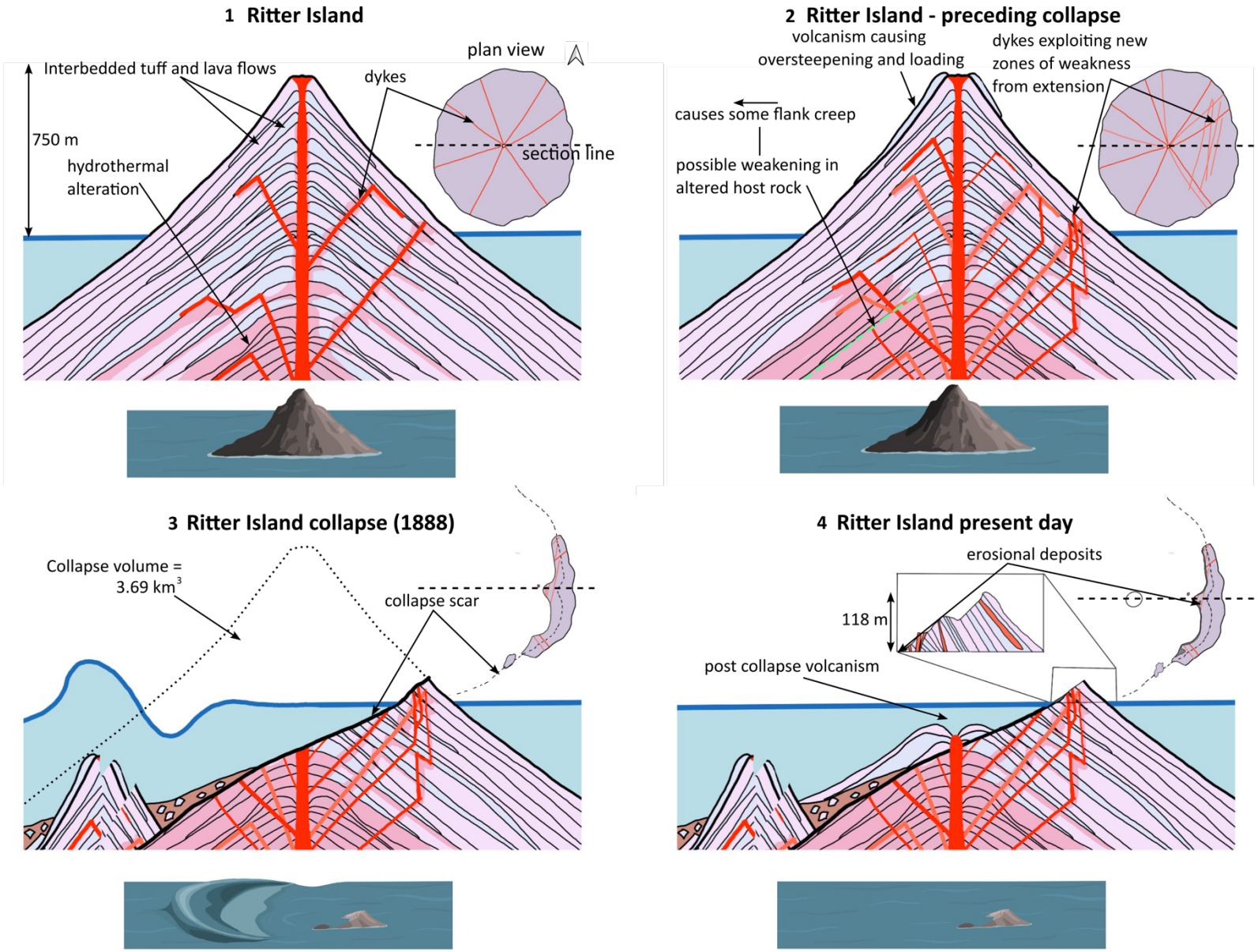

Figure 2.58: Schematic summary figure showing the probable evolution of Ritter Island leading up to and after collapse based on the results from this study.

3 Ritter Island: Mechanical and hydraulic properties

3.1 Introduction

The Ritter Island geology mapped in Chapter 2 described various lithologies that make up the present-day island. This includes interbedded pyroclastic and lavas cross-cut by numerous dykes with various zones of clear alteration across the cliff. This poses an insight into the make-up of the pre-collapse edifice and possible avenues for how instabilities could have developed. Further investigation into the properties of the rock types identified in this mapping will build up a clearer picture of the edifice strength.

Previous excursions to Ritter Island collected various sample sets from across the island and in the submarine collapse scar. This includes the SD sample set from the south cove, the Rit set from the north cove and the H set collected from the submarine scar (Figure 3.1). These samples were originally sampled for petrological analysis and so were biased towards fresh unaltered rocks. In addition, in some cases there were not enough sample to create cores for hydraulic measurements. Previous works on these samples include petrological analysis by Melanie Ray (2017) used in this chapter.

This chapter investigates the mechanical and hydraulic properties of these samples to characterise the strength and instabilities of the pre-collapse volcano. Of the available cored material, the porosity, permeability, Young's modulus and uniaxial compressive strength was measured. Small samples of the remaining rocks had porosity estimated from thin sections and using a wax pycnometer method. Empirical relationships were established to estimate the missing measured parameters.

The porosity and permeability are important to assess as these parameters control the ability of fluids to move around or pressurise within the edifice and control the location of hydrothermal alteration. Higher porosities tend to reduce the strength of volcanic rocks (Heap et al., 2014). Alteration has the potential to weaken or strengthen an edifice (Heap et al., 2021a, Heap et al., 2021b)). Pore fluid pressurisation caused by low permeability layers trapping fluids can weaken edifices. The uniaxial compressive strength and Young's modulus will dictate how the rock responds to pressures in the edifice. Therefore, understanding these parameters can help assess the strength of the pre-collapse edifice that eventually failed.

Using the results from this chapter within the context of the structure and geology described in chapter 2, an improved picture of the stability of the pre-collapse island can be created and weakening mechanisms postulated as a result.

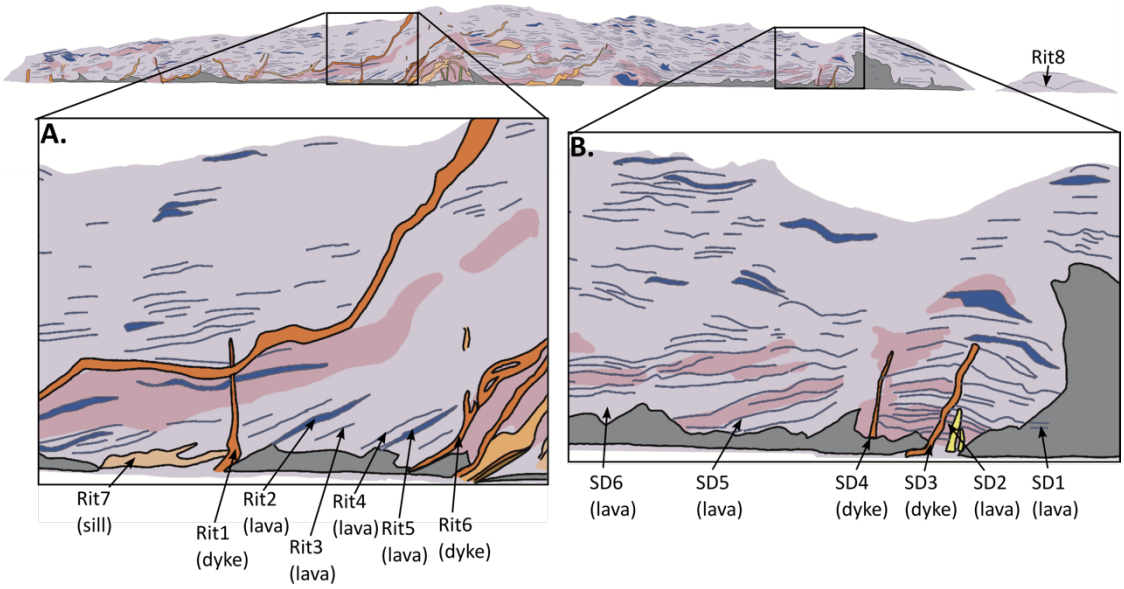

Figure 3.1: Western view on Ritter Island map highlighting the sample locations of the Rit and SD sample sets.

3.2 Methods

3.2.1 Petrology

Many of the sample sets from Ritter Island have been previously worked on by Melanie Ray (2017). This includes thin section imagery, analysis and XRF data for the SD and Rit samples. The petrology has been extended by using the thin section images of Rit and SD samples for porosity measurements and thin section mineralogy descriptions including percentage of crystal content and groundmass. New thin sections of the H samples were made and analysed in a similar way. Each sample section was described in terms of their mineral assemblages. Common minerals observed in each of the sections were plagioclase, olivine, pyroxenes many had vesicles present. Each of these were identified by using the following criteria (MacKenzie et al., 2017):

Plagioclase feldspar:

- Lath-shaped crystals which are colourless in plain polarised light (ppl) and show lamellar twinning in crossed polars light (xp).

Clinopyroxene

- Colourless, pale green to brown in ppl with two sets of cleavage at 90° with mid birefringence in xp.

Olivine

- Colourless to pale brown in ppl with high relief, irregular fractures and high birefringence in xp.

Vesicles

- Rounded shapes which are colourless in ppl but black in xp. The shape and distribution of pores are described visually ranging from circular – irregular. Measurements of vesicles are taken along their major axis.

New XRF data of the H samples alongside the data for the Rit and SD samples were used to create a Total Alkali Silica (TAS) plot of the complete sample collection thus defining their categorised rock types.

3.2.2 Measuring Porosity

Porosity is important in assessing other volcanic rock properties, as it strongly influences the permeability and the strength of a rock.

Porosity was measured using two methods. These included thin section analysis using image J software and using a helium pycnometer. Combining the two methods gives a more comprehensive view of the nature of the porosity. The pycnometer gives an accurate porosity for the connected pores in a larger volume sample whereas the thin section analysis uses a smaller 2-dimensional region but reveals more about the small-scale structure of the pores.

3.2.2.1 Thin section analysis

Thin sections for each of the subaerial samples from the RIT and SD suites were scanned using an Epson top-lit scanner using Epson software by Ray (2017). Thin sections were previously analysed and point counted by Melanie Ray, providing estimates of porosity, groundmass and crystal abundances.

Image J – Image segmentation process

To verify these earlier porosity estimations, the thin section scans were used with an image processing software, ImageJ. Quantitative analysis of thin sections provides the ability to find useful measurements of crystal size, type, shape and modal assemblages of rocks.

ImageJ is an open-source image processing software programme from the National Institutes of Health (NIH). It can calculate area and pixel statistics of defined selections and can be used to obtain an accurate modal analysis from a thin section quickly. It can therefore

be used to perform geometric and quantitative analysis to enable measurement of grainsize, grain shape and orientation of grains, pore structure and microstructure of materials.

Each sample was processed three times, so that it could be separated into three areas of interest, i.e., groundmass, crystals and vesicles (Figure 3.2):

1. The thin section scan was loaded into ImageJ and cropped to a rectangle to exclude the outer area of the image from processing, so that a representative section of the image was obtained. The cropped version of the scan was used in each stage of thresholding (Figure 3.2a)
2. The image was then segmented using values representing the hue, saturation and brightness of the image. The threshold values were changed to highlight and segment different areas of interest, i.e., crystals, groundmass and vesicles. For example, to highlight the vesicles high brightness values of ~200-255 were used because they appear pale to white in the plane polarised light scans (Figure 3.2b).
3. The image was then converted into a binary (black and white) image, highlighting only the segmented areas as dark pixels and everything else as light pixels (Figure 3.2c). As the thin section scans contain areas of similar colours that may not necessarily represent the intended feature of interest, the binary image needed to be processed further. For example, if the feature of interest was pore spaces, some crystals such as plagioclase that are pale in colour in plane polarised light are included and need to be removed (Figure 3.2c)i)).
4. Unwanted features were identified by viewing the thin section under a microscope alongside the ImageJ process and could be removed manually from the binary image.
5. Where bubbles appear in the thin section in the middle of vesicles, the ‘fill holes’ tool was used to fill these areas (Figure 3.2c)ii)).
6. Any noise and outlying pixels present in the image were then removed using ‘despeckle’ and ‘remove outliers’ functions.
7. A final segmented output representing the area of interest was exported in tiff file format. The white background was removed in illustrating software Inkscape and then overlain on the original image. Any issues in the resultant image could be fixed at this point by comparing to the original image (Figure 3.2d).

8. Using the ‘measure’ tool in ImageJ, the percentage area of the dark pixels, representing the feature of interest, was measured. The area of the vesicles represents the 2D porosity of the section.
9. 2D porosity values can be compared in different areas of the thin section to see how they vary. This was done in ImageJ where the different area of interest binary images were stacked and 4-5 smaller squares were randomly drawn over the section. For each square, the dark pixel area percentage was measured and recorded. The porosity variation was then be compared across the sample.
10. Each segmented area of interest was exported, the background removed and given a representative colour to produce a simplified map of each sample (Figure 3.2e).

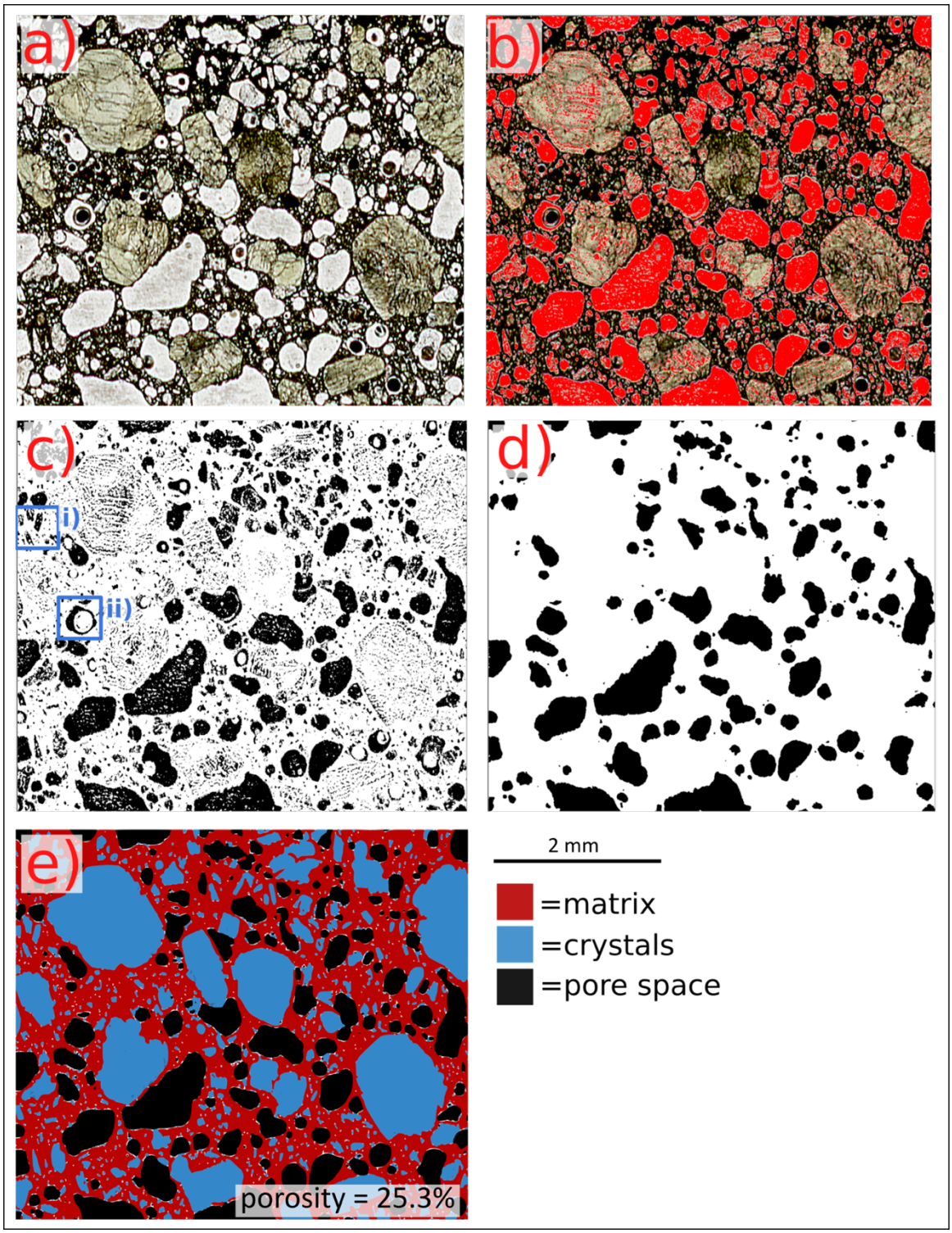

Figure 3.2: ImageJ segmentation process on thin section images showing a) the raw cropped image, b) thresholding paler values to highlight pore spaces, c) Binary image segmenting paler areas highlighting i) areas segmented representing pale crystals, d) edited porosity layer removing outliers and noise e) full section separating matrix, crystals and pore space.

This process produced useful measurements for porosity for several reasons. It provided an average result across the whole thin section and takes into account the apparent size of the pores. The map produced provides a simplified view of the rock and can highlight features such as the connectivity or regularity of the vesicles. It can also be useful to analyse the porosity variation across the sample thin section, in order to get an idea of the heterogeneity. It is relatively quick compared to point counting and removes some of the time and manual aspect of the process. However, the resultant porosity is only representative of the individual 2-dimensional thin section rather than the 3-dimensional unit itself. A thin section will cut across 3D vesicles and therefore will not represent their true size and shape, and are most likely be representing pores smaller than in reality, called the cut-effect, and with smaller vesicles having a lower probability of being intersected, called the intersection probability (Shea et al., 2010) (Figure 3.3). Therefore, the resultant 2D porosity is likely to be lower than the 3D porosity. In addition, micro-fractures containing porosity will not be accounted for in this way. Therefore, where possible, 3D porosity is also measured using a helium pycnometer to provide a more accurate porosity measurements that can be used to compare to this 2D porosity from image analysis.

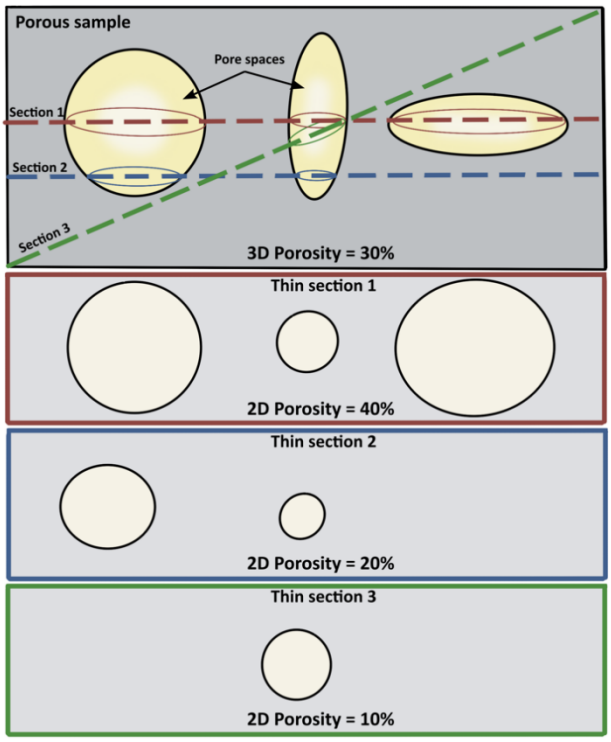

Figure 3.3: Schematic highlighting how thin sections may not represent the true 3D porosity.

3.2.2.2 Pycnometer

A micrometrics AccuPyc II 1340 constant volume pycnometer was used to measure the volume of the samples. Many of the Ritter samples were too small obtain a core from and therefore a bulk volume could not be measured. Therefore, a method was used whereby the samples were measured before and after the sample was coated in paraffin wax to obtain the measurements required to calculate the porosity.

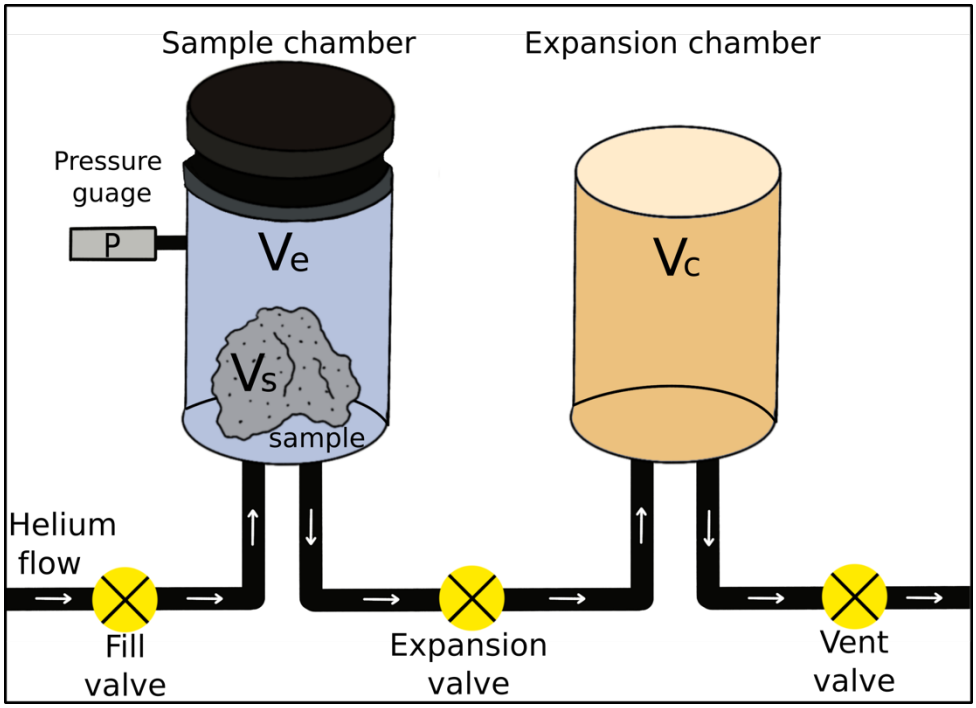

Figure 3.4: Schematic diagram of AccuPyc II pycnometer

The AccuPyc is a gas displacement pycnometer which uses helium to measure the solid volume of the sample (V_s) placed in the cell chamber. The pycnometer consists of two chambers with a known volume, the sample chamber (V_c) and the expansion chamber (V_e) (Figure 3.4). Helium is pumped into the sample chamber while the expansion valve is closed and the gauge pressure is measured in the sample chamber (P_1). The valve is opened and the pressure drops and is measured in the sample chamber again (P_2). The volume of the sample is then calculated by the following simplified Equation 3.1. For each measurement, this cycle is run ten times through and an average is taken for the final volume measurement with the standard deviation. When the mass of the sample is entered before the measurement is taken, an average density value and its standard deviation is calculated.

Equation 3.1: Volume of sample using pycnometer

$$V_s = V_c \left[\frac{V_e}{\left({}^{P_1}/_{P_2} \right) - 1} \right]$$

Where the sample has been cored into a cylinder, the bulk volume can be measured and calculated by using the equation for the volume of a cylinder (Equation 3.2) where ***r*** is the radius and ***h*** is the height of the cylinder. The effective porosity of the sample (Φ_{eff}) is measured using Equation 3.3. The effective volume (V_{eff}) is the volume of the sample (V_s) calculated from the pycnometer in Equation 3.1.

Equation 3.2: Bulk volume for cylindrical cored sample

$$V_{bulk} = \pi \, r^2 \times h$$

Equation 3.3: Effective porosity

$$\phi_{eff} = 100 \times \left[1 - \frac{V_{eff}}{V_{bulk}} \right]$$

Where the samples have not been cored and have an irregular shape, the bulk volume was calculated using a different method by dipping the sample in paraffin wax (Figure 3.5). Initially the sample is measured in its raw capacity (Figure 3.5a). The sample was weighed to get the raw mass (M_{raw}). The sample was then put in the pycnometer to measure its effective volume (V_{eff}). Then the sample was coated in paraffin wax with a known density (P_{wax}) by dipping the sample in a container containing the liquid paraffin wax with a temperature of ~55° (Figure 3.5b). When the sample and wax had cooled, the initial process was repeated with the waxed sample (Figure 3.5c). The mass of the waxed sample was then taken (M_{wax}) and it was then placed into the pycnometer for the volume to be calculated again (V_{wax}). Bulk volume (V_{bulk}) was calculated using Equation 3.4.

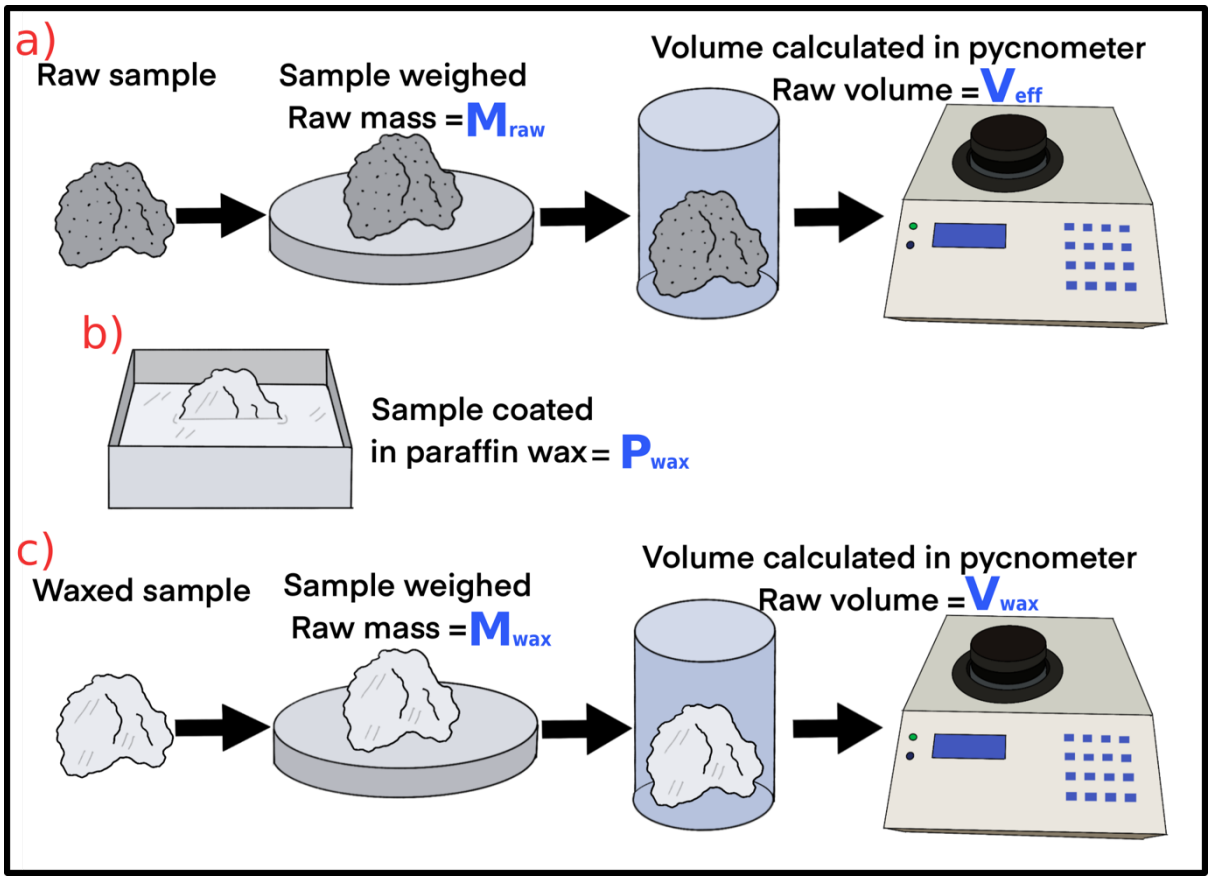

Figure 3.5: Pycnometer method for irregular shaped samples by using the a) raw sample, b) coating it in paraffin wax and c) measuring the waxed sample

Equation 3.4: Bulk volume of irregular sample using waxing process

$$V_{bulk} = V_{wax} - (\frac{M_{wax} - M_{raw}}{P_{wax}})$$

Error considerations

There are several errors that must be avoided when using this method. The pycnometer should be calibrated before every session of experiments or when changing the chamber size. The different chamber sizes are 10 cm^3, 35 cm^3 and 100 cm^3 and are chosen based on the size of the sample. The smallest chamber into which the sample would fit was used in order to get the most accurate volume measurements. When calibrating, chrome steel standards of a known volume from the manufacturer were used to calibrate the cell volume. The calibration is successful once the volume measurements were inside the acceptable variance for each standard, as calculated using Equation 3.5.

Equation 3.5: Calculation for acceptable variance when calibrating the pycnometer as per the Accupuc II recommendations

$$Variance = (chamber\ volume \times 0.0003) + (Known\ Standard\ volume * 0.0003)$$

The manufacturer recommends that the volume of the sample in the chamber is not < 10% of the volume of the chamber as this will introduce too much error in the results. When the sample is too large to fit into any other container but is still < 10% of the volume of the chamber, the chrome steel standards with a known volume were added to the chamber to reduce this error. The measurement given from these situations must then subtract the volume of the chrome steel standards used to get the sample result.

When using the waxing method for irregular samples, the wax may have entered fissures or pore spaces, however this has minimal effect on the calculated porosity. In addition, the pycnometer method will measure the connected porosity that can be filled with helium but not include the full porosity represented by non-connected pore spaces. However, as the ability of the rock to hold and transmit fluids is being assessed, it is more significant to measure the connected porosity.

Error can arise from measuring the shape of the rock core. The diameter and length of the cores were measured 4 times using a micrometer. From these, the maximum and minimum dimensions were recorded and used to propagate variance through the property calculations. The porosity measurements in the pycnometer give repeatability giving a standard deviation of effective volume and density. The effective porosity maximum is found by using the maximum bulk volume and minimum effective volumes and porosity minimum is found using minimum bulk volume and maximum effective volume.

3.2.3 Permeability

The permeabilities of samples was measured using a permeameter using the 'steady state' method. The permeability was measured using the 15 mm diameter cylindrical samples cored from the Ritter and Fogo samples. After coring, the samples were dried and the dimensions, porosity and mass were measured. The cores were then placed into a container holding deionised water and then into a vacuum to degas and saturate the samples.

The process for the steady state method for each sample is as follows. First, the sample was inserted into a rubber jacket and assembled with a 15 mm microporous steel spacer at either end to allow equal fluid distribution (Benson et al., 2005). High pressure seals were in place to ensure no leakage during the experiment. Steel end caps were then assembled allowing fluid flow into the sample from both ends. Steel tie bars were fitted to keep the sample assembly parallel and in place (Figure 3.6). The sample assembly is then placed and sealed into a hydrostatic pressure vessel which maintains high confining pressures using silicon oil controlled by an air pump (Figure 3.7) (Benson et al., 2005).

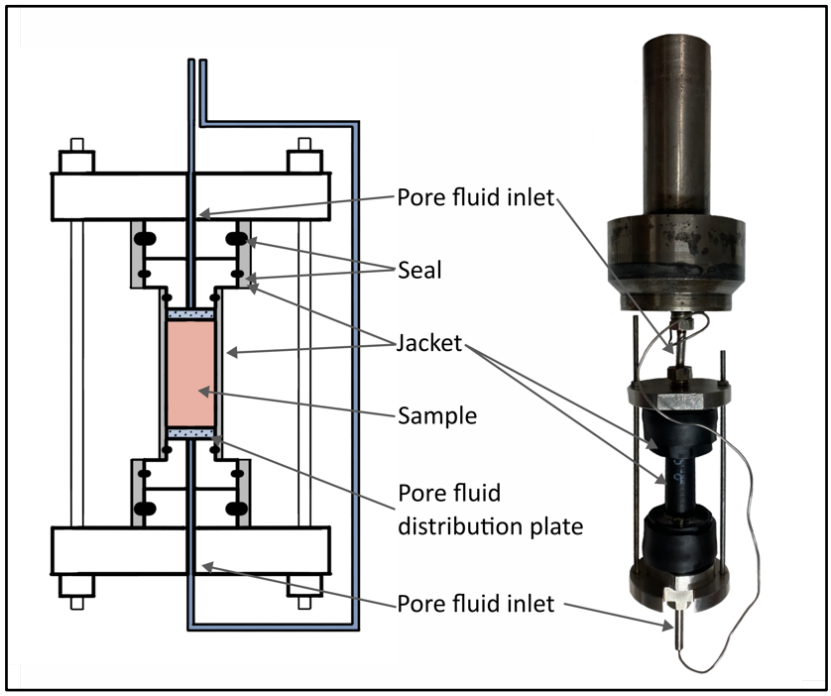

Figure 3.6: Simplified diagram of sample assembly for permeameter experiments adapted from Benson et al. (2005) (left) and an example of the sample assembly (right)

The two servo-controlled volumeters can each provide up to 70 MPa of pore fluid pressure to either end of the sample (Benson et al., 2005) (Figure 3.7). De-ionised water was

used to fill the intensifiers and the valves are opened to allow the water to saturate the sample until an equilibrium was reached. During an experiment, a gradient was set across the two intensifiers to create a constant pressure difference across the sample. This allowed a steady state of fluid to flow from one end to the other through the sample. The average constant pressure difference in the experiments at 5 MPa used was 0.6 MPa although varied slightly depending on the sample. 5 MPa was the starting confining pressure used to allow a pore fluid pressure of around 2.5 MPa to be set up without risk of a leak of oil into the sample. The intensifiers were fitted with displacement transducers monitoring the position of high-pressure pistons. This allowed the volume of fluid flowing into and out of the sample at each of the intensifiers to be measured over time. This steady state of fluid flow across the sample was achieved at a series of increasing confining pressures to measure how permeability is affected by pressure. The maximum confining pressure used for permeability measurements was 40 MPa. This was used as it would cover the overburden compressive stress possibly experience in the Ritter edifice. The experiment is also continued as the confining pressure was reduced after reaching high confining pressures to ascertain whether hysteresis had any effect on the permeability.

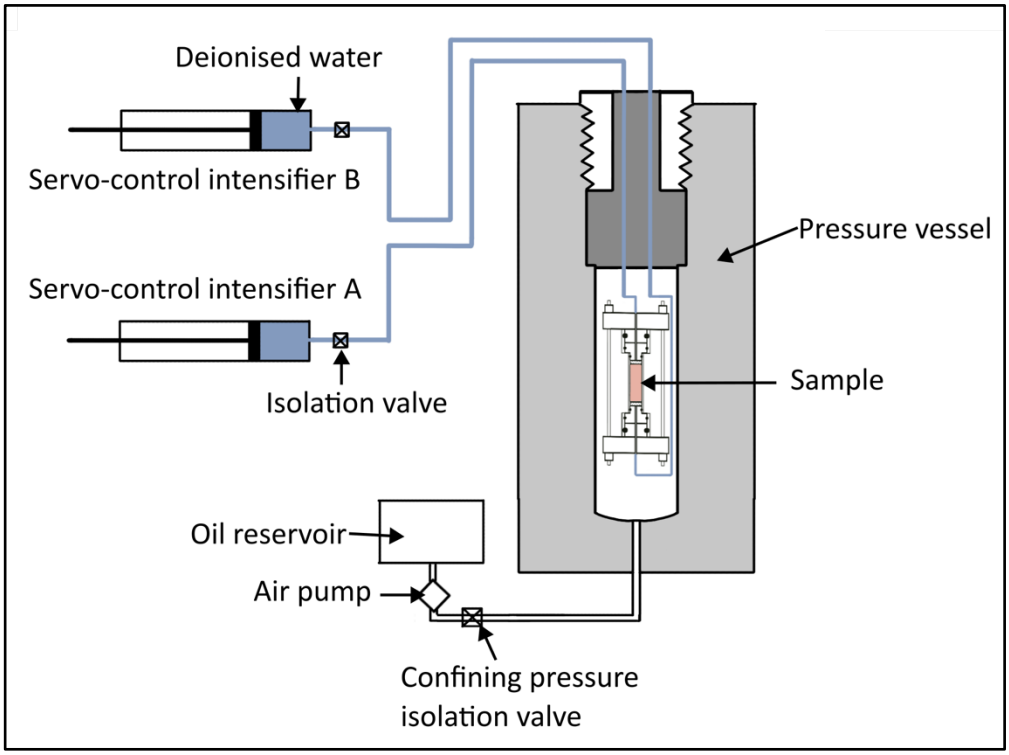

Figure 3.7: Simplified diagram of permeameter used for permeability measurements (adapted from Benson et al. (2005)).

While the experiment ran, data was collected and measured which was later used to calculate the permeability. The output data included the time (in seconds), confining pressure (MPa), pore fluid pressures at intensifiers A and B (MPa) and the volume in intensifiers A and B (cm^3). Figure 3.8A shows an example output graph from an experiment displaying time vs confining pressure and time vs pore fluid pressures. In Figure 3.8A, the confining pressure was stepped up to 40 MPa and back down over the course of an experiment. Figure 3.8B shows the effect that these higher confining pressures tended to have on the flow rate across the sample as the rate at which fluid moves through the sample was reducing with time creating a shallower gradient.

Permeability can then be calculated using Darcy's Law. This is a proportional relationship of the instantaneous discharge rate through a porous medium, the viscosity of the fluid and the difference in pressure over a distance expressed in Equation 3.6:

Equation 3.6: Darcy's Law

$$\boldsymbol{Q} = \left(\frac{\boldsymbol{K}}{\boldsymbol{\mu}}\right) \times \left(\frac{\boldsymbol{\Delta P}}{\boldsymbol{\Delta X}}\right)$$

Where $\boldsymbol{Q}$ is the total discharge (m^3/s), $\boldsymbol{K}$ is the permeability (m^2), $\boldsymbol{\Delta P}$ is the pressure difference, $\boldsymbol{\mu}$ is the viscosity (Pa) and $\boldsymbol{\Delta X}$ is the sample length (m). Using Darcy's Law, the permeability can be expressed as in Equation 3.7:

Equation 3.7: Darcy's Law rearranged

$$\boldsymbol{K} = (\boldsymbol{Q} \times \boldsymbol{\mu}) \times \left(\frac{\Delta X}{\Delta P}\right)$$

Using Equation 3.7 with each steady state flow, the $\boldsymbol{\Delta P}$ is the difference in pore fluid pressures at intensifiers A and B (MPa) and Q is the measured gradient from the steady state volume/time graph. A value of 0.001 Pa was used for the viscosity of water.

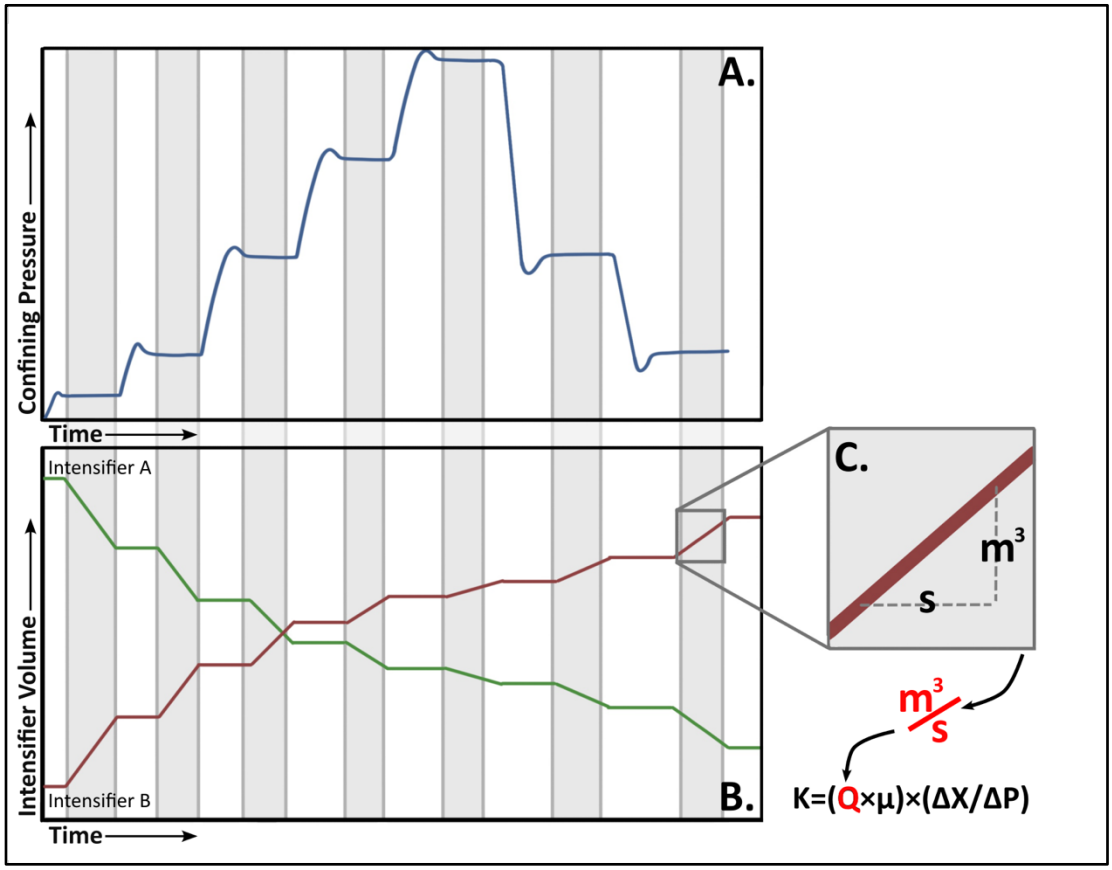

Figure 3.8: Example output graphs from data collected during permeability experiments. A. Time against confining pressure, B. Time against intensifier volume C. How this data was used to calculate permeability measurements

The permeability results contain errors over the measurement of the core as the diameter and length of the cored sample affect the result. Variance is calculated by using the maximum diameter with the minimum length for the minimum permeability and the minimum diameter with the maximum length is used to find maximum permeability.

3.2.4 Strength

The uniaxial compressive stress (UCS) of volcanic rocks has been studied to assess variations in the strength of rocks in these settings. The UCS has been shown to decrease as a function of porosity (Heap and Violay, 2021). Young's modulus represents the stiffness of a rock and describes the relationship between stress and strain. This is useful to determine how rocks will behave when deformed. The UCS tends to increase as a function of Young's modulus for all volcanic rocks (Heap and Violay, 2021).

Uniaxial compression strength (UCS) tests involve a cylindrical sample loaded axially at a constant rate while load and axial deformation is measured with time. Tests are used to gauge the yield and peak strengths of rocks as well as Young's modulus to make predications on the response of the rock under different conditions (Hawkes and Mellor, 1970).

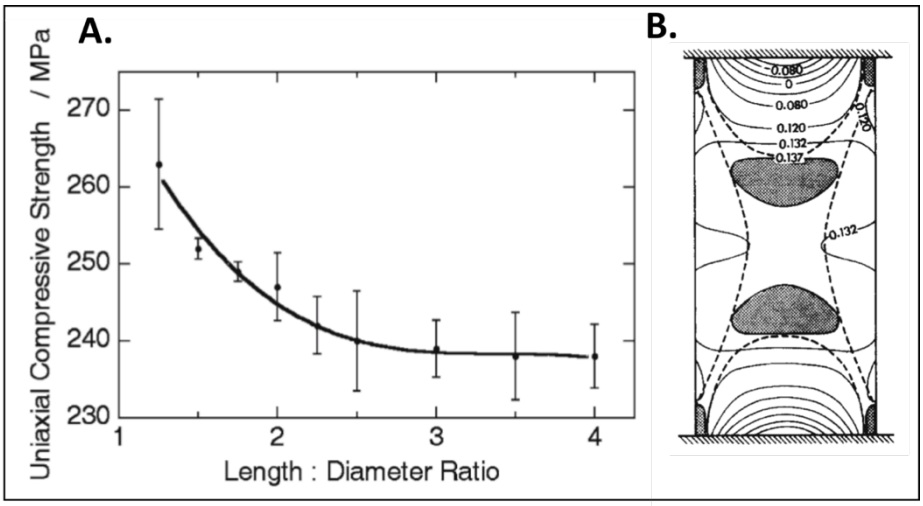

Figure 3.9: A. Dependence of UCS on L/D ratio B. Elastic stress distribution in uniaxial compression specimen (Paterson and Wong, 2005)

The sample length/diameter (L/D) ratio is important to consider when completing these tests. This is due to the frictional boundary effects where the sample is in contact with the pistons interfering with stress distribution across a sample (Figure 3.9B). These boundary effects impact the result of the test more the lower the L/D as indicated by Figure 3.9A. It is therefore recommended that the L:D should not be less than 2:1 or ideally 2.5:1 (Paterson and Wong, 2005). For the Ritter Island sample set, the longer cores were limited due to available sample size and therefore few tests could be performed.

The UCS apparatus involves a hydraulic press where the movement of the piston can be controlled by a set constant displacement rate. For all samples, this rate was kept the same

at 0.002 mm/s. This displacement is measured by a linear variable differential transformer (LVDT). The measured piston displacements are corrected for apparatus distortion.

Load and axial deformation are measured as the sample is loaded up at the constant rate. From this data alongside sample dimensions, stress strain plots can be made.
Strain is calculated by Equation 3.8. Stress is calculated by Equation 3.9.

Equation 3.8: Strain calculation using permeameter

Strain = displacement / initial length

Equation 3.9: Stress calculation using permeameter

Stress = load / sample cross-sectional area

The stress depends on the sample area and the strain depends on the sample length, both of which have small errors associated with the measurement. The apparatus is accurate to 0.13 kN. Variance is calculated using these factors.

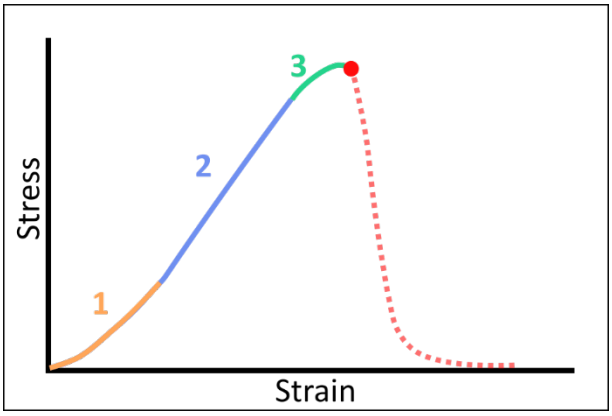

Figure 3.10: UCS stress-strain plot representing the different stages of compression. Adapted from Hawkes and Mellor (1970)

In a perfectly elastic material, a test will produce a constant stress strain graph. But in reality, results are often split into 3 main stages of deformation as represented in Figure 3.10 (Hawkes and Mellor, 1970). The first section has an increasing slope with increasing stress. This curve occurs due to the closing of cracks and pores under stress. This curvature stops in the second section where there is an approximate linear trend between stress and strain (Figure 3.10). This represents the elastic strain and its relationship describes the Young's modulus. As the graph approaches the maximum uniaxial strength, the plot should decrease in its stress-strain curve. This is where the rock has yielded and is associated with the formation of microcracks progressively reducing the load-bearing capacity of the rock causing

irreversible strain. When this curve approaches zero, the peak compressive strength of the rock is reached. As the test continues after this point, the rock will then fail (Figure 3.10).

3.3 Material property results

The results of the laboratory experiments outlined in this section will be discussed for the whole set and for each sample. Where SD samples are concerned, images and field descriptions are included as collected by Simon Day. Previous work by Ray (2017) will also be included here to help summarise the sample sets.

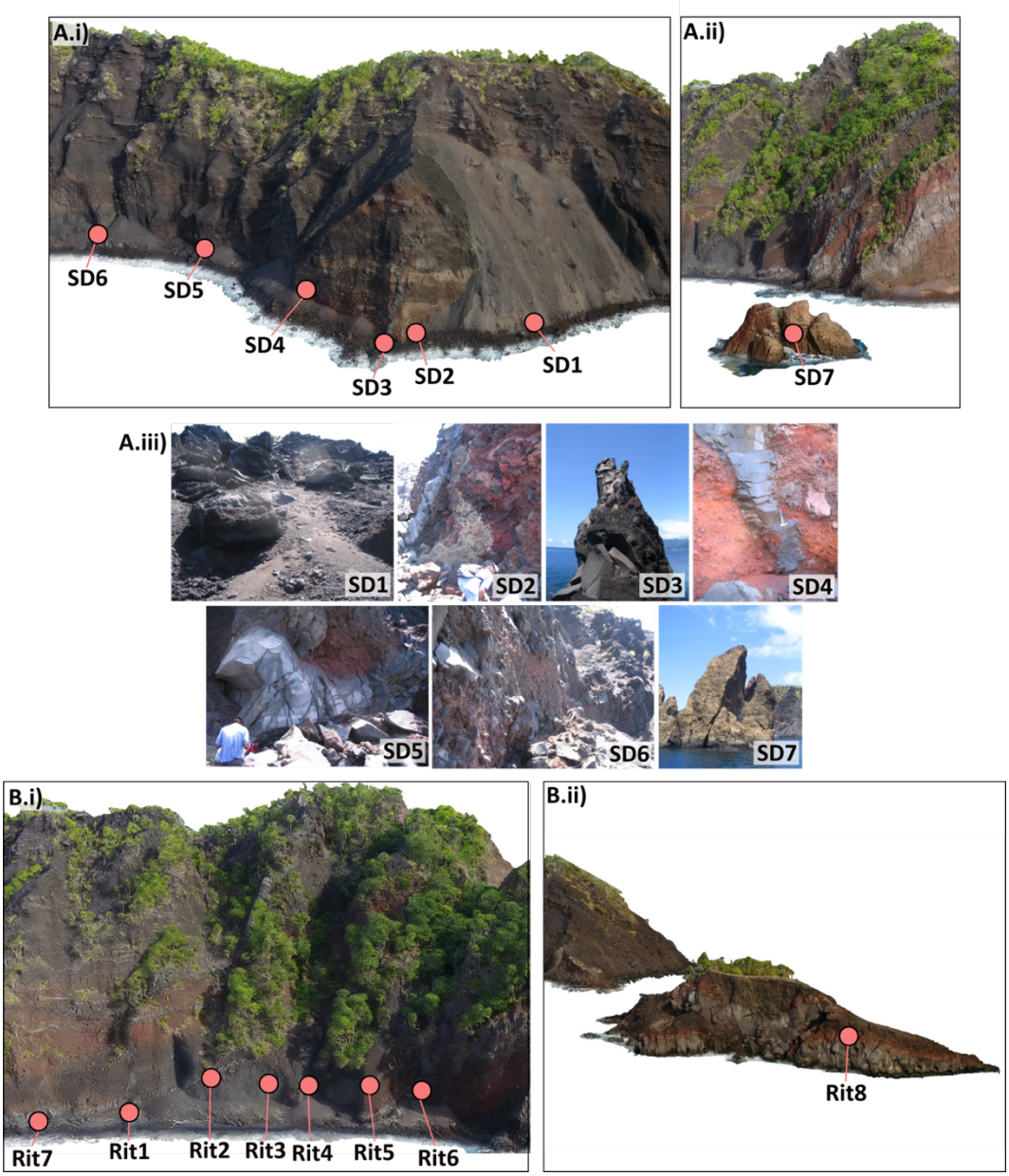

Figure 3.11: Subaerial sample locations placed on 3D model of Ritter Island A. SD samples in i) south cove and ii) central islet and iii) field photographs by Simon Day. B. Rit samples in i) the north cove and ii) the south islet.

The subaerial sample locations and field images are depicted in Figure 3.11. Examples of the cored samples used for hydraulic sample property measurements and their classification are in Figure 3.12. All sample results are summarised in Table 3.1.

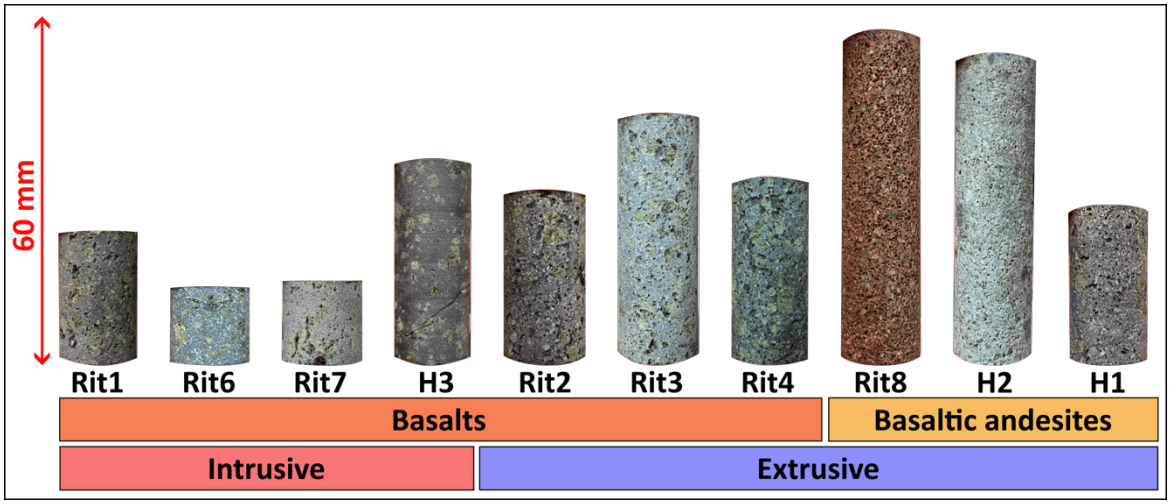

Figure 3.12: Showing examples of cored samples classified by origin and composition.

Table 3.1: All rock property measurement results of Ritter Island sample sets.

	POROSITY (%)			***DENSITY***	***PERMEABILITY AT***	***PEAK***	***YIELD***	***YOUNG'S***
SAMPLE	*2d porosity*	*Wax method*	*Pycnometer*	***(G/CM3)***	***5 MPA (M^2)***	***STRENGTH (MPA)***	***STRENGTH (MPA)***	***MODULUS (GPA)***
SD 1	22.23	30.3		3.13				
SD 2	18.09	18.4		3.07				
SD 3	0.00	2.4		2.77				
SD 4	2.65	10.4		2.98				
SD 5	7.64	14.0		2.89				
SD 6	6.49	14.1		2.97				
SD 7	8.94	26.1		3.03				
RIT 1	8.52		12.04 ±0.29	3.02	2.37×10^{-17} $\pm 1.15 \times 10^{-17}$			
RIT 2	14.73		16.65 ±0.10	2.99	5.44×10^{-17} $\pm 1.14 \times 10^{-17}$	56.16 ±0.85	53.00 ±1	13.41 ±0.32
RIT 3	11.13		13.82 ±0.64	2.99	2.30×10^{-14} $\pm 1.05 \times 10^{-15}$			
RIT 4	12.50		14.24 ±0.15	2.98	2.01×10^{-16} $\pm 4.10 \times 10^{-17}$			
RIT 5	4.83							

RIT 6	1.45	3.91 ±0.23	3.02	2.17 x10^{-17}±3.58x10^{-18}			
RIT 7	4.65	8.16 ±0.28	3.00	4.32 x10^{-16}±3.50x10^{-17}			
RIT 8	19.81	23.40 ±2.49	2.84	1.66 x10^{-13}±1.44x10^{-15}	34.24 ±0.75	32.50 ±1	10.33 ±0.04
H1		12.47 ±0.17	5.03	5.65 x10^{-18} ±3.20x10^{-18}			
H2		17.76 ±2.31	2.94	6.78 x10^{-18} ±9.65x10^{-19}	64.63 ±0.75	58.00 ±1	19.93 ±0.30
H3		2.35 ±1.99	2.96	1.77 x10^{-17} ±2.30x10^{-18}	92.86 ±0.8	78.00 ±1	18.39 ±2.70

3.3.1 Petrology

XRF analysis categorised the compositions of all three sample sets to be within the range for basalts to basaltic andesites. Figure 3.13 shows the Total Alkalis vs. Silica (TAS) plotted to highlight these compositions. The intrusion samples in this dataset are all basalts, whereas the lavas range between basalts and basaltic andesites.

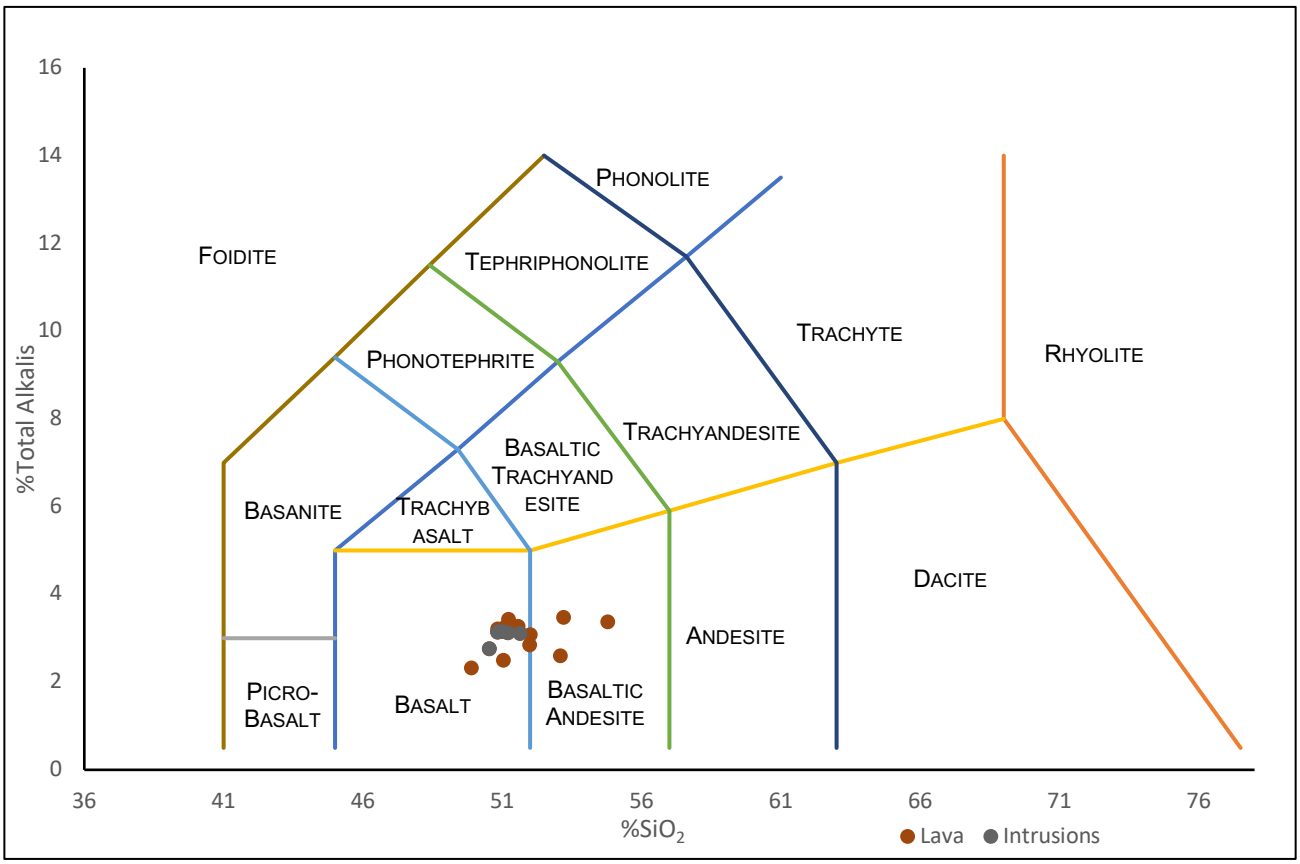

Figure 3.13: TAS diagram displaying compositions of all Ritter Island samples

3.3.2 Porosity

Different methods of calculated porosity across the Ritter sample sets were used due to size limitations on samples as discussed in section 3.2.2. Where possible, the pycnometer method was used with the cored samples to get the most accurate results. This was possible for all of the H samples and most of the Rit samples (Table 3.1). By analysing the thin sections using ImageJ, a percentage content between groundmass, crystals and pore space was calculated (Figure 3.14).

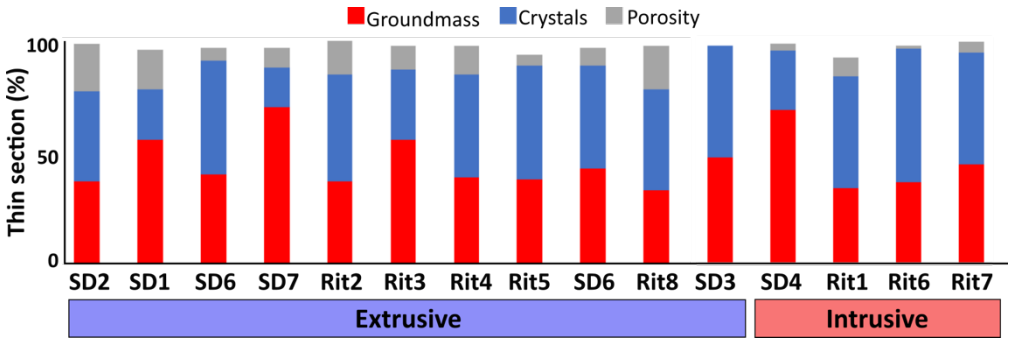

Figure 3.14: Thin section analysis results from SD and Rit samples in terms of % content.

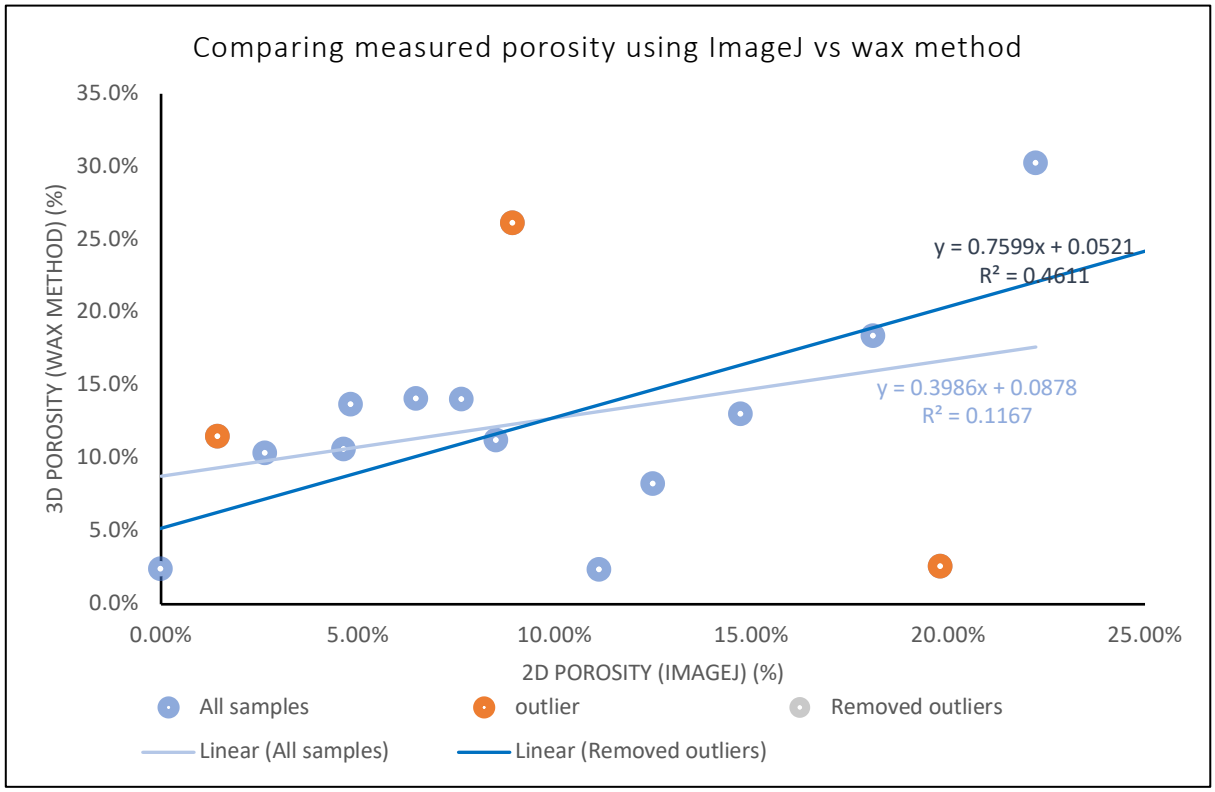

Figure 3.15: Porosity results using the Image J 2D analysis vs the wax pycnometer method, highlighting the outliers (which differ more than 10% from each method) and displaying trend lines with and without outliers.

Table 3.2: Effective porosity measurements using Helium Pycnometer on sample cores highlighting variance

Sample	Cores			Sample average		
	Effective porosity	minimum	maximum	Average porosity	minimum	maximum
Rit 1	**12.04%**	11.74%	12.31%	**12.04%**	11.74%	12.31%
Rit 2	**16.65%**	16.52%	16.73%	**16.65%**	16.52%	16.73%
Rit 3	**13.98%**	13.38%	14.65%	**13.82%**	13.38%	14.65%
	13.89%	13.45%	14.23%			
	13.58%	13.39%	13.92%			
Rit 4	**14.24%**	14.13%	14.43%	**14.24%**	14.13%	14.43%
Rit 6	**3.91%**	3.65%	4.10%	**3.91%**	3.65%	4.10%
Rit 7	**9.29%**	8.80%	9.63%	**8.16%**	6.77%	7.34%
	7.02%	6.77%	7.34%			
Rit 8	**26.36%**	26.31%	26.41%	**23.40%**	21.43%	26.41%
	21.76%	21.43%	22.04%			
	22.06%	22.02%	22.12%			
H1	**12.47%**	12.31%	12.64%	**12.47%**	12.31%	12.64%
H2	**19.30%**	18.90%	19.80%	**17.76%**	15.17%	19.80%
	17.12%	17.10%	17.15%			
	15.26%	15.17%	15.43%			
	19.37%	19.08%	19.68%			
H3	**1.76%**	1.59%	1.85%	**2.35%**	0.60%	4.57%
	1.84%	1.58%	2.09%			
	3.45%	0.60%	4.57%			

By comparing all the results from the ImageJ analysis and the wax pycnometer method, there is a weak positive trend which suggests the wax method overestimates the porosity relative to the images (Figure 3.15). The three outliers highlighted are the samples where the measured porosity from the wax method and ImageJ differ by over 10%. This may be as a result of a thin section or rock sample having very different porosities, as often within lavas porosity may increase close to the surface of the flow. Alternatively, it is due to an error with the method. If these outliers are discounted, then a stronger positive relationship is observed (Figure 3.15). When comparing the wax method to the core pycnometer method, there is no clear trend in the results again with multiple outliers. Although the wax method appears to be accurate when comparing to the measurements made from the core pycnometer or ImageJ method, these results show that the wax method can involve high levels of error and thus the results on their own may not be valid.

When comparing the results from the ImageJ analysis and the core pycnometer method, ie the 2D (x) vs 3D (y) porosity, we see a very strong correlation (Figure 3.16). This trend shows the 2D analysis method underestimates the 3D porosity consistently by around 2.8%. We can use this trend to estimate the 3D porosities for the SD samples where that was not enough material to produce a core, and as such only could produce a thin section that only had Image J analysis. Across all the samples for Ritter Island, the maximum porosity measured was 25% and the minimum was 2% with an average of 12%.

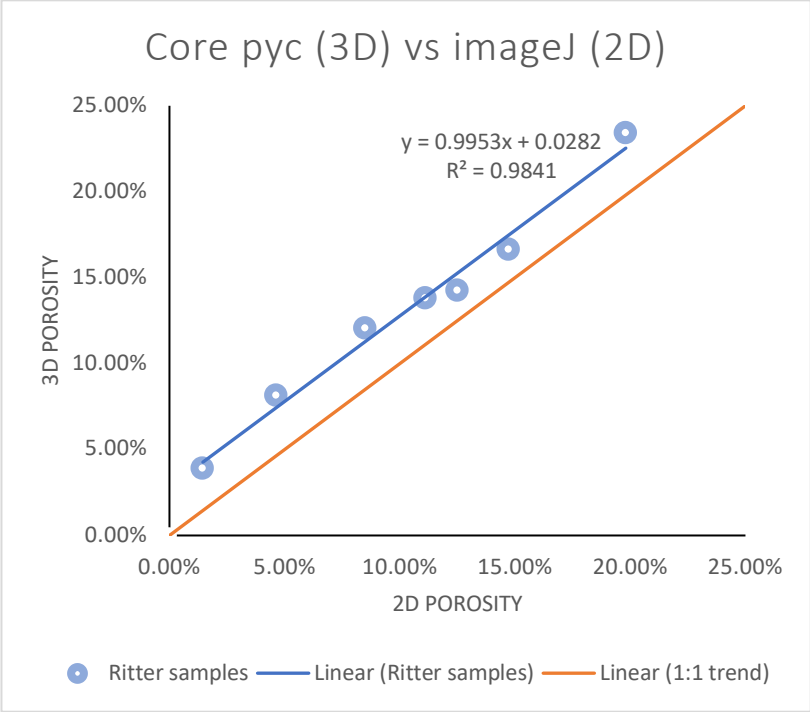

Figure 3.16: Comparing methods of measuring porosity for 2D (Image J) and 3D (pycnometer).

3.3.3 Permeability

Table 3.3: Permeability results on Ritter samples highlighting varience

Mpa	Rit1	min	max	Rit2	min	max	Rit3.2	min	max	Rit4	min	max
5	**2.37E-17**	1.22E-17	3.52E-17	**5.44E-17**	4.31E-17	6.58E-17	**4.61E-14**	4.50E-14	4.71E-14	**2.01E-16**	1.60E-16	2.42E-16
10	**2.12E-17**	8.54E-18	3.39E-17	**5.51E-17**	5.25E-17	5.78E-17	**4.90E-14**	4.81E-14	4.98E-14	**8.67E-17**	6.34E-17	1.10E-16
20	**7.32E-18**	5.88E-18	8.78E-18	**4.00E-17**	3.77E-17	4.24E-17	**4.24E-14**	4.21E-14	4.26E-14	**4.01E-17**	3.54E-17	4.49E-17
30	**3.92E-18**	2.58E-18	5.27E-18	**3.09E-17**	2.20E-17	3.99E-17	**3.83E-14**	3.64E-14	4.01E-14	**2.40E-17**	2.00E-17	2.79E-17
40	**2.66E-18**	1.54E-18	3.79E-18	**1.37E-17**	1.32E-17	1.43E-17	**3.94E-14**	3.90E-14	3.99E-14	**2.13E-17**	2.08E-17	2.17E-17
Mpa	**Rit6**	**min**	**max**	**Rit7**	**min**	**max**	**Rit8**	**min**	**max**	**H1**	**min**	**max**
5	**2.17E-17**	1.81E-17	2.53E-17	**4.32E-16**	3.97E-16	4.67E-16	**1.66E-13**	1.64E-13	1.67E-13	**5.65E-18**	2.45E-18	8.85E-18
10	**9.51E-18**	3.66E-18	1.54E-17	**2.83E-16**	2.60E-16	3.07E-16	**3.61E-13**	3.58E-13	3.63E-13	**3.93E-18**	2.93E-18	4.92E-18
20	**4.47E-18**	3.98E-18	4.96E-18	**1.33E-16**	1.17E-16	1.63E-16	**1.26E-13**	1.24E-13	1.27E-13	**1.99E-18**	1.79E-18	2.19E-18
30	**2.38E-18**	1.68E-18	3.09E-18	**6.25E-17**	5.82E-17	7.32E-17	**3.10E-13**	3.09E-13	3.10E-13	**1.27E-18**	1.11E-18	1.42E-18
40	**1.32E-18**	1.21E-18	1.42E-18	**3.23E-17**	2.90E-17	3.89E-17	**1.14E-13**	1.13E-13	1.14E-13	**9.00E-19**	4.93E-19	1.31E-18
Mpa	**H2**	**min**	**max**	**H3.2**	**min**	**max**	**H3.3**	**min**	**max**	**Rit3.3**	**min**	**max**
5	**6.78E-18**	5.81E-18	7.74E-18	**2.16E-20**	1.81E-22	2.51E-20	**3.54E-17**	3.35E-17	3.81E-17	**9.39E-18**	9.39E-18	1.03E-17
10	**6.03E-18**	2.55E-18	9.53E-18	**4.38E-21**	1.70E-23	7.07E-21	**1.70E-17**	1.64E-17	1.80E-17	**9.57E-18**	9.57E-18	9.87E-18
20	**6.68E-18**	5.92E-18	7.45E-18				**2.22E-18**	1.93E-18	2.56E-18	**2.91E-18**	2.91E-18	3.76E-18
30	**4.42E-18**	3.95E-18	4.89E-18				**5.06E-19**	2.59E-19	7.72E-19	**4.05E-18**	4.05E-18	4.58E-18
40	**3.58E-18**	1.75E-18	5.41E-18				**1.75E-19**	2.59E-19	2.99E-19	**4.98E-18**	4.98E-18	5.87E-18

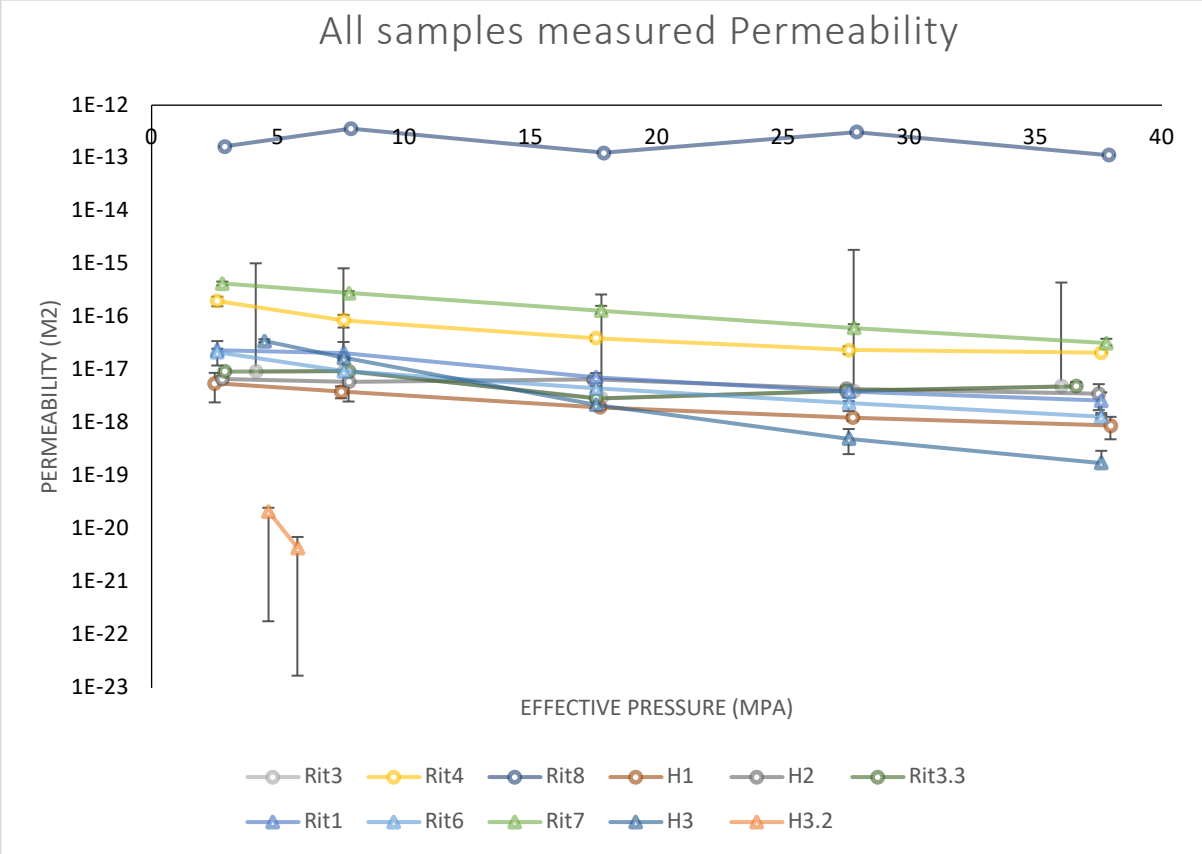

Figure 3.17: Permeability measured on Ritter Island sample sets. Triangular markers are used for samples from intrusions and circular markers are used for extrusive samples.

The permeability was measured across 12 of the sample set (Table 3.3). The general trend across all samples is that there is a decrease in permeability with an increase of effective pressure (Figure 3.17). At 5 MPa confining pressures, the measured permeabilities range from $1.7x10^{-13}$ to $2.2x10^{-20}$ m^2. This is a wide range of permeabilities, however most Ritter samples

fall between $1x10^{15}$ and $1x10^{18}$ m^2. Rit8 is by far the most permeable sample, which fits with it being also highly porous but it is also the only sample which displays obvious alteration. H3.2 is almost impermeable at $2.2x10^{-20}$ m^2 at 5MPa. However, a second sample with fractures along the long axis of the core was tested and showed a much higher permeability of $3.5x10^{17}$ m^2 suggesting the presence of the fractures is significant. The samples were also measured in conditions at 10 and 20 MPa confining pressures after having reached 40 MPa and this found that in most samples some hysteresis is observed.

When this measured permeability, at 5 MPa confining pressures, is plotted against the porosity measurements, a positive correlation is observed (Figure 3.18). This trend was used to estimate the permeability of the samples which were not large enough for cores to be obtained.

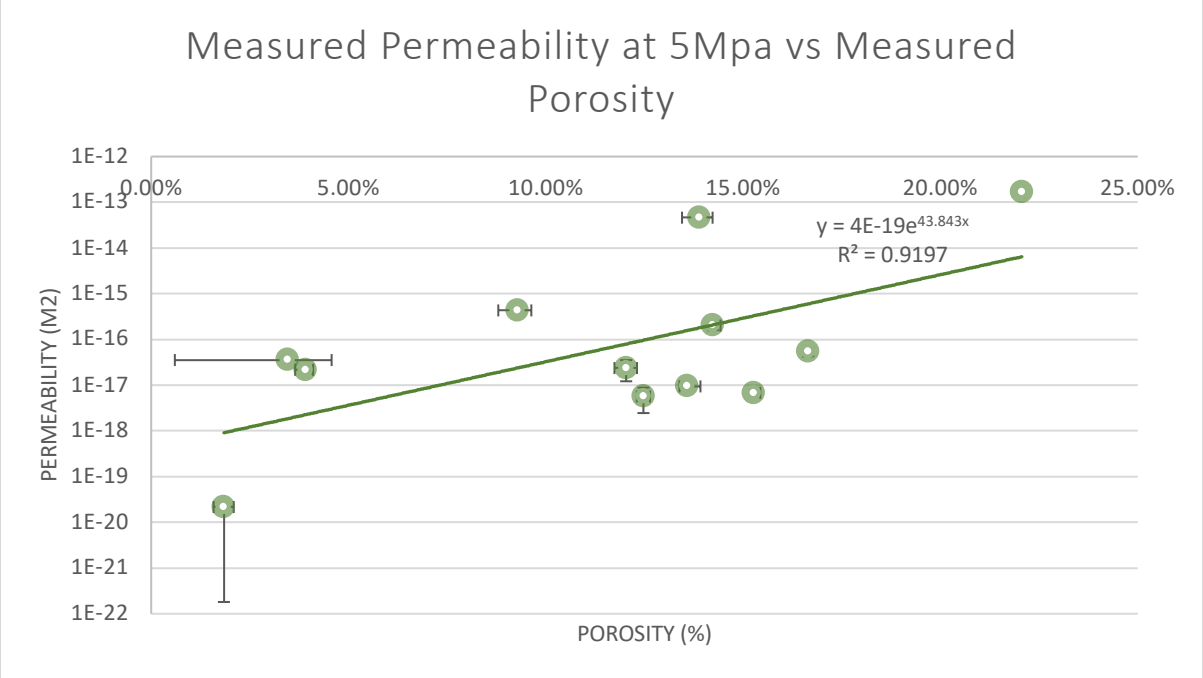

Figure 3.18: Relationship between measured porosity and measured permeability.

By using the 2D to 3D porosity relationship from Figure 3.16, 3D porosities can be estimated for the samples that were not big enough to obtain a core. From using the relationship between porosity and permeability at 5 MPa in Figure 3.18, the missing permeability measurements for these samples can be inferred. The standard error of regression was calculated from using this trend so the variance for these inferred results is $1 x10^{-15}$ m^2. The 5 MPa results were used to compare the properties of the rocks as close to surface pressure as possible. The trends from the increasing pressures are similar across all the samples and

therefore this measurement provides a good comparison. By comparing this measured porosity and permeability data to previously published datasets, a selection of porous andesites (Heap and Kennedy, 2016) and a range of volcanic rocks from Iceland (Eggertsson et al., 2020), a similar trend can be observed of increasing permeability with porosity (Figure 3.19). This data also shows a much wider range of permeabilities at medium to lower porosities where the Ritter results mainly lie.

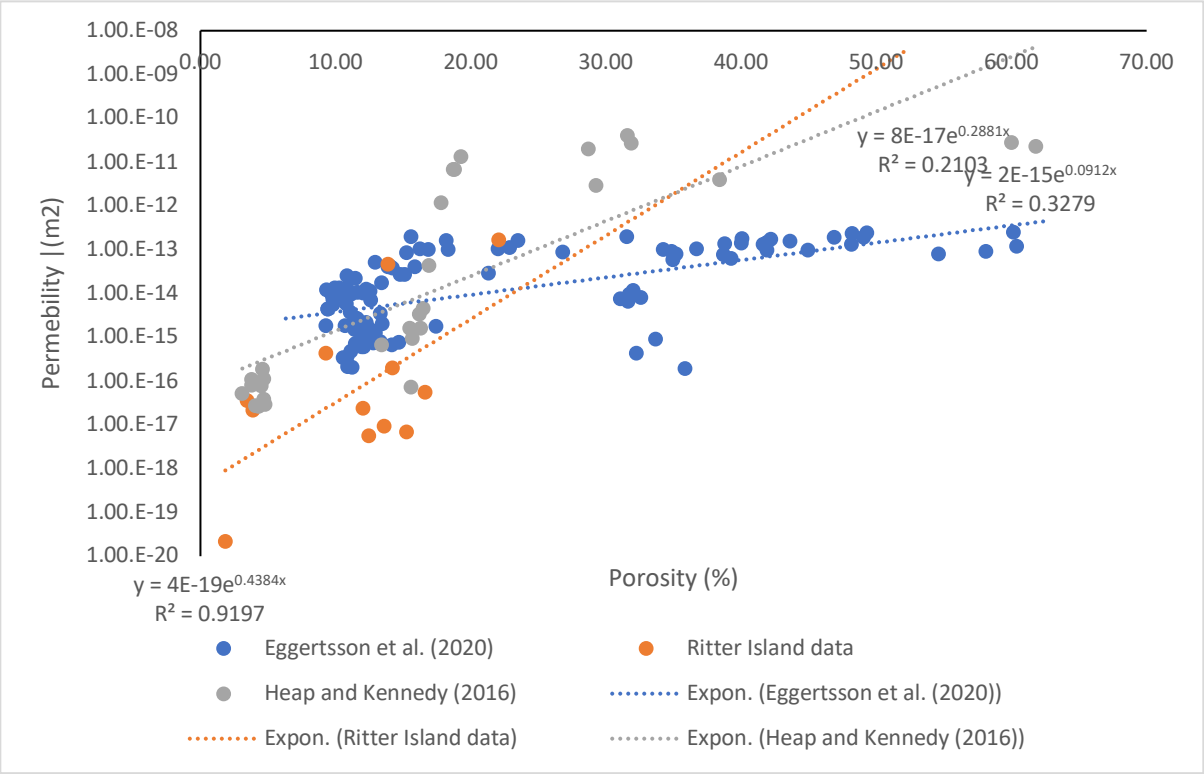

Figure 3.19: Comparing data from Ritter Island with previously published data from Heap and Kennedy (2016) (Heap and Kennedy, 2016) and Eggertsson et al. (2020) by plotting permeability against porosity.

3.3.4 Strength

Minimal material was available to collect strength measurements on from the sample set and only three fresh samples were used. Some samples that had been measured for permeability were tested in addition to estimate a strength for some samples. These may be less accurate due to changes due to hydrostatic compaction in the rocks structure after reaching 40MPa confining pressures in the permeability experiments. H2 was tested twice to assess the repeatability of the results and the amount of sample allowed a duplicate measurement to be taken. In Figure 3.20, Rit8 was tested twice, once using an unaffected core and once using the core that had been tested in the permeameter, denoted 'Rit8perm'. This sample shows a slightly stronger maximum stress than the unaffected sample. Therefore, the results for Rit 2 and H3 may be affected in a similar manner. The variance of the peak stress results was calculated based on the error associated with the measurement of the samples and the accuracy of the equipment (Table 3.4).

Table 3.4: Peak stress of Ritter samples showing variance in results

Sample	Peak stress (Mpa)	min	max
Rit 2	56.2	55.1	56.8
Rit 8	34.2	33.5	35.0
Rit 8	51.6	50.8	52.3
H2	59.9	59.1	60.6
H2	69.4	68.5	70.0
H3	92.9	92.0	93.6

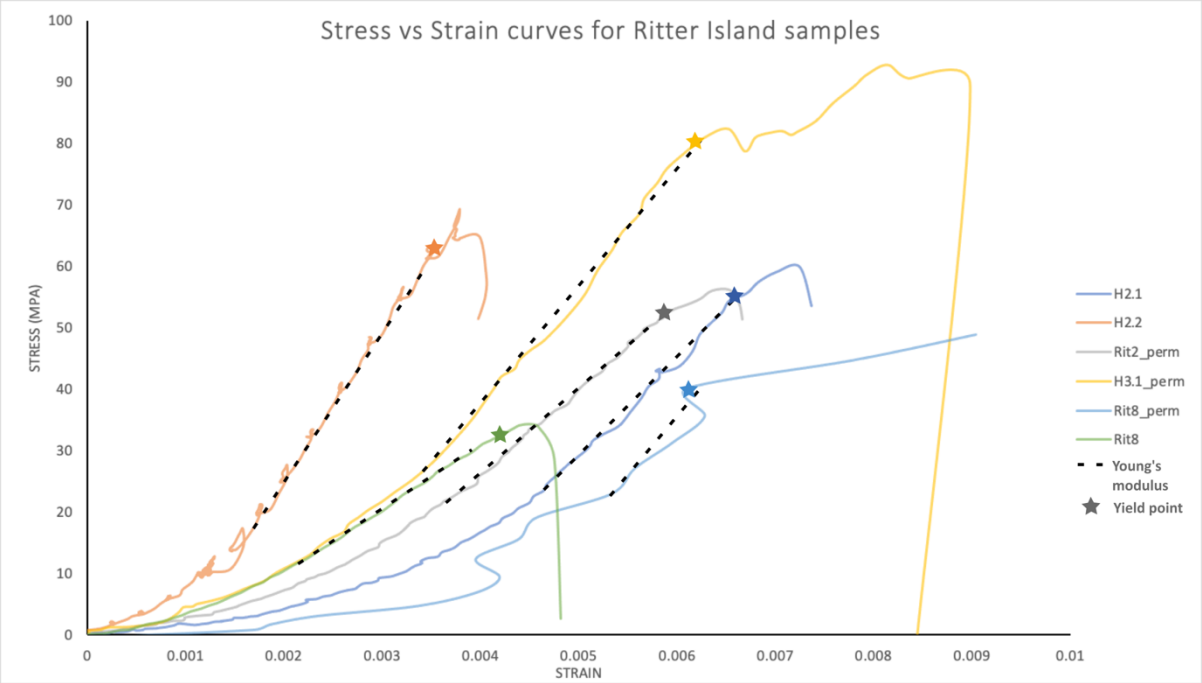

Figure 3.20: Stress vs. strain curves for all uniaxial Ritter Island sample experiments. '_perm' denotes samples that had previously been used in the permeability experiments,

Across all of these results the yield strengths ranged from 32.5 to 78 MPa and peak strengths ranged from 34.2 to 92.6 MPa. The Young's modulus ranged between 10 and 24 GPa. The highest uniaxial compressive strength measured was for H3, an intrusive sample and the lowest was for Rit8, a highly altered porous lava sample (Figure 3.20). The results for the less altered lavas tested, Rit2 and H2 show a much higher strength but less than that of the dyke strength. There is a positive correlation between the Young's modulus and the uniaxial compressive strength (UCS) (Figure 3.21). When assessing the relationship between the porosity and the UCS, a strong negative correlation is observed meaning that the more porous the rock, the weaker it is (Figure 3.23). In addition, by observing the trend between Young's modulus and porosity, an increase of porosity tends to mean the rock will behave more elastically under stress (Figure 3.22).

These relationships are compared to a compiled dataset of a range of volcanic rocks by Heap and Violay (2021) in Figure 3.24. The results from mechanical property experiments on the Ritter Island samples agree with the trends from this data and lies mostly within the mid-range of expected values. The trend in Figure 3.22 suggests there is an outlier from this set of results, being one of the two H2 experiments. However, when comparing these results to the wider dataset in Figure 3.24B, all of the Ritter data plots lie within the expected results. One sample that has very low porosity, H3, has lower than generally expected uniaxial compressive strength and Young's modulus as it lies on the outer edges of the range of data from by Heap and Violay (2021).

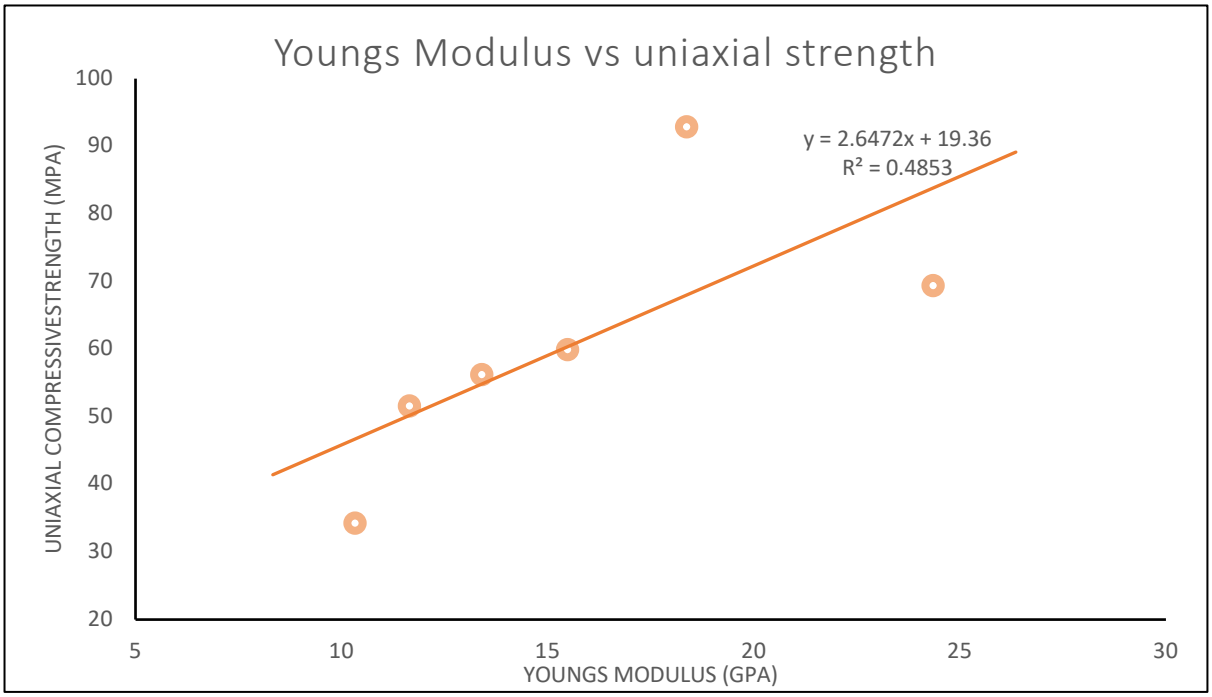

Figure 3.21: Relationship between measured Young's modulus and Uniaxial Compressive Strength.

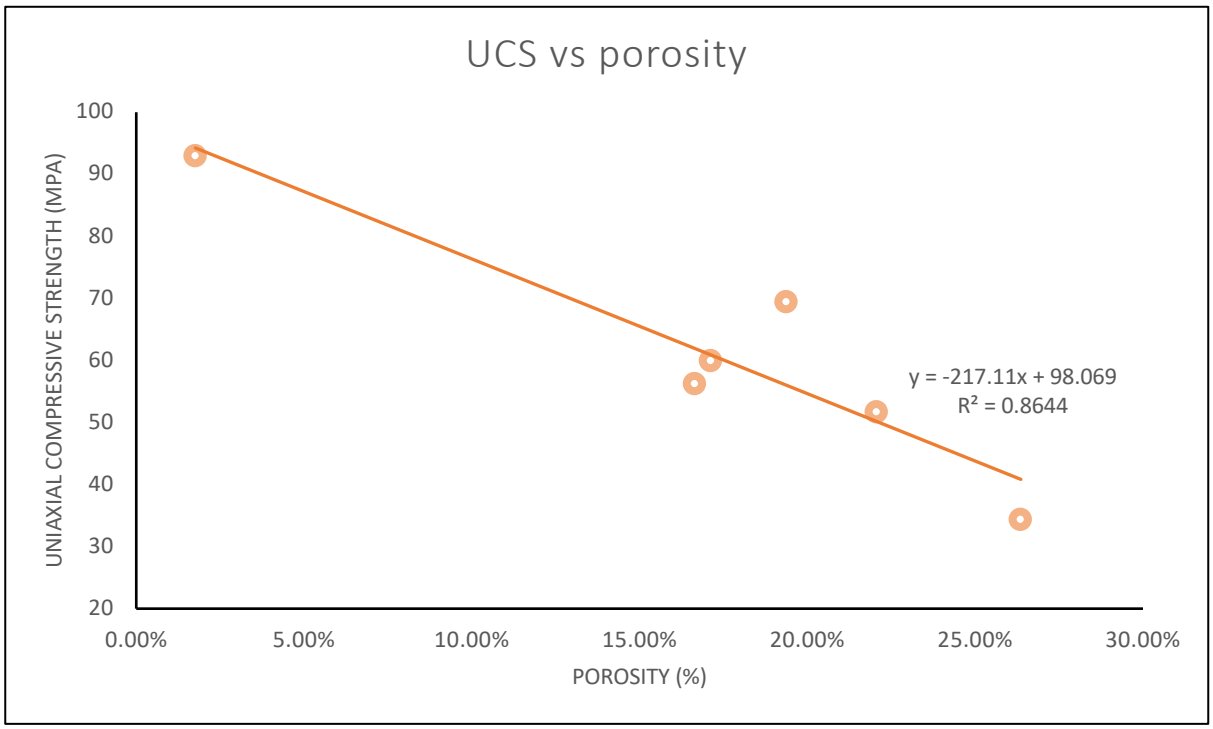

Figure 3.23: Relationship between measured Porosity and Uniaxial Compressive Strength.

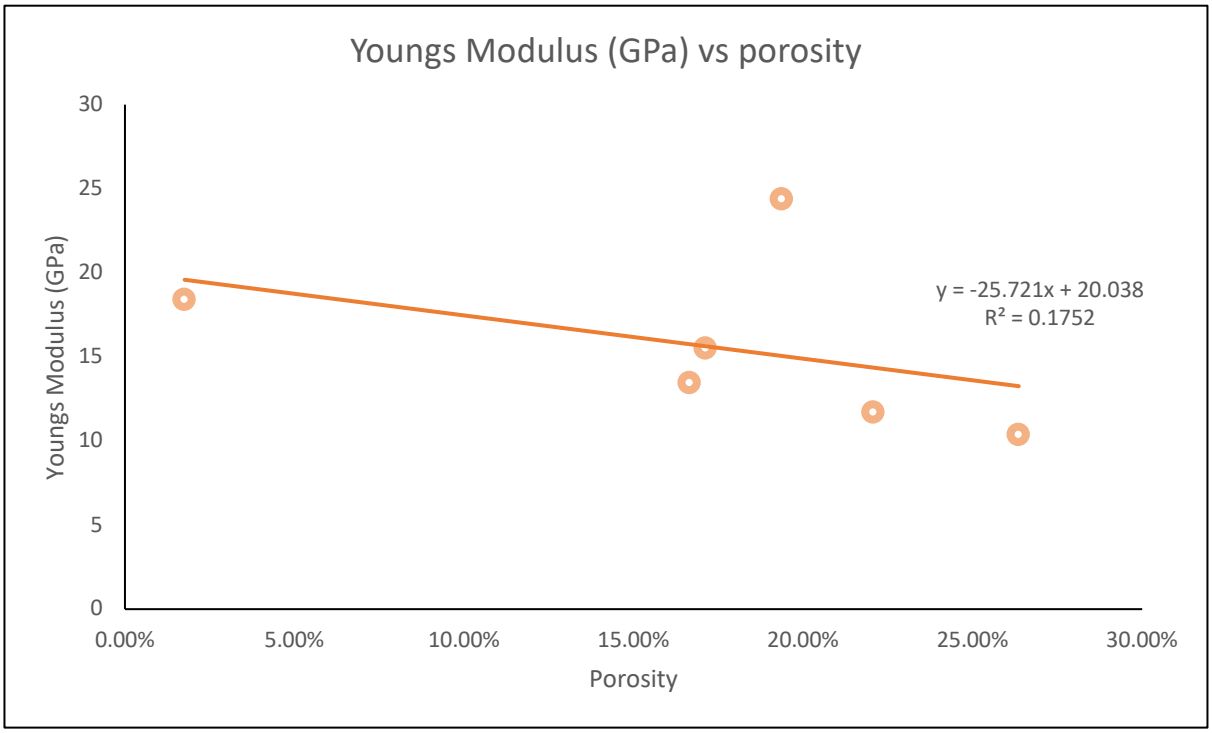

Figure 3.22: Relationship of measured porosity against Young's modulus.

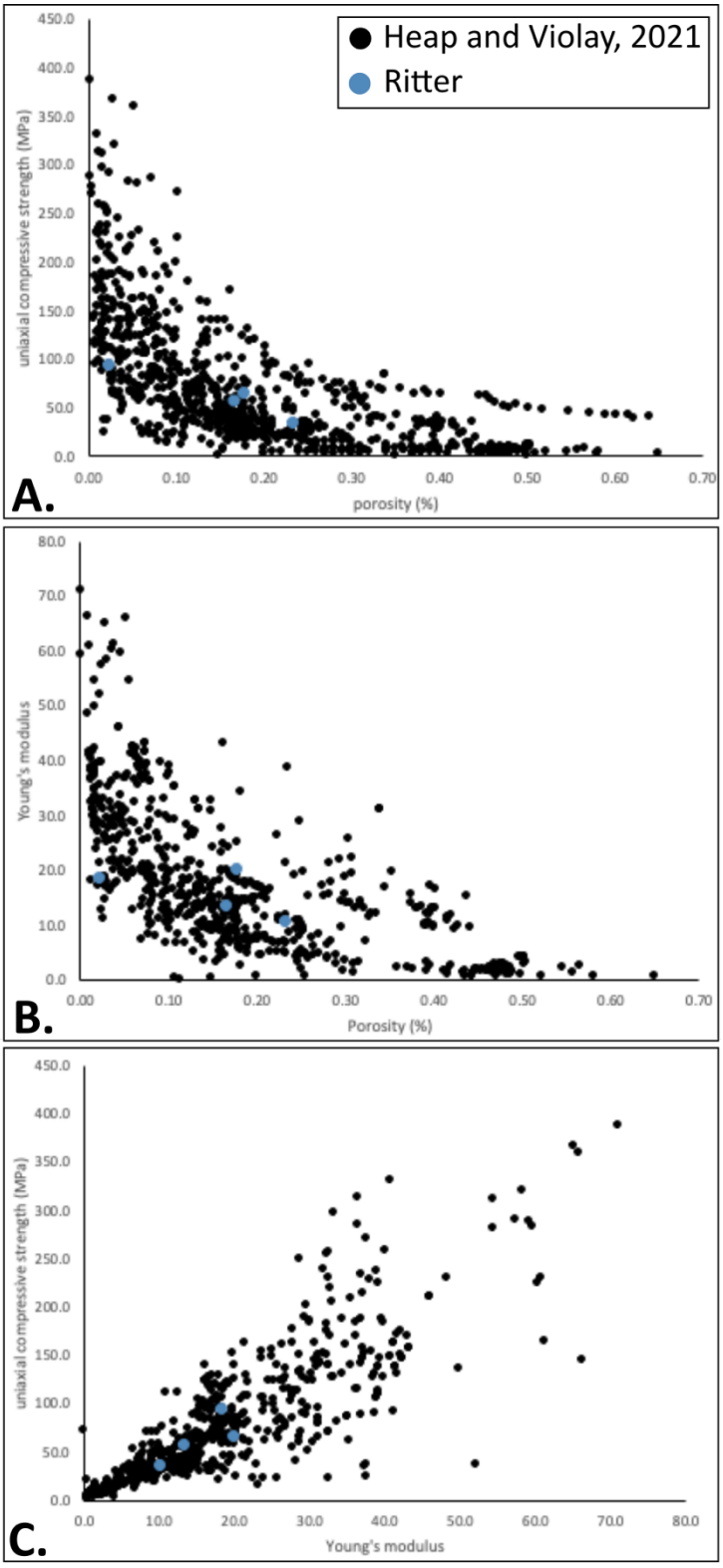

Figure 3.24: Comparing compilation of volcanic rock properties from Heap and Violay, 2021 with the results from Ritter. A. Porosity against uniaxial compressive strength. B. Porosity against Young's modulus. C. Young's modulus against uniaxial compressive strength.

3.3.5 Texture and mechanical properties of individual samples

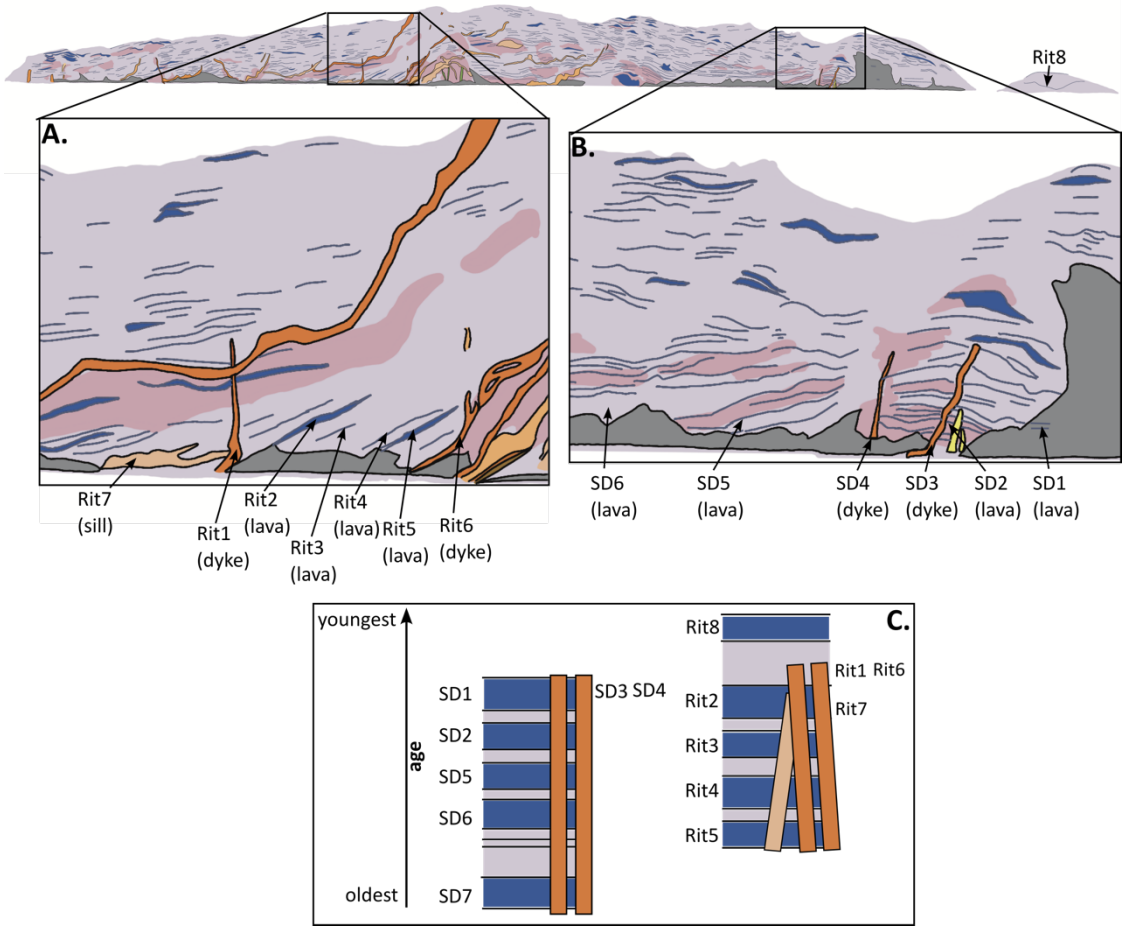

Figure 3.25: Sketch of western side of Ritter map with sample localities. A. Showing Rit sample sites B. showing SD sample sites C. Estimated relative ages of subaerial samples.

Figure 3.25 highlights the sampled locations for the intrusions and lavas from the Rit and SD sample sets on the western side of Ritter Island and their relative ages based on cross-cutting relationships. The microstruture and porosity was investigated for each of these rocks and the reults for their mechanical properties are summarised below.

3.3.5.1 Lavas

SD1: Basaltic Lava

Texture

SD1 is a basaltic lava with a rubbly top and base with low vesicularity core sampled from large scree slope on the south of the main island (Figure 3.11A, Figure 3.25). This sample was taken from the flow core from a block below inferred spatter-fed lava flows. The sample is quite vesicular suggesting it was from the rubbly top of the flow, with varying sized vesicles with an average of 0.5 mm, the largest being 1 mm. There are also large crystals and crystal

aggregates. Pyroxenes are the most abundant phenocryst with smaller plagioclases and rarer olivine.

Properties

From ImageJ analysis, vesicles account for 22% of this thin section (Figure 3.26). The vesicle shapes are generally sub-circular throughout the sample. Using the wax pycnometry method, the porosity is calculated at 30.3%. This may be higher than expected as, using the trend from Figure 3.16, the value for porosity is estimated at 24.9%. Using this latter porosity estimation and the relationship between porosity and permeability from Figure 3.18, the permeability of this lava flow at 5MPa is estimated to be relatively low at 2.24×10^{-14} m^2.

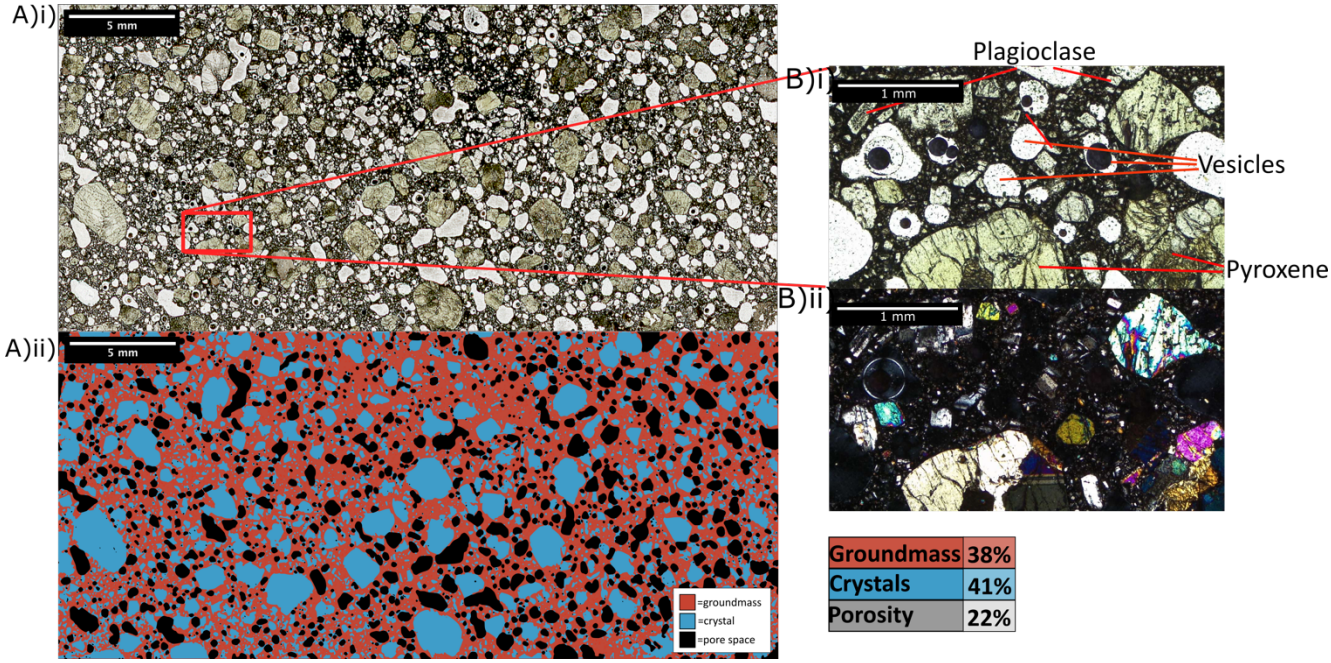

Figure 3.26: SD1 thin section analysis A.i) whole section and ii) ImageJ map, B. zoomed in portion in i) plane polarised light and ii) crossed polars. Percentage of area representing groundmass, crystals and porosity displayed.

SD2: Basalt Lava

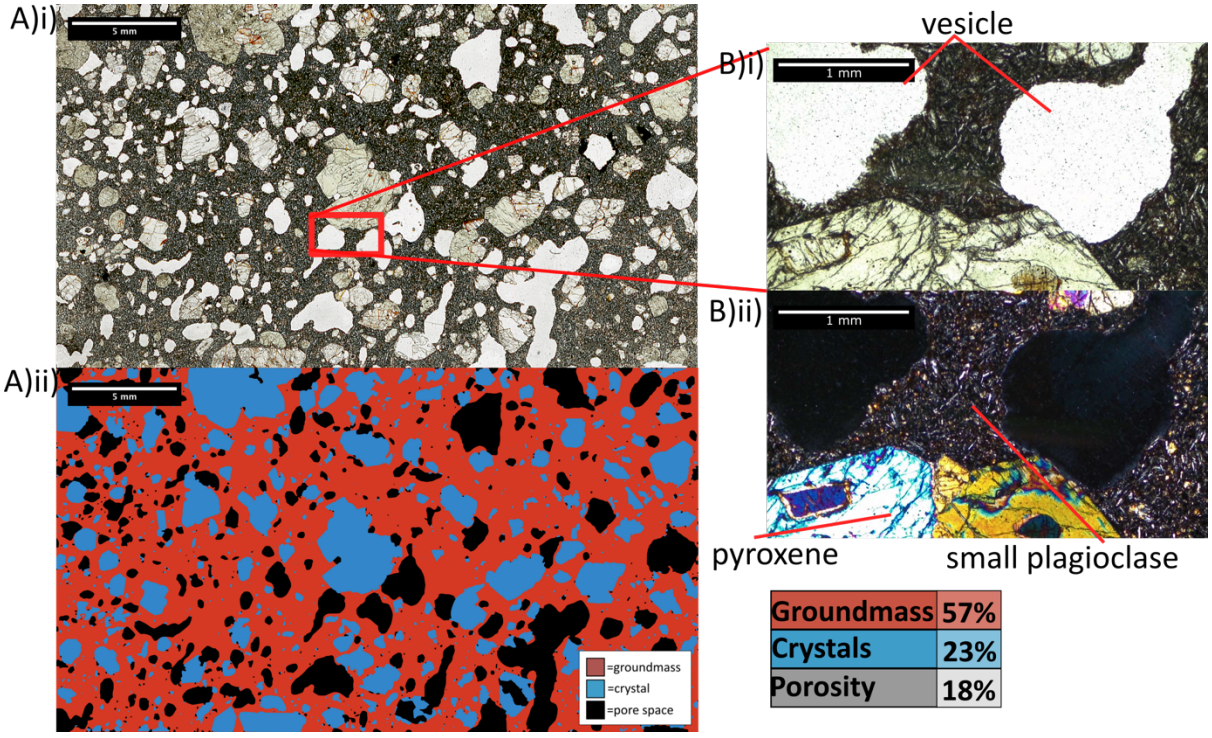

Figure 3.27: SD2 Thin section analysis A.i) whole section and ii) ImageJ map, B. zoomed in portion in i) plane polarised light and ii) crossed polars. Percentage of area representing groundmass, crystals and porosity displayed.

Texture

SD2 is a basaltic lava sampled from an altered rubbly lava flows adjacent to clastic dyke (mapped as dyke 41) and prominent dyke (mapped as dyke 37 and sample SD3) (Figure 3.11A, Figure 3.25). The vesicles are sporadic, bulbous and large in the central region with an average major axis of 2 mm but in some areas, vesicles are smaller and more clustered with an average width of 0.6 mm. This variation in size clearly seen in Figure 3.27A. The phenocrysts are sparse but large and often rounded aggregates of mainly pyroxene and some olivine up to 5 mm along their major axis. The groundmass dominates the thin section image and is glassy with some small plagioclase (Figure 3.27B).

Properties

From ImageJ analysis, the vesicles make up 18% of the area. From the wax pycnometry method, the porosity is 18.4% and from the 2D vs. 3D relationship, the 3D porosity is similarly estimated at 20.8%. Using the relationship between porosity and permeability from Figure 3.18, the permeability of this lava flow at 5MPa is estimated to be 3.70×10^{-15} m^2.

SD6: Basalt Lava

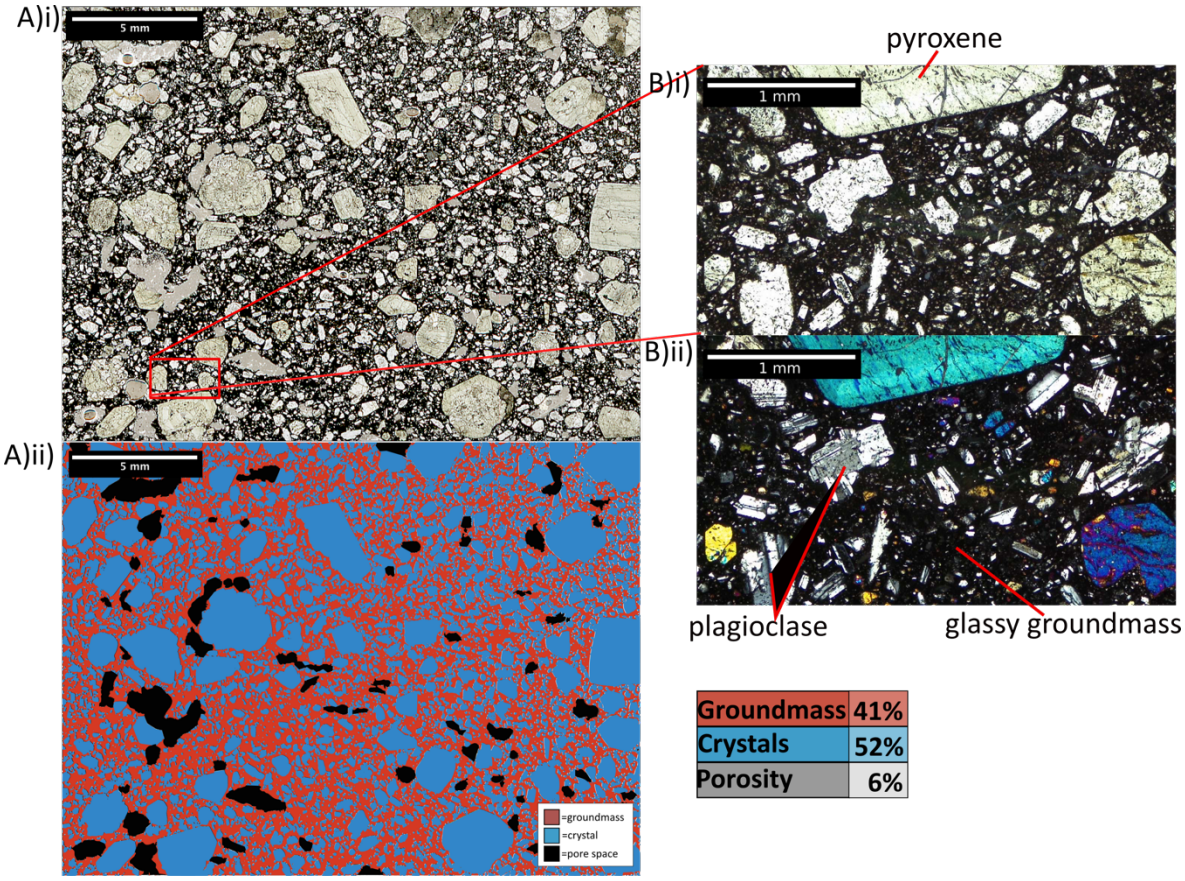

Figure 3.28: SD6 Thin section analysis A.i) whole section and ii) ImageJ map, B. zoomed in portion in i) plane polarised light and ii) crossed polars. Percentage of area representing groundmass, crystals and porosity displayed.

Texture

SD6 is a basaltic lava sampled from altered eastly dipping lavas at base of cliff. This area may have been covered by talus apron at the base of the cliff in model (Figure 3.11A, Figure 3.25). It is porphyritic, has a glassy groundmass, phenocrysts of pyroxene and some olivine within crystal aggregates and many smaller plagioclase crystals.

Properties

Vesicles are present but sporadic with an average major axis of 0.73 mm, giving it an apparent 2D porosity of 6%. The wax method gives a porosity of 14.1% and the 3D relationship estimates a 3D porosity of 9.28%. Using this estimate and the relationship between porosity and permeability, the permeability of this lava flow at 5MPa is estimated to be 2.34×10^{-17} m^2.

SD7: Basalt Lava

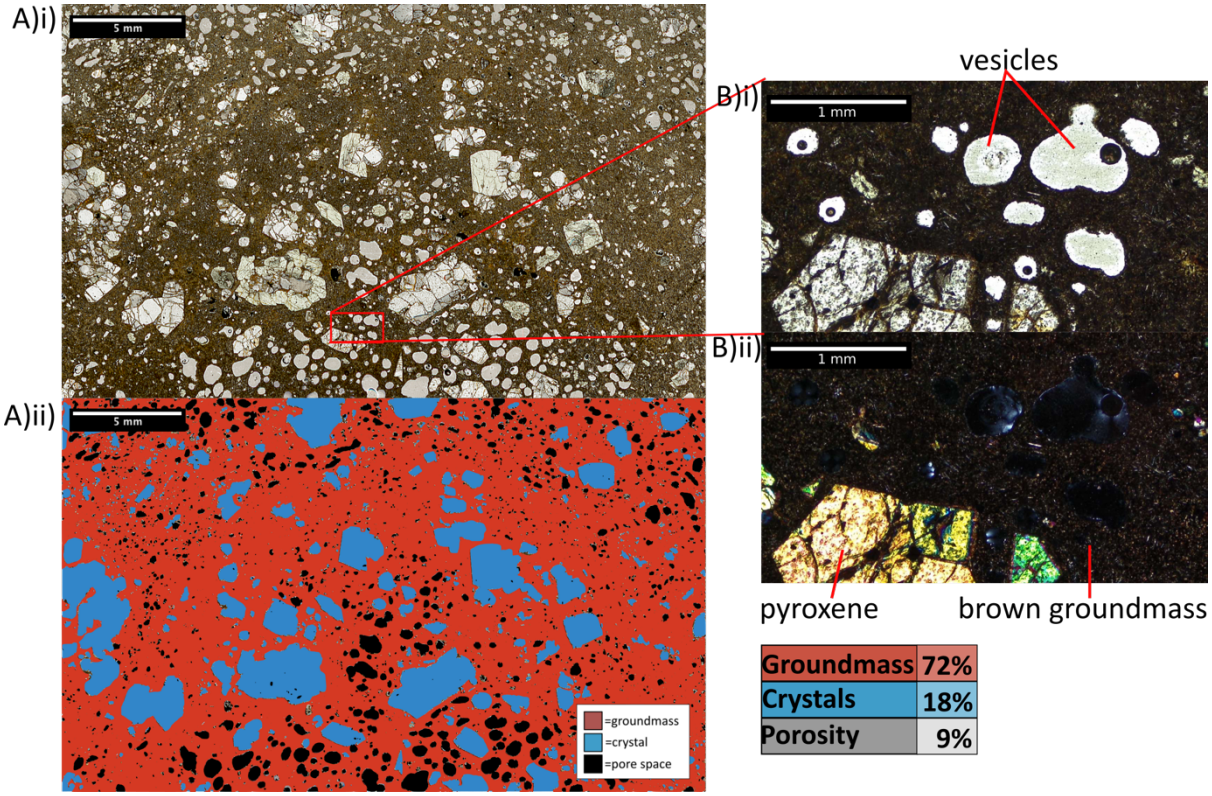

Figure 3.29: SD7 Thin section analysis A.i) whole section and ii) ImageJ map, B. zoomed in portion in i) plane polarised light and ii) crossed polars. Percentage of area representing groundmass, crystals and porosity displayed.

Texture

SD7 is a basaltic scoria clast sampled from small islet offshore of central cusp (Figure 3.11, Figure 3.25) containing bedded phreatomagmatic tuff. The islet is mainly composed of bedded yellow hyaloclastite tuffs, formed by brecciated lava formed during quenching when in contact with water, with laminae of coarser scoriaceous clasts dipping to the N-NE and is cut by N-S trending grey dyke. It is porphyritic but consists mainly of groundmass which is very fine and has a brown tinge due to alteration. The phenocrysts are pyroxenes and olivine and some aggregates. The groundmass contains small needle-shaped plagioclases and Fe-oxides.

Properties

There are many small vesicles but they are not regularly through the thin section, as there is a greater concentration towards the top and bottom of the section, and therefore may occur in bands. The average width of these vesicles is 0.4 mm and these yield a 2D porosity of 9%. The wax method produced a porosity result of 26.1% which shows a large discrepancy with

the ImageJ result. This difference could have been to an error induced from the wax method. Alternatively, the small chunk used for the wax experiment may have been a highly porous section and not representative of the unit. This is a likely possibility as the pores present are not distributed evenly across the sample (Figure 3.29). The 3D porosity estimated from the porosity and permeability relationship using the ImageJ estimate is 11.7%. The permeability of this lava flow at 5MPa is estimated to be 6.81×10^{-17} m^2.

Rit 2: Basalt Lava

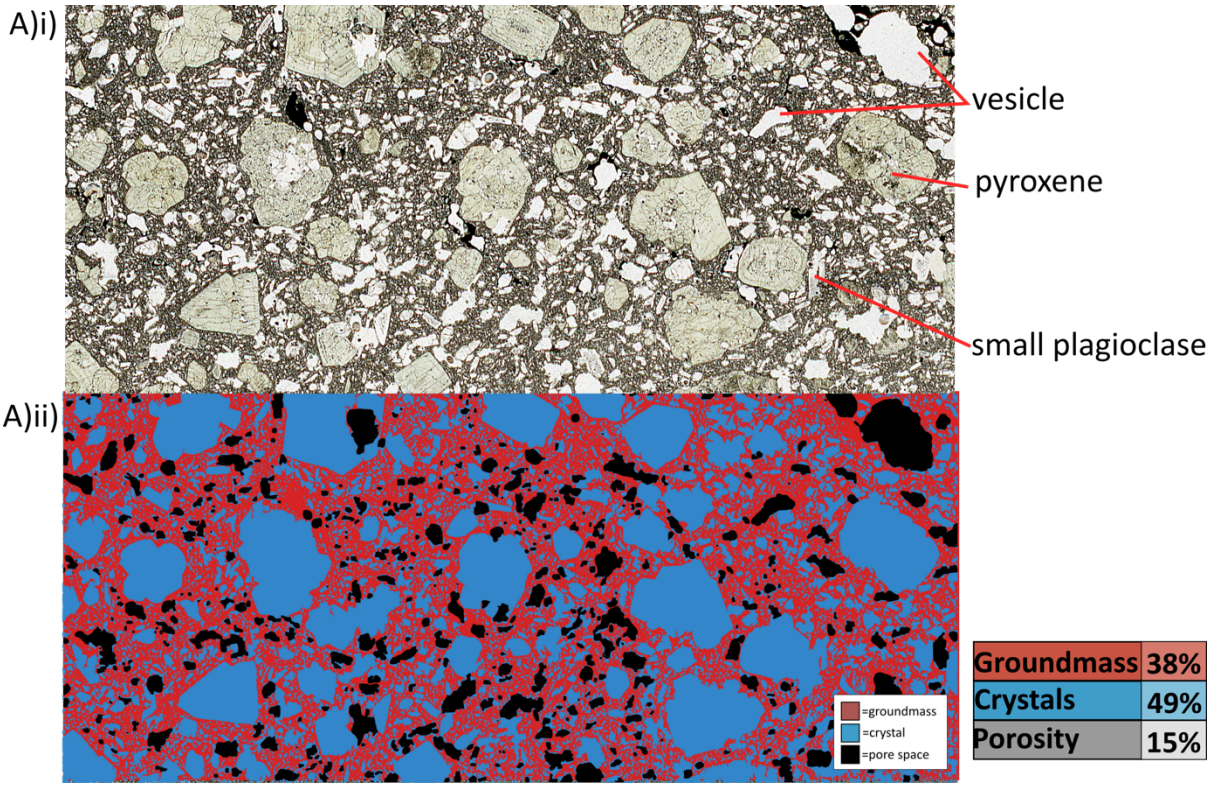

Figure 3.30: Rit2 Thin section analysis A.i) whole section and ii) ImageJ map. Percentage of area representing groundmass, crystals and porosity displayed.

Texture

Rit2 is a basaltic lava sampled from the series of dipping lavas to the north of the central cusp (Figure 3.11B, Figure 3.25). It is porphyritic consisting of mainly pyroxene and some olivine phenocrysts and smaller plagioclase crystals. The vesicles are small, irregularly shaped and numerous, with an average width of the vesicles is 0.55 mm.

Properties

The 2D porosity is measured at 15%. The cored sample of Rit2 had a measured 3D porosity of 16.7%. Figure 3.12 of the sample cores clearly shows these vesicles all the way through the sample. This sample had a measured permeability of 5.44×10^{-17} m^2. This sample also had a UCS of 56 MPa with a Young's modulus of 13.4 Gpa. However, in this case the sample had

already been up to confining pressures of 40 Mpa during permeability experiments which may have affected the results either positively due to the effects of compaction strengthening the rock, or negatively by inducing microcracks weakening the rock.

Rit3: Basalt Lava

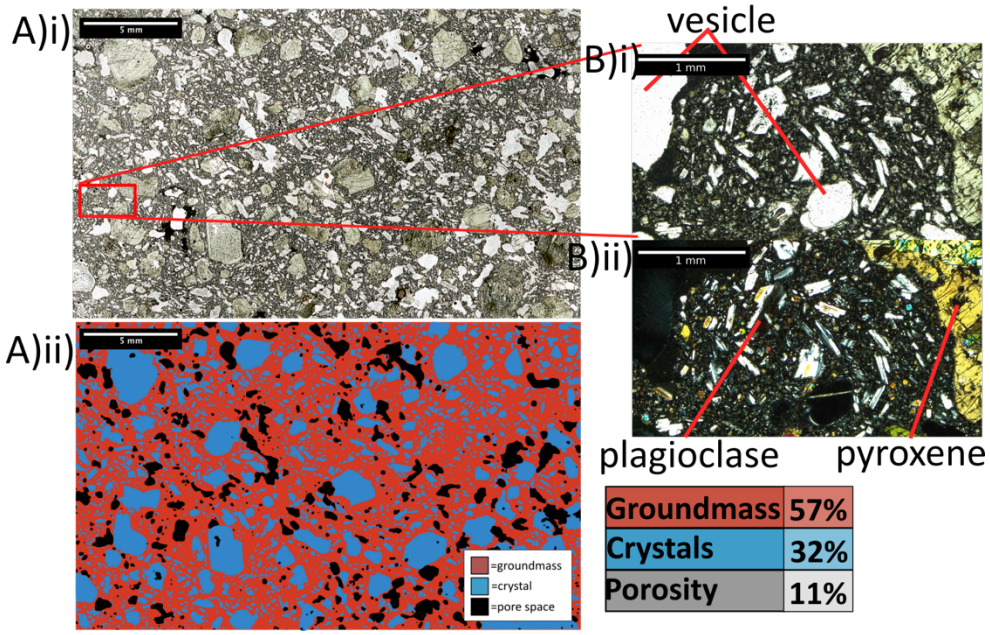

Figure 3.31: Rit3 Thin section analysis A.i) whole section and ii) ImageJ map, B. zoomed in portion in i) plane polarised light and ii) crossed polars. Percentage of area representing groundmass, crystals and porosity displayed.

Texture

Rit3 is a basaltic lava sampled from the series of dipping lavas to the north of the central cusp in series with Rit2, 5 and 6 (Figure 3.11B, Figure 3.25). It is similar to Rit2 in being crystal-rich with mainly pyroxene and olivine as phenocrysts and also looks similar in hand specimen cored (Figure 3.31).

Properties

Smaller but still abundant crystals of plagioclase are also present. Vesicles are common, irregularly shaped with an average width of 0.69 mm and represent 11% of the thin section. Three cores of this sample were measured in the pycnometer which had an average of 13.8%. It has a measured permeability of 4.605×10^{-14} m^2.

Rit4: Basalt Lava

Texture

Rit4 is a basaltic lava sampled from the series of dipping lavas to the north of the central cusp, older in sequence than Rit2 and Rit3. This basaltic sample is porphyritic and is composed

mostly of a very fine-grained groundmass. It is also fairly crystal-rich, with abundant larger clinopyroxene, smaller plagioclase and small amounts of olivine (Figure 3.32B).

Properties

The sample is slightly vesicular with 13% pore space, although this includes some plucking during sample preparation, so the true number may be more like 10%. These vesicles are irregularly shaped with an average width of 0.79 mm. It has a 3D measured porosity of 14.24%. It has a measured permeability of 2.01×10^{-16} m^2.

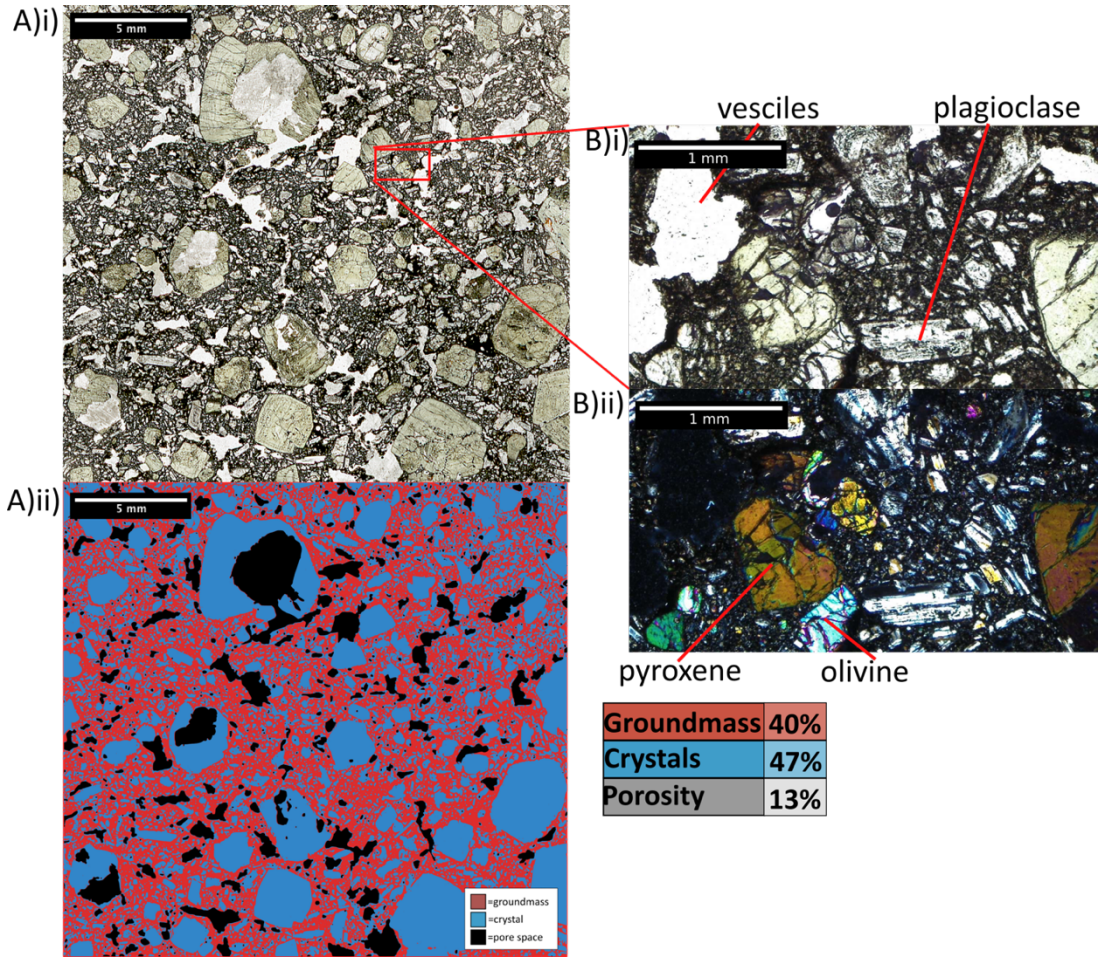

Figure 3.32: Rit4 Thin section analysis A.i) whole section and ii) ImageJ map, B. zoomed in portion in i) plane polarised light and ii) crossed polars. Percentage of area representing groundmass, crystals and porosity displayed.

Rit5: Basalt Lava

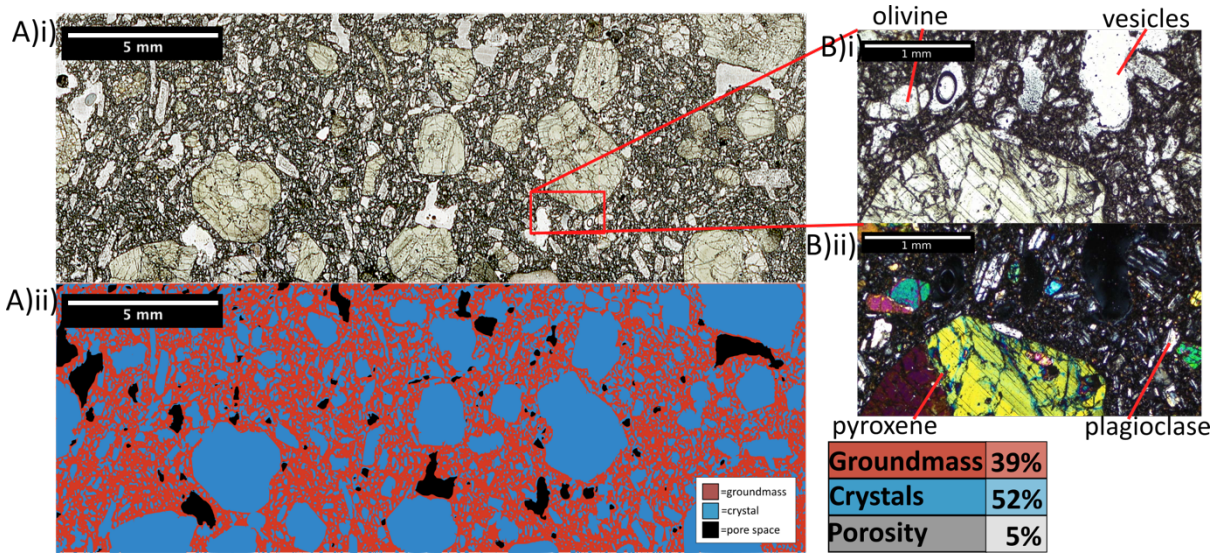

Figure 3.33: Rit5 Thin section analysis A.i) whole section and ii) ImageJ map, B. zoomed in portion in i) plane polarised light and ii) crossed polars. Percentage of area representing groundmass, crystals and porosity displayed.

Texture

Rit5 is a basaltic lava sampled from the series of dipping lavas to the north of the central cusp, the oldest in this sampled sequence. This sample is porphyritic, crystal-rich including some larger clinopyroxenes and aggregates with rare olivine and some smaller plagioclase crystals (Figure 3.33).

Properties

Vesicles account for 5% of this section and are irregularly shaped with an average width of 0.55 mm. It has an estimated porosity of 7.6% based on the 2D to 3D porosity trend and therefore an estimated permeability of 1.13×10^{-17} m^2.

SD5: Basaltic andesite Lava

Texture

SD5 is a basaltic andesite sampled from the core of an irregular lava flow at the base of the cliff, possible inferred as a channel filling flow. This area may have been covered by the talus apron at the base of the cliff in model. It is porphyritic with some larger crystals and crystal aggregates containing large pyroxenes, rare olivine and abundant smaller plagioclase crystals throughout (Figure 3.34).

Properties

Small vesicles form 8% of the thin section. On the hand sample, the vesicles are not apparent or not large enough to be visible. The wax method measured a porosity of 14% which is higher

than the porosity assumed from the 2D to 3D relationship at 10.42%. The permeability of this lava flow at 5MPa is estimated to be $3.86x10^{-17}$ m^2.

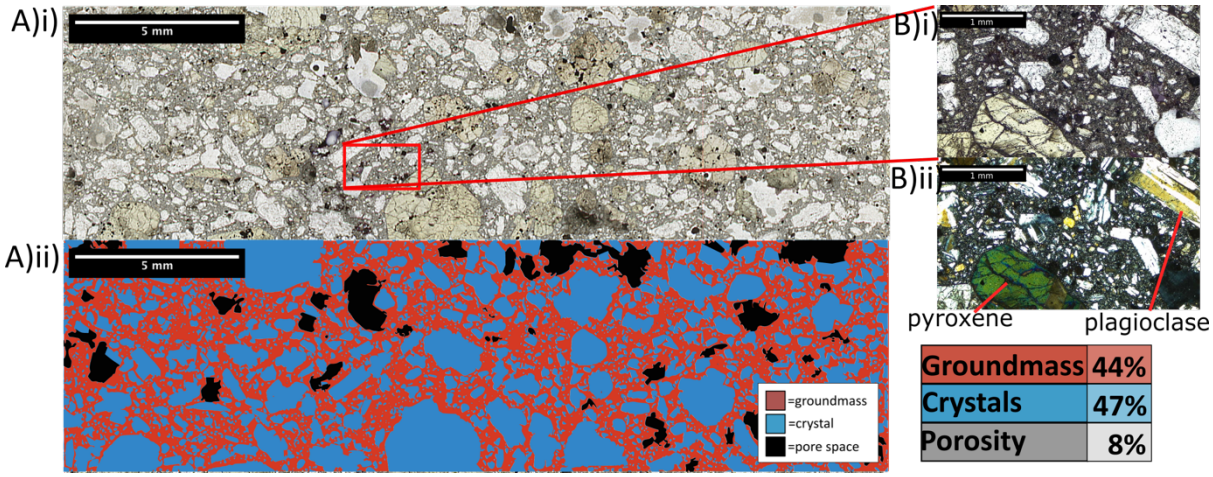

Figure 3.34: SD5 Thin section analysis A.i) whole section and ii) ImageJ map, B. zoomed in portion in i) plane polarised light and ii) crossed polars. Percentage of area representing groundmass, crystals and porosity displayed.

Rit 8: Basaltic andesite Lava

Texture

Rit8 is a basaltic andesite sampled from the rubbly surface of a lava flow on the southern islet. This is an extrusive sample which has been very altered indicated by the red colour, mainly observed in the groundmass indicating iron oxides present (Figure 3.35). There is a high crystal content which are often very altered, mainly consisting of plagioclase with some fractured pyroxenes and many opaque magnetites. The plagioclase crystals seem often altered particularly at their edges indicating the rock has been weathered significantly. The hand specimen is clearly much more altered than the other samples as it has a vibrant red colouration that can also be observed on the model in several places. We can assume that this rock type or alteration is similar in these places on the model.

Properties

This sample has a high 2D porosity of 20% where the vesicles are small but numerous with an average width of 0.63 mm. Three of this sample cores were measured and had an average 3D porosity of 23.4%. The permeability measured was the highest recorded for the Ritter Island samples at $1.658x10^{-13}$ m^2. Two samples were testing for uniaxial strength, one of which had previously been used in the permeameter at 40 MPa. The first sample, which had a higher porosity of 26.36% had a measured peak strength at 34.2 MPa and yielded at 32.2 MPa. It had a Young's modulus of 10.3 GPa. The second sample had a lower porosity of 22%, and

measured a higher peak strength of 51.6 MPa and yielded at 40 MPa. It had a slightly higher Young's modulus of 11.7 GPa. It is possible that the higher porosity may have affected its strength or also the fact that one may have compacted under high pressures during permeability tests and thus strengthening it. This sample has the lowest proportion of MgO and CaO than any of the other samples which points towards it being significantly weathered. It also shows evidence of iron oxide weathering throughout the sample. It's high porosity and permeability compared to other lavas measured suggest that this weathering may have been argillic alteration.

H1: Basaltic andesite Lava

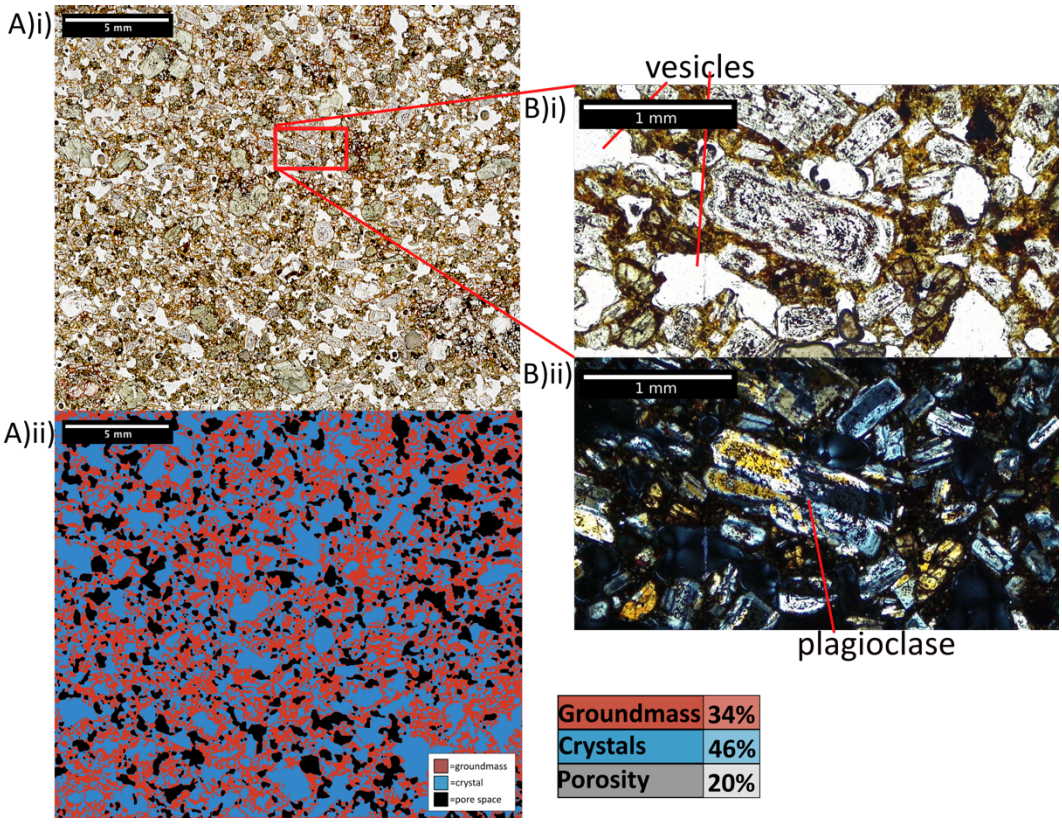

Figure 3.35: Rit 8 Thin section analysis A.i) whole section and ii) ImageJ map, B. zoomed in portion in i) plane polarised light and ii) crossed polars. Percentage of area representing groundmass, crystals and porosity

Texture

H1 is a basaltic andesitic lava sampled from the north flank of a submarine cone within the collapse scar interpreted as material from pre-1888 material (Berndt et al., 2017). It is highly crystalline with olivine and pyroxene present with small amounts of feldspar (Berndt et al., 2017).

Properties

The cored sample displays clearly visible pores (Figure 3.12). It has a 3D measured porosity of 12.5%. Its permeability was measured at 5.646×10^{-18} m^2.

H2: Basaltic andesite Lava

Texture

H2 is a basaltic andesitic lava block sampled from the slopes of a post-1888 new cone (Berndt et al., 2017). This sample is therefore not part of the original collapsed edifice however its properties may be representative of non-altered lava flows that did make up sections of the edifice. This sample is vesicular and contains pyroxene phenocrysts win a fine crystalline groundmass (Berndt et al., 2017).

Properties

Four cores of H2 were measured and gave an average porosity of 17.8%. A core with a lower porosity of 15.26% had its permeability measured at 6.779×10^{-18} m^2. Two cores were measured for uniaxial strength. The peak strengths were 60 and 69 MPa, whilst they yielded at 54 and 62 MPa, respectively. The Young's modulus was measured at 15.5 and 24.4 GPa.

3.3.5.2 *Intrusions*

SD3: Basalt Dyke

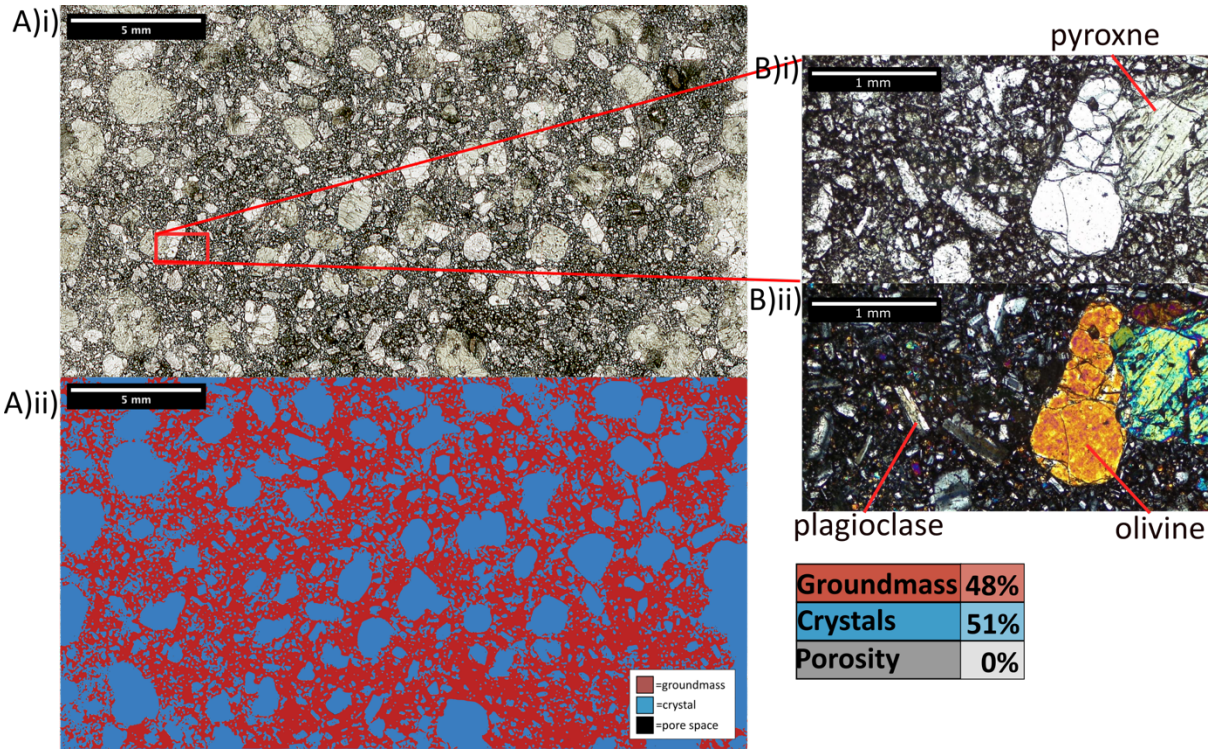

Figure 3.36: SD3 Thin section analysis A.i) whole section and ii) ImageJ map, B. zoomed in portion in i) plane polarised light and ii) crossed polars Percentage of area representing groundmass, crystals and porosity displayed..

Texture

SD3 is a basaltic dyke sampled from prominent dyke forming wall running out to see cross-cutting most of the sequence in the cliff (Figure 3.11A). This is equivalent to the mapped dyke 37. Field measurements show dyke is striking 320° and dipping 80°NE with a thickness of 2.7 m. Measurements from the model give a simialar average trend of 332° and dip of 80° NE. It is porphyritic with pyroxene and less abundant olivine forming most of the phenocrysts and crystal aggregates. There is an abundance of plagioclase crystals and microlites in the glassy groundmass.

Properties

There are no vesicles giving a porosity of 0%. The wax method suggests a 3D porosity of 2.4% and the suggested porosity from the 2D to 3D relationship is 2.82%. The assumed permeability based on porosity and permeability trends is 1.38×10^{-18} m^2.

SD4: Basalt Dyke

Texture

SD4 is a basalt sampled from an irregular dyke which thickens upwards trending 330°. This dyke may have been the same as mapped dyke 39 but the section of the cliff imaged during sampling may have been obscured by subsequent scree slopes. It has a very fine-grained groundmass with numerous plagioclase crystals. Phenocrysts of mainly pyroxene with some crystal aggregates.

Properties

Elongate vesicles with lengths of 1 mm on average make up 3% of the thin section. These vesicles appear to bend around the crystals in areas and are surrounded by a glassy material which also follows their path as seen in Figure 3.37. The estimated 3D porosity is 5.45% and thus the estimated permeability is 4.38×10^{-18} m^2.

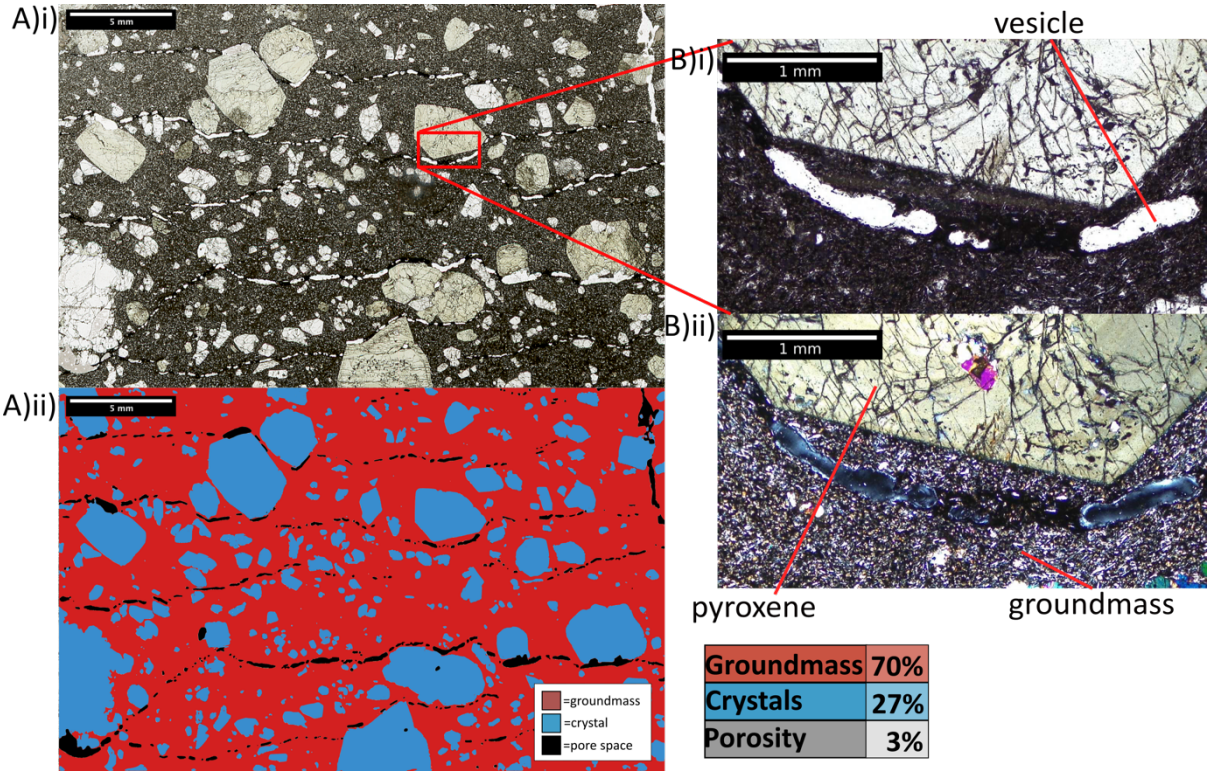

Figure 3.37: SD4 Thin section analysis A.i) whole section and ii) ImageJ map, B. zoomed in portion in i) plane polarised light and ii) crossed polars. Percentage of area representing groundmass, crystals and porosity displayed.

Rit1: Basalt Dyke

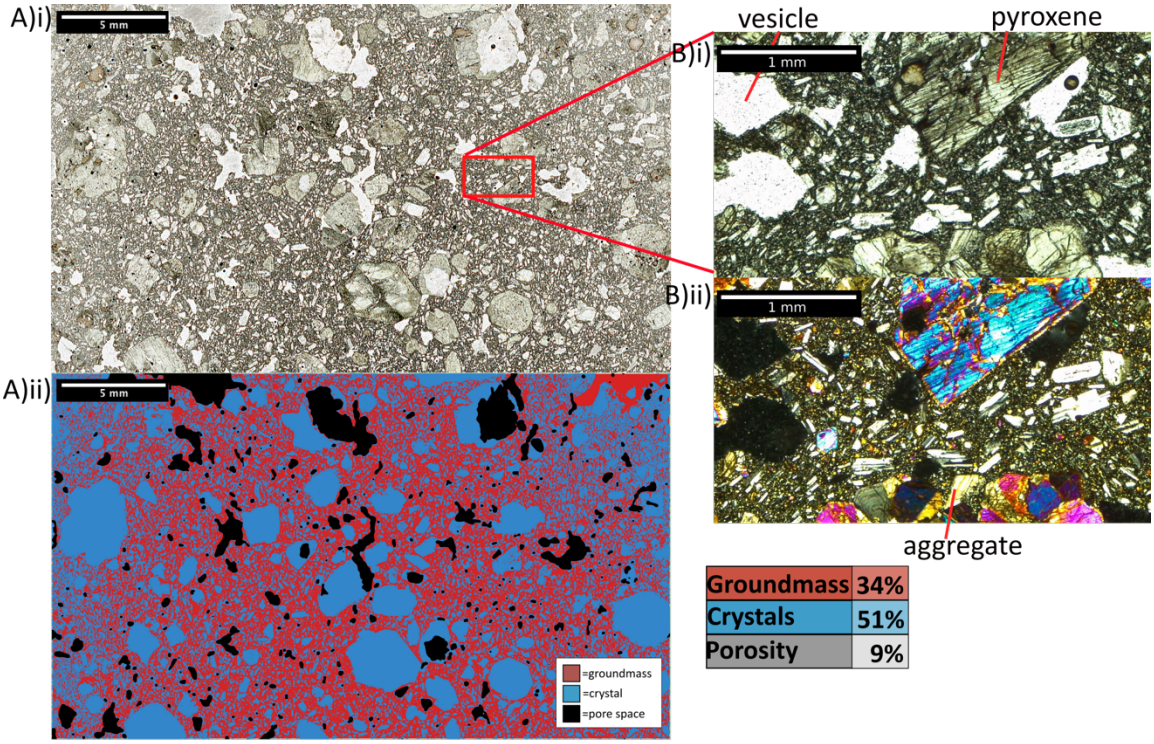

Figure 3.38: Rit1 Thin section analysis A.i) whole section and ii) ImageJ map, B. zoomed in portion in i) plane polarised light and ii) crossed polars. Percentage of area representing groundmass, crystals and porosity displayed.

Texture

Rit1 is a basaltic dyke that was sampled from a protruding dyke in the north cove (Figure 3.11B, Figure 3.25). It is crystal-rich containing mostly clinopyroxenes and some olivine and plagioclase.

Properties

It also contains some irregularly shaped pore spaces accounting for 9% of the section. Some of these irregularly shaped pore spaces may represent the opening of fractures, in particular the space in the centre of Figure 3.38A is elongate in the Y axis. Vesicles can also be observed throughout the hand specimen and the porosity measured from the core of this sample gives result of 12%. The measured permeability for this sample was 2.37×10^{-17} m^2.

Rit 6: Basalt Dyke

Texture

Rit 6 is sampled from a basaltic dyke in the central cusp of Ritter Island. The thin section has some clear areas have been plucked and therefore these areas to have been inferred as crystals. This sample is very crystal-rich including large crystal aggregates, clinopyroxene and

many plagioclase crystals exhibiting extensive fracturing. The groundmass is made up of fine plagioclase needles.

Properties

Apparent porosity is very low and, after discounting plucked areas, makes up only 1% on the sample section. The core 3D porosity was measured at 3.9%. The permeability at 5 MPa was measured at 2.17×10^{-17} m^2 which is a higher permeability than other samples of similar porosities suggesting permeability may have been increased by the presence of microfractures.

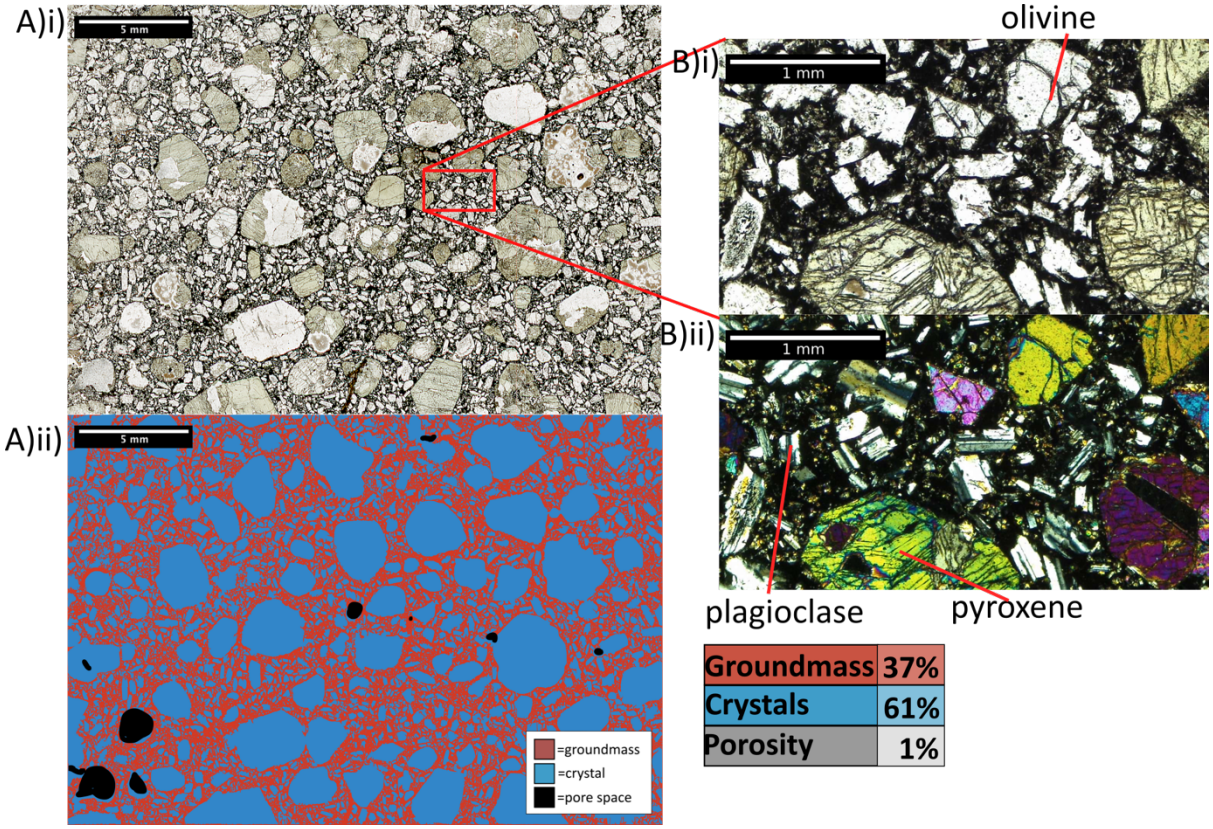

Figure 3.39: Rit6 Thin section analysis A.i) whole section and ii) ImageJ map, B. zoomed in portion in i) plane polarised light and ii) crossed polars. Percentage of area representing groundmass, crystals and porosity displayed.

Rit 7: Basalt Sill

Texture

Rit7 is a basaltic intrusion sampled from a sill in the north cove (Figure 3.40). This sample has a fairly equal split of crystals and groundmass. The crystals are mainly clinopyroxene and smaller plagioclases and rare olivine (Figure 3.40). There are some larger crystal aggregates also.

Properties

This sample has been plucked slightly during preparation and therefore the ImageJ porosity result indicated an apparent porosity of 4.65% but discounting these areas, the true porosity is likely to be closer to 2%. Vesicles are slightly elongated and may represent shrinkage cracks. Two cores were measured for their 3D porosity which had an average value of 8.16%. The permeability was measured at $4.32x10^{-16}$ m^2.

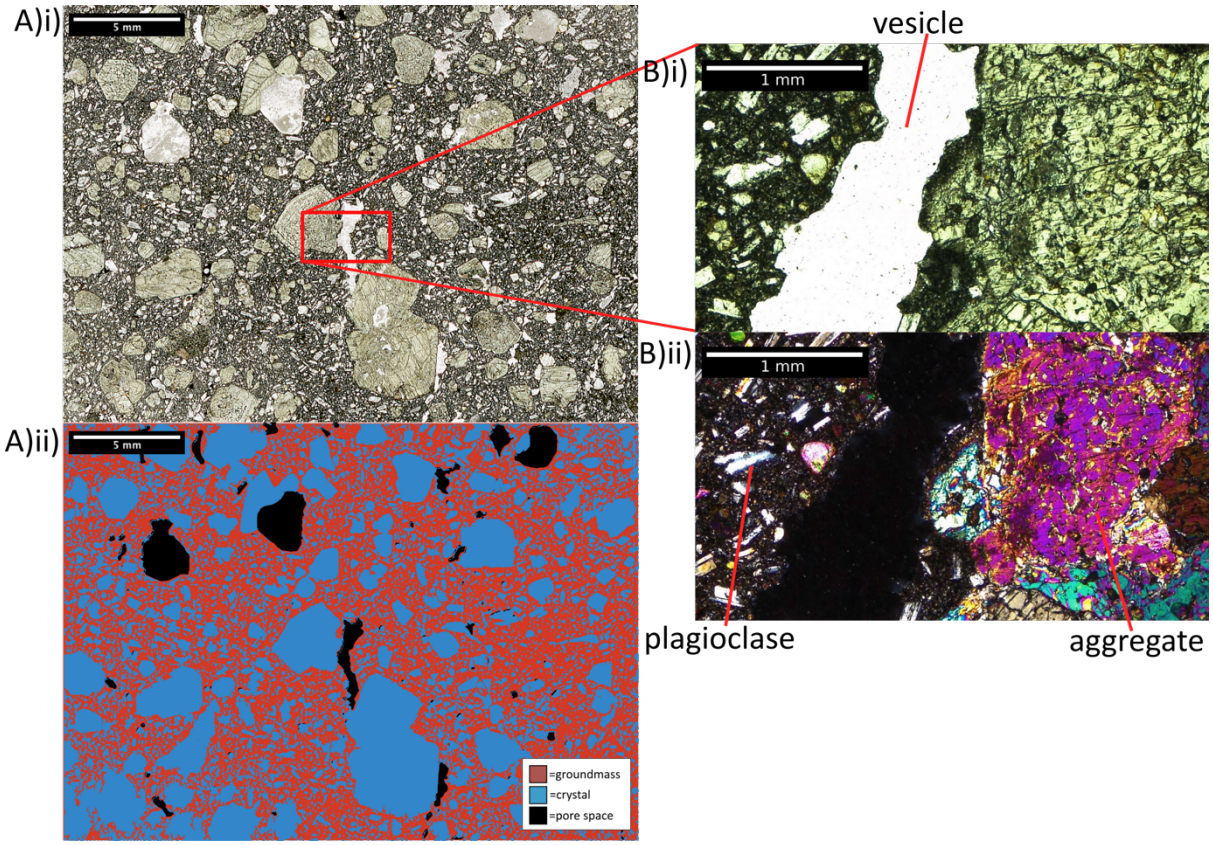

Figure 3.40: Rit7 Thin section analysis A.i) whole section and ii) ImageJ map, B. zoomed in portion in i) plane polarised light and ii) crossed polars. Percentage of area representing groundmass, crystals and porosity displayed.

H3: Basalt Intrusion

Texture

H3 is a basaltic submarine sample taken from the base of the northern side of the collapse scar (Berndt et al., 2017). It is unclear whether the source of this rock was intrusive or extrusive as both types of rocks were present at the collection site. However, the composition and crystal groundmass size suggest that it might be intrusive and therefore it is discussed alongside the other basaltic intrusions.

Properties

Porosity was measured using three cores which gave an average result of 2.35% porosity. The cores show that there are some significant fractures that affect this rock (Figure 3.12). The permeability was measured in two of these samples, one of which had a permeability of

$3.542x10^{-17}$ m^2. The other had very little or even no flow recorded through the sample. The one with higher permeability had a fracture present from the base to the top of the core, suggesting this may have influenced the flow of fluid through the rock. A uniaxial test was carried out on the sample displayed fewer fractures after having experienced 40 MPa during permeability testing. The UCS recorded was 92.8 MPa and it yielded at 78 MPa and had a Young's modulus of 18.4 GPa. This was the strongest sample measured from the Ritter Island set and may represent how dykes behave. However it was not a fresh sample and may not be representative.

3.4 Discussion

The sample set from Ritter Island was limited in terms of sample size for some of the experiments and contained a sample bias towards fresher rocks. Despite this, measurements made in this chapter have deduced the porosity, permeability, strength and Young's modulus of some of the rocks making up the edifice which collapsed. This has characterised various empirical relationships between properties and allows speculation of instabilities inherent to the volcano, discussed here.

The extrusive set of samples from Ritter Island include mainly rocks that made up the pre-collapse island. These include lava samples from the north cove, some from the south, one from the central islet as a scoria deposit, one from the southern islet and two submarine samples one of which is from post-collapse volcanism. This post-collapse sample can be used as a more fresh, unaltered analogue for pre-collapse rocks for comparison.

These extrusive basalts to basaltic andesites have an average porosity of 15.3%. Some porosities are as high as 25%, or as low as 7.6%. As estimated from Chapter 2, lava flows made up 25% of the pre-collapse host rock units and are interbedded with loosely consolidated pyroclastic and scoria units likely to be of similar of even higher porosities. The sample with the highest measured porosity was Rit8, which was taken from the rubbly surface of a flow. This was the most clearly altered of the samples due to its red colour. This also had the highest permeability measured and the weakest uniaxial strength. It is therefore inferred to have been affected by argillic alteration. All strength measurements that were undertaken on extrusive units produced a range of strengths. The trend of this data suggests the higher the porosity,

the weaker the rock. In addition, the trend of the Young's modulus suggests that the higher the porosity the stiffer the rock.

Rit8 was the most permeable, porous and weakest rock. The two UCS measurements taken showed that the possibly compacted sample appeared to be stronger than the fresh sample. However, this value may have been influenced by a higher porosity. This high porosity also may have influenced the level of alteration as it would have allowed more fluids into the rock. In the sequence of the cliff, this flow should have been relatively close to the surface of the cone and therefore its alteration may have been influenced by both groundwater or surface weathering. However, the same red colouration is seen throughout the cliff in various bands. Some of these layers may coincide with being the rubbly tops of lava exposed to weathering, but many seem to be within banded scorious deposits and in association with intrusions. From this sample we could conclude that these layers where alteration is present have similarly high porosities and permeabilities to allow fluids to flow and alter the sequence. While this increased porosity and permeability due to alteration reduces the likelihood of building up excess pore pressure, it also reduces the compressive strength and makes it mechanically weaker. As such, the alteration reduces the likelihood of hydraulic weakening, but makes mechanical failure more likely.

The sample H2 is the youngest of the samples as it is from post-collapse volcanism in the new cone forming in the collapse scar. This sample was analysed as an analogue of the fresh material that built up pre-collapse Ritter before any alteration occurred. By comparing the hand samples, Rit8 and H2 had many similarities in their structure. By comparing their chemistry, it can be noted that the concentrations of MgO and CaO are depleted in Rit8 compared to H2. This is typical pattern of weathered basalt (Romero et al., 2021). H2 has a slightly lower porosity than Rit8 however has a much lower permeability. The difference measured could be as a result of age or the presence of extensive alteration in Rit8 has had increased porosity and therefore an increased permeability. The uniaxial strength of H2 was also measured much higher suggesting that the fresher material is much stronger and once altered, the strength reduces. The peak strength measured of H2 was 69 MPa and of Rit8 was 34 MPa suggesting that the alteration here could reduce strength by 50%. Therefore, it can be inferred that the alteration here has increased porosity, permeability and reduced the strength of the rock. This is indicative of argillic alteration where high temperature acidic solutions percolate through permeable rocks causing acid-sulphate leaching which increases

porosity and permeability and decreases strength (Heap and Violay, 2021). This type of alteration could be further confirmed by investigating mineral assemblages of more of more samples of altered material from the edifice. By assuming this type of alteration was present for the whole of the island, this relationship formulates the idea that hydrothermal alteration across the edifice increases porosity and permeability in these areas. This means that high fluid pressures are harder to build up reducing the likelihood of pressurisation induced instability. However, the presence of this alteration suggests a reduction in strength by almost 50% creating weak zones in the edifice where it may have been likely to fail.

The dataset for Ritter Island is also limited as there are no samples of the poorly consolidated units in the edifice which are interbedded with the lavas. By using previously published values of such units from previous studies, these rock properties could be estimated. Previous studies of pyroclastic rocks suggest they are characterised by low Young's modulus and compressive strengths (Heap and Violay, 2021). An average UCS of tuffs measured by Dinçer et al. (2004) show an average of 42 MPa and a minimum of 33 MPa. These may also form weaker layers within the edifice at Ritter.

From the selection of intrusive rocks in the Ritter sample sets, it is noticeable that the porosity measurements are much lower than the extrusive units ranging from 2.4% to 12% and an average of 5.8%. This porosity seems to be as a result of smaller vesicles in some if the samples or the presence of fracturing or a combination. The example of H3 shows how the presence of fractures can significantly affect the permeability of samples. This sample was the only intrusive example to have the uniaxial strength measured and its results suggest that the low porosity and structure of these units make them much stronger where its yield strength was higher even then that of the highest peak strength of the extrusive material.

Observing where these rocks lie on the Ritter model can provide a relative ageing to be estimated (Figure 3.25). Within the SD sample dataset, the extrusive rocks are aged with SD1 as the youngest as its origin is from higher in the cliff, followed by SD2, SD5 and SD6. SD7 is older still as it lies at sea-level closer towards the centre of the pre-collapse cone. The SD3 dyke cuts through most of the in-situ sequence and is therefore younger with the exception of possibly SD1. SD4 cross-cuts most of this sequence also and has the appearance of a fresher dyke and therefore is inferred to be of a similar age or younger than SD3. Within the Rit data set, the extrusive lavas are inferred to be of a similar age to the SD extrusive set as they lie at a similar point in the cliff and the trend of the layers suggest as such. Relative to one another,

Rit5 is the oldest followed by Rit4, Rit3, and Rit2 being the youngest in this sequence. Rit7 is a sill that seems to intrude into this sequence making it younger. Rit1 and Rit6 cross-cut the layer sequence of lavas making them younger. Rit8 on the southern islet is inferred to be the youngest of all the sub-aerial samples as it lies close to the top of the pre-collapse succession. In hand specimen, Dykes SD3, SD4, Rit1 and Rit6 look very similar reflected by them all being mapped as 'mid-dark grey' on the geological map. These are all therefore inferred to be of similar ages. The Rit7 sill looks much paler in both hand specimen and on the model and therefore assumed to be of a different suite of intrusions.

By assessing the results alongside these relative ages, it could be noted that the most permeable intrusive rock aligns with the inferred older intrusion on the model. This may be as a result of more extensive fracturing within these rocks, potentially due to cyclic heating and cracking.

3.5 Conclusion

- The results from the mechanical and hydraulic tests suggest that the rocks at Ritter Island follow the expected trends of volcanic rocks. In this, the permeability increases with a function of porosity while the strength and Young's modulus decreases.
- The extrusive rocks are generally more porous, permeable and weaker than the intrusive rocks. The porosities range between 8-25% which is attributed to the presence of vesicles in most of the samples. These lava units make up 25% of the island's host rock, where the other rocks are possibly weaker scoriaceous tuff units. The layering of this weak material will have built up creating a generally weak edifice which allows fluids to flow through the volcano reducing hydrostatic pressure build ups but possibly influencing zones of alteration.
- The intrusive rocks in this sample set have lower measured porosities and permeabilities compared to the extrusive lava samples. Their range of porosities were measured between 2-12%. In these rocks, it was seen that the permeability was more influenced by the presence of fractures rather than vesicles. This was exemplified by the presence of fractures was seen to increase the permeability from 2.2 $x10^{-20}$ to 3.5 $x10^{-17}$ m^2 by comparing different cores of one example in different orientations of fractures. In addition, all of the intrusive samples showed a reduction of permeability with increasing confining pressure which is likely to be as a result of micro-cracks closing. Some unfractured or confined low permeability intrusions may also act as caps to fluid flow possibly increasing pore fluid pressure in localised regions deeper in the edifice and encourage alteration (Figure 3.41).
- By comparing the freshest of the sample set to a comparable altered sample suggests that the alteration in vesicular lavas results an increase of porosity, permeability and a significant reduction of strength and increase in brittleness of the rock. The strength reduces by almost half, a pattern which has been recognised in other localities experiencing alteration (Romero et al., 2021). This suggests the presence of argillic hydrothermal alteration, which appears to be prevalent on Ritter Island, reducing the strength of rock. Therefore, assuming altered regions were pervasive throughout the rest of the pre-collapse volcano, this could provide significant evidence for weak zones in the edifice which led to the eventual collapse (Figure 3.41).

- These results indicate that the presence of intrusions may have restricted or directed fluid flow to influence zones of hydrothermal alteration. The generally porous and permeable host rocks would have allowed the movement of hydrothermal fluids around the edifice. Reports of thermal springs at the present-day edifice highlights the influence of alteration within this edifice (Saunders and Kuduon, 2009). This alteration is shown to reduce the strength of porous lava flows by half and may have created weak layers on which the collapse may have occurred (Figure 3.41). These values of hydraulic and mechanical properties will be useful for computer modelling the strength of this edifice. Values used in numerical modelling for volcanic stability include bulk density, Young's modulus, Poisson's ratio, cohesion, angle of internal friction and pore pressure ratio which is dependent on porosity and permeability (Heap et al., 2021a).

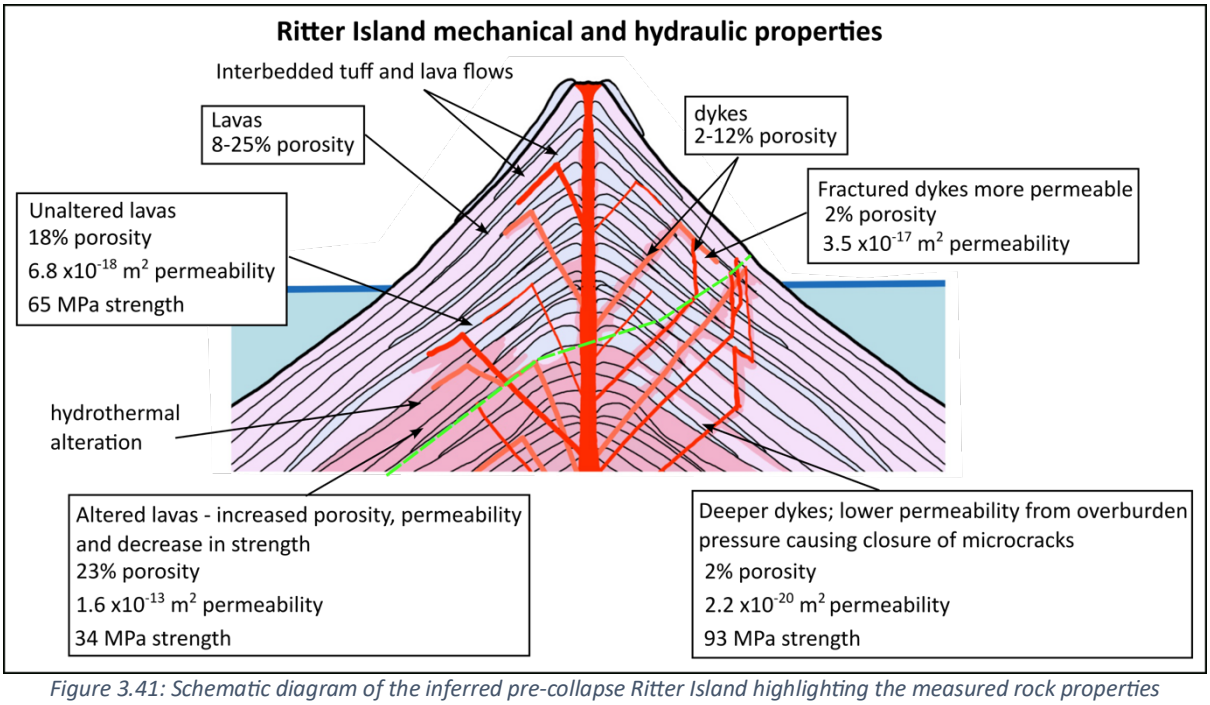

Figure 3.41: Schematic diagram of the inferred pre-collapse Ritter Island highlighting the measured rock properties measured and how this influence weakening of the edifice.

4 Fogo collapse scar morphology, mechanical and hydraulic properties

4.1 Introduction

Fogo is a volcanic island of the Cape Verde archipelago which has evidence of catastrophic collapse (Day et al., 1999). Its morphology is dominated by a curved east-facing scar and post-collapse volcanism. Evidence on neighbouring islands suggest this collapse generated a mega-tsunami (Ramalho et al., 2015). The precise nature of this collapse is still debated. There are also various suggestions for both collapse date and volume in previous literature. The latter is used in tsunami modelling as the volume is key in determining tsunami height and magnitude. The pre-collapse morphology is also debated but the well-preserved Bordeira cliff provides a window into the earlier structure of the volcano.

For this thesis, fieldwork to Fogo was undertaken to collect drone imagery and samples from the Bordeira cliff. The drone imagery was used for SfM modelling to create a high-resolution model of the Bordeira cliff. This was used to map major geological and morphological features primarily the extensive dyke network visible throughout the cliff. Over 2000 dykes were mapped and analysed to gain further information on the pre-collapse structure.

Radial dykes were used to estimate the location of pre-collapse eruptive centres. A study of the orientation of younger ankaramitic dykes was done to assess the validity of a concept that this set of dyke injection represented a plumbing reorganisation prior to collapse due to changing orientations of cross-cutting dykes highlighting stress changes within the edifice (Day et al., 1999). This is key to understand due to the recent magma plumbing reorganisation in eruptive activity on Fogo and is therefore key to assessing current flank stability.

It is also important to understand the mechanical properties of the rocks making up the edifice at Fogo, which have not yet been studied. This study measures the porosity, permeability, uniaxial compressive strength and Young's modulus of samples collected from a variety of lithologies in the Bordeira cliff. Results from this will allow identification of any intrinsic instabilities that may be present within the edifice that may have led to collapse.

This Chapter will discuss possible instabilities on Fogo Island leading to its catastrophic collapse and highlight how valuable SfM modelling datasets can be in this field of research.

4.2 Fogo literature review

4.2.1 Introduction

Fogo is one of ten islands making up the horseshoe-shaped Cape Verde archipelago, 570 km off West Africa between 15° and 17°N (Figure 4.1). Its island morphology is dominated by a curved scar opening to the east, likely to be the result of a prehistoric volcanic collapse. The nature of this collapse is widely disputed. However, evidence of tsunami deposits on neighbouring islands suggested that the event (or events) may have had devastating impacts (Ramalho et al., 2015). It has been proposed that the current morphology of Fogo and the recent eruptive history may suggest instability and the possibility of a future landslide (Day et al., 1999). Therefore, the understanding of the stability of this island will be useful for ongoing risk assessment.

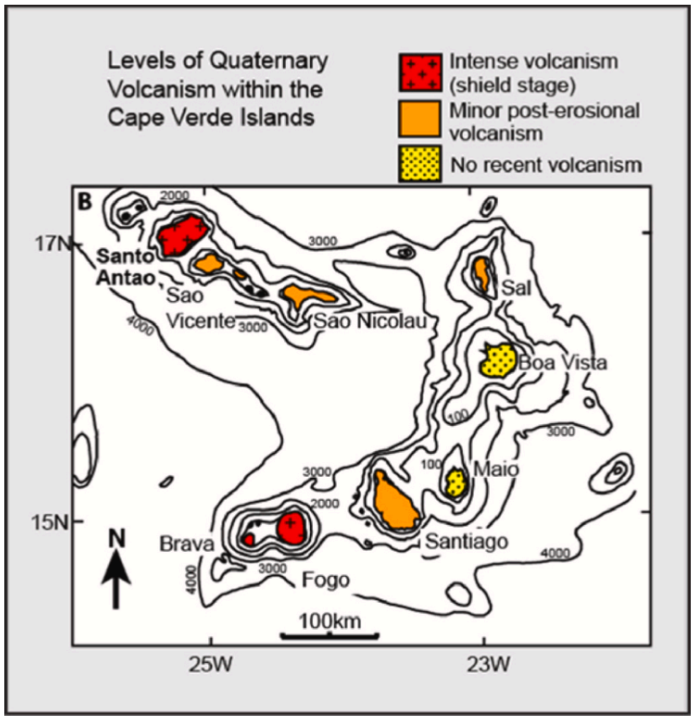

Figure 4.1: Cape Verde Archipelago categorised by volcanic stage from (Rolfe-Betts et al., 2024)

4.2.2 Geological background

The Cape Verde islands are seamounts and islands that lie on late Jurassic to Cretaceous oceanic crust on the topographic anomaly, the Cape Verde Rise, 2 km above the surrounding seafloor (Amelung and Day, 2002, Day et al., 1999). This elevated region of the seafloor is associated with an underlying 50 Ma old mantle plume (Amelung and Day, 2002). The islands emerged during the Miocene and all are associated with strongly alkaline magmatism

(Martínez-Moreno et al., 2018, Day et al., 1999). The African plate, on which Cape Verde lies, is moving SWS at 0.9 cm/year (Amelung and Day, 2002). The islands show an age progression from east to west (Cornu et al., 2021). Fogo, together with Santa Antao and Brava, are in the shield stage of volcanism, and are therefore the youngest islands of the archipelago and are the most recently active (Figure 4.1). Fogo has erupted 28 times in the last 520 years, the most recent of which was in November 2014 (González et al., 2015). This 77-day eruption produced lavas that destroyed three villages as well as areas of farmland (Worsley, 2015).

4.2.3 Island morphology

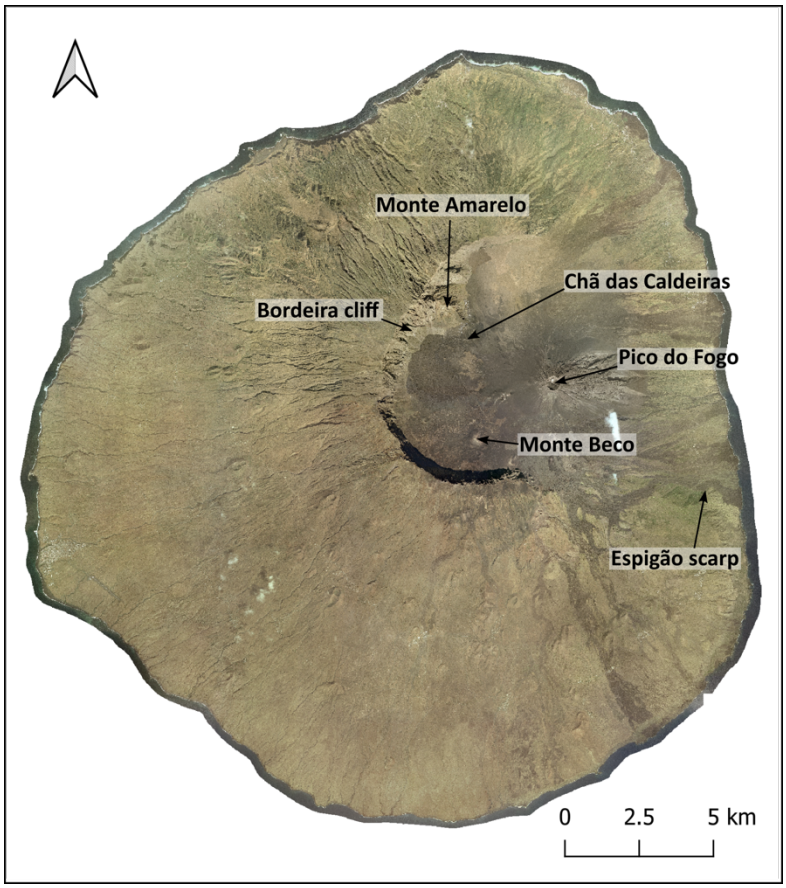

Figure 4.2: Fogo orthomosaic highlighting key named locations.

Fogo is the fourth largest island in Cape Verde with a surface area of 476 km^2, an average diameter of 25 km and a maximum elevation of 2829 m above sea level. The island is near conical with slopes ranging from 22° to 28° with some asymmetry due to the prevailing north-easterly trade winds meaning most precipitation falls on the windward flank. This makes the slopes on this eastern flank steeper and the stream network more established (Martínez-Moreno et al., 2018). The northern section of the coast has steeper cliffs due to wave action.

The morphology of Fogo is dominated by an eastward-opening depression surrounded by a 20 km long horseshoe-shaped wall up to 1000 m high, known as the Bordeira cliff (Figure 4.2). This feature has slope angles between 60°and 90° produced by one or more major volcanic collapses (Day et al., 1999). The Monte Amarelo spur juts out from the cliff and has lower slope angles (Figure 4.2). The Espigão scarp in the east of Fogo is also thought to be part of the collapse scarp (Figure 4.2).

The depression, called Chã das Caldeiras, is covered in lavas and lahar deposits and contains a younger stratovolcanic cone, the Pico do Fogo (Figure 4.2). This peak has a diameter of 1.5 km with a summit crater 500 m wide containing interbedded ash, scoria and fragmented lava (Worsley, 2015).

4.2.4 Volcanism

Fogo is the only island of Cape Verde to have experienced historic eruptions which have been mainly Hawaiian or Strombolian. Eruptions are estimated to occur approximately every 20 years (Marques et al., 2019). Since 1785, Pico do Fogo has been dormant and younger eruptions have emerged from lower cones (Worsley, 2015). An eruption in 1995 produced 4.7 km^2 of lava flows on the southwest flank of Pico do Fogo (Amelung and Day, 2002). The latest eruptions were in 2014 and 2015 persisting for 77 days. This event produced lava flows that destroyed several villages and cultivated land within the depression (Worsley, 2015). Past and present eruptions are thought to be fed by a relatively deep magma chamber (Carvalho et al., 2022, Amelung and Day, 2002).

4.2.5 Collapse theories

The Cape Verdes have a history of lateral collapses with 12 giant volcanic landslides identified through scars and submarine deposits (Blahut et al., 2018). Only those at Fogo and Santo Antao have occurred within the last 400 ka (Blahut et al., 2018). The Bordeira cliff escarpment on Fogo has been the source of some contention regarding the nature of its formation.

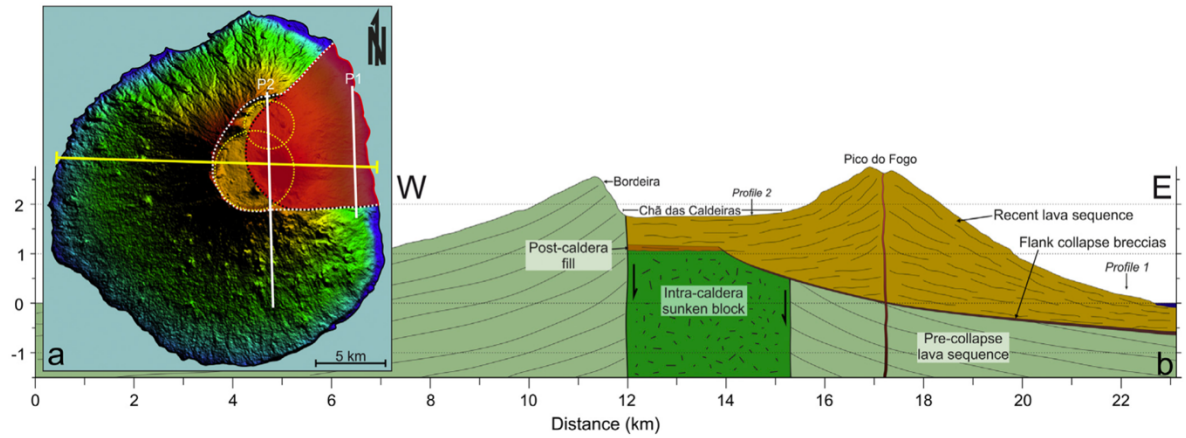

Figure 4.3: Proposed interpretation of the collapse at Fogo. a) showing two collapse theories in white (from Day et al., 1999) and yellow (from Madeira et al. 2008) and the red polygon showing the area used for volume calculations. b) profile of inferred geology by Martinez-Moreno et al., 2018

The first theory is that the morphology of Fogo has been shaped by two overlapping caldera collapses cut by a later flank collapse (Figure 4.3) (Martínez-Moreno et al., 2018, Brum da Silveira et al., 1997), the intersection of which is the Monte Amarelo spur. This theory was based on magnetotelluric data taken of the collapse scar which showed an elevation disparity of the base of the scar between the two inferred collapses (Martínez-Moreno et al., 2018)

The second theory (and the most widely accepted model of the collapse) was proposed by Day et al. (1999) in which the morphology was formed as a result of a single collapse towards the east and that the Bordeira cliff represents the exposed portion of the headwall of the scar agreeing with the inferred single tsunami event and collapse deposits (Figure 4.4). The shape of the scar with a central cusp is also observed at other single event collapses, as in the case of Ritter Island. Marques et al. (2019) suggested that the collapse consisted of multiple fault blocks where the upper fault partially collapsed leaving the flat topography of Chã das Caldeiras. Bathymetric surveys of the surrounding seafloor has identified evidence of collapse deposits consisting of typical hummocky relief, supporting this failure model (Figure 4.5) (Masson et al., 2008). This initial failure may have also triggered subsequent failures of the seafloor sediments (Barrett et al., 2020).

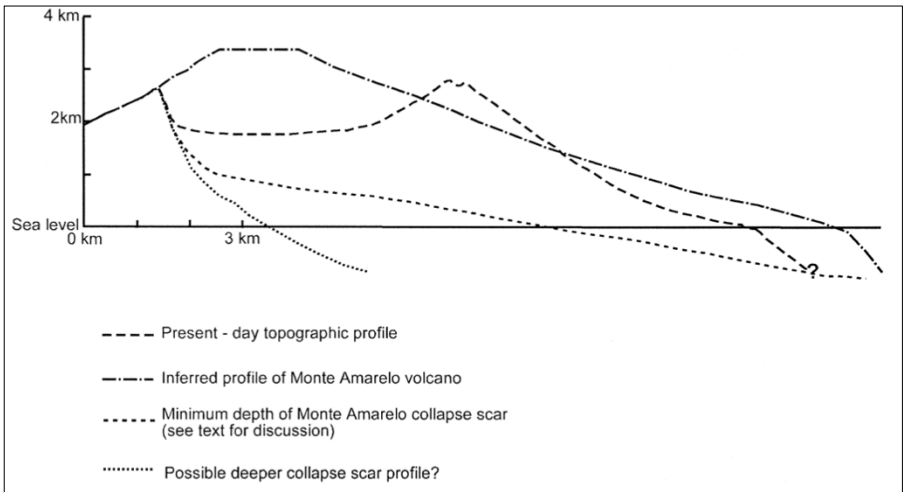

Figure 4.4: Cross-section showing inferred pre-collapse profile of Fogo and the inferred scar extends from lateral collapse from Day et al. (1999).

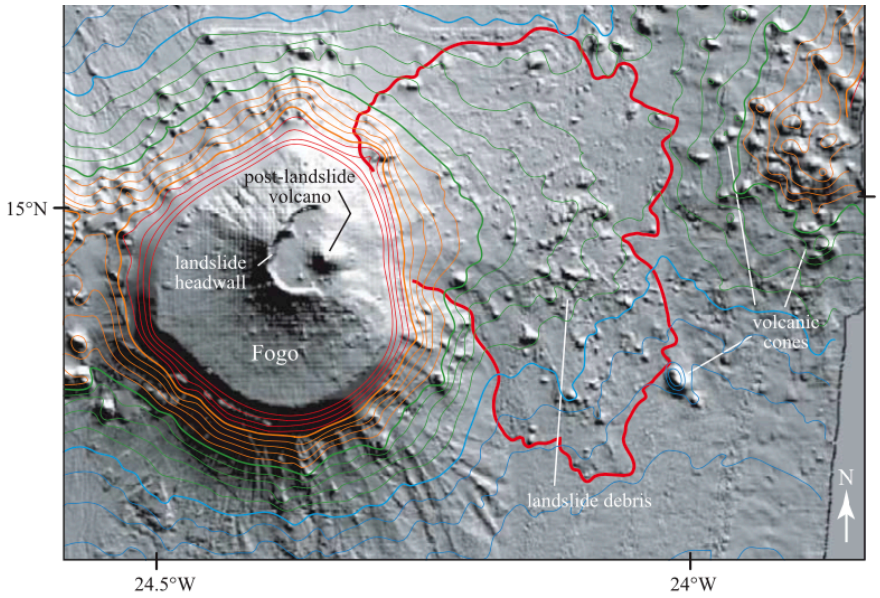

Figure 4.5: From Masson et al., (2008) highlighting the inferred debris avalanche deposits in a) 3D view and b) map view.

4.2.6 Collapse timing and volume

Evidence of tsunami deposits on the neighbouring island of Santiago suggests that the run-up exceeded heights of 270 m, highlighting the enormous size of the tsunami created (Ramalho et al., 2015, Paris et al., 2011). Santiago is 55 km east of Fogo, so was likely to be hit by the wave from this event. High in the northern plateau of this island are fields of mega-clasts and chaotic conglomerates made of the material exclusively found lower down on the cliffs, likely to have been transported there by the tsunami (Ramalho et al., 2015).

The timing of this collapse has been estimated by several different authors (Figure 4.6A). Foeken et al. (2009) used cosmogenic ^{3}He to date pre- and post-collapse lavas,

suggesting the collapse occurred between 62 and 123 ka. Paris et al. (2011) dated a coral in the Santiago tsunami deposit and a post-collapse lava on Fogo and suggested an age range for collapse of 86 – 123 ka. Cosmogenic ^{3}He by Ramalho et al. (2015) on the tsunami deposits suggest that the event occurred in the 65 – 84 ka interval. Lavas from pre- and post-collapse were analysed with K–Ar and ^{40}Ar/^{39}Ar dating by Cornu (2017) to suggest that the collapse occurred at around 68 ka. K-Ar dating from Marques et al. (2019) has estimated the collapse to be somewhat younger, between 43 and 60 ka. This younger age may indicate that the tsunami deposits may not be related to this collapse.

The volume of the Fogo collapse has also been disputed (Figure 4.6B). Day et al. (1999) suggested a volume of 150 – 200 km^3. Masson et al. (2008) used bathymetry to estimate a volume of 130-160 km^3. Madeira et al. (2008) suggested that 60-70 km^3 is a reasonable estimate. Paris et al. (2011) calculated the avalanche volume to be 115 km^3. A similar estimate by Martínez-Moreno et al. (2018) is 110 km^3. Marques et al. (2019) calculated a volume of 20 km^3 for a shallow scar and 120 km^3 for a deep scar. Estimates of the volumes of this collapse vary hugely, due to the different assumptions about the shape and size of the collapse scar and whether submarine failure is included or not. In addition, the assumed depth of the scarp can have a large influence on the resultant volumes, as suggested in Day et al. (1999) where a proposed deep slide plane and shallow slide plane were compared giving a large range of proposed volumes.

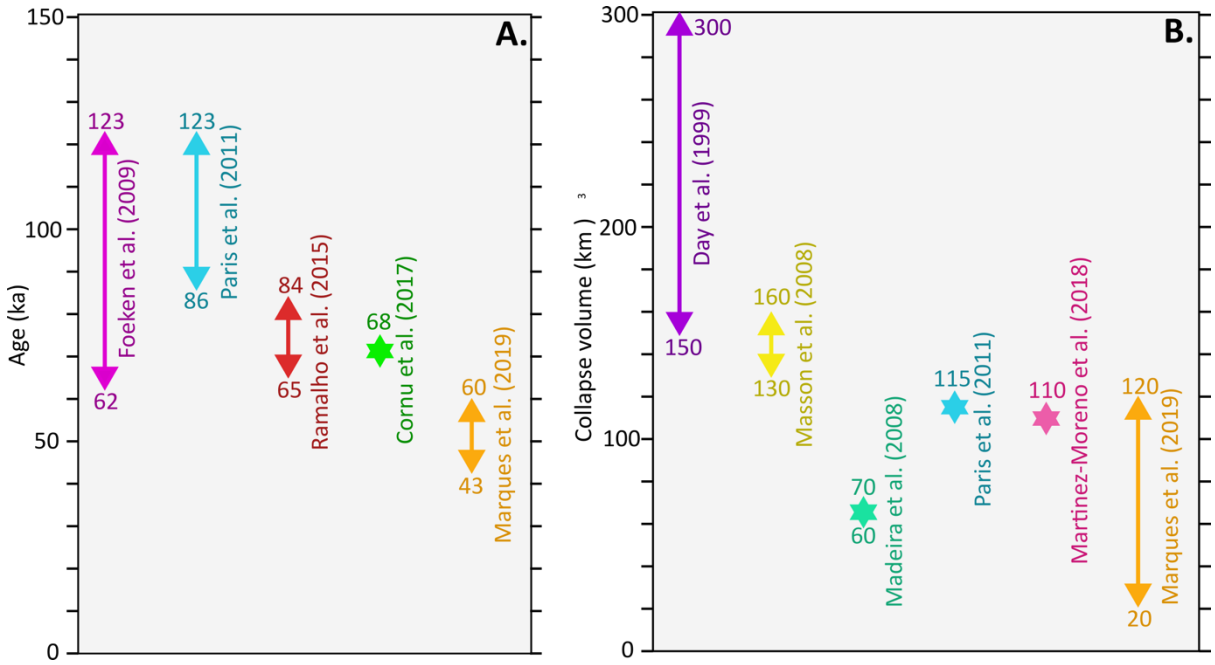

Figure 4.6: Summary figure of previous literature estimates of A. Age of collapse and B. Volume of collapse at Fogo.

There is a high probability of a future collapse occurring towards the east because of the morphology of Pico do Fogo increasing the weight of overburden on dipping unstable volcanic deposits (Marques et al., 2019, Day et al., 1999, Paris et al., 2011). The recent magmatism has now moved away from the central conduit of Pico do Fogo and is now exhibited in N-S trending eruptions on its western flank. This indicates a reorganising of volcanic plumbing that may be indicative of a change in stress regime as the Pico begins to move eastward (Marques et al., 2019, Day et al., 1999, Paris et al., 2011).

4.2.7 Fogo stratigraphy and evolution

The island's geology has been mapped and divided into various stages of construction. Units have been defined by Day et al. (1999) and Foeken et al. (2009), simplified in Figure 4.9 from Rolfe-Betts et al. (2024), subsequently described and renamed by Marques et al. (2019) and mapped by Martínez-Moreno et al. (2018) (Figure 4.7). The island began with its seamount stage with the oldest units as part of an uplifted seamount series consisting of carbonatites and alkaline basaltic dykes dated at around 4.5 Ma (Foeken et al., 2009). The first subaerial lavas, the 'Monte Barro Group', erupted unconformably onto this unit (Foeken et al., 2009). The lower sedimentary unit fills a major unconformity between this underlying complex and the 'Lower Volcanic Complex' (Marques et al., 2019).

The ‘Lower Volcanic Complex’ overlies the conglomerates of the Lower Sedimentary Group and is composed of lavas and pyroclastic deposits cut by dykes and dated between 160 and 212 ka (Marques et al., 2019). Marques et al. (2019) distinguished the Lower Volcanic Complex from the overlying Intermediate Volcanic Complex whereas Day et al. (1999) described them together as the ‘Monte Amarelo Group’ (Figure 4.9). These are seen throughout the Bordeira cliff. According to Marques et al. (2019), the green colour of the ‘Lower Volcanic Complex’ is metasomatic, because of the numerous dyke intrusions. This differentiates it from the ‘Intermediate Volcanic Complex’ rocks which are redder. The ‘Intermediate Volcanic Complex’ is composed of thick lava flows and pyroclastic strombolian deposits and extends to the top of the Bordeira cliff, includes cones dissected by the scar and dated between 59 and 158 ka (Marques et al., 2019). The ‘unconformity’ between groups is not suggested to be erosive but possibly due to a change in main vent location (Marques et al., 2019).

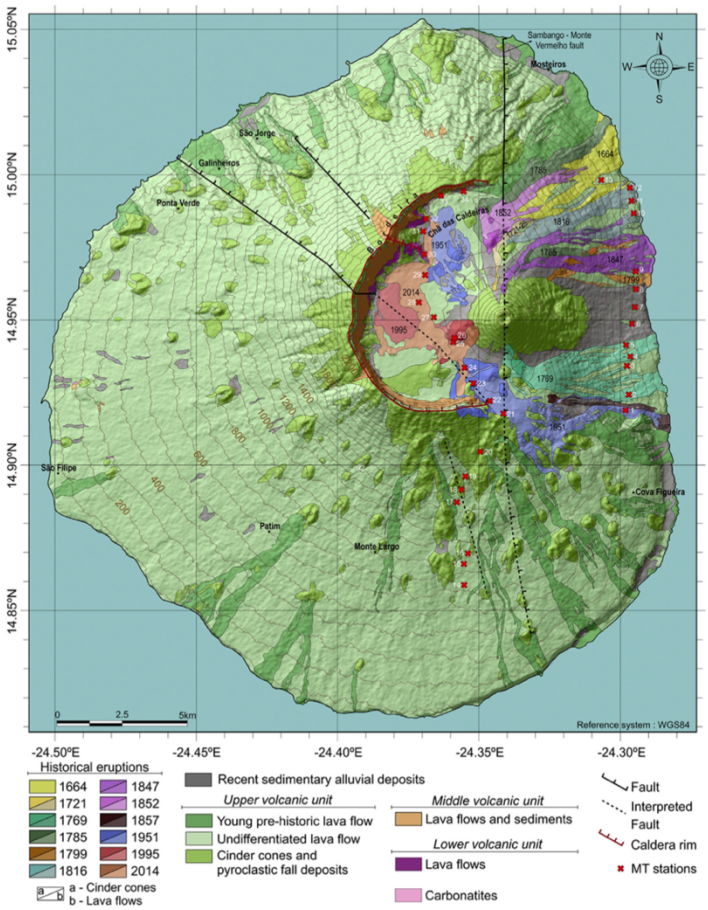

Figure 4.7: Geological map of Fogo from Martinez-Moreno et al. (2018)

The ‘Monte Amarelo Group’ was built by intense volcanism and consists of highly alkaline basic to intermediate lavas, scoria and spatter cones, lapilli and breccia units, with a

thickness of 2-3 km (Foeken et al., 2009). Dips within this group range from 20 to 40° and dip radially outwards. Day et al. (1999) used these directions to extrapolate an eruptive centre south of the Monte Amarelo spur. This was later revised to suggest that the lavas from the 'Bordeira Formation' were fed by radial dykes from three eruptive centres aligned on a N-S trend (Figure 4.10) (Rolfe-Betts et al., 2024).

Four major dyke swarms have been identified by Day et al. (1999). These trend S-SE in the SE Bordeira, trend WSW in the SW and west, trend WNW to the north of Monte Amarelo and NNE-N in the NE of the Bordeira cliff. Most dykes are vertical with some inclined sheets and sills (Day et al., 1999, Marques et al., 2019). Many of these radially trending dykes extend all the way up the cliff and are likely to have fed vent eruptions on the pre-collapse flanks. This agrees with the observed distribution of scoria cones. Marques et al. (2019) extrapolated these radially trending dykes to propose a centre of eruption. Figure 4.8 summarises the various published inferred locations of the pre-collapse volcano 'summit' or 'eruptive centre', highlighting the poorly constrained pre-collapse morphology.

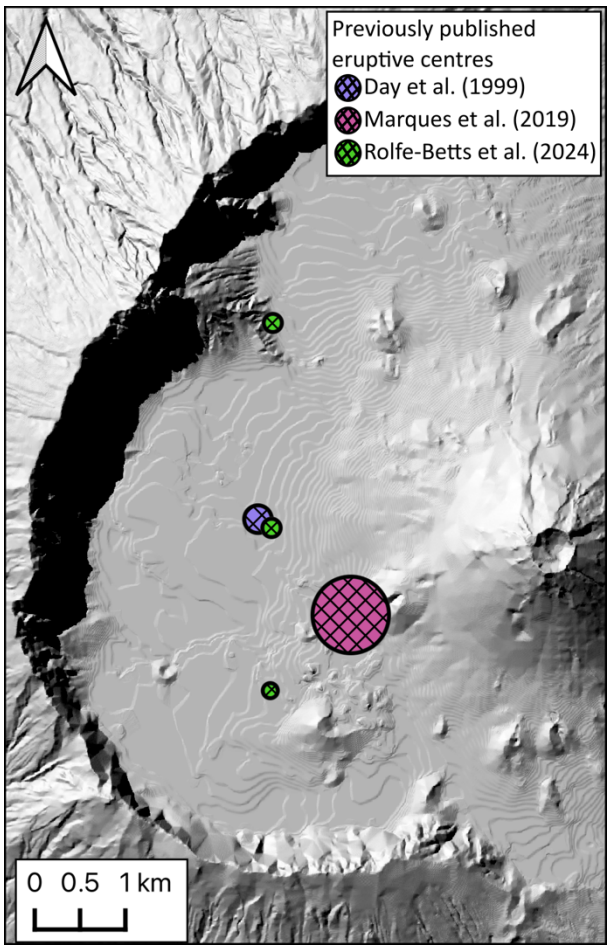

Figure 4.8: Summary of the locations suggested as the pre-collapse 'summit' or 'eruptive centre' as depicted in published works.

The younger formation within the 'Monte Amarelo Group', the 'Ribeira Aguadinha Formation', consists of ankaramitic lavas and are found primarily in the east where it is up to a few hundred meters thick (Rolfe-Betts et al., 2024). These flows were inferred to be fed by the N-S aligned dyke swarm and both the lavas and dykes are distinctive with abundant pyroxene phenocrysts (Rolfe-Betts et al., 2024). The shift to these younger N-S dykes marked a change in volcanic activity and the development of N-S trending dykes preceding collapse (Foeken et al., 2009, Rolfe-Betts et al., 2024). Prior to the Monte Amarelo collapse, the E-W trending rift zone was abandoned and activity became concentrated along the NNE-SSW and SE-NW zones (Foeken et al., 2009).

Cha das Caldeiras Group	**Monte Orlando Formation**	**All historic lavas since 1785 BCE Erupted from vents within collapse scar, mainly on N-S fissure trends**
	End of summit eruptions from Pico do Fogo (18th Century)	
	Portela Formation	**Continued intense eruptive activity within the collapse scar Scattered lavas outside collapse scar from vents on NE and SW rifts**
	End of coastal cliff formation (early Holocene?) and cessation of eruptions in SW of Fogo (~9 ka)	
	Monte Duarte Formation	**Thick sequence of lavas within collapse scar (earliest post-collapse rocks poorly exposed). Varied lavas forming thin veneer outside collapse scar**
	Monte Amarelo lateral collapse	
Monte Amarelo Group	**Ribeira Aguadinha Formation**	**Strongly pyroxene-phyric lavas erupted from vents on dominant N-S dike swarm**
	Structural reconfiguration of Monte Amarelo volcano	
	Bordeira Formation	**Lavas erupted from three overlapping volcanic centres each with radial dike swarms**
Major unconformity – valley incision and coastal erosion		
Monte Barro Group (earliest subaerial lavas)		
Major unconformity – emergence of island		
Ribeira de Almada Group (alkali basic seamount series with carbonatite intrusions)		

Figure 4.9: A Simplified stratigraphy for Fogo from Rolfe-Betts. (2024).

The post-collapse stratigraphic units, named the 'Chã das Caldeiras Group' or 'Upper Volcano-Sedimentary Complex', overlies the 'Monte Amarelo Group' or 'Intermediate Volcanic Group'. This group is split into the 'Monte Duarte Formation', 'Portela Formation' and the 'Monte Orlando Formation', the latter separated by the halt of eruptive activity from the Pico do Fogo in the 18th century (Foeken et al., 2009, Rolfe-Betts et al., 2024). This series of post-collapse rocks also includes lahar units, talus and thin lavas at the base of Bordeira cliff

and lavas that flow over the scarp, dating this unit to between 43 and 0 ka (Marques et al., 2019).

The 'Monte Orlando Formation' marks the end of activity from the summit of the Pico. It also marked the development of new N-S aligned vent zones on the western flank of Pico do Fogo in the last 11 ka (Figure 4.9). This might suggest a similar reorganisation of magmatic plumbing and be an indication of instability (Day et al., 1999, Foeken et al., 2009, Rolfe-Betts et al., 2024).

A study of pre- and post-collapse lavas has indicated that there is no major shift in composition between them (Rolfe-Betts et al., 2024). The lavas show a generally increasing trend of alteration with increasing age (Rolfe-Betts et al., 2024).

A NE-SW trending normal fault thought to outcrop on the northern flank of Fogo is suggested to extend to the SE beneath the post-collapse lavas (Carvalho et al., 2022).

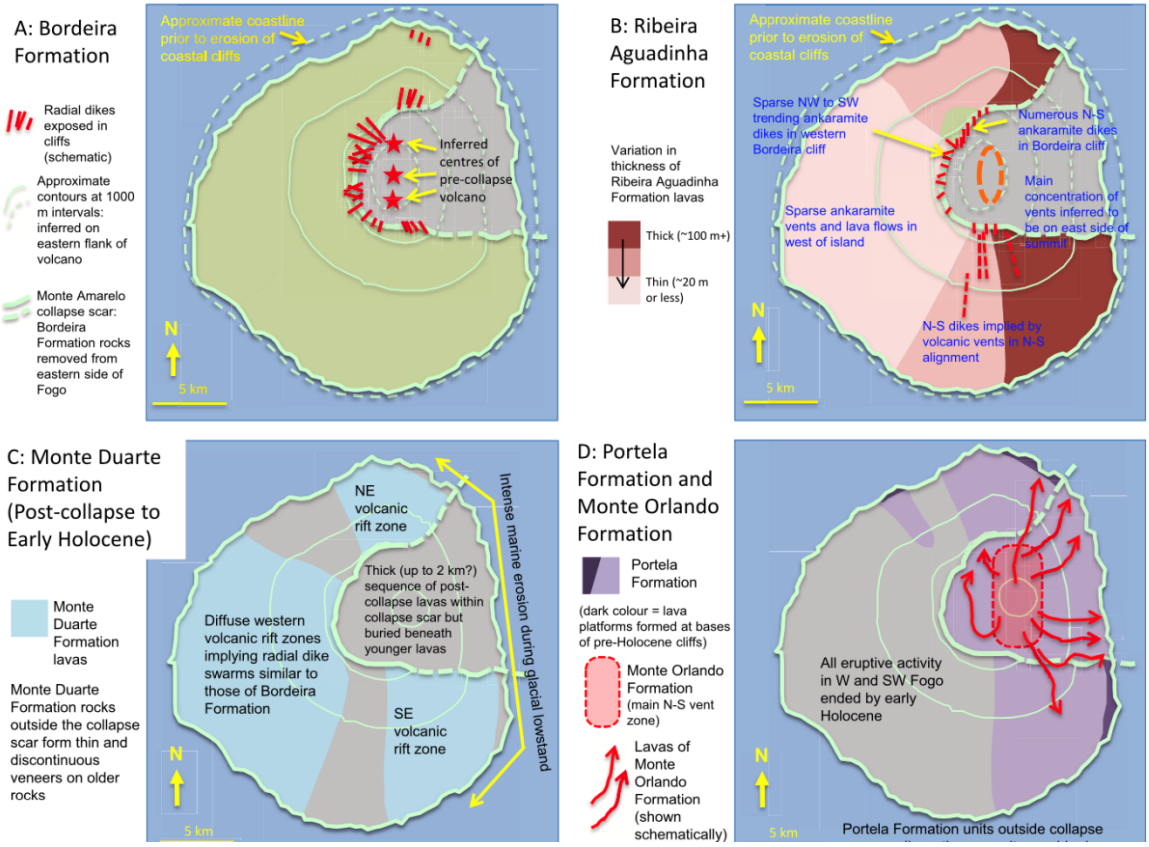

Figure 4.10: Geological history of Fogo Island highlighting the major stages of formation pre- and post-collapse from Rolfe-Betts et al. (2024)

4.3 Fogo methodology

4.3.1 Summary of available data

Some pre-existing data relating to Fogo Island was used in this chapter, summarised here:

- STRM 30 m resolution DEM from USGS Earth Explorer. In this thesis it is referred to as '30 m DEM' (Figure 4.11B). This dataset contained gaps in elevation along the Bordeira cliff and on Pico do Fogo.
- Fogo Orthomosaic tiles with resolution of 50 cm/px (Figure 4.11), (sourced from Bruno Faria, National Institute of Meteorology and Geophysics, Cape Verde)
- Fogo Hill shade raster (sourced from Bruno Faria, National Institute of Meteorology and Geophysics, Cape Verde)

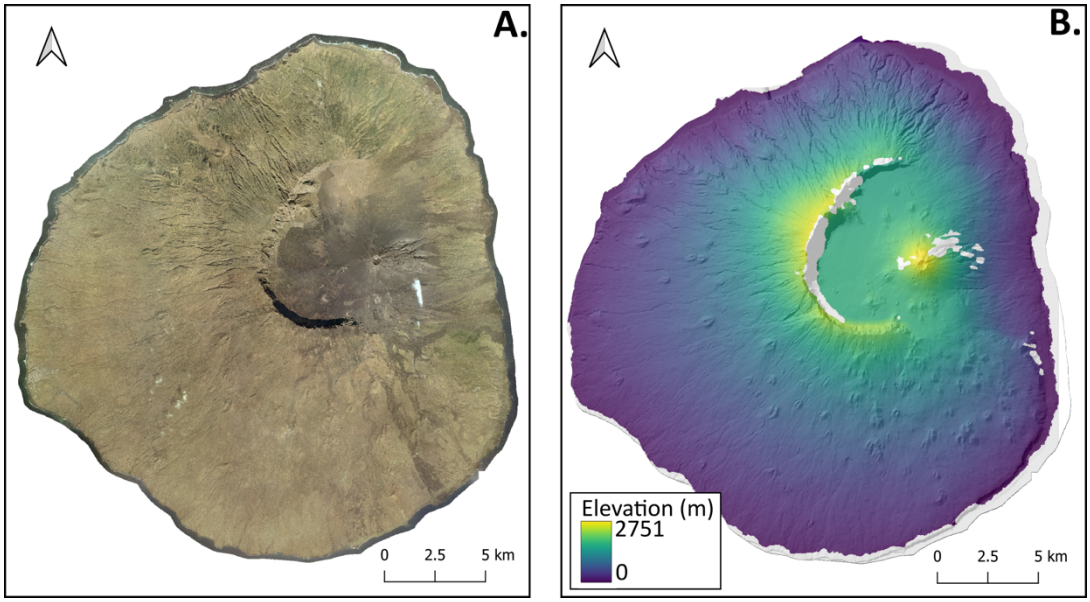

Figure 4.11: A. 50 cm/px orthomosaic dataset of Fogo. B. 30 m resolution DEM of Fogo.

4.3.2 Fieldwork methods

4.3.2.1 Fieldwork objectives

Although available data for Fogo was good, the elevation dataset had large chunks missing particularly over the area of the cliff and the resolution of the orthoimages and elevation were too coarse to analyse the structures in the cliff in detail (Figure 4.11). Therefore, the main aim of the fieldwork to Fogo was to collect drone imagery of the Bordeira cliff in order to create a high resolution orthoimage and elevation dataset for this region. In addition, no work has previously been done to assess the mechanical properties of the rocks of Fogo so a second

aim was to collect material for this purpose. Fieldwork was undertaken on Fogo over 11 days in December 2022 with several proposed data collection activities planned to further understand the Monte Amarelo collapse. The objectives included conducting a drone imagery survey of the Bordeira cliff, sample collection, taking structural measurements and geological observations.

4.3.2.2 Drone Survey

A drone survey was carried out to collect imagery of the Bordeira cliff. This data was collected with the intention of generating a high-resolution SfM model of the upper detachment scarp of the prehistoric volcanic collapse of the Island. Although datasets of Fogo were available, such as a set of orthophotos and a low resolution DEMs, further data collection was essential to study the Bordeira cliff in detail. The area of the Bordeira cliff was not covered in the 30 m resolution DEM available and the orthomosaic tiles were too coarse to be able to map individual structures in the cliff in detail. The 3D model generated from drone imagery produced a georeferenced DEM (digital elevation model). In addition to the DEM, a high resolution orthomosaic was produced. This orthomosaic was generated as plan view and from a side view facing the cliff. These both were essential in mapping the cliff.

Some indoor preparations were required before taking the UAV into the field before each launch point. This included charging the drone batteries and controllers, backing up drone images from the previous flight and ensuring SD cards had enough space for the next survey. Images were also backed up twice onto a rugged hard drive. The next excursions were also planned based on the prevailing weather and lighting conditions.

UAV laws in Cape Verde and worldwide state that a drone can only fly at an altitude of 120 m from the take-off elevation. As the Bordeira cliff reaches 1 km in height in some locations, careful considerations were made so the whole cliff could be imaged in the best quality possible. As the top of the cliff was too high in places to capture from different angles, the images of this were captured at an upward angle only. This means that the upper section of the model will be less confident due to eastward shallower dipping slopes of the structure being missed from this way of image acquisition. As described in Section 2.3.1, this is not the ideal method of image acquisition due to restrictions of the target object and topography.

The drone launch points were distributed evenly across the cliff base and were chosen to be as elevated as possible, as well as being flat. On some occasions where a flat surface

could not be accessed, a hand launch and landing method was used. A pre-plotted grid flight could not be used, as the intended feature to be imaged is vertical. Therefore, the drones were flown and images were captured manually. Where possible, the drone was flown and images were captured at a constant distance from the cliff to produce a model with a consistent resolution. Image overlap was insured for each consecutive image by keeping some of the field of view the same in each shot as the drone advanced.

Each flight started at a distance from the cliff to collect wider view shots to capture the whole cliff face. Following this, the drone was flown in vertical sections up and down the cliff, capturing images at many angles to increase coverage. Vertical sections were used rather than horizontal ones as long horizontal sections would have experienced the changing length of shadow as the drone travelled from one side to the other. Vertical sections were also favourable to be able to keep the drone within visual range whilst in flight.

Each launch location was accessed when the section of cliff was illuminated in the most optimal lighting conditions. Optimal lighting conditions include being in direct sunlight with minimal areas of shadows to reduce contrast between lighter and darker areas. For example, the central part of the cliff had more direct sunlight from late morning to mid-afternoon and the northern portion of the cliff had direct sunlight later in the evening. The southern part of the cliff was the most difficult to image, as it was in shadow for most of the day. Therefore, this portion of the cliff was only imaged in the afternoon to evening as, at these points of the day, the entire area was in shadow. This meant there would be no overexposed or underexposed areas of the images. This aspect introduced some error into the model, particularly in the orthomosaic as the lighting is poorer and provides less contrast for the different rock types in the cliff.

Weather conditions also had to be considered as the drone was unable to fly in wet or windy conditions, with wind speeds > 19 mph. Generally, the conditions were favourable for drone flights due to the time of year, chosen for this reason, with only a few aborted launches due to high wind conditions. Wind conditions were assessed using weather forecasts and a test flight if the winds were approaching maximum wind speeds.

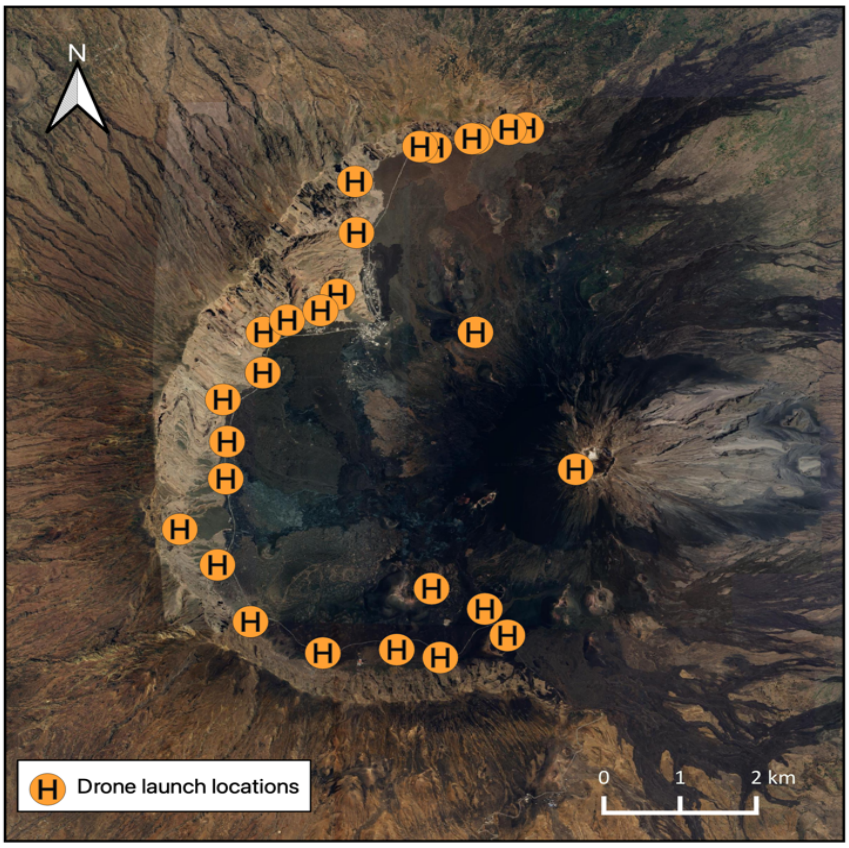

Figure 4.12: Drone launch points in Fogo, Cape Verde.

The primary drone used was a Mavic 3, which has an average flight time of 30 minutes per fully charged battery. As three batteries were used, this limited flight time before the need to return to base and recharge. Generally, two flight locations per day were achieved, depending on weather and light conditions. The secondary drone was a Mavic Pro which was carried in case of any malfunction of the Mavic 3. This was used as the secondary drone due to the reduced flight time and thus distance. In addition, the camera of the Mavic 3 has an improved ISO level which improves the ability to capture light, which was particularly important when imaging the southern cliff in shadier lower light conditions. A map of drone launch locations can be seen in Figure 4.12. The drone launch points were marked by a launch pad with GPS

coordinates taken to represent this point visually in the drone imagery to act as ground control points (GCPs) when generating the model (Figure 4.14B).

4.3.2.3 Sampling

Samples of different representative rocks across the Bordeira cliff were collected for laboratory experiments following fieldwork. By collecting a variety of samples, a dataset can show how different properties vary across the scarp. The intention was to collect samples from host rocks including different types of lava flow and pyroclastic units, and younger cross-cutting intrusion. Figure 4.13 shows the sample location map.

Samples were taken of common rock types encountered and categorised into 'host rock' or 'cross-cutting intrusion'. Samples were taken from the base of the cliff and therefore have a sampling bias due to the sample elevation being similar and therefore age of the rocks sampled are assumed to be of relatively similar ages compared to the entire stratigraphy of Fogo. Samples were cut down to a manageable size for travel but were at least large enough to obtain 15 mm cores for laboratory investigations.

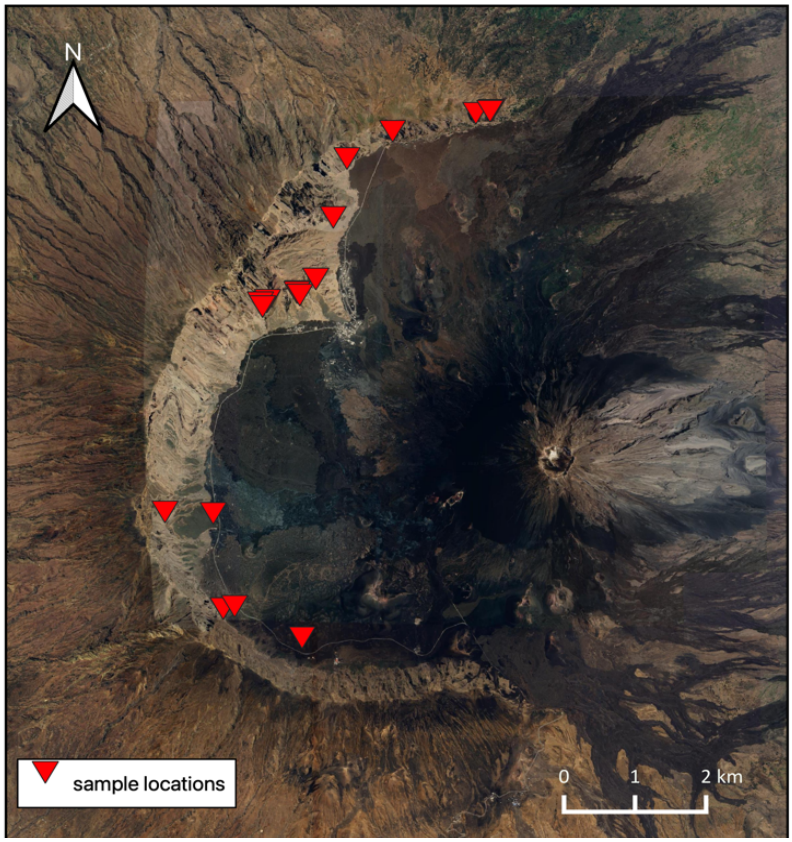

Figure 4.13: Sample locations in Fogo, Cape Verde.

4.3.2.4 Mapping and measurements

Measurements were taken of geological features with the intention of using these data points as ground-truthing points when digitally mapping the Bordeira cliff using the 3D model, DEM and orthomosaic. Measurements included the dyke and lava base orientation, as well as thicknesses and descriptions. To make the most of the time, outcrops were visited in the same localities as the drone launch sites. Measurements using a compass clinometer and recorded in a field notebook and on 'Field Move'.

Figure 4.14: Images of equipment used during fieldwork in Fogo; A. Bad Elf GPS. B. Mavic 3 Drone on orange launch pad. C. Screenshot of Field Move interface.

4.3.2.5 Other kit and applications

The GIS-based application 'Field Move' was used on an iPad Pro to record launch sites, sample locations and field measurements with their locations (Figure 4.14C). A 'Bad Elf' GPS device was used with Bluetooth connection to the iPad which gave accurate GPS locations (Figure 4.14A). These locations often had a greater associated error when very close to the base of the cliff at the highest point, due to the lack of satellites that could be used by the device. This application is useful as satellite layers were loaded into the project as a map and everything

is recorded within one project. This project and associated data were later exported and separated into GIS compatible shapefiles.

A Garmin 360 camera was also taken in the field and an image was taken at launch points, outcrops and key localities with the intent of generating a 360° tour around the volcano to use as a resource following the trip.

4.3.3 Agisoft methods

The same SfM modelling technique was used as described in section 2.3.2.1 using the images of the Bordeira cliff collected from fieldwork. The 16,000 images were subdivided into sections based on the location. Four sections of the Bordeira cliff are defined in Figure 4.15, including the 'Southern', the 'Central', 'Monte Amarelo' and 'Northern' chunks, as well as an additional chunk, 'Monte Beco'. Overlap of the chunks using the same images across different chunks were used to aid chunk alignment. A summary of camera count for each section can be seen in Table 4.1. As suggested here, the number of images does not necessarily reflect the resolution of the model, as it depends on the distance from the drone to the object. Additionally, a selection of the wider shot images was sampled for the whole Bordeira cliff to create a low-resolution model of the cliff.

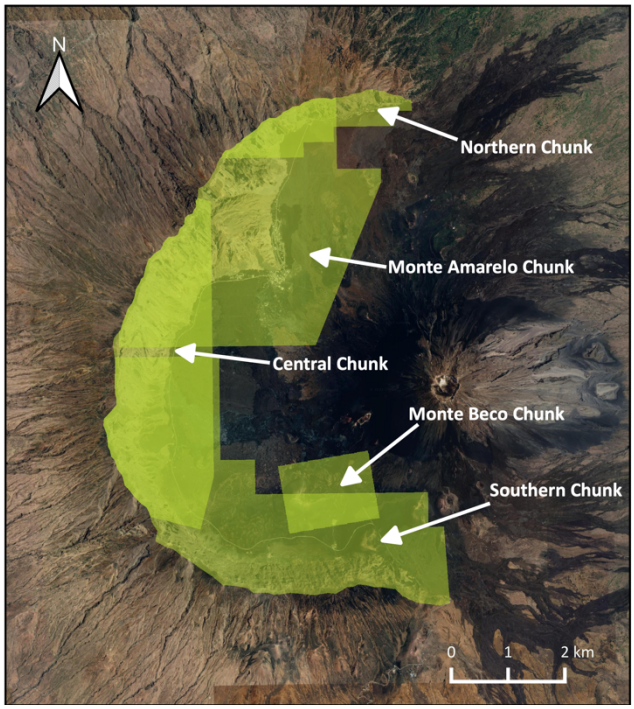

Figure 4.15: Bordeira Cliff separated into the chunks used for SfM modelling in Agisoft software.

Table 4.1: Table summarising number of cameras used per chunk and the maximum resolution of each chunk.

Chunk	No. cameras	maximum resolution (cm/px)
Northern	4149	6.09
Monte Amarelo	4002	7.75
Central	4502	5.09
Southern	3363	2.67
Monte Beco	550	4.36

The resultant orthoimages were overlain onto georeferenced base maps to determine the accuracy of the placement of the model based on the metadata of the drone imagery. The launch point GCPs were compared to the orthomosaic produced. Where the GCP was visible on the orthomosaic, the coordinates were compared to those collected at this point in the field (Figure 4.16A). These differences are summarised in Table 4.2. From this, it can be inferred that the longitude and latitude positioning of the orthomosaics and DEM is accurate to 3.5-6 m, with the maximum difference of around 10 m. However, the z values are consistently incorrect by an average of -111 m compared to the GPS coordinates. This elevation discrepancy is often the case in drone coverage. The GPS records of altitude, however, are also not wholly reliable in places due to the presence of the Bordeira cliff. These were compared to the 30 m/px DEM to validate elevation readings. Accuracy from this greatly varies and therefore the whole resultant model DEM was compared to the 30 m DEM to assess the average elevation difference which was calculated at -133 m. This value was used to adjust the whole model (Figure 4.16B).

Table 4.2: Table summarising the difference in coordinates from the GPS measurements and the SfM model produced

	X difference (m)	Y difference (m)	Z difference (m)
Mean	3.5	1.5	-111.2
upper quartile	5.9	3.5	-84.1
lower quartile	0.3	-1.7	-129.4
maximum difference	11.3	10.8	-145.6

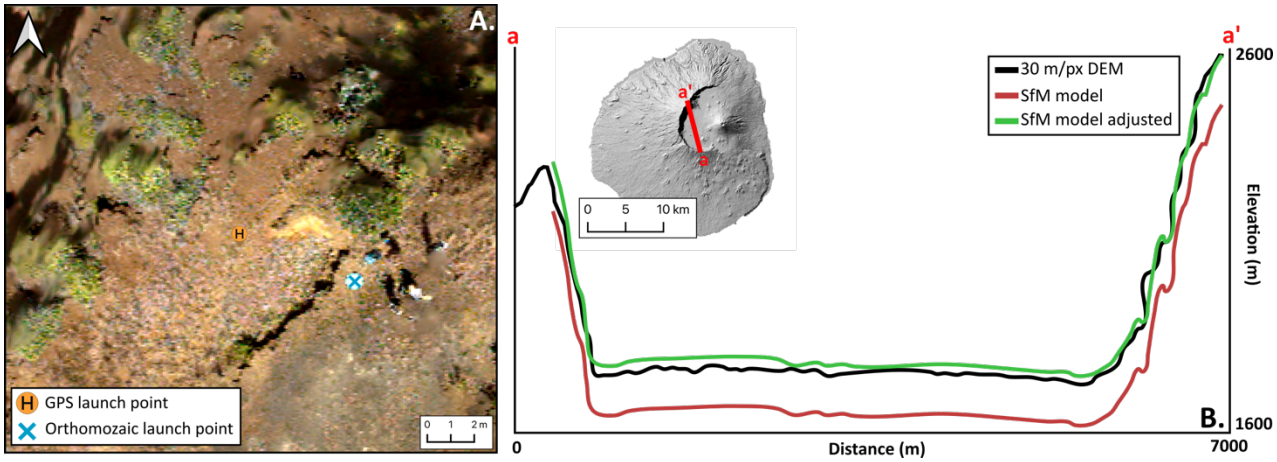

Figure 4.16: A. The orthomosaic image generated from the SfM model indicating the location of the drone launch GCP and the GPS recorded GCP. B. A section through Fogo representing elevation of the 30 m/px DEM alongside the DEM of the SfM model before and after elevation adjustment.

High resolution 3D models were also built of areas of interest (Figure 4.17). These areas of interest include a feeder dyke that can be traced to the surface. This dyke was identified by Marques et al. (2019) and the cone which the dyke fed was dated at 59 ka. Another close up is a region of crosscutting dykes on Monte Amarelo. This region shows the complexity of cross-cutting relationships and a key example of the N-S darker dykes. An area of cross-cutting dykes in the south was also generated as a 3D model. These 3D models will be referred to in the results section with links to view the models. All model links can be found in appendix 2.

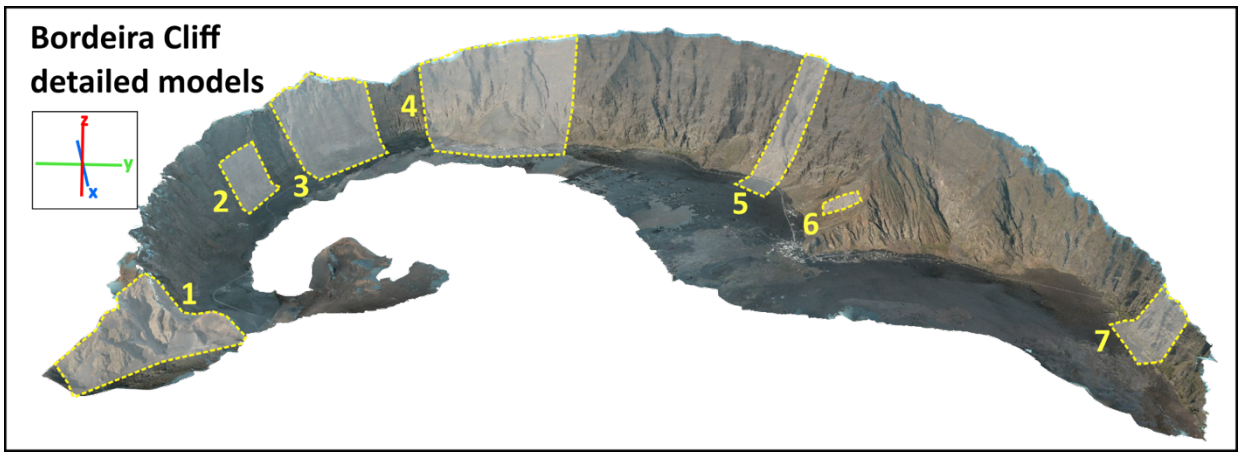

Figure 4.17: Highlighting areas where detailed 3D models were made of key features: 1. Shows dip of host rock beds at south edge of cliff. 2. Shows zone of high density of dykes in south cliff. 3. Shows dykes in cliff and sampled area. 4. Shows layering in cliff, cross-cutting dykes and post-collapse slopes. 5. Shows feeder dyke in cliff. 6. Shows cross-cutting dykes and N-S dykes in Monte Amarelo. 7. Shows layering and dykes in north cliff.

4.3.4 GIS analysis

4.3.4.1 GIS project settings

The local CRS (Coordinate Reference System) for the Cape Verde islands is UTM zone 26N ID: EPSG: 32626. Where some datasets used were originally projected in WGS84 or other, they were reprojected into UTM for consistency.

The 50 cm orthomosaic 30 m DEM were used to define the cliff top with a line shapefile. The orthomosaic produced in this chapter was used to define the cliff base. These line shapefiles were converted into a polygon shapefile to represent the cliff. This was then used to clip the DEM results to this shape.

4.3.4.2 DEM analysis

Slope analysis

The slopes of the 30 m DEM were analysed to assess the slope changes with elevation and to estimate a pre-collapse central peak. The morphology of the pre-collapse island is unknown; however, the current morphology indicates that slopes might have continued upwards to form a central summit. Assuming this, the slope analysis and the following process, similar to that used on Ritter Island in section 2.3.3.5, extrapolated slopes for a suggested pre-collapse peak and topography.

Initially, the topography was examined using transects across the island. This and whole slope analysis on the 30 m DEM allowed the trends of the slope to be identified. Separate slope analysis was done for different elevations to the west of the scar to define these differences. This was achieved by using contour lines to define the edges of polygons as the analysis areas according to specific elevations (Figure 4.18A)

This process was repeated to gauge the most representative average slope on the upper parts of the flank using the top of the scarp as the outer boundary to analysis areas (Figure 4.18B).

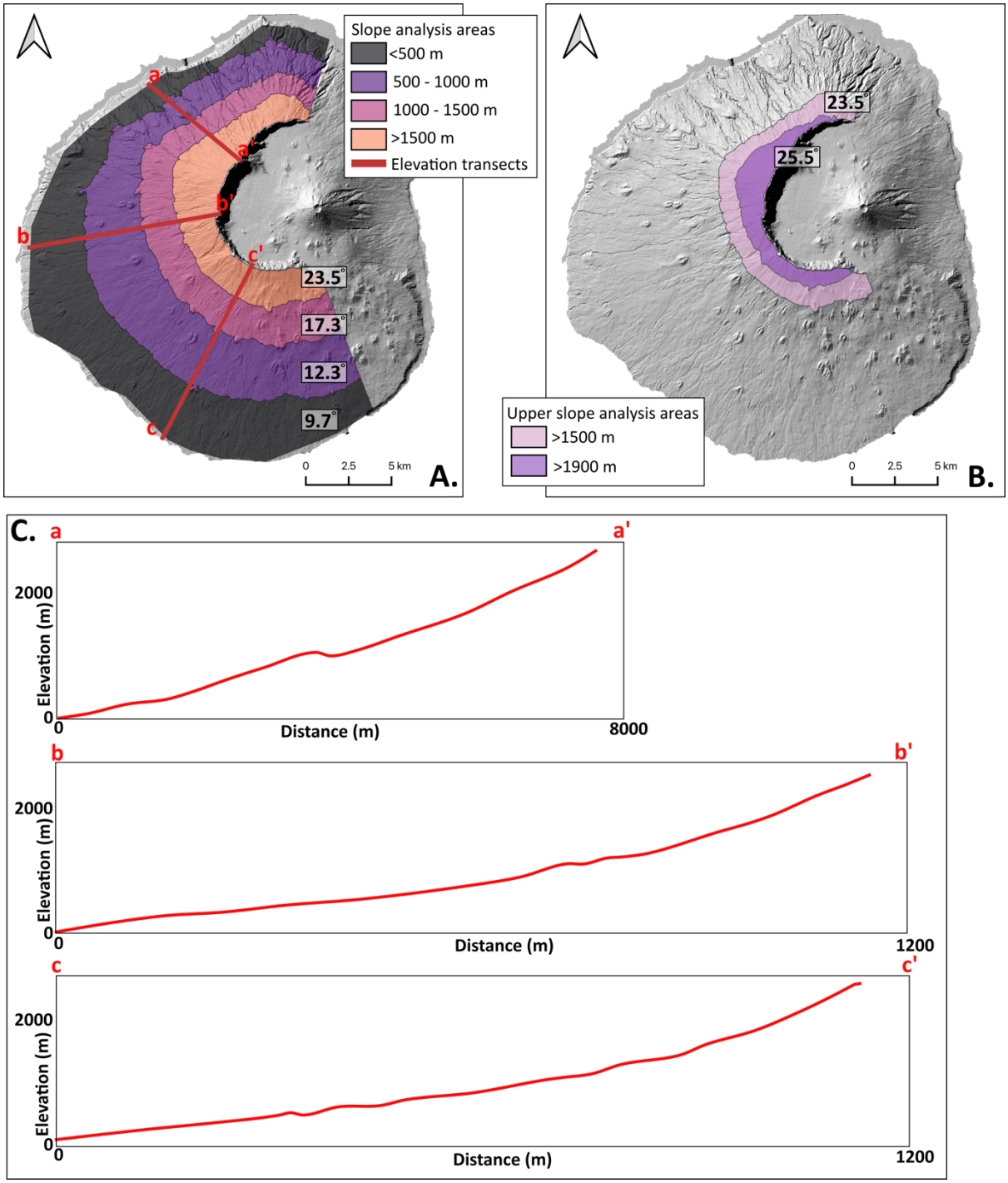

Figure 4.18: Slope analysis results on the western slope of Fogo using 30 m DEM. A. Shows comparison of average slopes by elevation. B. Shows the upper parts of the slopes average angle. C. shows elevation cross-sections through the slope in sections highlighted in A

Slope analysis was also done for the new cliff DEM. This used whole slope terrain analysis of the whole DEM and along transects (Figure 4.19A)Comparative slopes were estimated for the cliff face compared to the post-collapse deposits at the base of the cliff by using the shapefiles created for each area (Figure 4.19B).

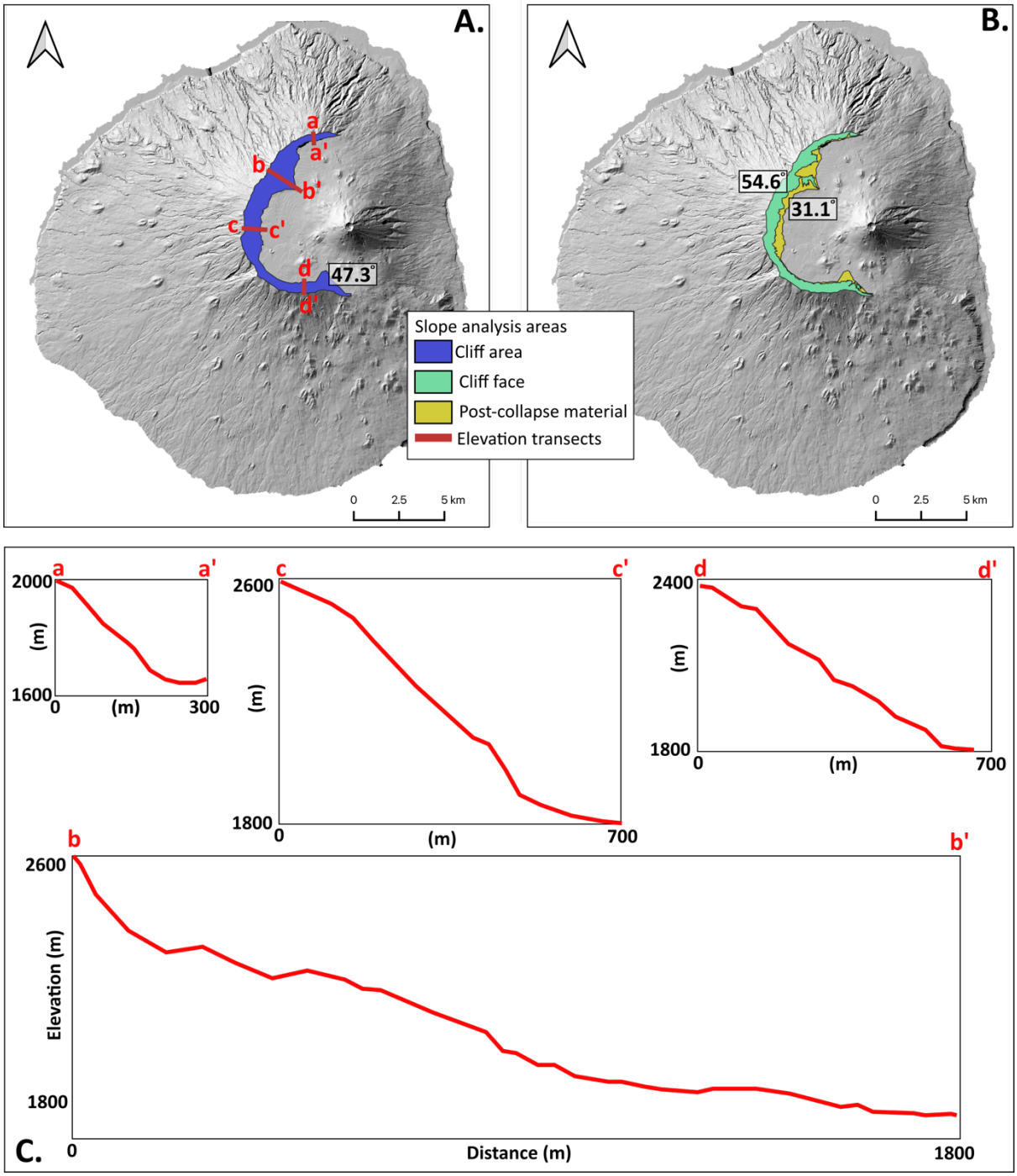

Figure 4.19: Slope analysis of the new DEM for the Bordeira cliff. A. shows the whole slope area B. shows the slope separated into the cliff and post-collapse deposits with results. C. shows elevation sections through the cliff at various transects depicted in A.

Assuming the outer slopes continued to rise at this angle consistently on the pre-collapse volcano, this value was used to project the slopes upwards and estimate the location of the peak of the island and hence the eruptive centre. Other estimates of the central summit of the pre-collapse volcano have been made by Day et al. (1999) using the dips measured on host rocks from the Bordeira cliff and also by other authors using dyke orientation, discussed later in this section.

To find this centre, points were created at 200 m spacing along the cliff top line shapefile and elevation data from each point was extracted from the 30 m STRM layer. The horizontal distance to an elevation of 3500, 3700 and 4000 m at this angle were calculated from each point to find the best-fit peak elevation based on this slope. For each cliff top point, polygon buffers were created with a spacing using this calculated horizontal distance to each the elevation from the point. Following the process in section 2.3.3.4, the intersecting areas between the polygons represent the regions at this elevation on the pre-collapse volcano and the central peak is deduced from the highest elevation. Other estimates of the centre are compared to this as discussed later.

Recreating pre- and post-collapse surfaces

Pre- and post-collapse surfaces have been estimated to gauge scar parameters and volume calculations.

The pre-collapse surface was made from the central peak estimate and the present-day western morphology. Points from the cliff top were joined to the central area and 100 m contour spacing was calculated finding the length to the centre and dividing this by the elevation difference over 100. To the east, the contours were constructed by eye and kept the steeper topography compared to the west, as it was suggested this is formed by the prevailing wind direction. TIN (Triangulated Irregular Network) interpolation of these contours was carried out with a pixel size of 50 m. TIN interpolation produces a triangulated network from known nearest point elevation information to produce a surface and is commonly used to interpolate elevation data. This was selected over using IDW (Inverse Distance Weighted) due to the regularity of the points taken from the contour lines and the smoother resulting surface.

The post-collapse topographies used the western morphology and also included the new cliff elevation data, minus the post-collapse deposits and the cliff scarp to the SE of the island, assumed to be part of the scarp.

The depth to the scar beneath the post-collapse deposits is difficult to estimate and therefore the resultant volume calculations using this surface will be uncertain. To calculate uncertainty, a minimum value was calculated using a shallow surface. The first post-collapse surface used a shallower scar to provide a minimum result, 100-200 m lower than the observed scarps and the contours were constructed manually using a constant slope to the east curving inwards slightly towards the scar. This surface is used to form the lower estimate.

The second surface uses the present-day slope within the collapse scar, with the Pico do Fogo rise flattened off. Then, using the average thickness of post-collapse lavas at 700 m suggested in (Martínez-Moreno et al., 2018), this value was removed from the present-day surface and merged onto the collapse scar manually. This forms an upper estimate of volume. Neither of these estimates extend the scarp underwater due to the insufficient data for the bathymetry available therefore the true volumes may be significantly higher than these estimates.

Volcanic scar metrics

As described in section 2.3.3.5, a series of scar metrics proposed by Bernard et al. (2021) were measured using the surfaces created above. Constraints on the morphology of the scar are difficult to assume for Fogo. For example, the depth of collapse is disputed though some previous estimates have been used here. Additionally, the positioning of sidewalls is debated and previous studies have suggested various placements. This uncertainty is due to the extensive post-collapse volcanism infill. The southern sidewall is more easily agreed upon than the northern due to the presence of a steep cliff which is assumed to be part of the scarp (Figure 4.20).

- For the scar length, the minimum was measured as the length to the observed scarp end and the maximum was measured to the coast. These are both subaerial estimates and may still be a minimum if the scar extends underwater, however the bathymetry data does not allow confirmation of this.
- The scar aperture width was also measured at the observed width where the scar is exposed and the estimated width at the coast where the scar is extrapolated east (Figure 4.20).
- The scar height, slope, depth, thickness and volume ranges were calculated from the two end-members of the post-collapse topography as described above.
- The ratios and factors were all calculated using the upper end of the values.

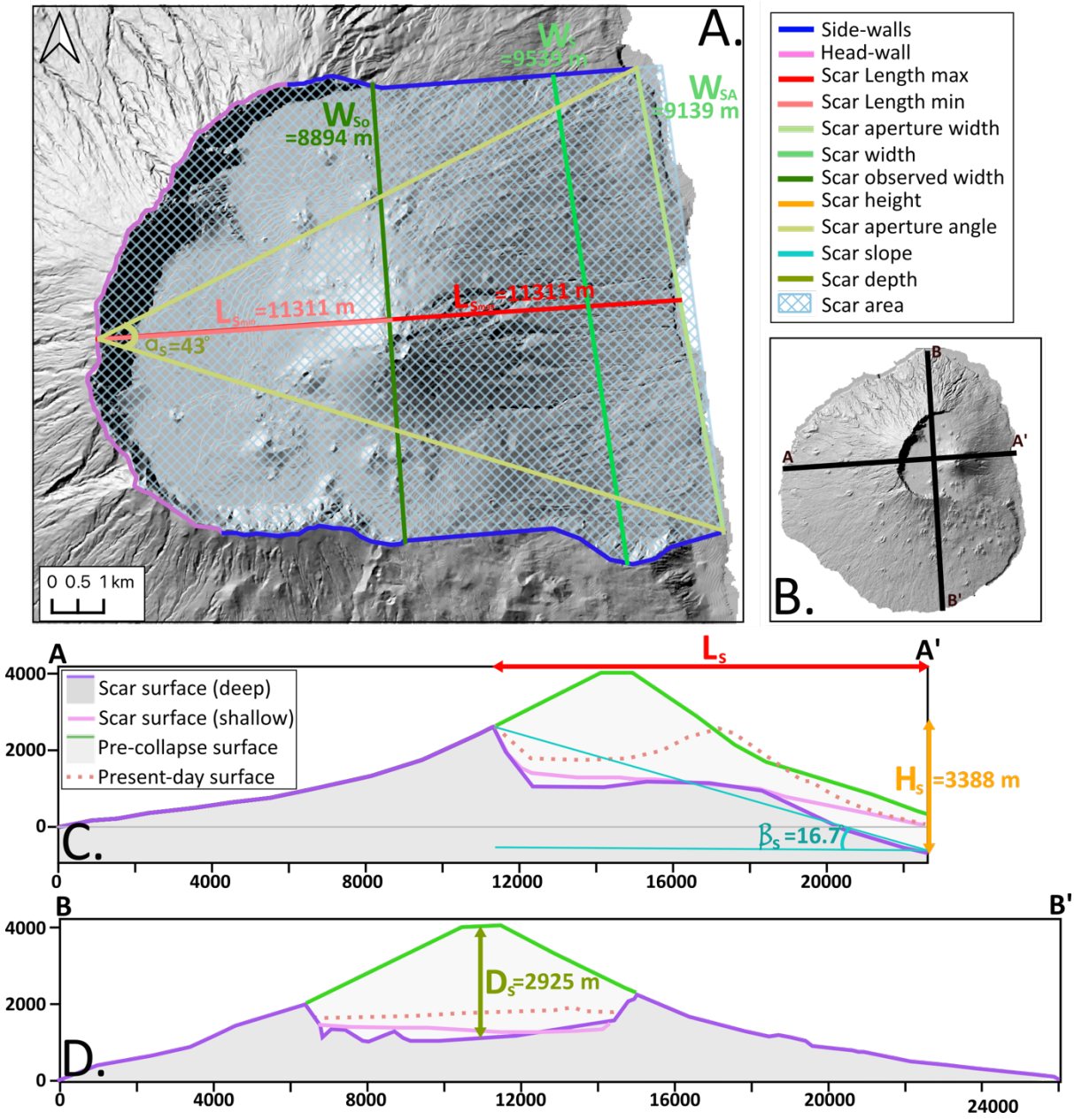

Figure 4.20: Results of scar measurements at Fogo A. map view B. showing where cross-sections are drawn. C. cross-section through section A, D. cross-section through section B.

4.3.5 Digital mapping

Several key mappable features were identified both in the field and in the drone imagery. These include the cross-cutting network of dykes, layering of the host rock, and the post-collapse material (Figure 4.21). These were mapped as line shapefiles overlaying the 3D model built on Agisoft using the process described in section **Error! Reference source not found.**.

One of the most prominent features of the Bordeira cliff is the network of cross-cutting dykes throughout. Identifiable dykes that could be seen on the model or on the overlain drone images were mapped as dyke traces as line shapefiles to their extent onto the 3D model.

Mapping as lines was chosen over polygons due to the scale of the cliff and the number of dykes to be mapped. The vertices of the line were positioned in the centre of the observed dyke so the line shape followed the trend. Due to the uncertainty identifying layers as sills or lava flows at this scale, sills were mapped only where they were distinct. Where the model is less accurate or reliable toward the top of the cliff due to accessibility issues, the 50 cm orthomosaic was also used to identify any further dykes.

In the field, some much darker dykes were often seen to cross-cut older dykes and generally trend N-S (Figure 4.21). These matched the description in Day et al. (1999). As these were distinguishable, particularly in the central spur, they were mapped separately to allow for separate analysis.

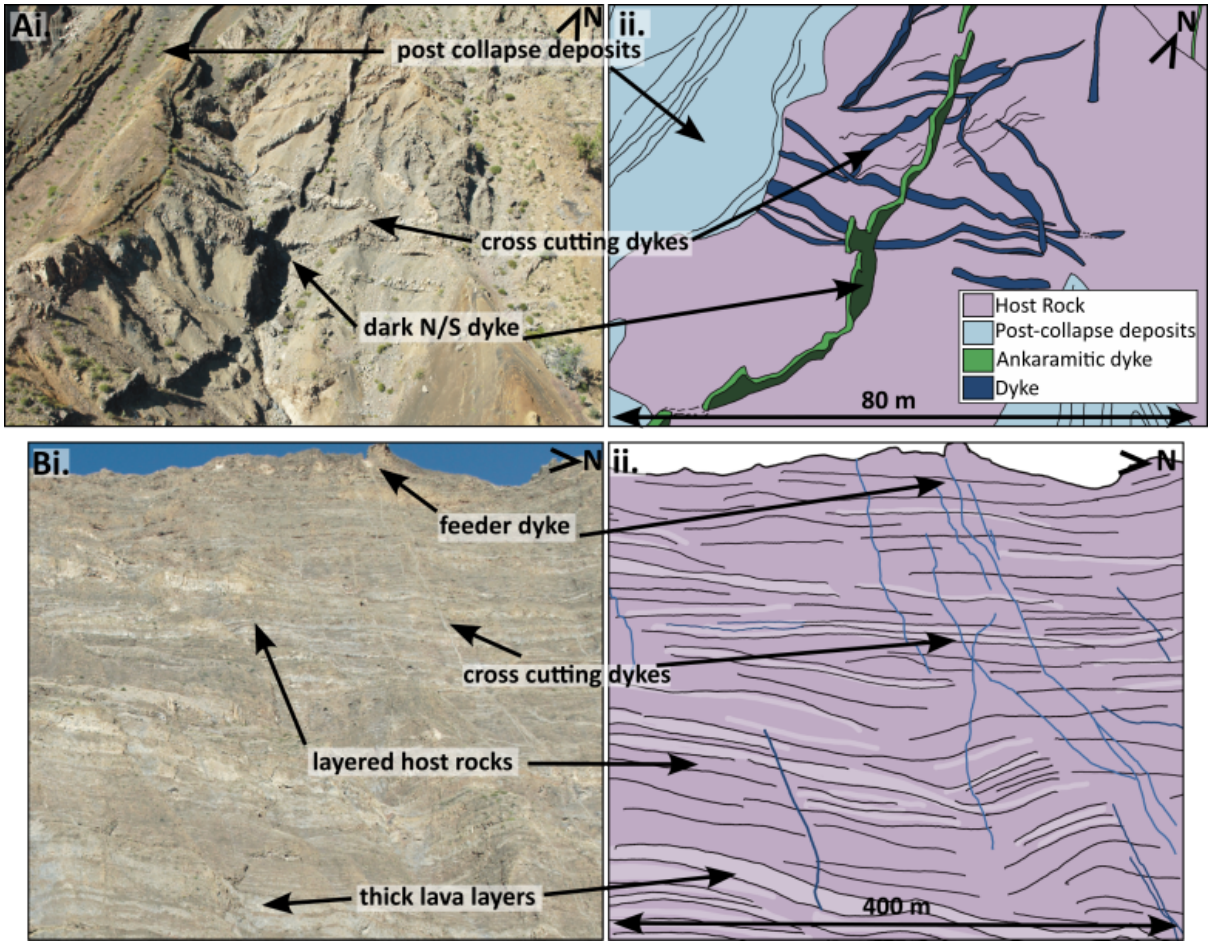

Figure 4.21:Field drone imagery with a sketch highlighting key mappable features at A. Monte Amarelo where examples dykes and post-collapse material are seen and B. in the central cliff face where the layered host rock can be seen with cross-cutting dykes and

Towards the base of the cliff there were some regions which represented post-collapse deposits. These included ash deposits and some lavas. The unconformity between this and the scarp beneath was mapped as was any bedding identified (Figure 4.22B).

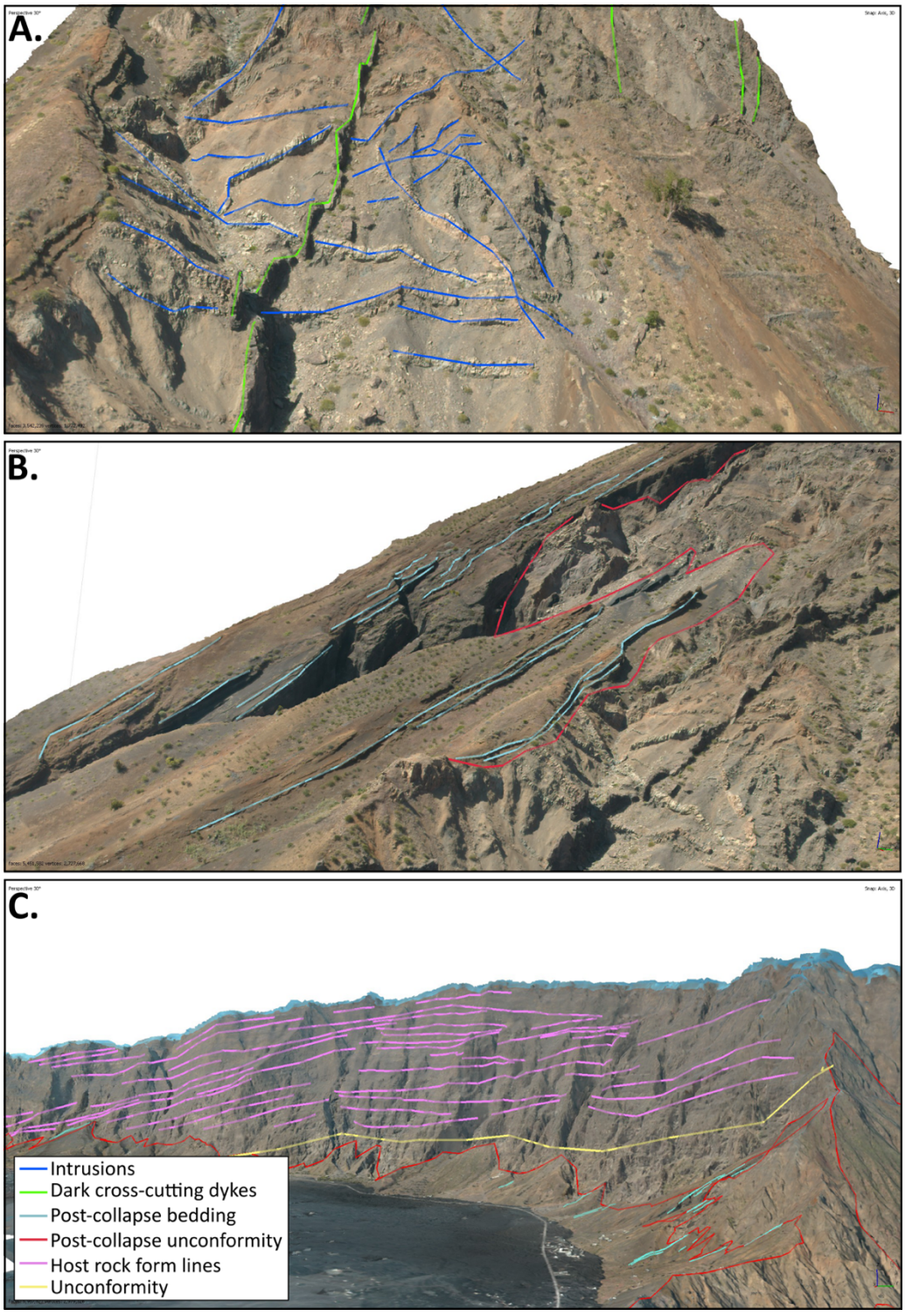

Figure 4.22: Examples of mappable features mapped as line shapefiles onto Agisoft mesh models. A. Monte Amarelo with mapped dykes, B. Monte Amarelo with mapped host rocks and C. Monte Amarelo and central cliff with mapped host rocks and post-collapse rocks.

The trend of the layered host rocks could be clearly seen on the wider drone shots, and these were mapped across the cliff (Figure 4.21B). These layers were mapped as form lines (Figure 4.22C).

Using the method described in section **Error! Reference source not found.**, strike and dip measurements were estimated for some of the dykes and post-collapse layering. Due to the large number of dykes mapped, only a selection of the dykes had their structural measurements taken using 'Move' software. A selection of the 142 dykes were measured in the central Monte Amarelo spur to characterise the 526 cross-cutting intrusions in this area. A collection of 52 dykes were also measured along the length of the Bordeira cliff to assess how the trends change by location. Rose plots were made of these orientations for analysis.

In addition, the orientation of the line traces was collected from all the mapped dykes using GIS to output the bearing from the start to the end point of the line. However, this will only represent the strike measurement on the steepest dykes. These were identified on the model as the dyke trends which cut in a straight line across the topography. 96 of these steep dykes were selected. The accuracy of this method was checked by comparing the line azimuths to the measured strikes. This found that the degree of error was ±5°.

Previously, Marques et al. (2019) measured 273 dykes to gauge trends and extrapolate their directions to infer a position of pre-collapse emission centre (Figure 4.24). Also using this dyke orientation method, three eruptive centres were inferred in Rolfe-Betts et al. (2024). This method was done for the dykes mapped in the Bordeira cliff here.

A combination of these orientations, measured dykes and field measurements was extrapolated along strike to find where they would cross in map view (Figure 4.23). This location of intersection may represent a centre of eruptive activity. The directions of the younger dykes were extrapolated along strike and compared to this location. In QGIS, this was done by extending from a point along each line or at the point of measurement using the 'Project points' tool and 'Points to Path' tool. The 'Line intersections' tool was used to find where these lines intersected and a Kernel density heatmap with a radius of 400 m was used to analyse the density of intersections and hence infer the central vent. This same method was used for the separately mapped N-S dykes to compare their trends to this.

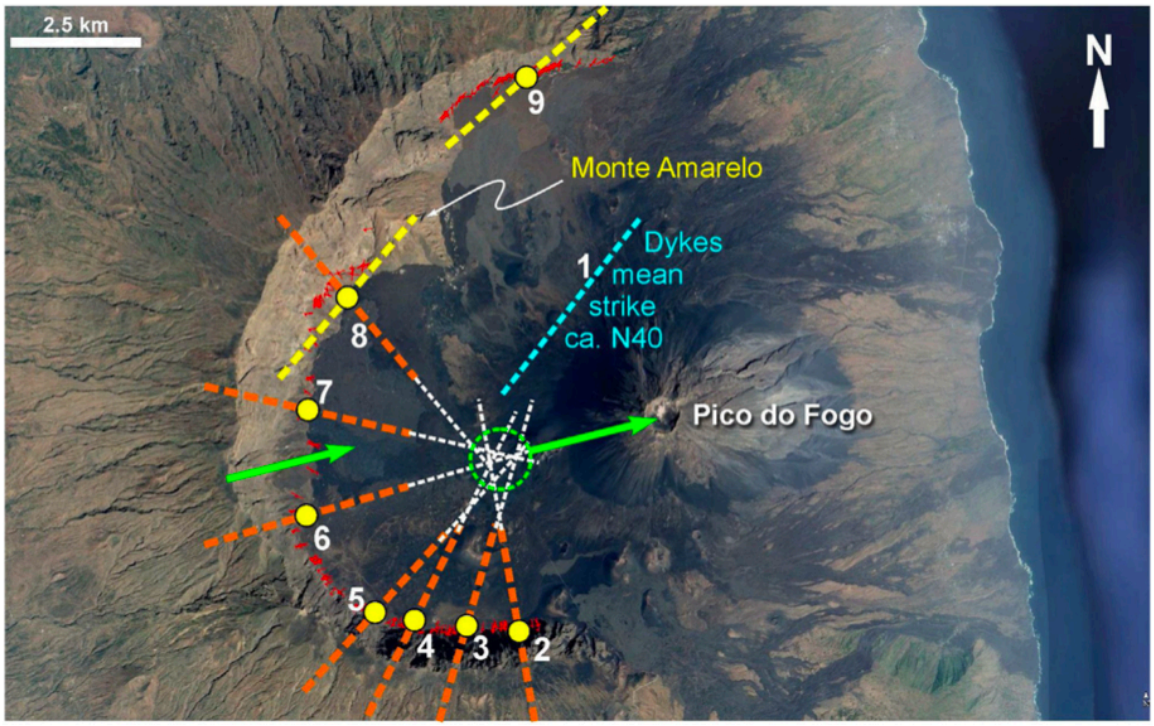

Figure 4.24: From Marques et al. 2019. Dyke trends measured at Fogo extrapolated to represent the centre of the volcano. Red: dykes, Orange: Fogo volcano trend of dykes, Yellow: Monte Amarelo trend of dykes, Blue: mean strike, Green compares displacement to collapse.

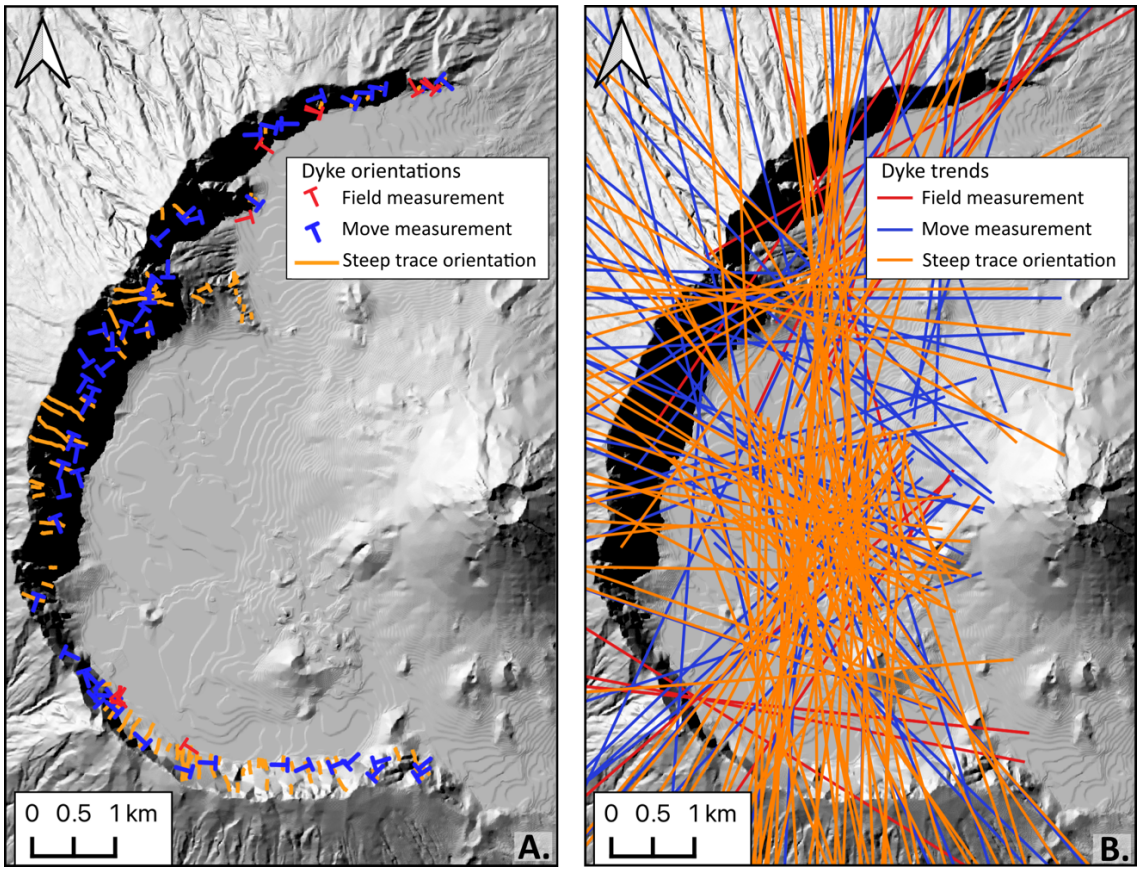

Figure 4.23: Method of extrapolating dyke trends to find eruptive centre. A. Source of orientations. B. Dyke trends according to measurement source.

An analysis of the density of dykes across the morphology of Fogo was then carried out. The line density was produced using GIS with a pixel size and search radius of 80 m. This was then repeated for the younger separated dykes and for the remaining dykes to assess their effect on the overall dyke density.

The dyke density was assessed in the X, Y and Z orientations. However, due to the curved shape of the scarp, apparent high densities occur where the traces are stacked. To remove this from the trend, sections were drawn 'stepped' to view how the density changed from east to west (Figure 4.25). The transect line was intersected with the dykes' shapefile to create an intersection-point shapefile. A grid was generated, spaced at 300 m, and used to count the number of points in each section to create a density histogram of dykes.

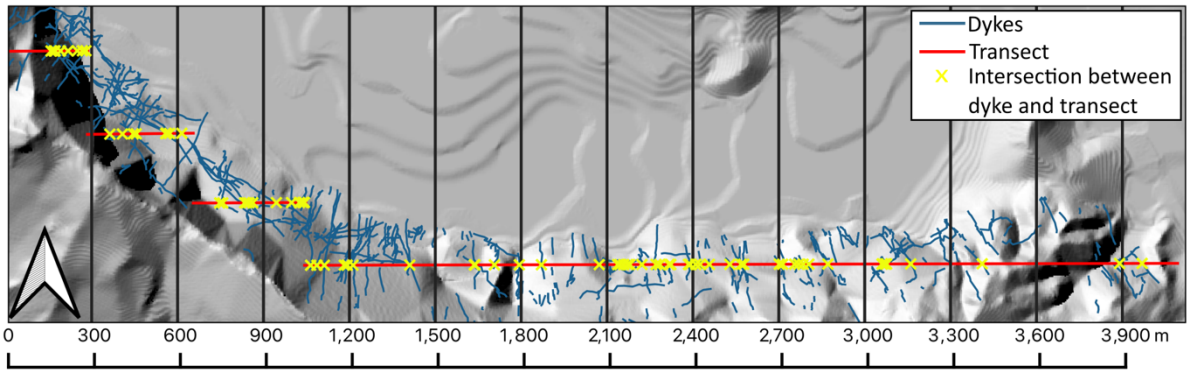

Figure 4.25: Method for creating a density histogram through a representative section of the south cliff.

4.3.6 Sample analysis

The samples collected in the field, as shown in Figure 4.13, were prepared into 15 mm cores for property measurement and analysis. The methodology for measuring porosity, permeability and uniaxial compressive strength of the sample cores was used as described in Chapter 3.

4.4 Fogo results

4.4.1 Model results

Using SfM modelling, a high-resolution model was produced of the Bordeira cliff, both as a whole and in smaller chunks. The resolution for some areas of the model was high enough to be centimetres per pixel. However, when dealing with the outputs as a whole, this resolution is too high for many computer systems to handle and therefore was decimated to a manageable level. For most chunks, this was 15 cm/px, however the following results will mention the maximum resolution using the denotation 'from'. The model outputs include:

- Whole cliff DEM and orthomosaics (map and side view) from 30cm/px (Figure 4.26A and Figure 4.28) (link to model: https://sketchfab.com/3d-models/fogo-bordeira-cliff-model-a4bc147fec8b4378a64d8bb799cf5b7e)
- Monte Amarelo chunk DEM and orthomosaic from 8 cm/px
- Central chunk DEM and orthomosaic from 5 cm/px
- Southern chunk DEM and orthomosaic from 3 cm/px
- Basemap using DEM data (Figure 4.26C)

Figure 4.27 displays the 3D model of the Bordeira cliff, in sections and in terms of the model confidence. This highlights how most of the cliff face model is well-constrained. The main areas of low confidence occur at the very top of the cliff face and in locations near the top facing upward or above protrusions in the cliff. This is due to the limitations of drone flight elevation. Other areas of low confidence occur on the flat plains of Chã das Caldeiras where drone coverage was minimal. These areas of low confidence are reflected in the orthomosaic as gaps or areas of low resolution or blur (Figure 4.26). In addition, some errors in chunk alignment and georeferencing in the northern chunk have resulted in a section of the model with a raised altitude although the latitude and longitude positioning is accurate. As a result of lighting restrictions, described in Section 4.3.2.2 , the portion of the south cliff imaged in shaded conditions result in a darker orthomosaic compared to the rest of the model (Figure 4.26 and Figure 4.28).

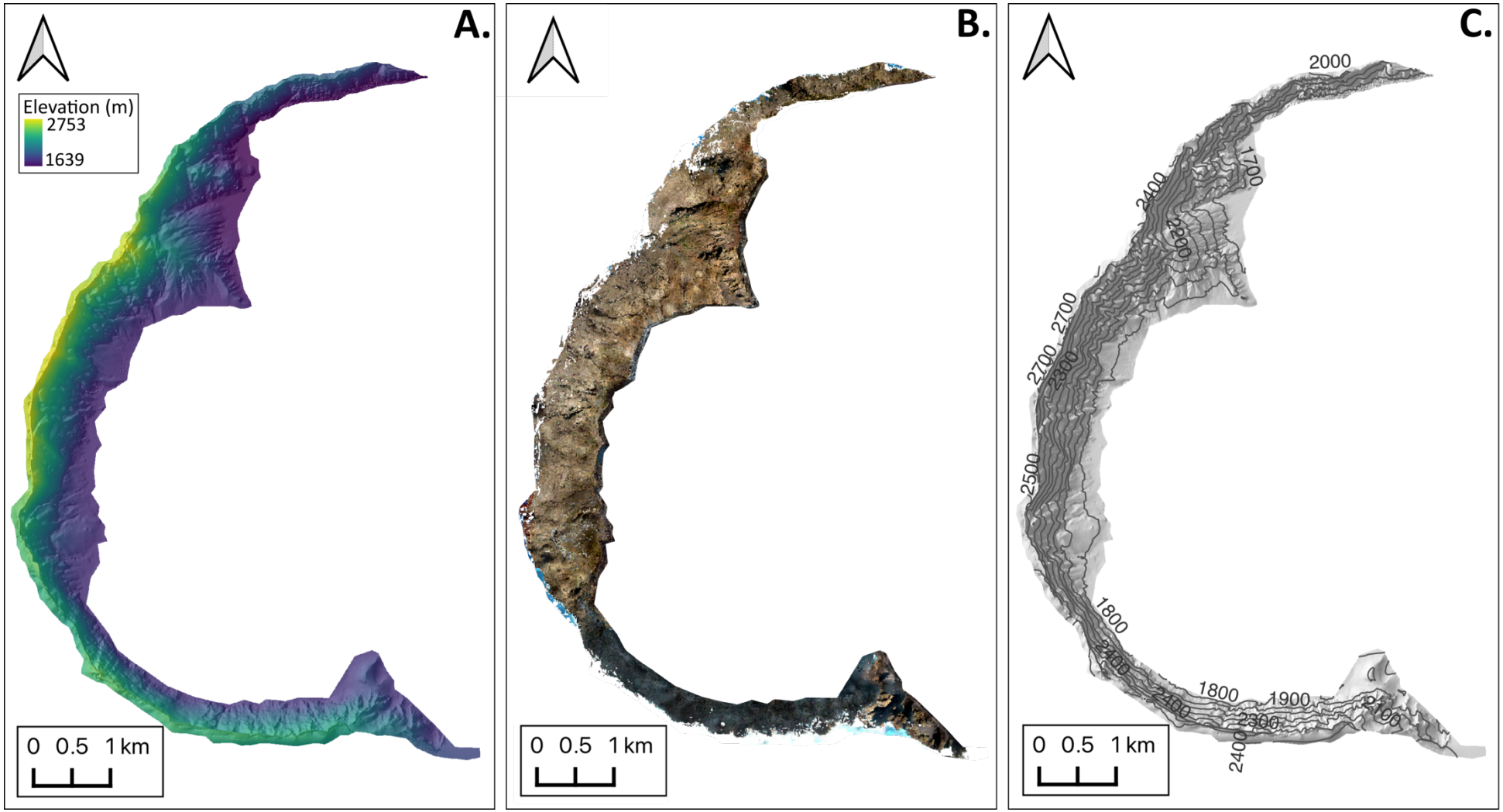

Figure 4.26: SfM modelling results of the Bordeira cliff, Fogo. A. DEM. B. Orthomosaic. C. Base map from hillshade and contour lines.

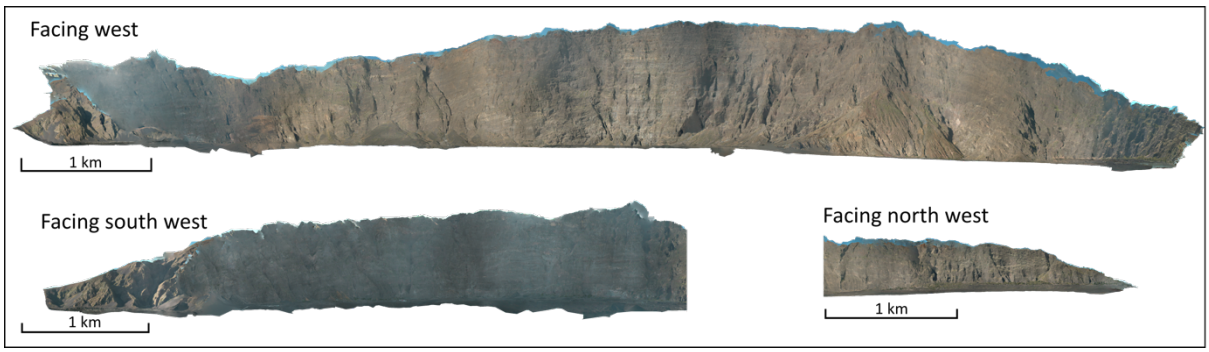

Figure 4.28: SfM modelling results of the Bordeira cliff, Fogo showing the side facing orthomosaics of the cliff.

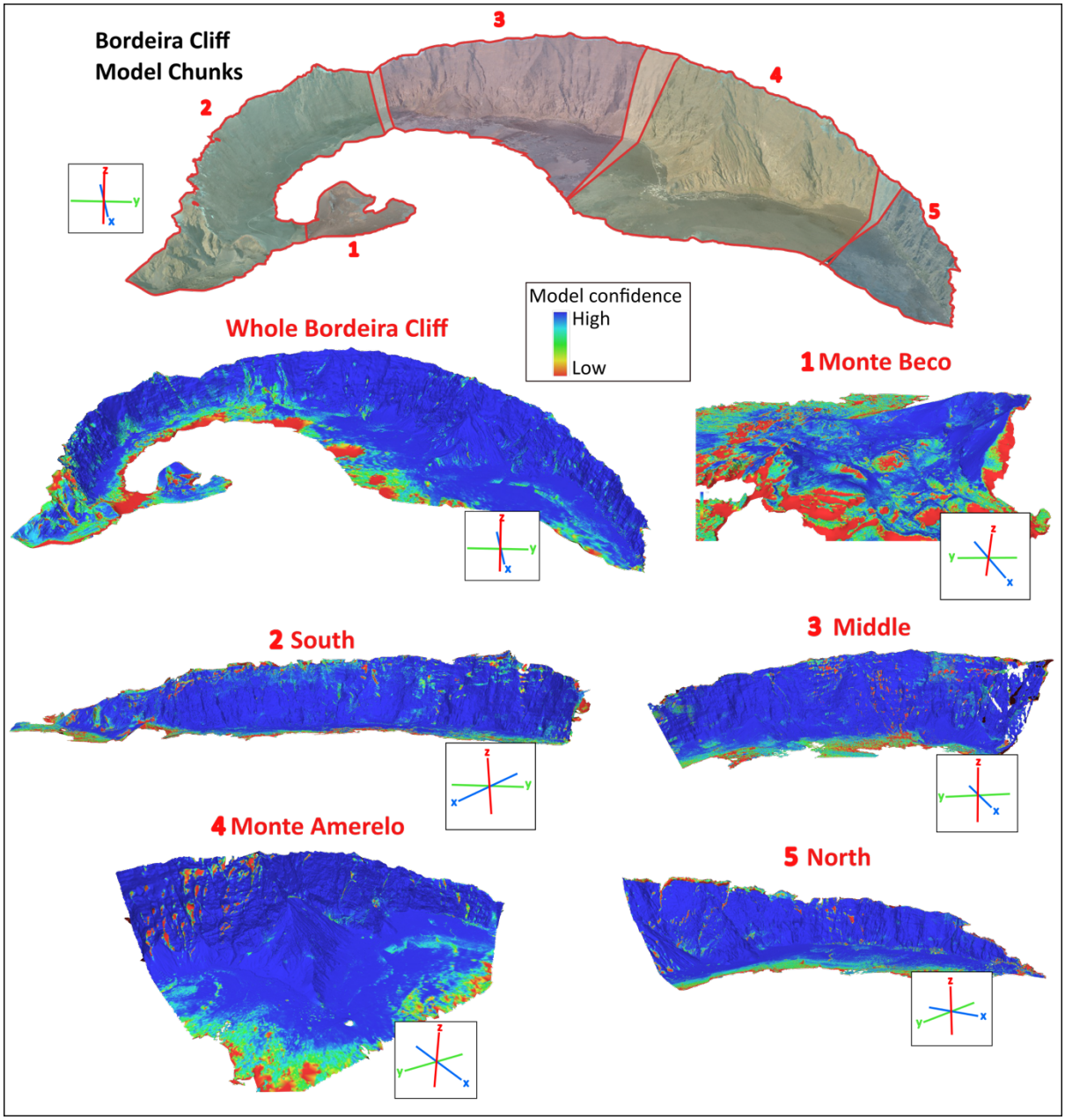

Figure 4.27: Highlighting model confidence of the different chunks of the Bordeira Cliff model.

4.4.2 GIS analysis

The output from the SfM models were used in GIS alongside the regional Island DEM to investigate the structure of the island and collapse scar.

4.4.2.1 Slope analysis

Slope analysis was performed on the western slopes of 30 m/px island DEM to find the most accurate representation of the flanks of the pre-collapse volcano. This shows that the volcano was not symmetrical and had steeper slopes to the north compared to the south and west (Figure 4.18C). Each of the sections through the west of the island also show a steepening trend with elevation. This was analysed further using whole slope analysis at varying elevations on the western slopes (Figure 4.18A). A clear steepening above 1500 m shows this change in topography from a shield into a stratovolcano. To find a representative slope angle for the peak of the pre-collapse volcano that is missing, this analysis was done for elevations over 1900 m providing an average slope result of 25.5° (Figure 4.18B). This value was used in reconstruction of the pre-collapse topography as described later.

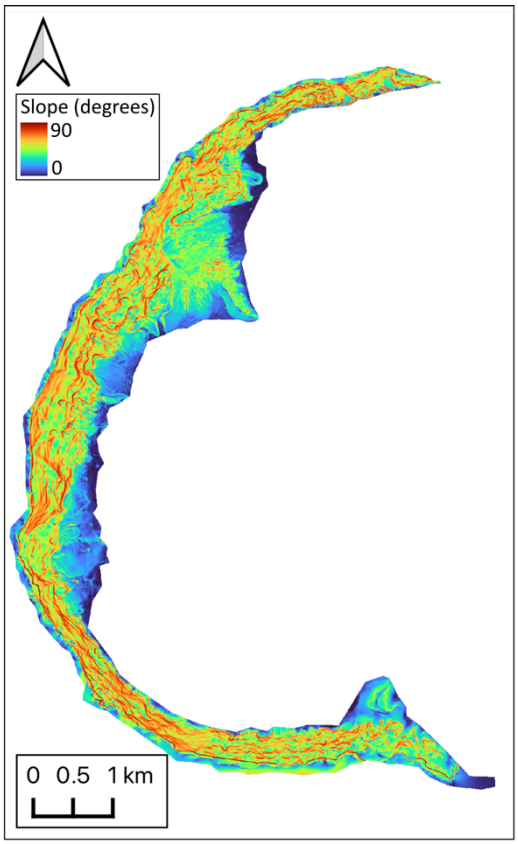

Figure 4.29: Slope analysis for the new DEM of the Bordeira cliff.

Slope analysis was performed on the new DEM of the Bordeira cliff (Figure 4.29). Transects show how the topography of the cliff is steep around all sections except for those passing through the Monte Amarelo cusp. Here, the topography is shallower and more undulating and the cliff section is therefore much wider (Figure 4.19C). The slope analysis was compared between the area mapped as the cliff face compared with the area mapped as the post-collapse deposits (Figure 4.19B). This highlights how the cliff area had a steeper average slope of 54.6°, with some areas reaching vertical faces (Figure 4.29). The post-collapse deposits have average slopes of 31.1°.

4.4.2.2 Scar Metrics

The scar metrics set out by Bernard et al. (2021) were measured on the reconstructed surfaces made using the method described in section 4.3.4.2. Their results are displayed in Figure 4.20 and Table 4.3.

The errors associated with the length measurements are dependent on if it was made using the 30 cm/px cliff orthomozaic or the 50cm/px island orthomozaic. Because of the uncertainties surrounding the base of the scar due to extensive post-collapse infill, a minimum and maximum estimate of the surface was used and therefore the results of these measurements are presented as a range of values. In addition, any area offshore was not included, again due to the unknown length of the scar reaching out beyond this point and the lower resolution of the bathymetry available. These results may also therefore be a minimum estimate if any submarine material was involved in the initial collapse.

The maximum volume calculated here was 109.2 km^3 which is similar to estimates by Paris et al. (2011) at 115 km^3, Martínez-Moreno et al. (2018) at 110 km^3, and Marques et al. (2019) with a range between 20-120 km^3.

Table 4.3: Measurements taken from reconstructed topographies in Figure 5 using parameters set out by Bernard et al. (2021).

Parameter Acronym	Parameter description	Results
Ls	Scar length subaerial (min)	5662 m ±0.5
	Scar length subaerial (max)	11310 m ±0.5
Ws	Scar width	9538 m ± 0.3
Wsa	Scar aperture width (observed)	8894 m±0.3
	Scar aperture width	9139 m ±0.5
Hs	Scar height	2688-3388 m
as	Scar aperture angle	43.4 -77.1°
Bs	Scar slope	13.4 - 16.7 °
ys	Scar azimuth	85.8- 86.8°
As	Scar area	97.73 km^2 ±0.2
Dsa	Scar depth	2750.5-2924.7 m
Vsa	Scar volume	86.8-109.2 km^3
Tsa	Scar thickness	0.89 - 1.1 km
Ars	Scar aspect ratio	0.159
Efs	Elongation factor	0.115
CFs	Closure Factor	0.96

4.4.3 Mapping

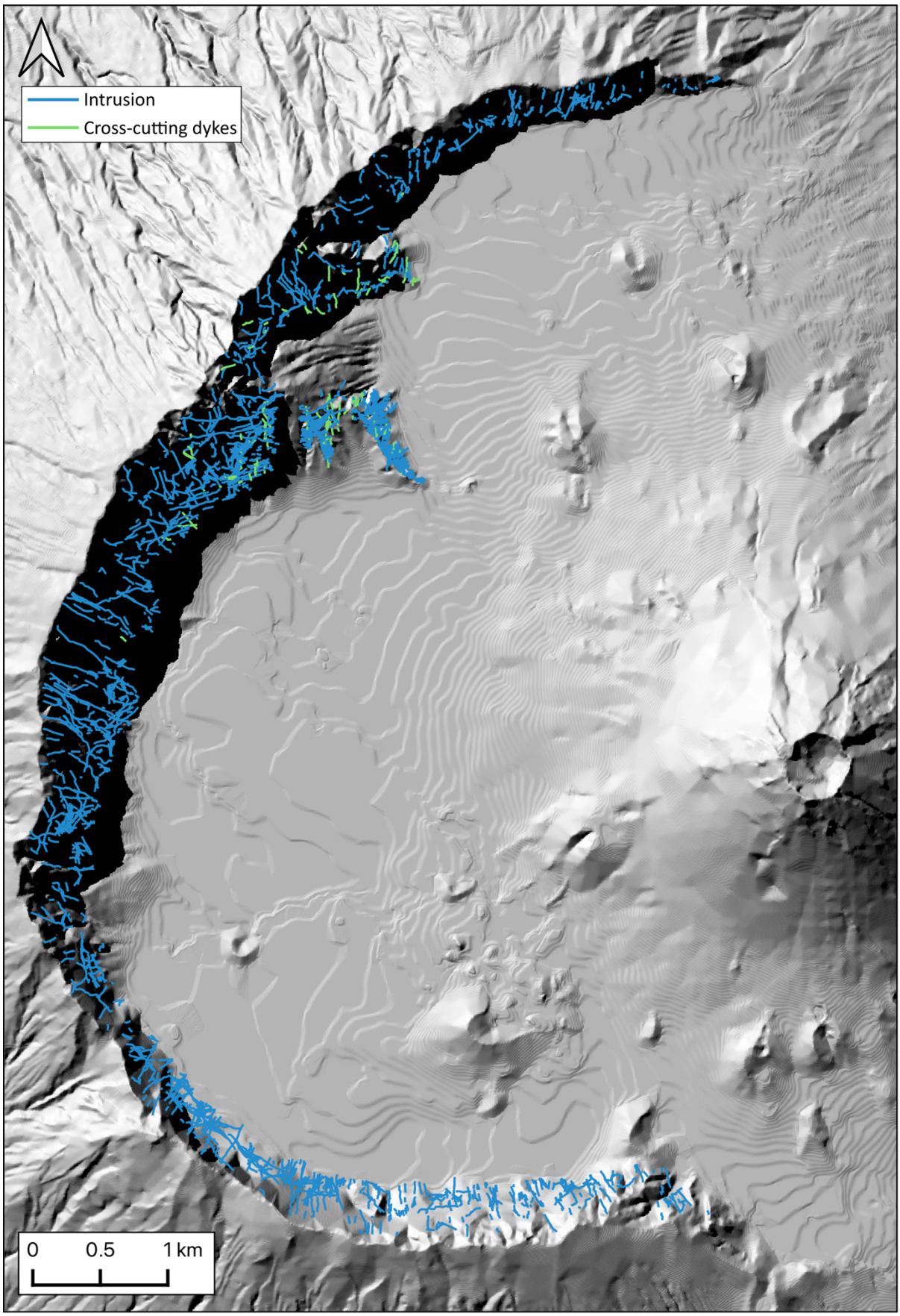

Figure 4.30: Mapped dykes of the Bordeira cliff.

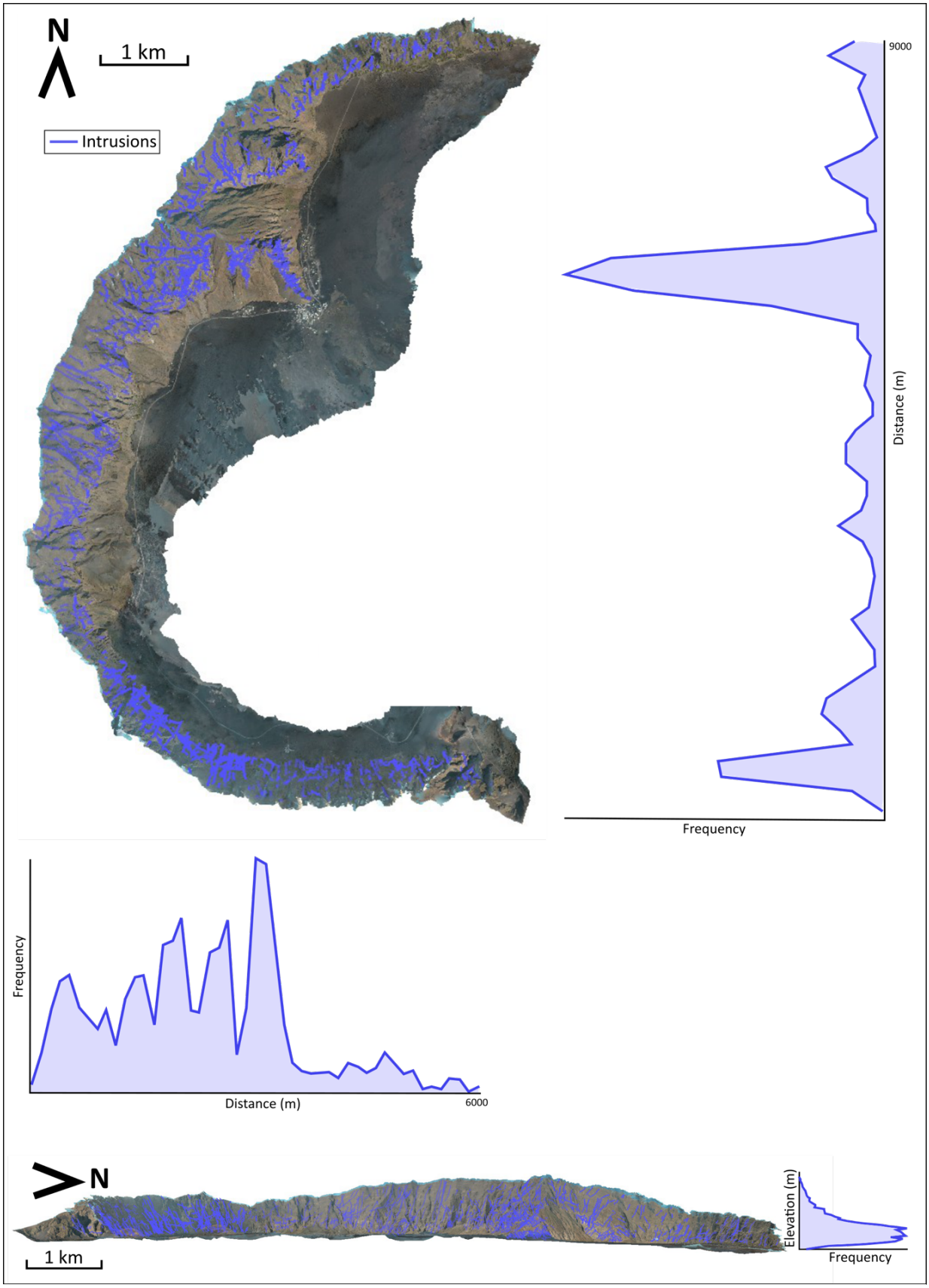

Figure 4.31: Dyke density of the Bordeira cliff along the X, Y and Z axis.

A total of 2070 dykes were mapped onto the 3D model as line shapefiles, the traces of which can be seen in Figure 4.30. This shows how extensive the dyke network is on Fogo, as dykes were seen along all sections of the cliff.

4.4.3.1 Dyke density

The dykes were analysed for their spatial density across the X, Y and Z axis (Figure 4.31). Both the X and Y density plots show a clear spike over the region of Monte Amarelo. However, due to the curved shape of the scar, there are apparent densities shown in the south and north of the Y plot and to the east of the X plot. The density of the dykes extending vertically up the cliff shows a peak between 1630 m and 1850 m. At elevations lower than this, most of the cliff falls below the post-collapse deposits. Higher than this range, this plot shows a gradual reduction of dyke density towards the upper part of the cliff. This is indicative of the number of dyke injections that reached the surface to feed eruptions and also relates to the age of the host rock. The younger the host rock is, the less time for dykes to intrude it and therefore resulting in a lower density of dykes higher in the cliff. In some sections of the cliff, feeder dykes can be directly identified as extending all the way to the top of the cliff and sometimes accompanied with a parasitic cone (model 5 in Figure 4.17: https://sketchfab.com/3d-models/bordeira-cliff-feeder-dyke-19771f7364d64b3f8e63b496b6cc6307). Other factors affecting this reduction could be the poorer resolution of the top of the cliff in the model resulting in fewer dyke identifications and also the fact that the cliff does not reach such high elevations along its extent.

To reduce the stacking effect on the X axis density, a stepped transect was drawn on the south limb to create a histogram of dyke frequency (Figure 4.32). This shows a clustering of dykes in the centre of the southern limb and towards the east and a sparse area in between.

The density of dykes is also shown as pixels in map view (Figure 4.32). Figure 4.32A of all dyke density shows a big clustering in the Monte Amarelo spur. This section of cliff is inferred to be the oldest and hence contains many phases of crosscutting dykes. Within the southern limb of the scar, there is also a clustering of dykes to the SW and the E. An example of these dykes clustering in the south can be seen on a more detailed model to the south (model 2 in Figure 4.17: https://sketchfab.com/3d-models/bordeira-cliff-south-ae894fc728d84e8895992cb5867e3fc7). Within the northern limb there is a small clustering in the centre of its length.

An additional feature observed in the Monte Amarelo cusp in addition to the high density clustering of dykes, is the series of younger, cross-cutting darker dykes, inferred as 'ankaramitic dykes' described by Day et al. (1999) and Rolfe-Betts et al. (2024). This can be seen in the detailed model from this area (model 6 in Figure 4.17: https://sketchfab.com/3d-models/monte-amerelo-dykes-40c9850434624573b519a559f9e6408e). As seen in this model, some of these dykes exhibited en echelon morphologies. These ankaramitic dykes were mapped independently (Figure 4.30). These dykes were mainly observed in the Monte Amarelo area (Figure 4.33). However, their effect on the overall dyke density is not significant, as indicated by comparing Figure 4.33A and Figure 4.33B, where a cluster in still seen on the spur and a smaller cluster to the SE and E and a smaller cluster in the N. This indicates some overall dyke trends which were also described in Day et al. (1999) as NW-SE, NNE-SSW and E-W.

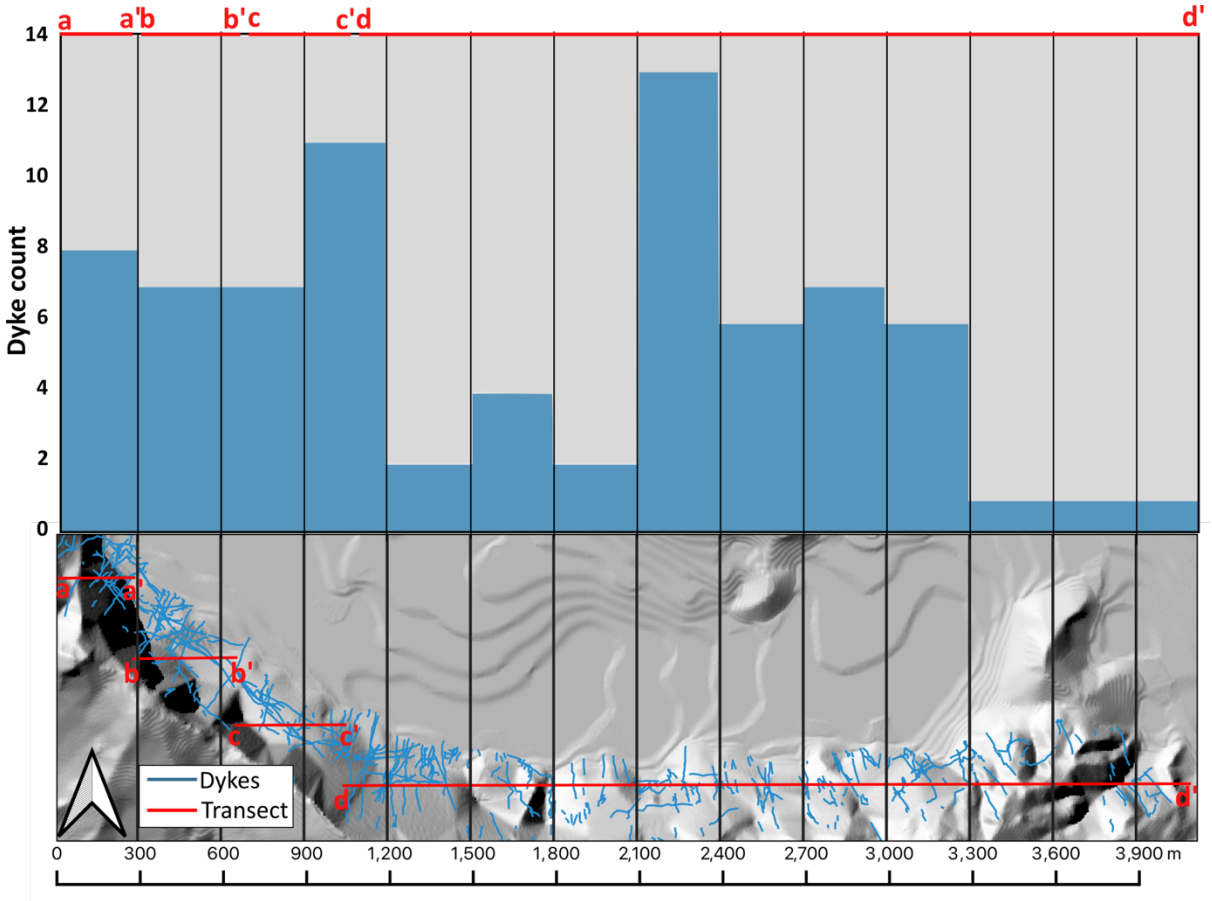

Figure 4.32: dyke frequency histogram over stepped transect through the southern cliff.

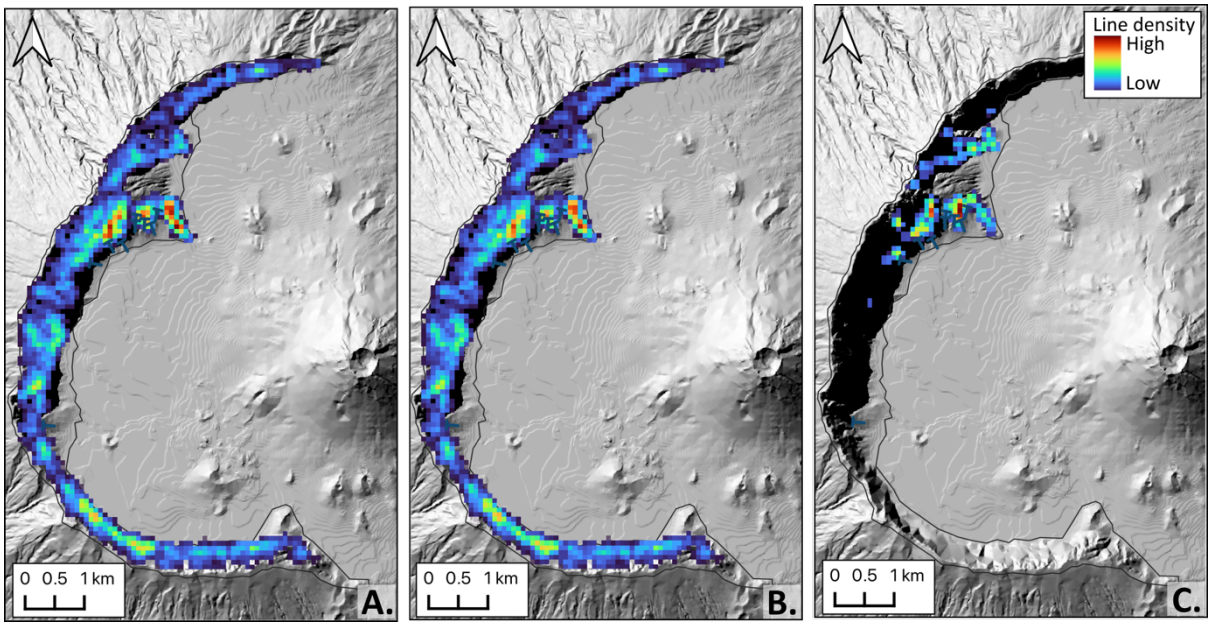

Figure 4.33: Dyke density maps. A. of all mapped dykes. B. Of radial mapped dykes. C. Of 'ankaramitic' dykes

4.4.3.2 Dyke orientation

Dyke measurements were made for a selection of dykes along the extent of the cliff and also focussed to the areas of Monte Amarelo (Figure 4.33). These dykes are categorised into radial dykes and 'ankaramitic dykes', based on their appearance. The ankaramitic dykes were distinct in their darker colour and often much more prominent in the cliff and more often cross-cut older dykes. This is due to their distinct composition and younger age (Rolfe-Betts et al. (2024). Figure 4.33B shows the orientations of the radial dykes and how in the north, dykes are mainly oriented NNE-SSW. To the north of Monte Amarelo, the trends are more NW-SE. In the central cliff to the south of Monte Amarelo, the dykes trend towards NWW-SEE and in the southern limb there are a range of directions as it represents a wider area.

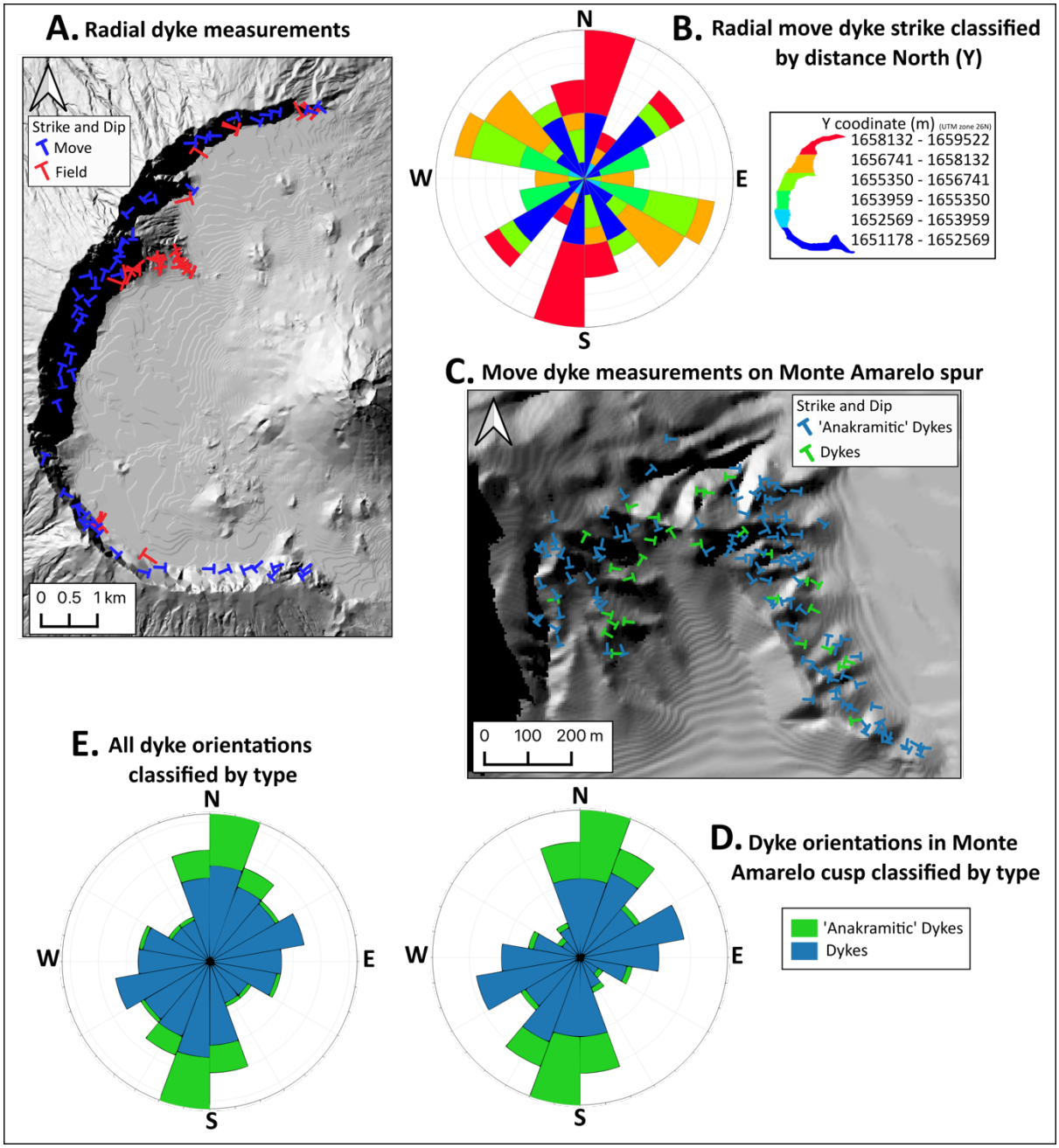

Figure 4.34: Dyke orientations in the Bordeira cliff. A. shows the measurements of the radial dykes measured in Field Move and the dykes mapped in the field. B. Shows the directional trends of the radial dykes separated by distance north. C. Shows strikes and dips measured on Field Move in the Monte Amarelo spur. D. Shows the orientation dykes in Monte Amarelo and E. Shows the orientations of all measured dykes.

Figure 4.34**Error! Reference source not found.**E and Figure 4.34D shows the trends of the dykes identified on the whole cliff and more specifically on Monte Amarelo, comparing the radial dykes against the cross-cutting 'ankaramitic' dykes. The major trends are to NE-SW, NNE-SSW and N-S. In addition, the 'ankaramitic' dykes show a strong N-S trend. This corroborates previous descriptions of these dykes by Day et al. (1999).

4.4.3.3 *Eruptive centre inferences*

Using digital GIS methods set out in section 4.3.5, the dyke orientations were extrapolated centrally to determine whether their intersections form a common overlap. The results of this analysis can be seen in Figure 4.35A. A strong clustering of dyke orientations occurs east of the present-day Pico do Fogo. Additional intersections can also be seen to the north alongside Monte Amarelo and a weaker clustering to the south, close to the southern limb of the scar. From this, eruptive centres have been inferred with a clearer central zone and two less clear zones to the north and south. Comparing these centres to the summit estimation from slope analysis, there is some overlap of this and the central, most dense cluster. The latter two inferred centres are less certain but also seem to corroborate the suggestion of three eruptive centres in Rolfe-Betts et al. (2024).

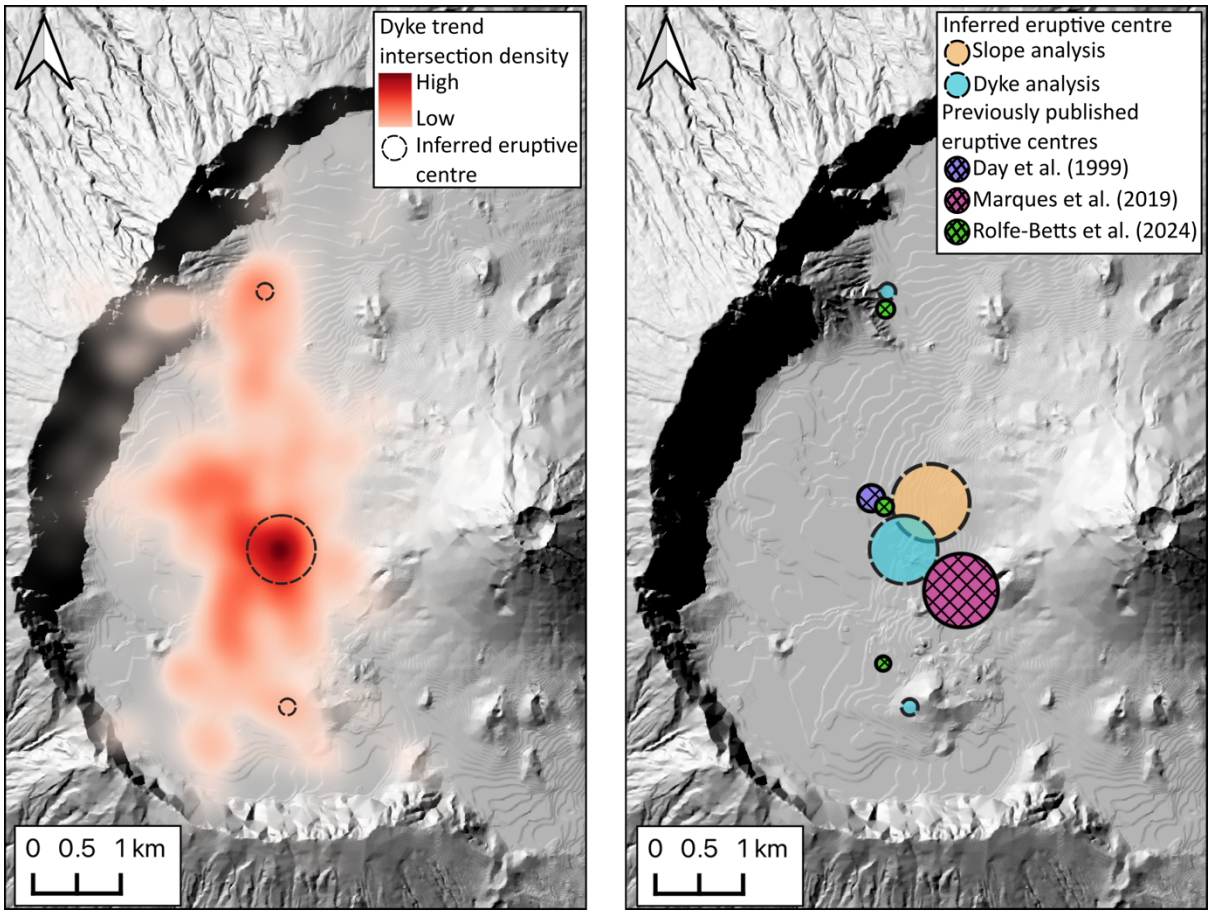

Figure 4.35: A. results from dyke orientation intersection analysis with inferred eruptive centres from clusters. B. Inferred eruptive centres and summit estimation alongside previous suggestions from publications.

The location of the main cluster, and therefore the main eruptive centre is 2900 m to the west of present-day Pico do Fogo with a bearing of 275°.

The ankaramitic dyke traces were then analysed separately to determine how their general trends differ from those of the older dykes (Figure 4.36). From this analysis, a clear N-S trend appears as indicated by Figure 4.36A. Figure 4.36B compares this N-S trend to the inferred eruptive centres, discussed above. This trend does not align with any of these zones, although it is in a similar orientation to the alignment joining the three inferred centres.

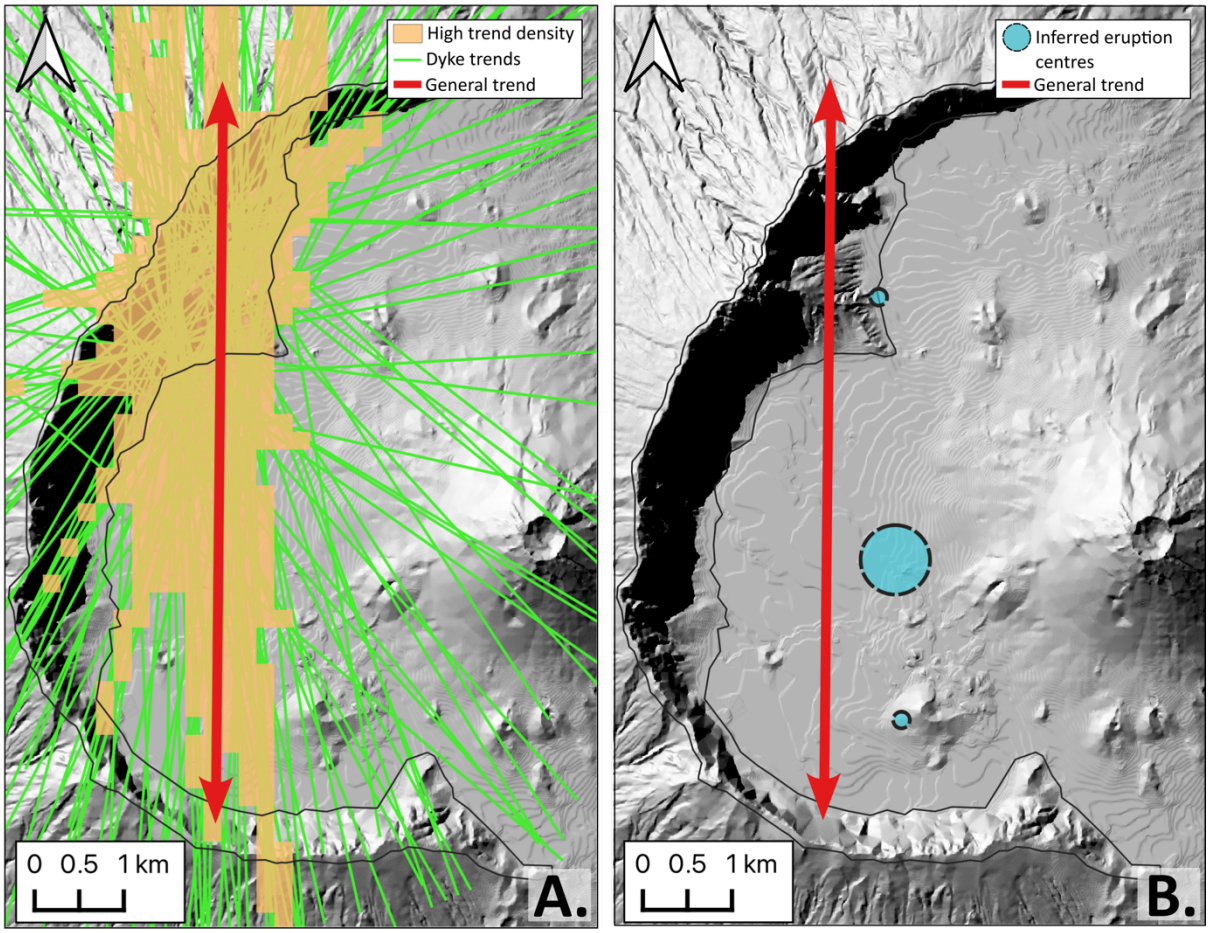

Figure 4.36: A. extrapolated orientations of ankaramitic dykes highlighting their density and overall inferred trend. B. Comparing this overall trend to the inferred eruptive centres.

4.4.3.4 Host rock and post-collapse mapping

Some other features could be mapped from the SfM models. The host rock making up the Bordeira cliff is clearly layered and therefore the trends of these were mapped as form lines (Figure 4.37). The host rocks dip radially outwards, and in some areas this can be seen more clearly (model 1 in Figure 4.17: https://sketchfab.com/3d-models/bordeira-cliff-southern-cusp-b726200ffe1e470fac22f1c2ae4ceb5dT). There are some areas where individual layers can be identified, for example in the central portion of the cliff where a series of thick lavas can be seen. The host rocks do appear to be fairly laterally continuous and layers can be traced

along the cliff to an extent however the lithologies observed at similar elevations appear to vary slightly in appearance when comparing the middle of the cliff where lavas can be quite thick compared to the northern portion of the cliff where the interbedded lavas and ash deposits are bedded on a smaller scale. This might be a horizonal change of same lithology or represent slightly different ages or eruptive styles (model 7 in Figure 4.17: https://sketchfab.com/3d-models/bordeira-cliff-north-b73f6d777b6b427796c284891edd457f).

The unconformity described by Marques et al. (2019) as the contact between the 'Lower Volcanic Complex; and 'Intermediate Volcanic Complex' is possibly identified on the model as the change from a paler host rock to a slightly darker colour midway up the cliff seen towards the spur (Figure 4.37). This has also been inferred as a region of hydrothermal alteration possibly by the presence of a water table (Day et al., 1999). This can be seen towards the central section of the Bordeira cliff (model 4 in Figure 4.17: https://sketchfab.com/3d-models/bordeira-cliff-mid-section-c6d565a6d538436c88c4c1cadba51424).

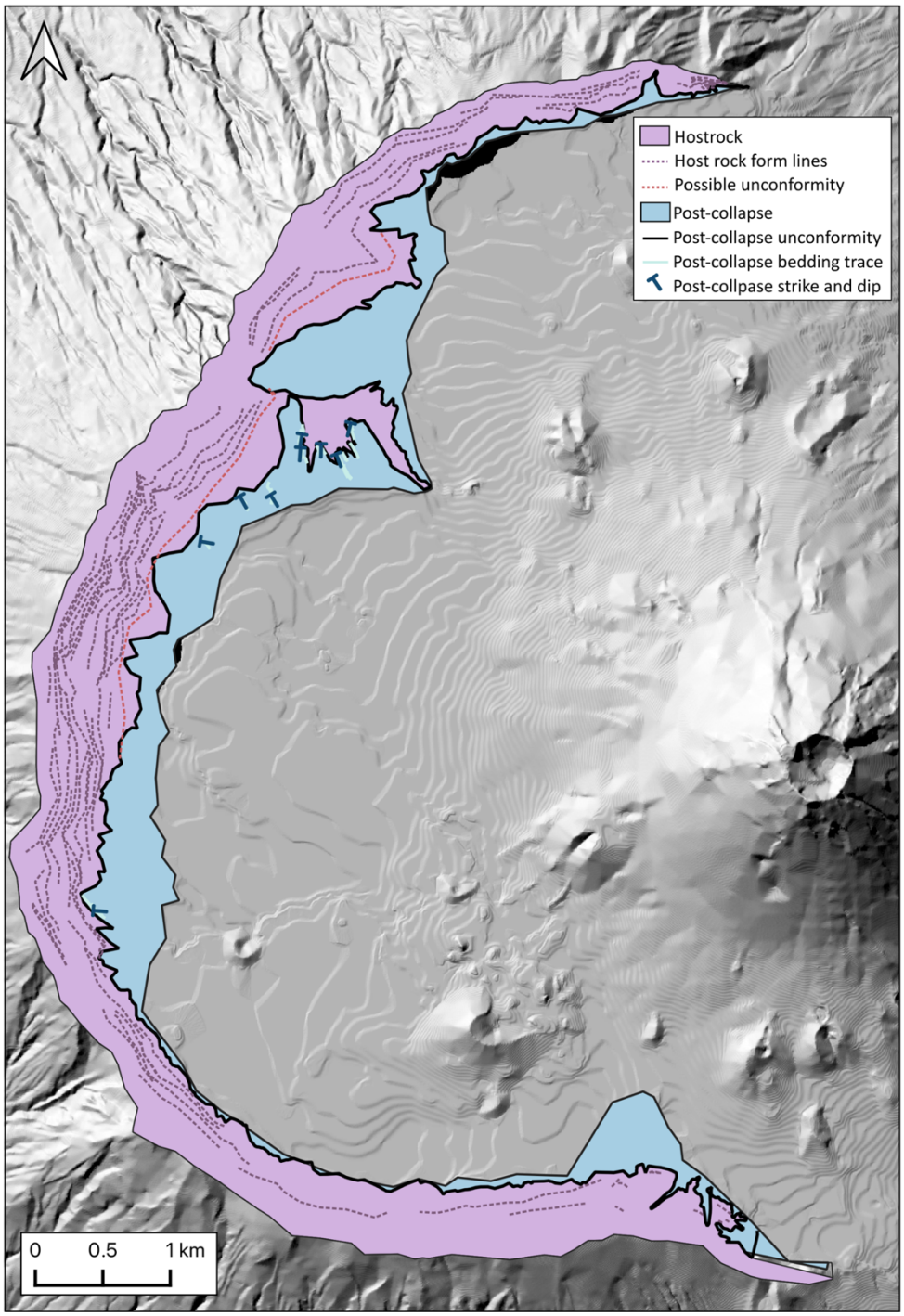

Figure 4.37: Bordeira cliff separating areas of host rock and post-collapse material.

The post-collapse deposits dipping away from the Bordeira cliff within the Chã das Caldeiras were identified in the field as consisting of layered ash deposits, eroded material from the cliff face and in some areas, lava flows possibly originating from vents inside the cliff. Some dips could be measured from the trace lines and all show this unit dipping away from the cliff face (Figure 4.37).

4.4.4 Sample properties

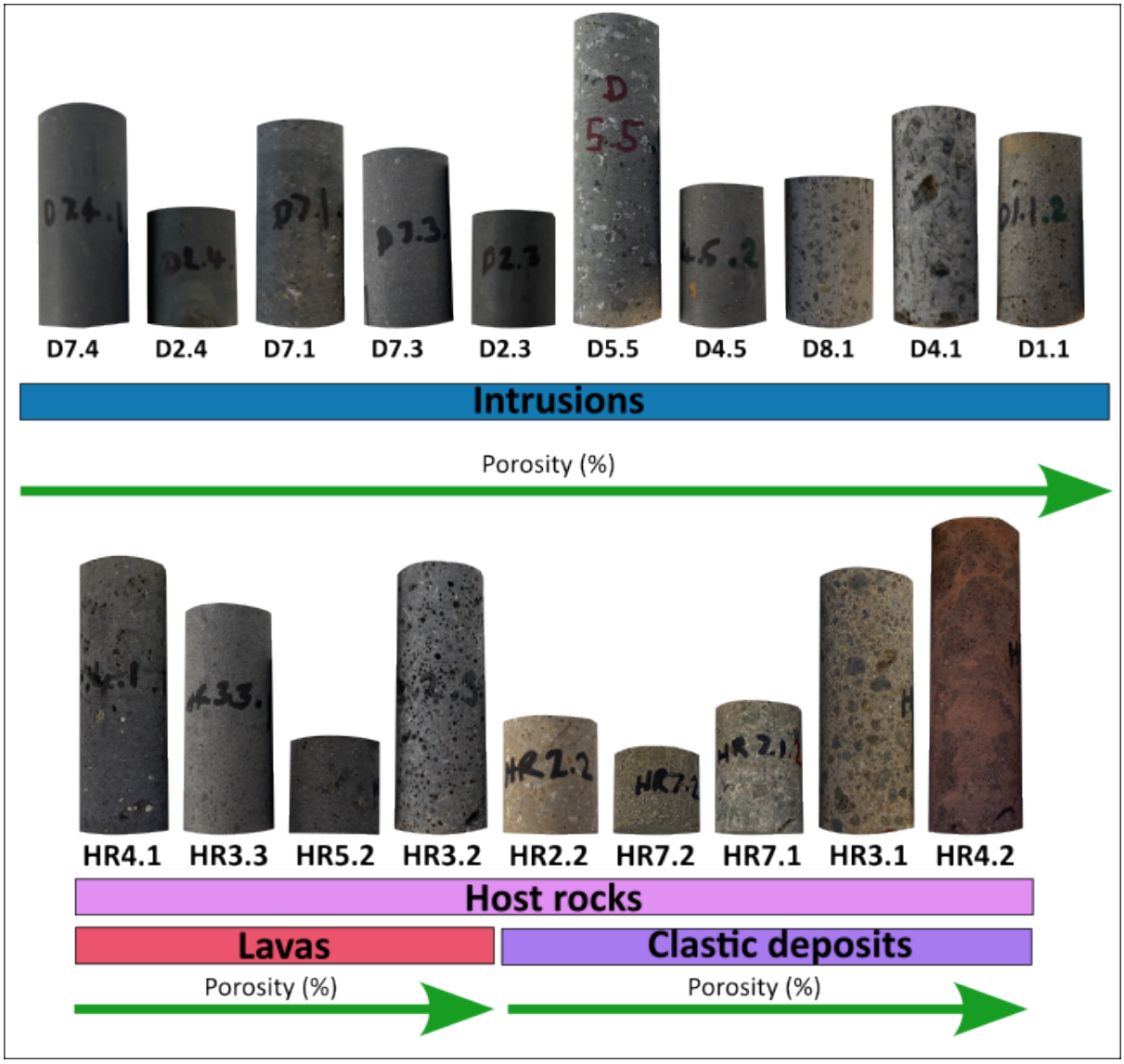

Figure 4.38: Fogo sample set collected in 2022 fieldwork highlighting the classification of dykes and host rocks and showing the porosity trends.

The 19 samples collected from Fogo were separated into the host rock units making up the Bordeira cliff and the cross-cutting dykes. Figure 4.38 shows example cores for each tested sample and further subcategorization based on their lithology. The dykes ranged from fine-grained and aphyric, for example D7.4 and D2.4, to having a higher proportion of phenocrysts, for example D4.1. D4.1 is one of the 'ankaramitic' dykes discussed above and is quite distinct from the other dyke samples (Figure 4.38). The host rocks were further subcategorised into lava flows and 'clastic deposits' including inferred pyroclastic fall material or reworked volcanic material. The lavas showed a range of vesicularity which is reflected in their porosity measurements. The 'clastic' samples were all quite different in appearance and often appeared very altered. The results from the sample mechanical properties tests carried out

on the Fogo samples are summarised in Table 4.4. Where there was enough sample to obtain multiple sample cores, additional tests were performed to improve sample measurement averages using repeatability. Individual sample types are names with two number, for example D1.1. Where there are multiple sample cores measured from this sample, cores are named with a third number. For example, D1.1.1 and D1.1.2 are both cores from sample D1.1. Average results are displayed in Table 4.4 and minimum and maximum results from this repeatability are included in the error considerations.

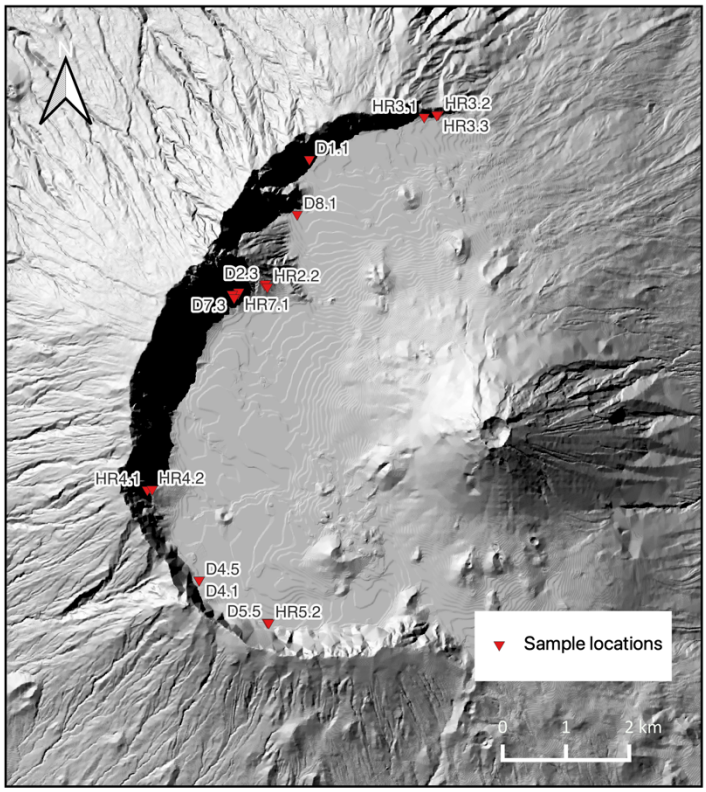

Figure 4.39: Sample locations along Bordeira Cliff

Table 4.4: All sample property results for Fogo sample set

SAMPLE	*Porosity (%)*	*Density (g/cm^3)*	*Permeability (m^2)*	*Peak stress (MPa)*	*Yield strength (MPa)*	*Young's modulus (GPa)*
DYKE 1.1	21.55 ± 1.34	3.03 ±0.03	1.86E-15±5.97x10^{-17}	43.32±5.55	40.50±6.50	4.28±0.30
DYKE 2.3	3.77 ± 0.20	3.07 ±0.02				
DYKE 2.4	0.18 ± 0.24	2.54 ±0.02				
DYKE 4.1	16.09 ± 2.09	2.93 ±0.04		219.59±1.20	213.00±1.00	24.57±0.05
DYKE 4.5	9.29 ± 2.04	3.09 ±0.02		231.81±0.9	231.00±1.00	25.16±0.01
DYKE 5.5	4.38 ± 1.44	2.71 ±0.03		194.04±0.09	180.00±1.00	22.25±0.02
DYKE 7.1	0.51 ± 0.26	2.96 ±0.02		212.68±0.85	188.00±1.00	25.37±0.06
DYKE 7.3	0.76 ± 1.04	2.84 ±0.02				
DYKE 7.4	0.00 ± 0.21	2.89 ±0.01	2.65E-19±1.97x10^{-19}			
DYKE 8.1	10.46 ± 1.00	3.18 ±0.04	3.80E-14±2.55x10^{-17}	99.96±30.55	93.00±34.0	20.77±1.58
HR2.2	15.41 ± 0.07	2.47 ±0.02	1.17E-12±3.41x10^{-16}			
HR3.1	24.36 ± 2.55	2.80 ±0.09	1.21E-15±1.43x10^{-17}	36.10±3.35	33.50±3.50	7.61±0.70
HR3.2	20.29 ± 2.96	2.93 ±0.01	2.78E-18±2.31x10^{-18}	55.96±0.75	50.00±1.00	15.84±0.00
HR3.3	6.32 ± 0.75	3.02 ±0.01	8.57E-20±4.23x10^{-21}	88.50±0.80	79.00±1.00	13.15±0.00
HR4.1	2.86 ± 2.20	2.92 ±0.10		212.57±8.65	209.50±8.50	28.28±0.97
HR4.2	39.58 ± 6.73	3.02 ±0.10	4.59E-16±9.02x10^{-17}	19.38±3.40	18.00±3.50	4.14±0.19
HR5.2	8.04 ± 1.28	2.82 ±0.01				
HR7.1	23.09 ± 1.56	2.66 ±0.01	1.02E-16±1.65x10^{-17}			
HR7.2	20.73 ± 0.74	2.64 ±0.03				

4.4.4.1 Porosity

The porosity was measured for all samples using pycnometry, the methods described in section 3.2.2.2, to give accurate results of 3D connected porosity. Table 4.5 summarised the main statistical parameters of these results. The overall average porosity is 12% with a standard deviation of 10.83. For the dykes, the average porosity is much smaller at 6% with some cores having 0% porosity. The host rocks have a higher average of 18% and some have almost 40% porosity. However, some host rock samples can have low porosities with minimum of 3%. This is due to the wider range of lithologies that these encompass.

Table 4.5: Statistical results of measured porosity for Fogo samples.

	Minimum porosity (%)	*Maximum porosity (%)*	*Average porosity (%)*	*Standard deviation*
All samples	0.00	39.58	11.98	10.83
Dykes	0.00	21.55	6.70	7.49
Host rocks	2.86	39.58	17.85	11.27

Table 4.6: Statistical results of density for Fogo samples.

	MINIMUM DENSITY (G/CM^3)	*MAXIMUM DENSITY (G/CM^3)*	*AVERAGE DENSITY (G/CM^3)*	*STANDARD DEVIATION*
All samples	3.18	2.47	2.87	0.19
Dykes	3.18	2.54	2.92	0.18
Host rocks	3.02	2.47	2.81	0.19

4.4.4.2 Permeability

The permeability was measured for 9 samples. For very impermeable samples showing minimal flow at lower pressures, the higher pressures were not measured. The results from these measurements are in Figure 4.40 and the general statistics are shown in Table 4.7.

Table 4.7: Statistical results of measured permeability for Fogo samples at 5 MPa confining pressure.

	Minimum	*Maximum*	*Average*	*Standard deviation*
Permeability (m^2)	8.57×10^{-20}	1.17×10^{-12}	1.35×10^{-13}	3.89×10^{-13}

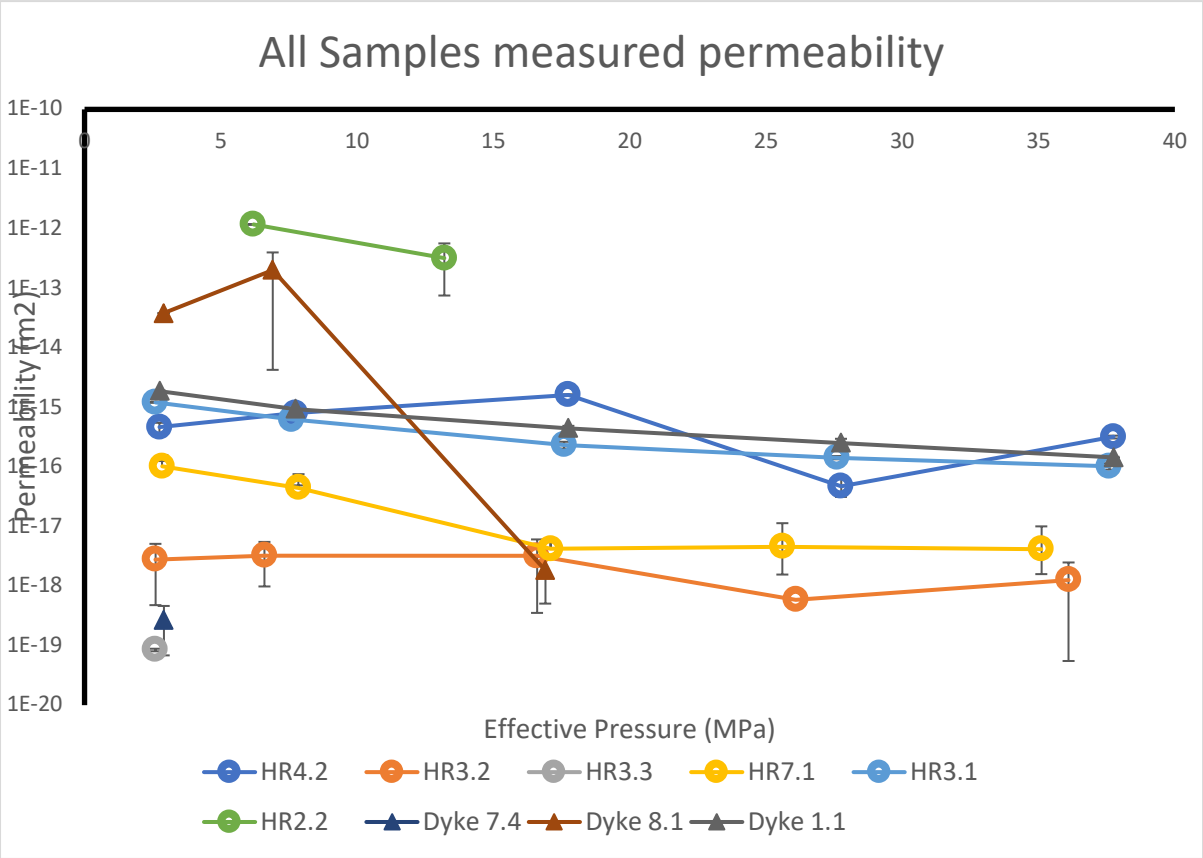

Figure 4.40: Permeability measured on Fogo sample set. Triangular markers are used for samples from intrusions and circular markers are used for host rock samples.

The permeability at 5 MPa confining pressure was plotted against porosity to identify any trends (Figure 4.41). The overall trend, for all the samples, shows a positive correlation with increasing porosity and permeability. The trend for the dykes appears to be much steeper than for the host rocks, however this may be due to a lack of data points. The highest permeability from all measured samples was HR2.2. This is a very altered lapilli deposit from the oldest part of the scar and contained some fractures. Higher porosities, for example in HR4.2, did not yield as high a permeability as expected. The lowest permeabilities measured included Dyke7.4 which had 0% porosity and consists mainly of fine groundmass. The other low permeability sample measured was HR3.3 which was a lava flow with 6% porosity.

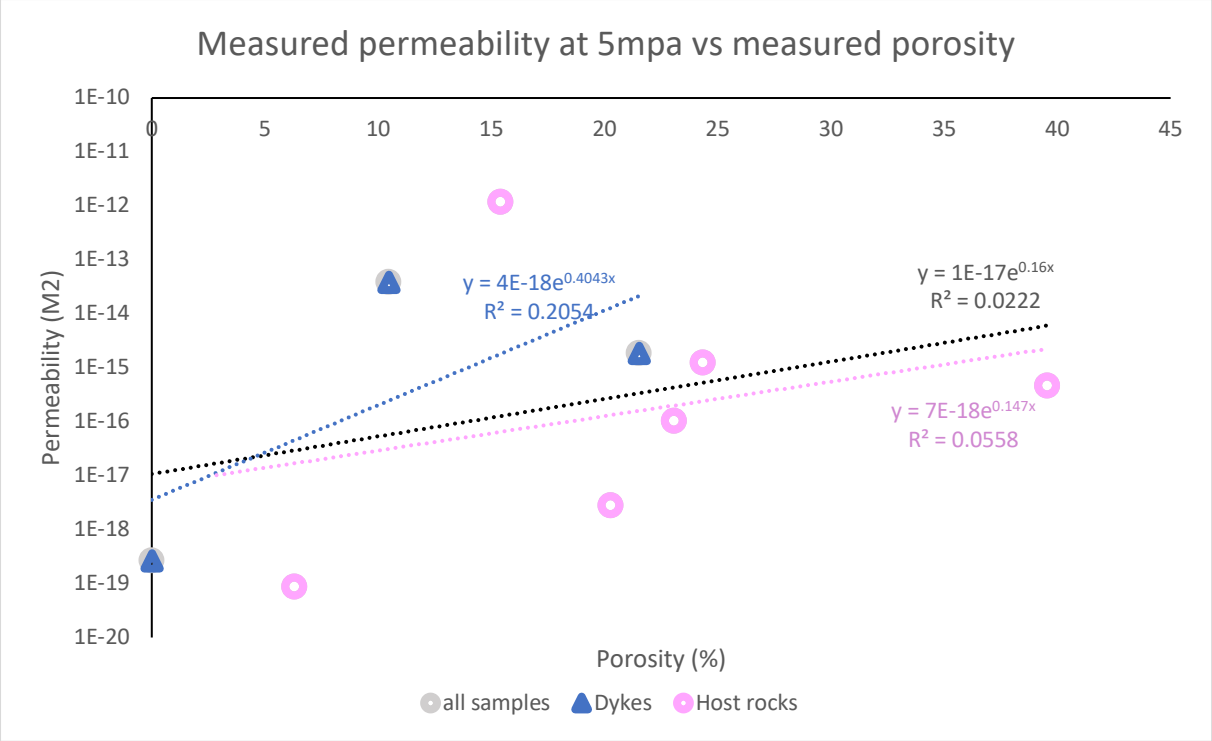

Figure 4.41: Relationship between measured permeability and porosity for Fogo samples

4.4.4.3 Strength

The uniaxial compressive strength was measured for 11 samples. Samples HR3.1, HR4.1, HR4.2, D1.1, D8.1 had several tests done due to core availability for repeatability. Their stress-strain curves are presented in Figure 4.42. From this the peak uniaxial strength, yield uniaxial strength and Young's modulus was calculated. The general statistics of these, comparing host and dyke rocks are in Table 4.8,

Table 4.9 and
Table 4.10. The average peak strength and yield strength of the dykes is almost double that of the host rocks. Overall, the average Young's modulus is higher in the dyke samples compared to the host rocks, meaning that the dykes are generally stiffer.

Table 4.8: Statistics for Peak uniaxial compressive strength (MPa) for Fogo samples.

	Average (MPa)	*Minimum (MPa)*	*Maximum (MPa)*	*Standard deviation*
All samples	128.54	19.38	231.81	85.32
Dykes	166.90	43.32	231.81	76.91
Host rocks	82.50	19.38	212.57	77.13

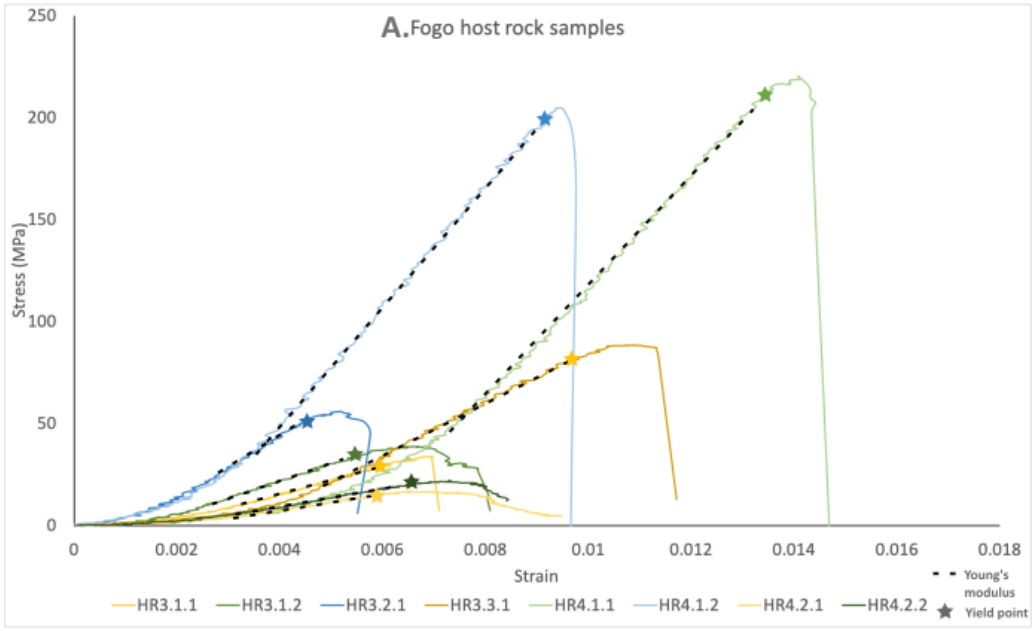

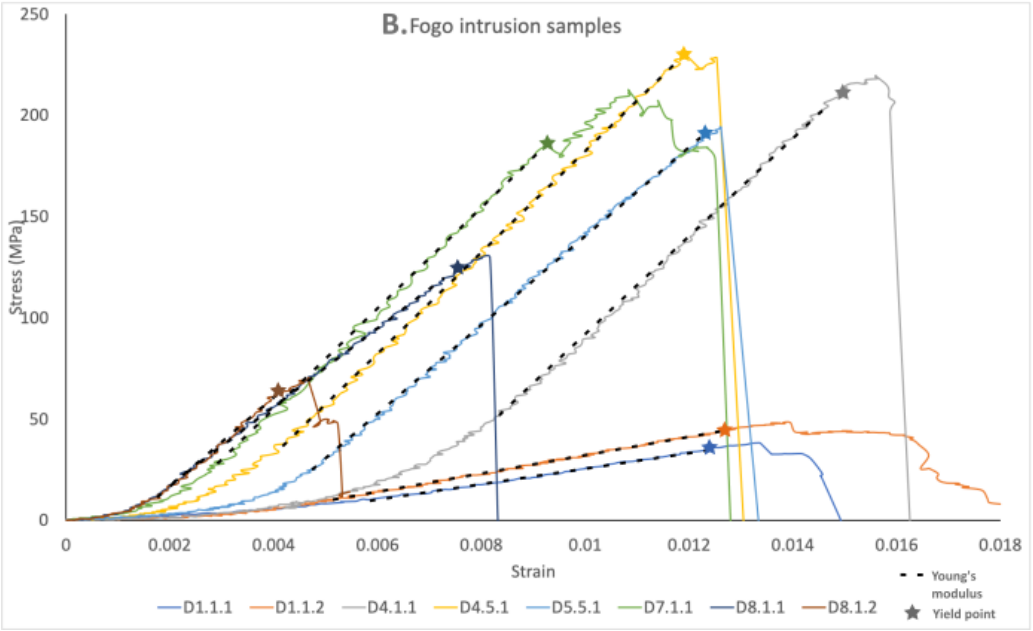

Figure 4.42: Stress vs strain curves for A. Host rock samples and B. Intrusion samples

Table 4.9: Statistics for yield uniaxial compressive strength (MPa) for Fogo samples.

	Average (MPa)	*Minimum (MPa)*	*Maximum (MPa)*	*Standard deviation*
All samples	120.05	18.00	231.00	83.77
Dykes	157.58	40.50	231.00	74.52
Host rocks	75.00	18.00	209.50	77.15

Table 4.10: Statistics for Young's modulus (GPa) for Fogo samples

	Average (GPa)	*Minimum (GPa)*	*Maximum (GPa)*	*Standard deviation*
All samples	17.40	4.14	28.28	8.90
Dykes	20.40	4.28	25.37	8.10
Host rocks	13.80	4.14	28.28	9.30

The stress strain curves for all samples shows a large variation in the strengths and stiffness from the rocks that make up Fogo's edifice (**Error! Reference source not found.**). The curves are split between dykes and host rocks in Figure 4.42 and **Error! Reference source not found.**. By comparing the curves for the intrusions, most of the samples have similar gradients, i.e. Young's modulus at around 23.6 GPa. The exception to this is the two samples measured for Dyke 1.1 which has a more elastic response to uniaxial stress. Dyke 1.1 also had the lowest peak strengths measured of the intrusions at 43.3 MPa. The next weakest dyke was D8.1 where both tests had generally lower peak strengths, although quite different from one another, with one measured at 130 MP and the other at 70 MPa. The cores exhibited evidence of fractures infilled by minerals which may have contributed to this weakness and also the reason between the difference of the two experiments on the same sample as more fractures may have been present in one than the other. The strongest of the dykes was D4.5 with a peak uniaxial compressive strength of 231.8 MPa.

The host rocks show a range of Young's moduli and strengths due to the range of lithologies that they encompass (**Error! Reference source not found.** and Table 4.4). The strongest and stiffest of these experiments is the two experiments on HR4.1, which is a low porosity lava. The next strongest is HR3.3, also a low porosity lava sample but which has some phenocrysts present. HR3.2 is a lava sample and is the next strongest of this set, however it is much lower than HR4.1 and HR3.3 with a peak stress of 56 MPa. This sample has a much higher vesicularity and hence porosity. The response to uniaxial compressive stress is much more elastic in samples HR3.1 and HR4.2 which are both flow deposits.

There is a strong positive correlation between Young's modulus and peak strengths indicating the stiffer the material, the higher the strength at failure (Figure 4.45). In addition, there is a negative correlation between porosity and UCS, suggesting that the more porous material is weaker (Figure 4.43). This is consistent with many published studies on volcanic rocks. This is because the porosity is proportional to the strength of a rock as more pore spaces are zones of weakness from which fractures can propagate. For example, Heap and Violay (2021) used a compiled data set of various volcanic rocks to suggest that the uniaxial compressive strength of volcanic rocks decreases nonlinearly as a function of increasing porosity. This paper also suggests that the range of strengths is high at low porosity and low at increasing porosities (Heap et al., 2021a). This trend is also shown by the data for Fogo (Figure 4.46A). The Young's modulus of the measured rocks shows a decreasing trend with respect to increasing porosity. This relationship is also observed in the spread of data from Heap and Violay (2021) (Figure 4.46B). These compiled datasets are large so it is expected that the Fogo samples should fit into them. These comparison plots also show, however, that the Fogo sample set also shows a lot of scatter. This may be as a result of differing factors that also affect the strength of a rock aside from porosity. The Fogo sample set includes rocks from different volcanic sources including dyke intrusions, lava flows and reworked pyroclastic material. Because of these different sources and other factors such as hydrothermal alteration, crystal content or groundmass type which could explain this scatter in both the whole dataset and in the Fogo samples (Heap and Violay, 2021).

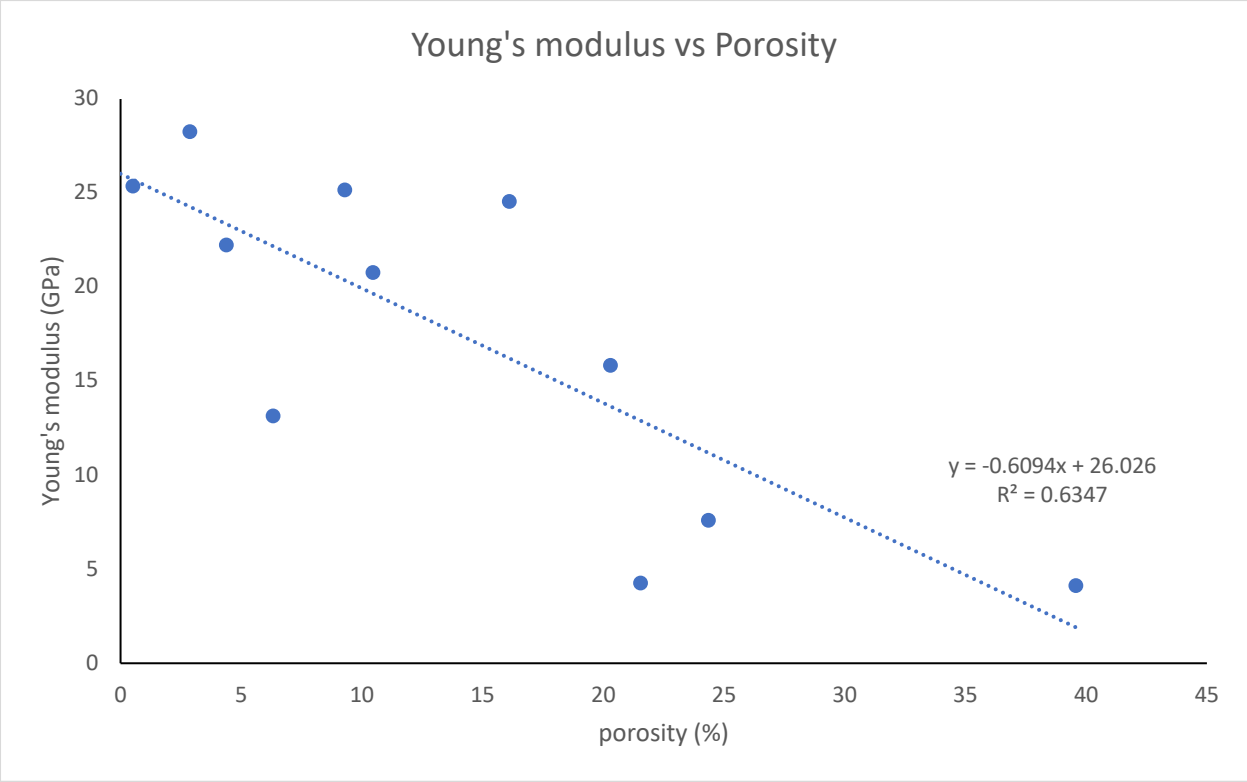

Figure 4.44: Young's modulus vs porosity of Fogo samples

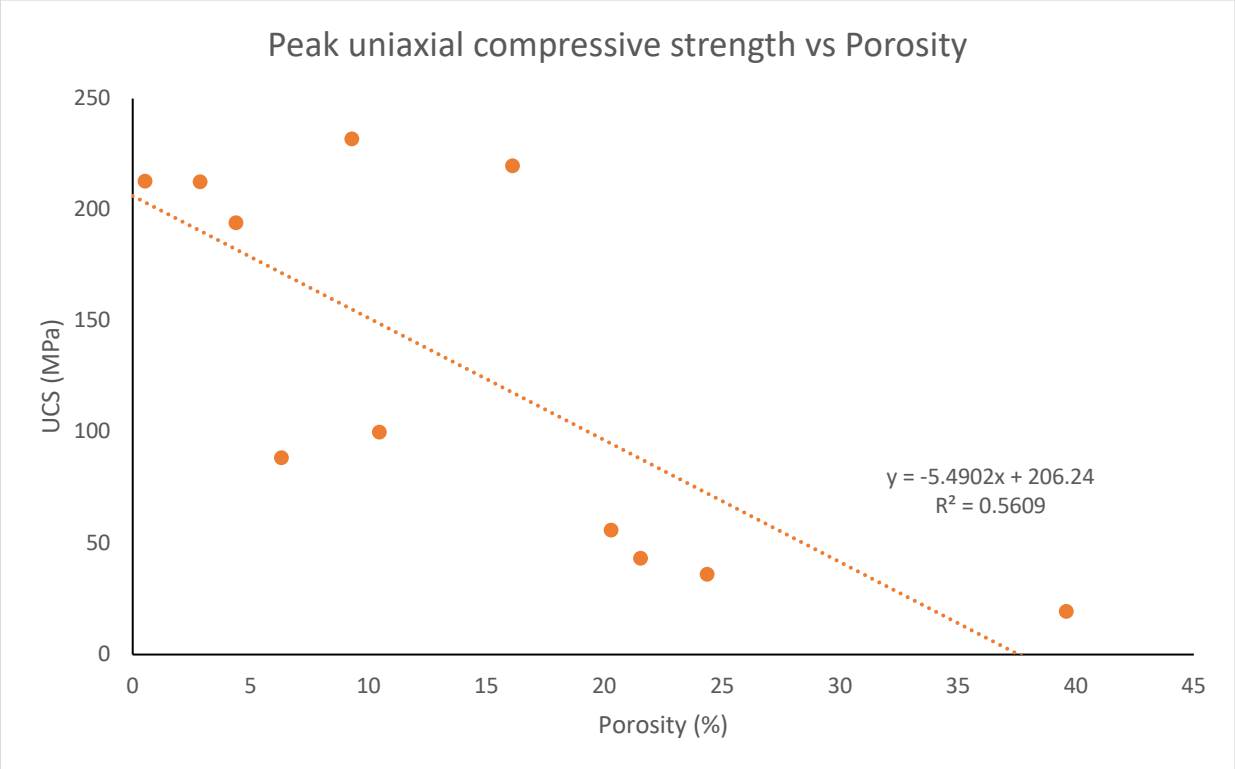

Figure 4.43: Relationship between measured Porosity and Uniaxial Compressive Strength.

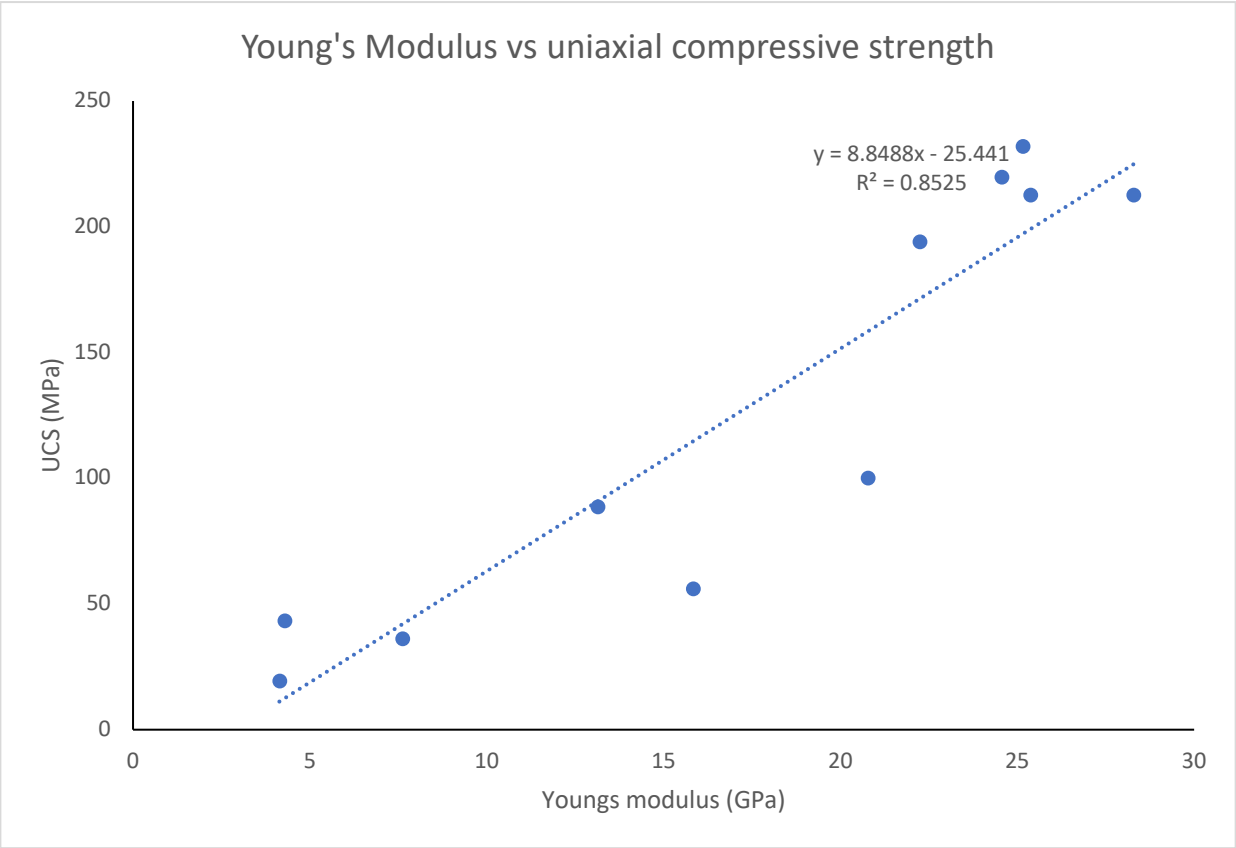

Figure 4.45: Relationship between measured Young's modulus and Uniaxial Compressive Strength and line of best fit.

There is a strong positive correlation between the Young's modulus and the uniaxial compressive strength of the rocks from Fogo (Figure 4.45). This agrees with the trend from Heap and Violay (2021) (Figure 4.46C). The weaker and more elastic samples from the Fogo set are the host rock pyroclastic deposits HR3.1 and HR4.2. The compiled dataset from Heap and Violay (2021) also shows that pyroclastic materials are represented in the low Young's modulus and low compressive strength section of the trend due to their high porosity. Further information on how these relationships form could be discovered through further work on analysing the microstructure of these samples.

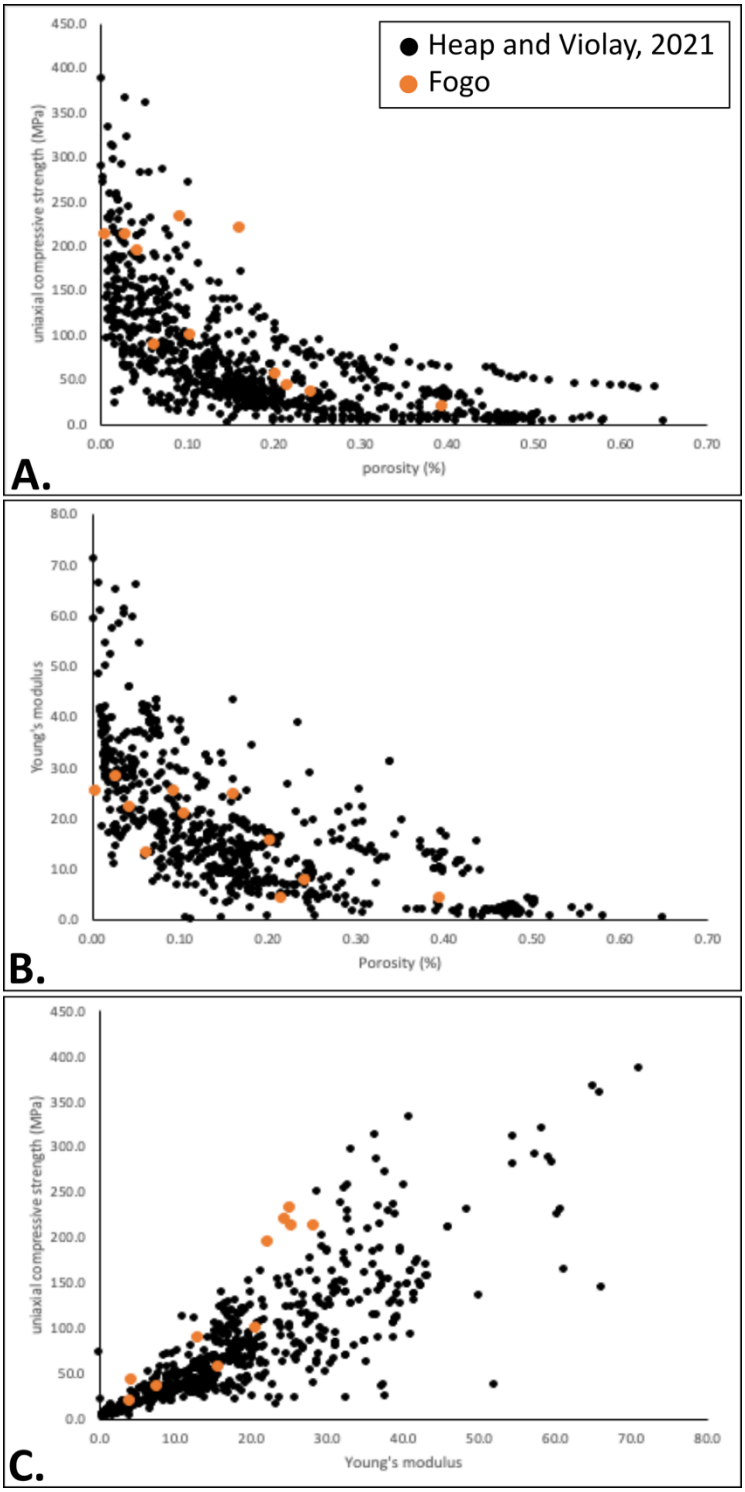

Figure 4.46: Comparing compilation of volcanic rock properties from Heap and Violay, 2021 with the results from Fogo. A. Porosity against uniaxial compressive strength. B. Porosity against Young's modulus. C. Young's modulus against uniaxial compressive strength.

4.5 Discussion

The high-resolution model generated from SfM techniques has allowed detailed analysis of the structure and morphology of the Bordeira cliff, providing insight into the structure of the plumbing of the pre-collapse volcano and hence indicating possible changes in stress regimes that led to collapse. The analysis of rock samples collected from the cliff has parametrised hydraulic and mechanical properties that made up the pre-collapse edifice. This has shown the expected relationships between porosity, permeability and strength for volcanic rocks. This also highlighted the stronger rocks are dykes and lava cores which show the lowest porosity and the weakest rocks were pyroclastic samples.

Mapping of dyke density has highlighted areas of clusters of dykes cross-cutting the cliff. The main cluster is in the central Monte Amarelo spur. This is likely because this section of the cliff protrudes inwards towards the centre of the pre-collapse edifice and therefore represents the oldest rocks in the cliff. Therefore, it follows that this section has had more time to be intruded. Other reasons for the higher dyke density in this region could be due to the edifice being weaker in this region due to faults or heterogenies and therefore making it a preferential route for magma to fracture and exploit (Gonzalez-Santana et al., 2023). In addition, the location of this higher density region is closest to estimated centres of eruption and could therefore represent a higher proportion of feeder dykes. The dyke density throughout the rest of the cliff shows some other, distinct clusters to the SE and to the E of the cliff and some less obvious clusters to the NW and SW of the cliff. This agrees with the approximate rift zones set out in Day et al. (1999).

The dyke orientations from around the cliff suggest a radial pattern of intrusions. In the NE, dykes are mainly oriented NNE-SSW. To the north of Monte Amarelo, the trends are more NW-SE. In the central cliff to the south of Monte Amarelo, the dykes trend towards NWW-SEE and in the southern limb the dykes trend to the N-S and NNE-SSW. The extrapolation and intersection of these dyke trends has allowed an estimation of the location of eruptive centres in pre-collapse Fogo. This technique of dyke orientation extrapolation had previously been performed at Fogo to find a centre (Marques et al., 2019). Their study measured 273 dykes and found a convergence point to the southeast of the main centre inferred from this study. Their inference was similar where that the direction of the landslide was the same as the movement of the eruptive centre. However, this study measured over 2000 dykes throughout the Borderia cliff as a result of the new high-resolution model. It can

therefore be concluded that this study's inference is more accurate as it is based on more dyke orientation evidence. Additionally, this investigation showed that showed a major convergence of dyke orientations to the west of Pico do Fogo and some smaller, less well-defined clusters to the north and south of this. The dykes inferred to belong to the smaller clusters are distinct enough from the major cluster to have stemmed from a different source. The indication of this is that there was a major eruptive centre, with two possible secondary centres aligning on a N-S axis (Figure 4.48). This agrees with the eruptive centres set out in Rolfe-Betts et al. (2024) (Figure 4.35B). The location of the major eruptive centre also similar to the location of the summit estimated from slope analysis.

The N-S trending 'ankaramitic dykes' have previously been identified as the feeders of the 'Riberira Aguadinh Formation' of lavas (Rolfe-Betts et al., 2024). These dykes consistently cross-cut radial dyke swarms but are cut by the collapse scar. This formation is also petrologically distinct from previous lavas, therefore suggesting a change preceding the collapse event (Rolfe-Betts et al., 2024). The younger 'ankaramitic' dykes, when mapped, show a different orientation than the older dykes. These trends align on a N-S trend and, when extrapolated, do not line up with the estimated eruptive centres. Instead, they align 770 m west of the main eruption centre. This indicates a change of plumbing patterns within the edifice during the intrusion of these dykes. The orientation of dykes implicates the large scale stress regimes within an edifice (Walter and Troll, 2003). This suite of cross-cutting dykes are the youngest dykes mapped in this sequence and therefore this change of intrusion orientation and petrology preceded the major collapse and is assumed to have been caused by the changing stress conditions. They may show evidence of the edifice becoming unstable and possibly be the cause behind and evidence of the beginning of spreading to the east. The continued intrusion along this axis also could have been a positive feedback mechanism for further spreading from increased magmatic pressure pushing outwards along E-W orientation, perpendicular to the dyke trend axis (Figure 4.48). This phenomenon has been observed at other volcanoes where inferred intrusive events or eruptions coincide with periods of accelerated flank movement. This includes the ongoing movement of the southern and eastern flanks at Mount Etna (Battaglia et al., 2011). This orientation fits with the direction of the collapse being towards the east with an azimuth of 87°. This theory of late intrusion of distinctly N-S trending dykes highlighting pre-collapse instability was set out in previous literature (Rolfe-Betts et al., 2024, Day et al., 1999, Foeken et al., 2009) and is strongly

supported by the data presented here. This result is significant when considering present-day flank stability and hazard management on volcanic flanks and also at Fogo itself. The evidence presented here supporting the theory that a change in eruptive pattern of dyke intrusions may be a precursor to catastrophic volcanic collapse highlights the importance of monitoring such occurrences to identify vulnerable edifices. In particular, when considering the recent shift in eruptive activity away from Pico do Fogo to the western flanks might be a possible present-day indication of instabilities in the edifice (Rolfe-Betts et al., 2024, Day et al., 1999, Foeken et al., 2009). This suggests that investment in monitoring this developing situation is key in improving preparedness for a potential collapse at Fogo in the future. Monitoring techniques could include using InSAR technology (Interferometric Synthetic Aperture Radar) to monitor ground deformation alongside known shallow intrusion events, using the already installed seismometer network, or eruptive events to indicate if any significant lateral movement occurs during these events. Ground-based SAR has been applied to monitoring of landslides or volcanic deformations (Di Traglia et al., 2021, Calvari et al., 2016). In the case of Anak Krakatau, InSAR data was analysed retrospectively and accelerations in the flank preceding collapse coincided with shallow intrusions evidencing that this kind of precursory signals can be captured (Zorn et al., 2023). The difficulty still remains, and therefore further work must be done in interpreting these signals to understand when a situation turns from unstable to critical.

These results also indicate that the main eruptive centre shifted to the east (with an azimuth of 85°) 2900 m from the inferred pre-collapse main eruptive centre following the catastrophic collapse to where Pico do Fogo stands. The azimuth of this eruptive centre shift is similar to that of the azimuth of the collapse scar, indicating that this change in location is as a result of the collapse edifice reducing confining pressures.

The results from sample analysis for mechanical and hydraulic properties has highlighted trends and empirical relationships between parameters. The results show that with increasing porosity, permeability increases, strength decreases and the elasticity of the rock increases. Generally, the intrusive dyke samples are less porous, ranging between 0-22% porosity, and hence are stronger and fail in a more brittle manner compared to the host rocks (Figure 4.47). Generally, the more porphyritic samples have higher porosities. This may be due to the presence of microfracturing within the crystals. The presence of larger fractures in dykes also may cause significant reduction of strength based on D8.1 experiments which

showed a difference in peak strengths of 60 MPa as a result of fracturing extent. The dykes strength range between 43-232 MPa where the lower results represent the rocks with the higher porosities. The lava samples can have higher average porosities due to the presence of vesicles and range between 3-20%. The clastic samples are much weaker, with peak strengths measured at 19-36 MPa, fail elastically and, despite having the potential for high porosities, between 21-40%, can also have low permeabilities than expected. This is possibly due to the presence of clay minerals within these layers (Figure 4.47).

The complexities of the layered host rock which makes up most of the edifice involves several rock properties that could lead to the development of instabilities. In particular, the presence of fractures can weaken once strong intrusive rocks. This may be caused by the continued heating and cooling from continued dyke intrusions, as demonstrated from the many dykes mapped on the Bordeira cliff. Additionally, the presence of pyroclastic and clastic lithologies may create weak layers within the edifice where failure could occur (Figure 4.47).

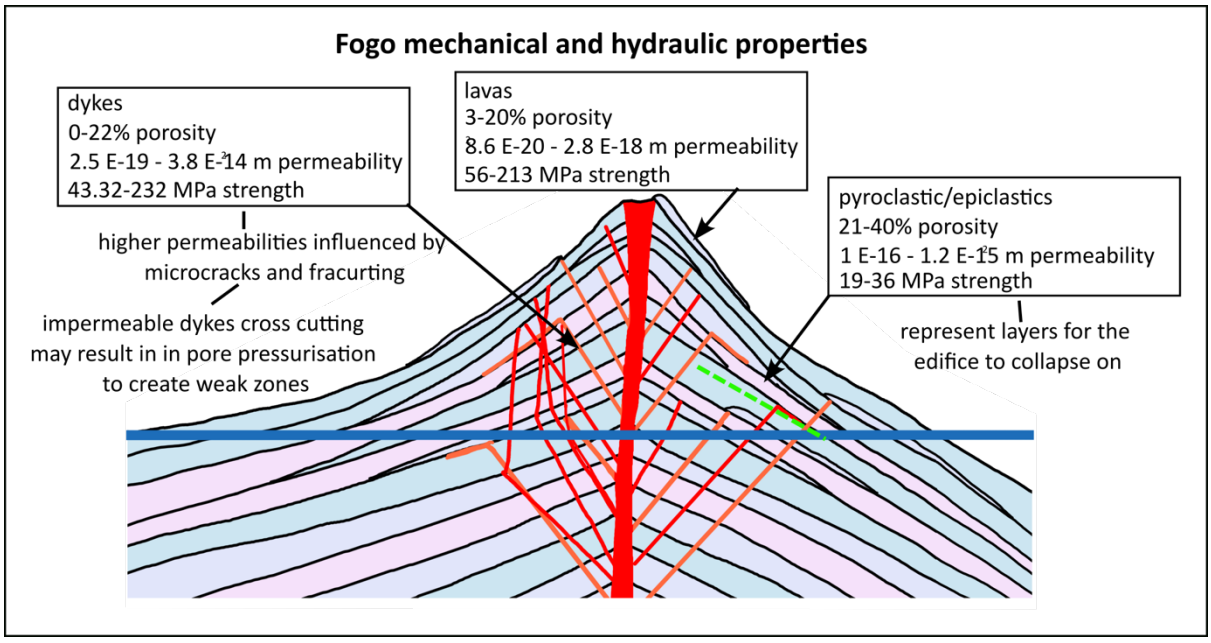

Figure 4.47: Schematic diagram of the inferred pre-collapse Fogo highlighting the measured rock properties measured and how this influence weakening of the edifice.

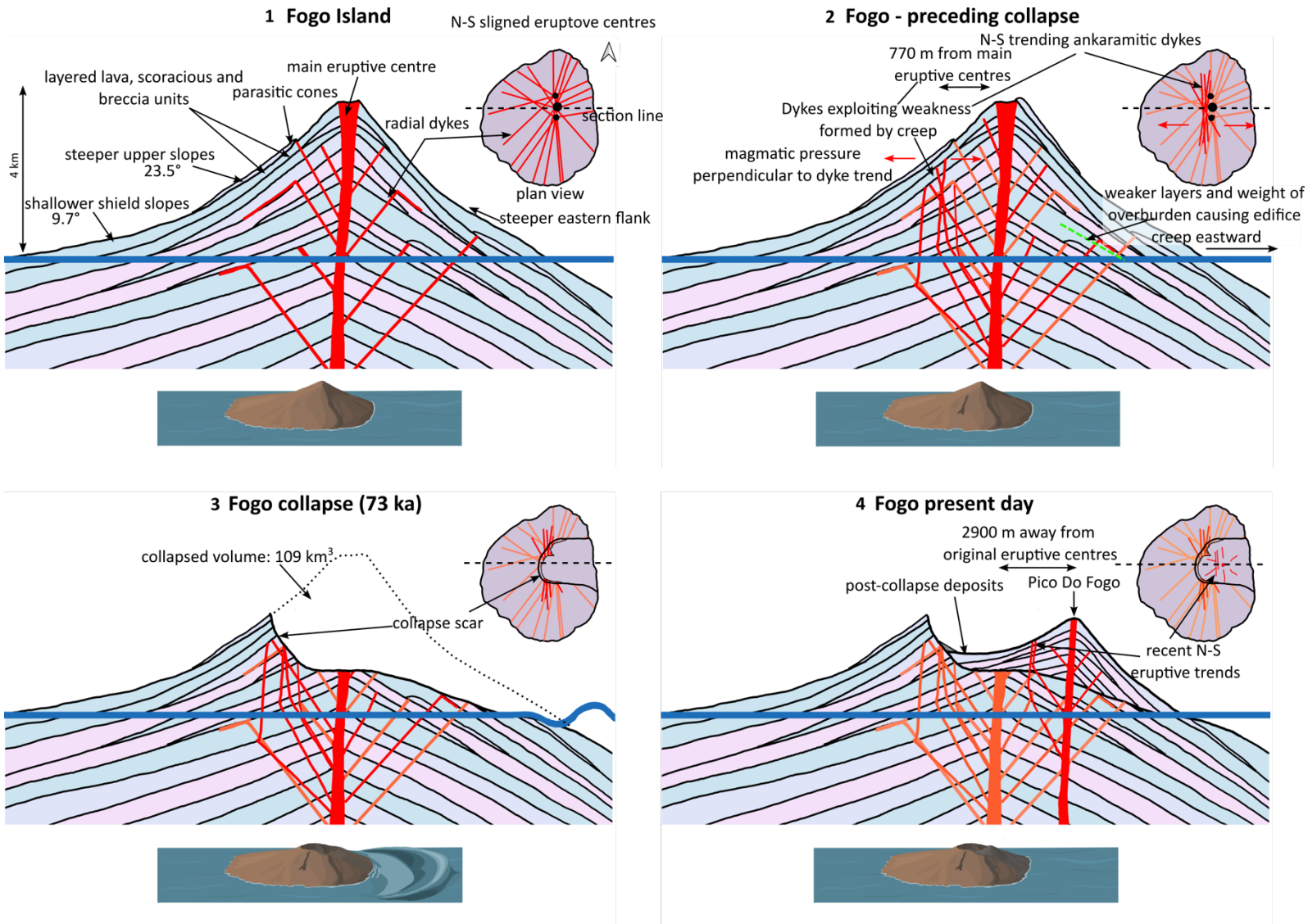

Figure 4.48: Schematic summary figure showing the probable evolution of Fogo leading up to and after collapse based on the results from this study.

4.6 Conclusions

- The extensively exposed dyke systems in the Bordeira cliff on Fogo have provided an indication of the pre-collapse structure of the volcano. SfM modelling was used to map over 2000 dykes in detail and measure and infer orientations.
- From these measurements, radial orientations of dykes in the cliff have been identified and used to infer a main central eruptive centre as well as two smaller centres along a N-S axis west of the present-day Pico do Fogo agreeing with previous suggestion of the pre-collapse magmatic plumbing system (Rolfe-Betts et al., 2024).
- The eruptive centre is inferred to have migrated from this position 2900 m at an azimuth of 85° following the collapse of 109 km^3 of material towards the east at an azimuth of 87°. This highlights the influence of overburden confining pressures on the location of magmatic conduits.
- Preceding this collapse, a series of N-S trending 'ankaramitic' dykes intruded the edifice 770 m west of the inferred eruptive centres. These dyke trends do not coincide with any of these centres and are inferred to be of a different magmatic plumbing reorganisation. This reorganisation is likely to have been a result of an eastward creeping edifice and also may have caused further instability in this orientation eventually leading to collapse.
- The edifice already had some inherent instabilities due to the mechanical properties of the array of lithologies that make up the volcano. These include dykes that may lose their strength through fracturing resulting from continues heating and cooling by intrusive volcanism. In addition, pyroclastics form weak layers within the edifice and may form collapse surfaces.
- This Chapter highlights the benefits of using drone imaging and SfM modelling in this area of research by gaining increased knowledge of the morphology and structure inside the pre-collapse volcano. Previously, the available elevation and imagery data on the Borderia cliff was of poor quality and incomplete. This dataset has improved analysis on the slope of the cliff as well as allowed detailed mapping of the complex and extensive dyke network within the cliff.

- This data collected for Fogo has the potential for further analysis. One of which is to make more measurements such as dyke thicknesses. This could open avenues of research into how dyke emplacement behaves in different materials as well as what the magmatic overpressures were within the edifice during emplacement. Additionally, detailed observations of host rock sequences in the cliff could also be made. This would provide further evidence on the construction of volcano.

5 Discussion: A comparison of Ritter Island and Fogo

5.1 Introduction

Volcanic collapses are a highly destructive hazard and can pose high risks to many populations, particularly those that occur at island volcanoes due to their tsunamogenic potential. These events occur frequently, with an estimated occurrence rate at 5 events per century, and these events are common at all volcanic plate boundaries and so are distributed globally (Dufresne et al., 2021). Studies of global evidence of volcanic collapses show that they are more common in arc settings and can be much larger at ocean island settings (Watt et al., 2021). Understanding these events is therefore important in hazard assessment, monitoring and risk mitigation.

The two volcanic flank collapses studied in this thesis are a subduction arc volcano, Ritter Island (Papua New Guinea) and an ocean island volcano, Fogo (Cape Verde). These collapse events both generated tsunamis which affected neighbouring coastlines. Ritter Island collapsed in 1888 and therefore pre-collapse morphology and activity is better constrained. The collapse volume of this event estimated in this thesis was 3.7 ±0.4 km^3. Fogo collapsed at 73 ka and the nature of the collapse and pre-collapse morphology is less well-constrained. The minimum collapsed volume at Fogo estimated in this thesis was 86.8-109.2 km^3.

Although collapse volumes and tsunami heights are of a different magnitude at these two islands, their collapse scar morphology is remarkably similar. This forms an interesting comparison as despite the two volcanoes being distinct in geological setting and size, they may have shared common morphology or weakening mechanism that led them to look so similar in their collapsed state. Investigating their similarities may provide insight into common processes at other volcanoes vulnerable to flank collapse.

This thesis has used ‘structure from motion’ (SfM) modelling to generate 3D models of the exposed collapse scars at each island to characterise their geomorphology. In particular, a new methodology was developed for restoring pre-collapse volcanic structure using the SfM model at Ritter Island. The method presented in this thesis can be used for other similar collapse scars to improve estimations on pre-collapse morphology and hence improve volume estimates which feed into tsunami modelling. In addition, hydraulic and mechanical properties have been determined for a range of rock samples taken from both islands.

Ritter Island's geology is dominated with interbedded lava flows and scoriaceous tuff with cross-cutting dykes and zones of hydrothermal alteration. This thesis has found that the host rock consists of 25% lava flows, dipping away from a single assumed centre at an average of 32.9°. This host rock is intruded by a series of cross-cutting dykes clustered in a central cusp that show some radial trends and also strong N-S orientation. Alteration is seen often at the base of the cliff (parallel to the landslide slip plane) and surrounding intrusions, suggesting it is as a result of hydrothermal fluids. Hydraulic and mechanical property experiments on samples from Ritter have characterised the strength of rocks found at Ritter.

The results from fieldwork and subsequent analysis undertaken at Fogo include a high-resolution model of the collapse scar, and mapping of the dyke network including analysis of morphology and identifying radial and non-radial dyke trends. Samples collected from Fogo show a range of host rock lithologies, much wider than those from Ritter, and mechanical and hydraulic tests show a range of porosities, permeabilities and strengths.

In this chapter, a discussion of the structure from motion methodology will highlight the value of this tool in this field of research including using it for morphological analysis and reconstruction of volcanic edifices. The features these models highlighted will be discussed and compared across both volcanoes including the scar parameters, geological structure and rock properties. This will highlight key differences and similarities and allow discussion of common instabilities and address the implications for hazard and monitoring.

5.2 Use of SfM modelling for volcanic scarp analysis and edifice reconstruction

Drone imagery and structure from motion (SfM) modelling was used in this project to image and build 3D models of the collapse scars at Ritter Island and Fogo. The drone surveys were performed 6 years apart, which meant that drone technology had moved on between the two field campaigns in terms of the quality of images collected. In addition, the Ritter imagery was taken over the ocean, with only three flights, whereas the Fogo imagery was taken on land, with vastly more flights.

The Ritter Island imagery was collected in 2016 and was shared for use in this project. The imagery used consisted of frames taken from videos of three flights around the island. This was sufficient to build a high-resolution 3D model and orthomosaic and DEM outputs with resolutions of up to 5.53 cm/px. This has improved the data surrounding the subaerial

portion of the collapse scar where satellite imagery and previous elevation models were poor. Figure 5.1A shows an example of the high quality orthomosaic of Ritter Island where individual dykes and lava units can be identified compared with previously available satellite imagery.

Figure 5.1: Examples of high-resolution areas of orthomosacis from the Ritter Island and Fogo SfM models compared to existing imagery for each area. A. showing area of central cusp at Ritter Island i) from ESRI satellite data ii) using orthomosaic generated from this study. B. showing area of the southern cliff from Fogo on i) existing Google satellite data and ii) using orthomosaic generated from this study.

On Fogo, an 11-day field trip was undertaken in 2022 where drone imagery was collected for the purpose of SfM modelling of the Bordeira cliff which represents the headwall of the collapse scar. Here 16,000 georeferenced images were collected which can be used to create models and outputs with resolutions up to 2.67 cm/px of a 11.5 km^2 cliff face. Although satellite imagery and previous elevation models of Fogo were of good quality, the generation of these SfM models allowed detailed observations on inaccessible portions of the cliff that are up to 1000 m high and often near vertical. For example, Figure 5.1 shows a portion of the southern cliff orthomosaic showing a dyke extending up the cliff compared with existing satellite imagery.

The models generated in this project were used in several ways to gain results for improving the knowledge of volcanic collapse. The 3D model and orthomosaics were used at

Ritter Island to make a geological map of the present-day island and at Fogo to map the dyke network. This process is key to understand and interpret the pre-collapse geological structure and processes. DEMs of both islands were used for slope analysis to characterise the collapse fault scarp and constrain the slopes of the pre-collapse island at Ritter Island. This latter measurement was used to reconstruct the geometry of the pre-collapse island and estimate collapse volumes. Collapse geometry and volumes are both key parameters that feed into tsunami modelling, as they control the volume of water displaced and the direction of the tsunami propagation. A similar method was followed at Fogo, but using pre-existing elevation data rather than using the new models as the drone imagery did not cover any of the outer slopes of the island.

5.3 Collapse scar parameters: comparing scale of collapse

Ritter Island was a conical stratovolcano which grew to around 750 m elevation as a result of arc-subduction volcanism. In contrast, Fogo is a shield edifice evolving to a stratovolcano resulting from intraplate hotspot volcanism and having an estimated 3.5-4 km elevation prior to collapse. Their respective catastrophic collapses had collapsed volumes of similar scale to their size. Fogo's minimum subaerial collapse volume is estimated in this study to be 86.8-109.2 km^3 (Figure 5.3). This estimate uses average slopes of the present-day Fogo to calculate a likely central peak and thus volume. The result corroborates with previous studies by Paris et al. (2011) at 115, km^3, Martínez-Moreno et al. (2018) at 110 km^3, and Marques et al. (2019) with a range between 20-120 km^3. However, it is still poorly constrained due to the unknown pre-collapse morphology, depth of the scar and if it extended to include the submarine flanks.

The Fogo collapse is two orders of magnitude larger than the collapse at Ritter Island, estimated in this study at 3.7 km^3. This is a 12% reduction (0.5 km^3 lower) than the estimate from Day et al. (2015) of 4.2 km^3. Karstens et al. (2020) had a shallow slide plane scenario with an estimated volume of 2.59 km^3 which is 42% lower than the estimate from this study. The estimation made here included a better constrained pre-collapse topography due to the SfM 3D model generated, which demonstrates the power of the use of such technology. Reconstructions are better estimated at Ritter due to historic descriptions of the pre-collapse edifice made before the collapse in 1888.

The pre-collapse slopes of Ritter Island are inferred to be 38.4°, whereas the upper slopes of Fogo are much shallower at 25.5° (Figure 5.3). This reflects the different geological

settings where these volcanoes are built and highlights how, despite this, they both built up unstable edifices which shared common processes that led to their collapse.

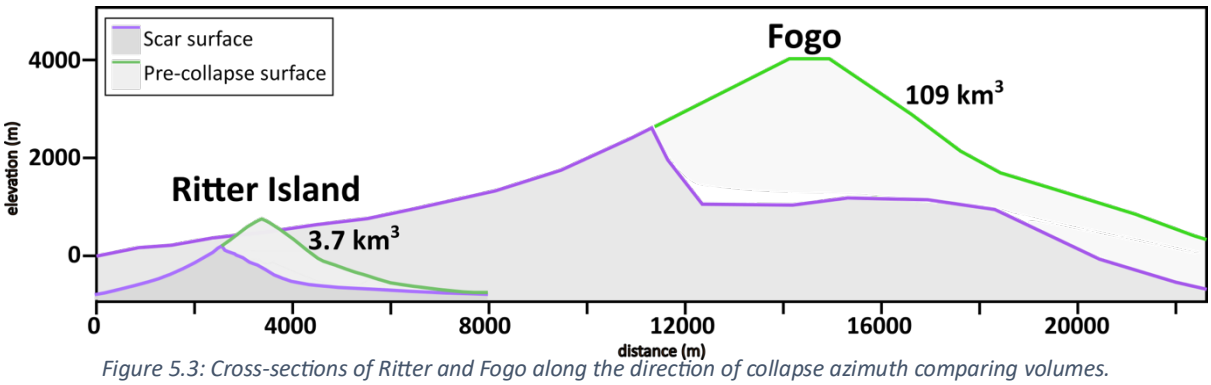

Figure 5.3: Cross-sections of Ritter and Fogo along the direction of collapse azimuth comparing volumes.

Comparing these volumes to other volumes of volcanic collapses using the database from Blahůt et al. (2019), Ritter Island falls within the most common volume range for island-arcs and Fogo falls within the most common volume range for intraplate ocean islands (Figure 5.2).

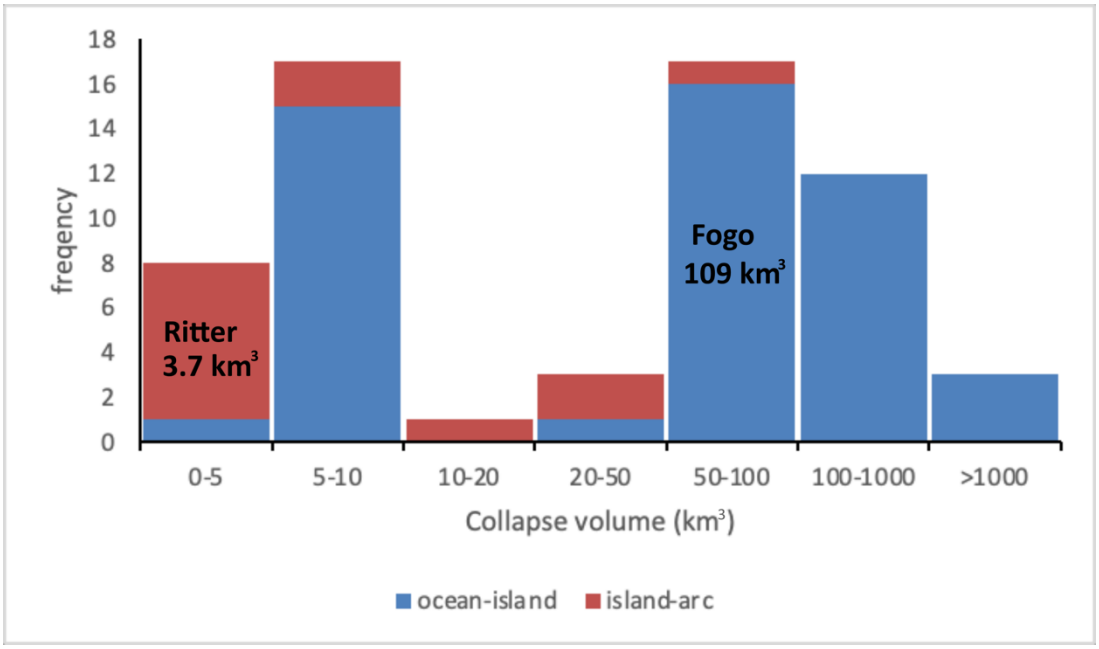

Figure 5.2: Histogram of collapse deposit volumes by volcano type using data from (Blahut et al. 2019) highlighting where the volumes calculated in this thesis of Fogo and Ritter relate to this. (In style of figure from (Watt et al., 2021))

The scar metrics as defined by Bernard et al. (2021) were calculated for Ritter Island and Fogo using estimated pre- and post-collapse surfaces based on the 3D models from this study. These are useful parameters to compare the scale and morphology of volcanic collapse scars, between these events studied in this work and for future studies of other collapse scars. These are summarised in Table 5.1 and displayed comparatively to scale in Figure 5.4. The

scale of collapse is very different, however the aperture angles and scar slopes are similar for both. These measurements depend on the placement of the base of the scar which is difficult to estimate in both localities due to post-collapse volcanism covering the extent of the side walls.

Table 5.1: Scar metrics as described by Bernard et al. (2021) for Ritter Island and Fogo

Parameter Acronym	Parameter description	Ritter Island	Fogo
Ls	Scar length subaerial (m)	4374.8	11310.6
Ws	Scar width (m)	3919.6	9538.7
Wsa	Scar aperture width (m)	3919.6	9139.2
Hs	Scar height (m)	970.6	3388
as	Scar aperture angle (°)	48.0	43.4
Bs	Scar slope (°)	12.5	16.7
ys	Scar azimuth (°)	287.5	86.8
As	Scar area (km^2)	13. 8	97.7
Dsa	Scar depth (m)	1102.5	2924.7
Vsa	Scar volume (km3)	3. 7	109.2
Tsa	Scar thickness (m)	266.5	1100
Ars	Scar aspect ratio	0.13	0.16
Efs	Elongation factor	0.31	0.12
CFs	Closure Factor	1	0.96

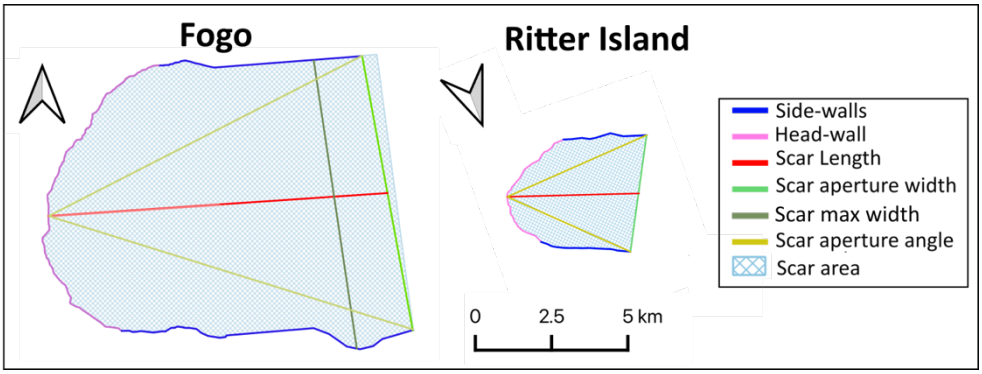

Figure 5.4: Scale comparison in map view of Ritter Island and Fogo highlighting key features and measurements from Table 5.1.

The collapse scarps at both volcanoes have both been eroded back since the time of collapse, as evidenced by the presence of gullies and eroded material at the base of the cliffs. Despite this, they still provide the best evidence of the collapse fault geometry.

Both scar shapes could be described as U-shaped to triangular due to the parallel side walls slightly diverging in the collapse direction (Figure 5.5). At Ritter, this is well-constrained as most of the top of the scar is visible except for at the base where post-collapse volcanism flows over the side walls. On Fogo, this shape is better estimated to the south where the Espigão scarp, a cliff which appears to be the extension of the side wall, is situated. However, in the north post-collapse infill means the shape is poorly constrained. In this study, it is inferred to continue along the trajectory of the northern cliff, however this has been inferred differently in other publications (Martínez-Moreno et al., 2018, Rolfe-Betts et al., 2024). This assumption affects the results of the scar metrics and shape and reduces any volume estimation.

Another similarity is that both exposed scars have a central cusp that protrudes in the middle region of the headwall (Figure 5.5A). In these regions, the cliff is wider, less steep and the topography is more undulating. Other instances of this morphology can also be identified on other volcanoes. For example, the Las Cañadas caldera of Tenerife in the Canary Islands shows a similar trend of a depression surrounded by an curved wall with a central spur (Martí, 2019). The origin of this feature has been the source of much controversy with many suggesting it was formed as a result of successive vertical collapses and other suggesting it was due to lateral collapses (Martí, 2019)

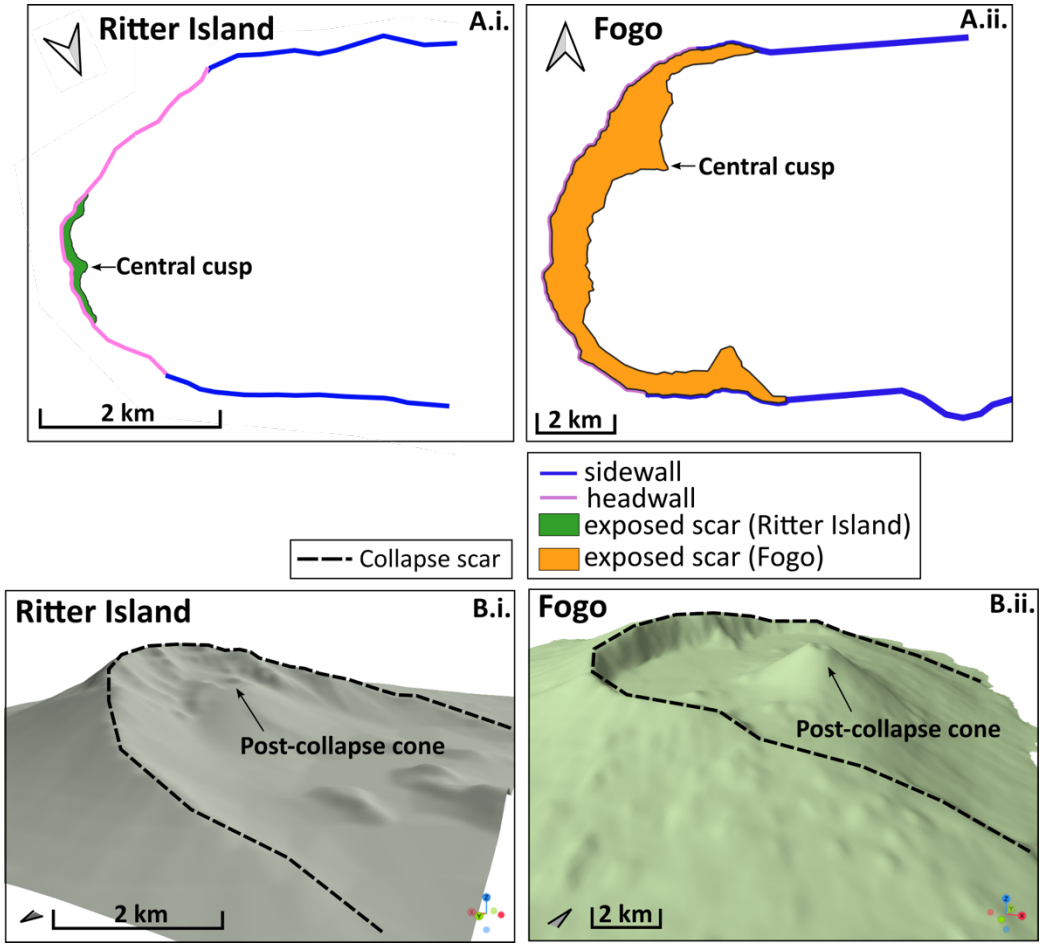

Figure 5.5: Comparing collapse scar shape of Ritter Island and Fogo. A. showing in map view the shape of the exposed scarp and the inferred headwalls and sidewalls of the scar. B shows the islands DEMs (and bathymetry for Ritter Island).

The slopes of the headwall cliffs of the collapse scars, without the influence of post-collapse deposits, are steep and have almost vertical faces included in their topography (Figure 5.6). At Ritter the average slope of this area is 48.5°, whereas at Fogo, the average slope slightly steeper at 54.6°.

Both volcanoes are still active and have built new cones within their collapse scars (Figure 5.5B). At Ritter Island, analysis of the island reconstruction suggests the post-collapse cone lies almost directly beneath the estimated central peak of the pre-collapse island. This suggests the new volcano is being fed by the same magma plumbing system as the pre-collapse volcano with minimal reorganisation.

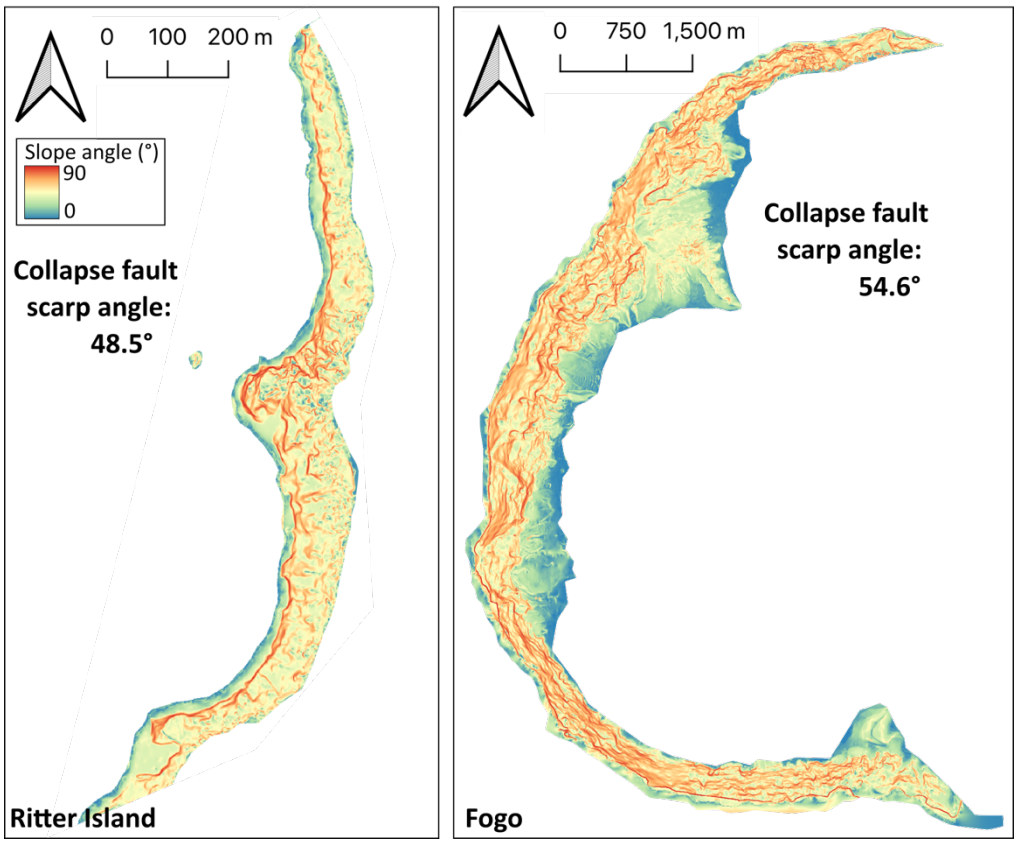

Figure 5.6: Slope maps for the cliffs representing fault scarps at Ritter Island and Fogo with the average slope angle displayed (this value was calculated removing the influence of vegetation and post-collapse erosional deposits).

At Fogo, the post-collapse Pico do Fogo cone lies 2900 m east of the inferred main volcanic centre at an azimuth of 85°. The azimuth of the collapse direction is measured at 87°. This suggests that the collapse of Fogo has led to a major change in stress conditions in the edifice which was sufficient to reorganise the volcanic plumbing, resulting in a shift of activity toward the direction of collapse. The difference between these two scenarios indicates that the change in eruptive centre may be related to the volume of the collapsed material. The removal of a large portion of the edifice may only be relevant when the volume is much larger, releasing more of the overburden pressure on the underlying magma, allowing easier avenues for the magma to migrate towards the surface. The depth of the magma chamber may also affect this process as, if it is shallower, the overburden pressure change would have less effect

of the plumbing of the eruptive centre. In contrast, if it is deeper, the path to the eruptive centre will be more complex and be more influenced by the change and reduction in overburden pressure.

5.4 Geological structure: comparing host rock patterns and intrusion patterns

Both collapse scars provide a window to the internal structure of the pre-collapse islands. The host rocks in both islands consist of lava flows alternating with other volcaniclastic deposits. The Ritter Island edifice appears more regular with thin lava flows and layers of scoriaceous units interbedded at a meter scale. On Fogo, the host rocks similarly include lavas but these vary greatly in thickness with some flows up to 10s of meters thick. Volcaniclastic flow deposits were common also. At Ritter, the host rock appears to be less variable than at Fogo.

Cross-cutting dykes are present in both cliffs. Analysing the locations and trends of these dykes gives insight into the structure and relative stresses within the edifice. At Ritter Island, 39 intrusions (sills and dykes) were observed whereas in Fogo, 2070 dyke traces were mapped.

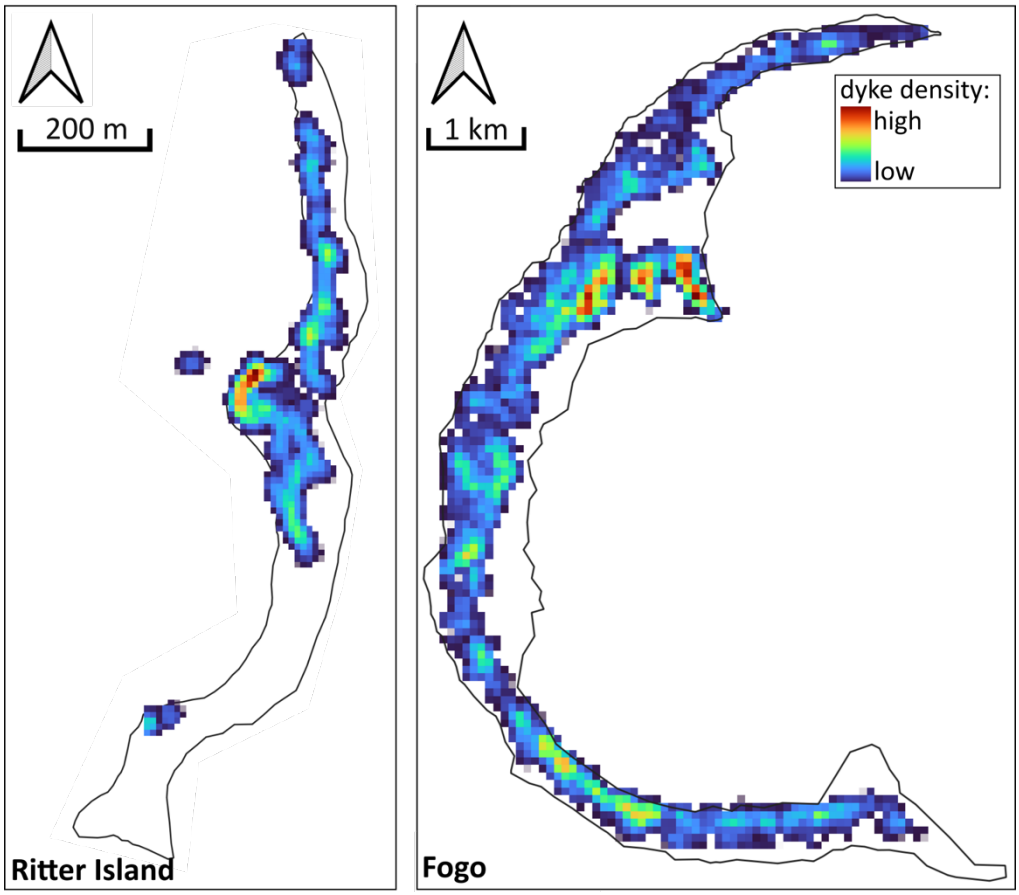

Figure 5.7: Comparing relative dyke density in Ritter and Fogo.

On both islands, most dykes were seen in the lower half of the cliff and the density of intrusions reduced with elevation. The density of dykes highlights a clustering of intrusions in the central cusp in both localities (Figure 5.7). This higher density of dykes may be as a result of the central cusp being an older portion of the edifice. In addition, this density may reflect the closer proximity to the volcanic centres and preferential intrusive pathways into already intruded and fractured rocks.

By measuring and assessing the orientations of these intrusions, some patterns have been observed. Both islands show evidence of radial dykes, typical of volcanic edifices. On Fogo, these radial dykes showed higher densities in certain orientations which may be indicative of a triple-armed rift morphology. In addition, both scars show evidence of a strong orientation of dykes perpendicular to the collapse direction. This is seen in the central cusp at both volcanoes. This trend is distinctively different to the radial trends and may indicate an additional zone of weakness into which the dykes were intruding (Figure 5.8). These zones of weakness could have been created by the extension of the volcanic edifices from gradual spreading on a weaker layer from the increasing weight of overburden. This gradual spreading

accompanied with the onset of perpendicular intrusions to this would have increased magmatic pressures acting in the E-W direction at both volcanoes. This includes mechanical and thermal energy. At both volcanoes, the collapse occurred perpendicular to these trends suggesting that this process had a considerable influence on the eventual collapse. At Ritter Island, these dykes are of various ages and composition. By contrast, these non-radial dykes on Fogo are clearly younger and of a distinct 'ankaramitic' composition that cross-cut older dykes and fed a number of lava flows in the east (Rolfe-Betts et al., 2024).This may suggest that the zone of weakness in this orientation may have been present over a longer timescale at Ritter. On Fogo, as suggested by Day et al. (1999), the indication is that these dykes may represent a weakness in this orientation preceding the collapse. This study has supported this theory, strengthening the evidence of this late intrusion tend and highlighting the likely direction of collapse and the post-collapse migration of eruptive centre being perpendicular to this trend.

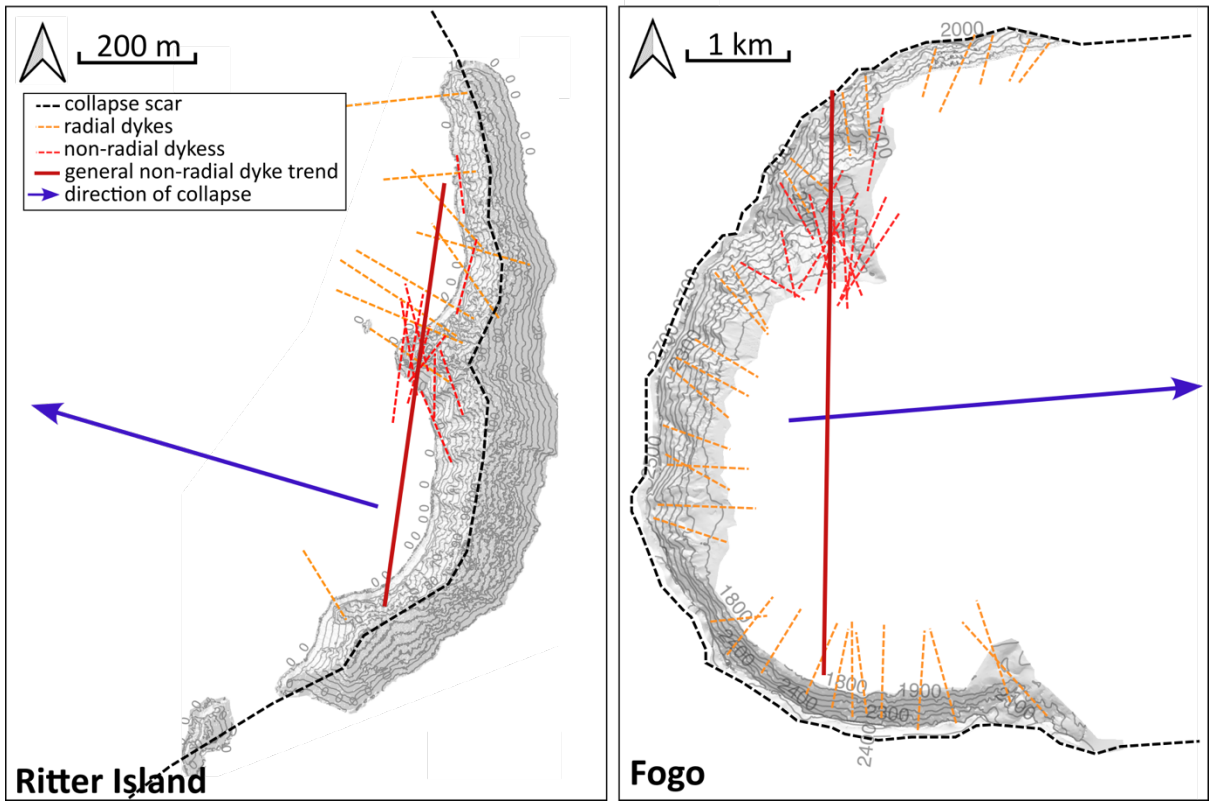

Figure 5.8: Schematic diagram comparing dyke orientations at Ritter Island and Fogo highlighting the difference between inferred radial and non-radial intrusions, the non-radial general trend and the direction of the flank collapse at each.

5.5 Comparing rock properties

Sample results for hydraulic and mechanical properties for both Ritter and Fogo are compared here with published data to place them in the context of each other and of data for other volcanic rocks.

Both islands show the same trend that permeability increases as a function of porosity due to the empirical relationship between these properties. Both islands also show much lower permeability trends compared to published data. The Fogo results show a much wider range of porosity values, between 0 and 40%, compared to Ritter, which ranges from 2 to 23%. This results from the wider range of rock types sampled at Fogo and the limitations of the sample set from Ritter.

Both islands exhibit a decreasing uniaxial strength with increasing porosity which agrees with published trends for volcanic rocks (Figure 5.9A). The trend for Fogo suggests that these rocks are stronger with a given porosity compared to the Ritter results. This is particularly apparent at low porosities, where the Fogo results show high compressive strengths. These points relate to the dyke samples rather than the lavas and pyroclastics.

Both islands also show a decreasing trend of Young's modulus with increasing porosity. This suggests an increasing elastic response with increased porosity. The trend of the Fogo samples suggests that, in general, these rocks are stiffer than those from Ritter (Figure 5.9B).

The strength also increases with Young's modulus of the rocks at both islands. This trend is steeper with the rocks at Fogo. The results are similar at low strengths, which fits with the smaller degree of scatter of the published data. At higher Young's modulus, Fogo rocks are stronger than the Ritter rocks (Figure 5.9C).

At Ritter Island, the remaining edifice shows evidence of alteration. Using an altered porous lava compared to an unaltered lava, results suggest the influence of this alteration increases porosity, permeability and reduces strength by 50%. This reduction in strength is typical of argillic alteration, and therefore indicates that the type of alteration here may be argillic acid-sulphate leaching and may contribute in generating instability within the pre-collapse edifice leading to. Alteration has also been identified at Fogo but was not investigated mechanically. However, it could pose a similar relationship and form weaker zones within the edifice.

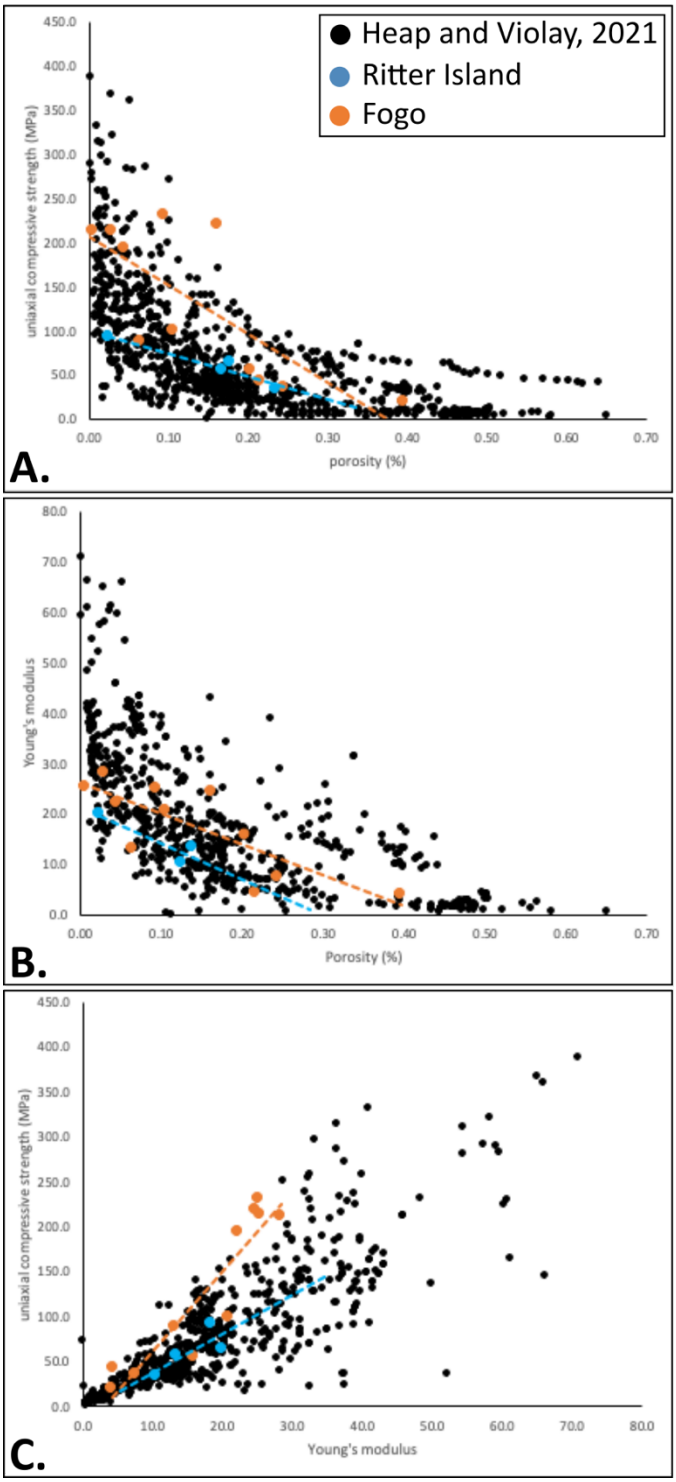

Figure 5.9: Comparing compilation of volcanic rock properties from Heap and Violay, 2021 with the results from Fogo and Ritter Island. A. Porosity against uniaxial compressive strength. B. Porosity against Young's modulus. C. Young's modulus against uniaxial compressive strength.

5.6 Insights into flank collapse instability

From historical descriptions of the pre-collapse Ritter island, it is known that the island grew from repeated Strombolian eruptions which build a steep-sided conical volcano (Ray, 2017). There was one main vent at the summit but occasional reports of parasitic cones

suggest that dyke-fed eruptions also occurred (Ray, 2017). This can be seen in the collapse scar at Ritter Island in its present-day morphology with numerous dykes cutting through the layers of lavas and scoria (Watt et al., 2019, Day et al., 2015). The SfM 3D model of Ritter made in this study has improved the accuracy of measurements of the island. For example, the length of the subaerial island, is 1623 m, its width at the cusp is 308 m and its maximum elevation is 117 m. From this work, an improved estimate on the slope angle of the pre-collapse volcano has been estimated at 38.4°. This is significantly shallower than previous estimates of 44° (Johnson, 1987). This new result has been used to reconstruct the pre-collapse volcano to provide an improved estimate of the collapsed volume of 3.69 km^3 (Figure 5.10). This was compared to a volume estimate using the originally proposed 44° which estimated a much lower 3.22 km^3. This difference highlights the importance of this improved slope estimate as the resultant volume estimations can vary significantly with this change in angle. The new volume estimate of 3.69 km^3 also differs from previous estimates which also reconstructed pre-and post-collapse surfaces. It is lower than the estimate of 4.2 km^3 from Day et al. (2015), but is higher than the estimate of 2.59 km^3 from Karstens et al. (2020). The result from this study uses a more accurate representation of the pre-collapse edifice from the SfM model. The critical parameters in tsunami modelling are the collapsed volume of material and the speed of emplacement. Therefore, this results from this work can contribute in the reconstruction of the tsunamigenic event at Ritter in 1888. As there is evidence of tsunami run-up heights from this event, this more accurate estimation of the collapse volume based on the new sub-aerial DEM generated, will mean a more accurate estimation of the speed of the collapse.

Previous suggestions of instability and triggering included pore fluid pressurisation from deep magmatic intrusion or a weak seafloor sediment basement (Day et al., 2015). Volcanic activity is not necessarily recorded before the event but may have occurred as a result of the collapse (Watt et al., 2019). From this study, it can be assumed that most of the lava flows that make up around 25% of the pre-collapse had porosities which ranged up to 23% (Figure 5.12). Porous lavas had higher permeabilities than lower porosity rocks; this would have allowed hydrothermal fluids to flow around the edifice and enhance fluid rock interaction leading to alteration. In present-day Ritter, hydrothermal alteration affects arounds 13% of the cliff face, often apparently associated with the intrusions. These intrusions may have been volatile-rich and therefore introduced acidic hydrothermal fluids to the surrounding areas (Engvik et al.,

2005). Hydrothermal alteration can either increase porosity by dissolution or decrease porosity by mineral precipitation (Heap et al., 2019, Heap and Violay, 2021). Both of these occurrences can both lead to destabilisation in an edifice. This current study indicates that an altered porous lava flow can have its porosity and permeability increased, and its strength reduced by almost half from 69 MPa to 34 MPa, compared to a fresher lava sample (Figure 5.12). Similar results have been seen in basalts elsewhere and is therefore indicative of acid-sulphate leaching argillic alteration (Romero et al., 2021, Heap and Violay, 2021). This indicates that with the presence of possible argillic hydrothermal alteration abundantly found within the edifice at Ritter, zones of host rocks can have strengths reduced by 50%. This is a key identification of instability within the pre-collapse edifice and could have contributed to the initiation of collapse.

The dyke samples have lower porosities and permeabilities than the lavas. The more permeable intrusive rocks were mainly affected by the presence of fractures. The results here show that older dykes may have higher permeabilities due to cyclic heating and cooling which would cause cracking. Permeability measurements taken at higher confining pressures show a reduction of permeability in all the rocks tested including the dykes. This is caused by the closure of cracks from 3.5 $x10^{-17}$ m^2 to 2.2 $x10^{-20}$ m^2. The low permeability dykes may also trap or compartmentalise fluids in into certain layers increasing alteration or possibly causing pockets of pressurisation (Figure 5.12). However, increases in permeability due to alteration may serve to reduce this effect. This may suggest that the presence of the strength reducing alteration might have been a more important weakening mechanism contributing to the volcanic collapse. This is supported by alteration being consistent through the remaining edifice and parallel to the slip plane in steeper sections of the cliff.

The dataset is limited as there are no samples of the poorly consolidated units at Ritter. Previous studies of pyroclastic rocks suggest they are characterised by low Young's modulus and compressive strengths (Heap and Violay, 2021). An average UCS of tuffs measured by Dinçer et al. (2004) show an average of 42 MPa and minimums of 33 MPa. These may also form weaker layers within the edifice at Ritter.

Mapping of the intrusions on the exposed cliff face at Ritter Island revealed a strong orientation of dykes in the N-S orientation (Figure 5.8). This has been noted previously and can also be seen in outcrops in the shallow areas around the island (Saunders and Kuduon, 2009, Day et al., 2015). Some dykes were also inferred to be radial dykes to the north and

south but towards the centre more N-S dykes were seen (Figure 5.10). There is a clustering of these dykes in the central cusp. This strong orientation of N-S dykes may have increased the magmatic pressure acting and extension in the E-W orientation and caused increased strain in this orientation eventually leading to collapse. The dykes may have intruded in this orientation due to extension caused by the gradual spreading of the edifice as suggested in Karstens et al. (2019) for which there is evidence in possible compressional deformation in seafloor sediments. The N-S intrusions are inferred to be of different ages and compositions due to the different colours of the cross-cutting dykes, suggesting this creep occurred over a long period of time developing a weakness in the N-S orientation.

The uniaxial compressive strength of the dykes on Ritter shows that the intrusions are much stronger than the surrounding host rock with a measured UCS of 93 MPa. The dykes make up most of the central cusp and so their presence may have been the reason behind this morphology where the initial fault could have propagated and deflected around a stronger region of rock.

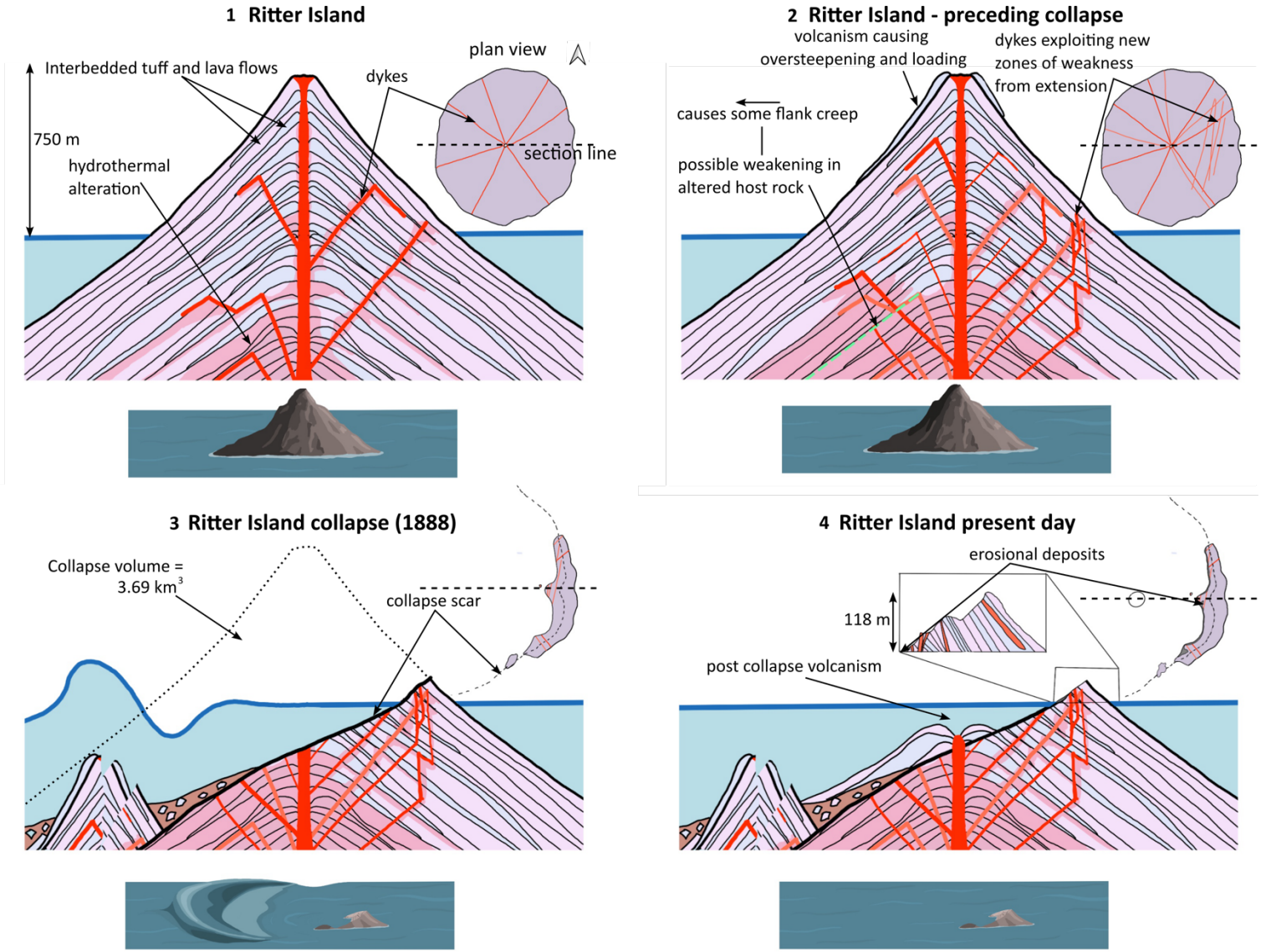

Figure 5.10: Schematic summary figure showing the probable evolution of Ritter Island leading up to and after collapse based on the results from this study.

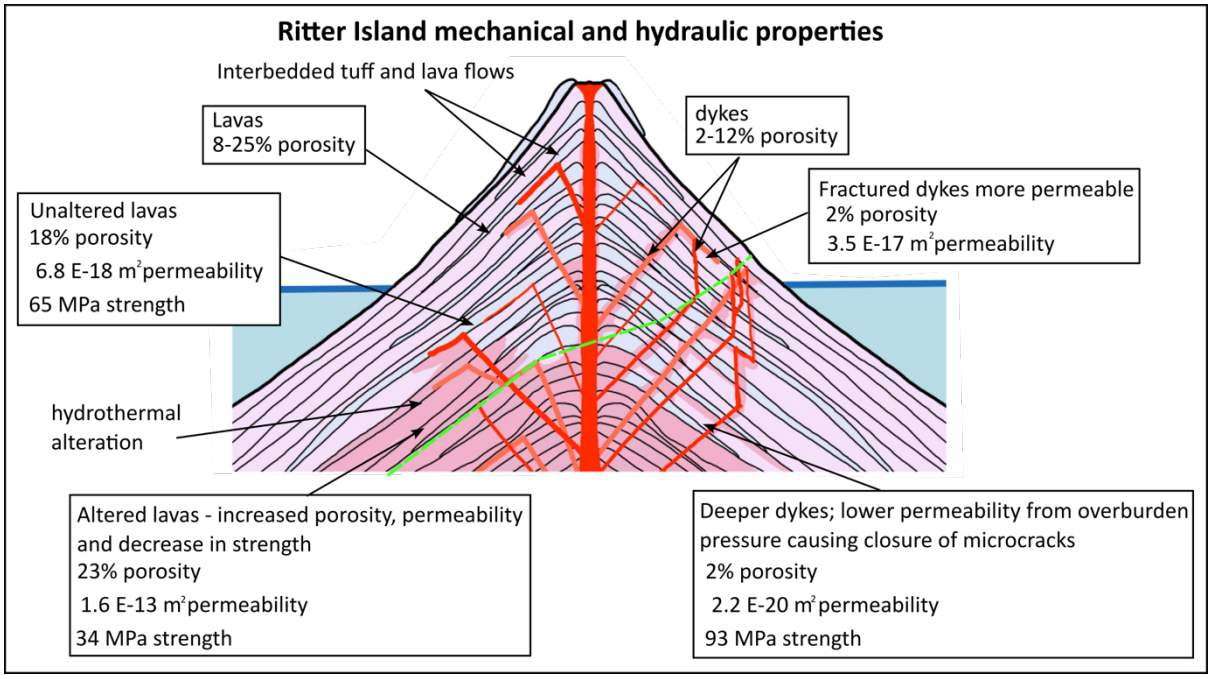

Figure 5.12: Schematic diagram of the inferred pre-collapse Ritter Island highlighting the measured rock properties measured and how this influence weakening of the edifice.

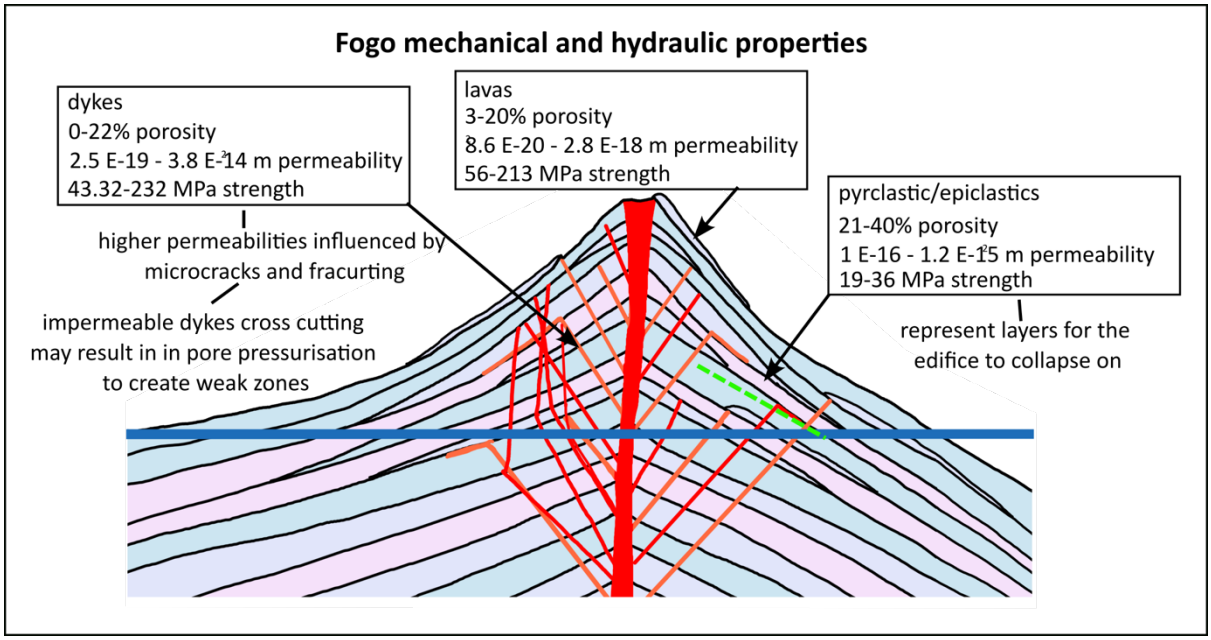

Figure 5.11: Schematic diagram of the inferred pre-collapse Fogo highlighting the measured rock properties measured and how this influence weakening of the edifice.

The collapse of Fogo occurred around 73 ka and its nature is still widely debated (Ramalho et al., 2015). Some publications suggest the collapse scar was made by several caldera collapses and a subsequent lateral collapse due to the two curved sections of the cliff with different base elevations, separated by the Monte Amarelo central cusp (Martínez-Moreno et al., 2018). Others suggest that this morphology was caused by a single flank collapse to the east

(Day et al., 1999). In this thesis, the latter model has been accepted after studying the morphology of the collapse scar at Ritter Island. The collapse at Ritter Island is understood to be a singular collapse event based on the evidence of tsunami timings and run ups. Therefore, this provides evidence that a scar with central protruding cusp can result from a single flank failure and therefore is the likely scenario at Fogo.

At Fogo, uniaxial compressive strength tests on dyke samples show that they also have high compressive strengths with maximum strengths measured of 223 MPa. These are much higher than the surrounding host rocks with an average strength of 167 MPa, being almost double the average of the host rocks strengths at 82.5 MPa (Figure 5.11). This is similar to Ritter where the strength of the dyke was much higher than that of the lava samples. As there is also a high clustering of intrusions in the central cusp at Fogo, the high strength of this region due to the presence of numerous dykes may have formed a strong region of rock for the collapse fault to deflect around, similar to the suggestion at Ritter.

The host rocks sampled at Fogo were very varied and consisted of lava flows, volcaniclastic and epiclastic units. This shows that Fogo is a much more complex and diverse edifice. Previous work has suggested these host rock layers dip outwards at 20-40° (Day et al., 1999). There were some areas of alteration on Fogo, including the paler yellow areas of host rock in the area of Monte Amarelo amongst the older units and some redder units in the base of the cliff to the south (Day et al., 1999, Marques et al., 2019). This suggests different kinds of alteration may have occurred at Fogo. In contrast, at Ritter Island, the evidence in the cliff suggests that one sort of alteration dominated, providing the areas of reddened material at the base of the cliff and surrounding intrusions. In this study, this alteration is suggested to be advanced argillic which affects the edifice strength by weakening the layers. This may also be apparent at Fogo, although was not confirmed in this research.

Comparing the lava flows to the pyroclastic units at Fogo showed that the lavas can be very strong, with strengths measured up to 213 MPa in the less porous samples. However, the weaker flow units were very weak, with strengths as low as 19 MPa (Figure 5.11). This means that the edifice is built up of layers of variable strengths with the pyroclastic units possibly forming some weaker layers on which the collapse plane could have slipped. The stronger lava cores and dykes at Fogo compared to Ritter coincide with them having lower porosities. The different eruptive style on Fogo producing stronger rocks allowed the edifice to grow larger and at shallower slope angles compared to Ritter.

The dykes had low porosities with an average of 6.7% and some of the low porosity lava cores had low permeabilities unless they were highly fractured. These may have formed impermeable barriers to fluids and formed pockets of high pore fluid pressures generating instable zones within the edifice, particularly as in some areas there are many cross-cutting impermeable intrusions (Figure 5.11).

This builds up a picture of the various ways the Fogo edifice developed instabilities. From this research, it has been shown that the pre-collapse volcano had one major eruptive centre and possibly at least two others located along a generally N-S axis. This corroborates the suggestion in Rolfe-Betts et al. (2024). The continued extrusion and deposition of fresh material creating slopes of around 25.5° or greater, with probable steeper sides to the east due to the prevailing wind direction based on present-day morphology, would have increased stress on this axis. The weight of overburden could have led to the edifice beginning to slip eastward on a weaker pyroclastic layer deep in the edifice. This movement would have had extensional effects on the edifice, opening up new pathways for intrusions to exploit (Figure 5.13).

The orientation of dykes shows evidence of radial patterns as well as later cross-cutting ankaramitic dykes with a strong N-S orientation. These have been suggested to represent a different phase of eruptive activity indicating instability preceding the collapse in previous studies (Day et al., 1999, Foeken et al., 2009, Rolfe-Betts et al., 2024). In this study, detailed mapping of these dykes and orientations corroborates this theory and shows how this general N-S trend lies 770 m to the west of the main volcanic centres. The continued intrusions in this zone, as a result of a developing instability, are likely to have pushed the edifice closer to collapse due to the outward magmatic pressure induced in the E-W orientation (Figure 5.13). This is a similar mechanism suggested for Ritter and may also be a reason of their similar collapse morphologies.

The work completed in this project has various implications in terms of hazard assessment and monitoring unstable flanks.

- SfM 3D modelling of collapse scars is shown to be valuable for reconstructing historical collapse events. The use of this method shows how 3D models can improve collapse volume estimates which is critical for tsunami modelling simulations. Additionally, their use can develop the characterisation of the geology and morphology of collapse scars which can build up a clearer picture of instabilities which led to volcanic collapse.

- Evidence of alteration inducing a reduction of rock strength identified at Ritter Island is considered to be a key weakening mechanism leading up to this collapse. This has highlighted the importance of understanding this mechanism further to identify how it affects vulnerable edifices and how extensive it is within the edifice.
- From both Ritter and Fogo there is a suggestion that changing patterns of dyke emplacement within an unstable volcanic edifice leading to collapse reveals underlying stress changes from edifice creep. This may be a key indicator in identifying unstable edifices that may collapse. From the recent collapse of Anak Krakatau, inSAR data in the years preceding the collapse showed the flank was moving and that intrusion events caused this movement to accelerate until the eventual catastrophic collapse (Zorn et al., 2023). This provides evidence that dyke emplacement can lead to collapses and that the movement of flanks can precede catastrophic collapse events. This may be relevant at present-day Fogo as discussed in Day et al. (1999). The cessation of eruptive activity from Pico do Fogo and the evidence of fissure style activity on the western flanks of it in a N-S orientation may be a precursor to developing instability within the flanks. Monitoring flank movement alongside dyke emplacement and orientation will be key in examining a flanks predisposition to collapse.

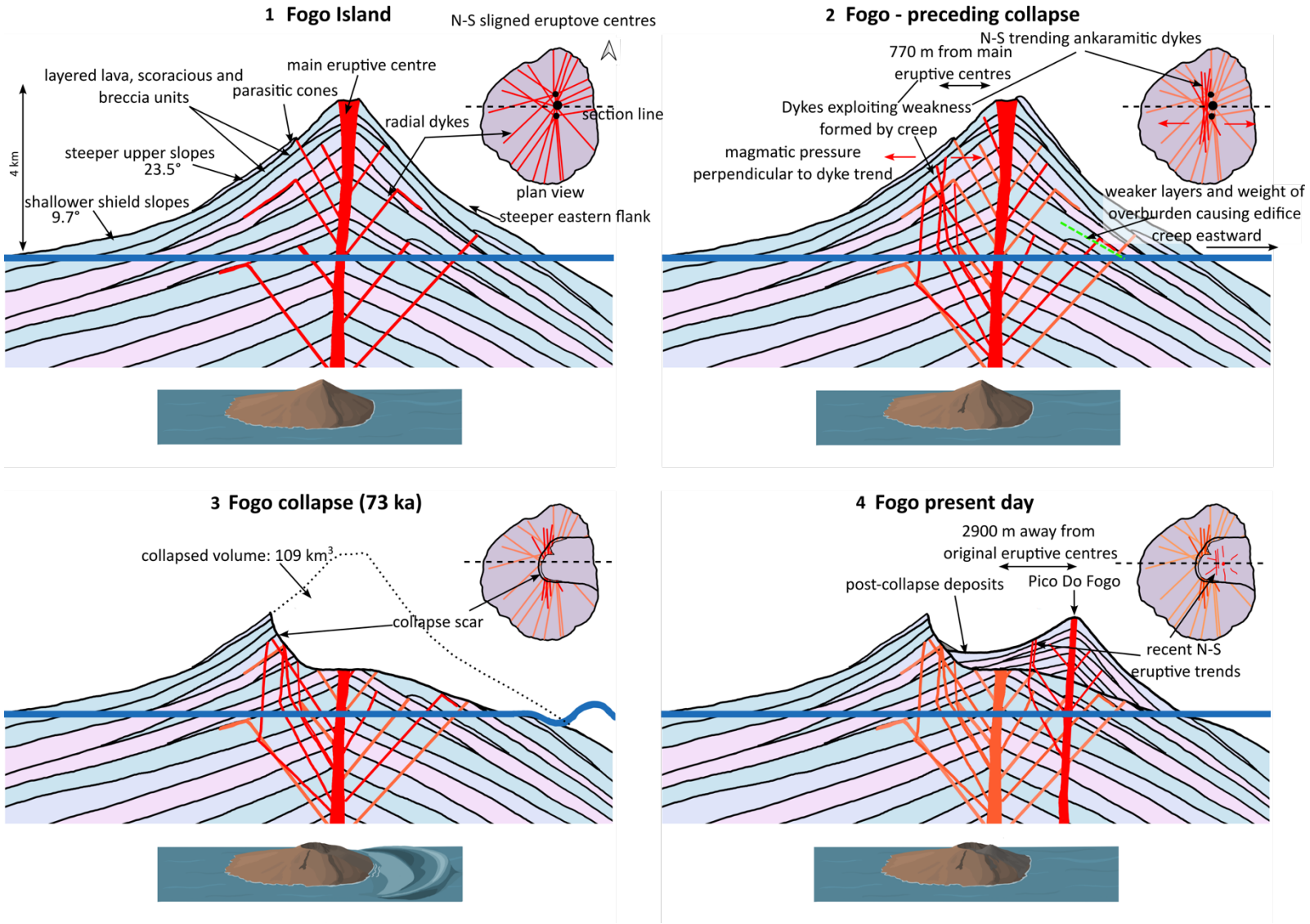

Figure 5.13: Schematic summary figure showing the probable evolution of Fogo leading up to and after collapse based on the results from this study.

6 Conclusions and Future work

6.1 Future work

The work undertaken for this project has improved the datasets and understanding for collapse scars. Future work at both localities could further this work and the knowledge in this field. In addition, following similar methodologies used in this thesis could also increase knowledge about other collapse scars and improve overall knowledge about volcanic collapse events. This would further improve identification of flanks vulnerable to collapse hence progress monitoring for such events in the future.

- At Ritter Island, future work on the rock properties could develop the work done in this thesis. In particular, the identification of the weaker altered material leads has led to a hypothesis for a weakening mechanism in this location. By collecting and examining more of the altered material to confirm the nature of alteration will indicate how it may have weakened the flanks which eventually collapsed.
- At Fogo, further work on the drone image dataset could improve models. For example, further fieldwork could be undertaken to capture more imagery of the top of the cliff and upper slopes of the island would better constrain this section of the model and improve 3D pre-collapse reconstructions and volume calculations by using the methodology presented in this thesis.
- The high-resolution model identified over 2000 dykes in the cliff at Fogo, however many more dykes are present which could be identified using this same model. Further work on mapping the dykes in more detail could improve constraints on the locations for the pre-collapse eruptive centre and the investigation into the change in dyke plumbing.
- The Fogo SfM model made in this project could be used to further investigate the host rock. This could be used to assess eruptive history from changes in host rock with elevation. It can also be used to investigate the possibility of the presence of the Galinheiros Fault extending through the cliff suggested by previous authors (Carvalho et al., 2022).
- This SfM model of Fogo could also provide an excellent dataset of dyke thicknesses and lengths compared to the medium of host rock intruded which would be informative of dyke propagation, magma overpressures during emplacement and the

dynamics of magma movement within the volcano (Geshi et al., 2010, Geshi et al., 2020, Browning et al., 2015).

- The work from this project has set up work to be done in computer modelling of the instabilities, as in Heap et al. (2021a), by using the improved dimensions of the pre- and post-collapse island as well as key rock properties to feed into models to test weakening mechanism theories.
- Having highlighted the power of SfM models in this field, it is important to state the lessons learned for future work of a similar nature which could be used in other localities. When collecting data for generating models, it is useful to consider several factors that affect the collection and the resultant model:
    - Using drones with the capability of producing geolocations and camera orientations within metadata is preferable. This improves the quality and reduces the time taken for image matching to generate tie points. This also means the resultant model is correctly georeferenced. The Ritter data was not referenced like this and had to be retrospectively geolocated after the model was made. This has introduced some error into the model. The Fogo model is therefore more accurately placed as images were georeferenced.
    - Using ground control points (GCPs) is helpful in validating georeferencing of the model and can help image matching. GCPs were unable to be used on Ritter due to accessibility and therefore there was some error in image matching.
    - Considering legal flight restrictions in place at the location of data collection is essential. For Fogo, the high elevation of the cliff in parts meant that the entirety of it was difficult to capture in the same quality all the way up the cliff.
    - Considering the battery flight time, the number of spare batteries and the ability to charge batteries efficiently is needed for an efficient drone survey.
    - Checking the weather conditions that may affect the ability of drone launch should be done. In addition, considering the weather effect on the lighting conditions for the images is important as it affects the quality of the model.
    - Considering the time of day that will affect shadows on the intended object. Unavoidable shadows have affected both models created in this project and is therefore a limitation of the resultant orthomosaics.

- Processing the images also requires appropriate software. In this project, Agisoft software was used on machines with high specifications and processing power and high graphic capabilities. Processing also took place away from the field area in both Fogo and Ritter, due to restricted internet access to transfer data to the computers. To process many images at the highest quality, processing times can take weeks to produce models. However, model processing can be run at lower quality to provide preliminary models if needed.

6.2 Conclusion

Catastrophic volcanic collapses occur often on a geological timescale and globally in a variety of volcanic settings. These events produce volcanic debris avalanches which can be tsunamigenic at island volcanoes, increasing their destructive capacity and reach. Investigations of scars at known collapses is important to ascertain how instabilities developed in collapsed edifices and to reconstruct pre-collapse morphologies to accurately estimate collapsed volumes. These volumes directly feed into simulating tsunami scenarios and improved knowledge on instability is therefore essential hazard assessment and monitoring.

In this thesis, two volcanic collapse scars of different scales are studied, both with evidence of having generated tsunamis; Ritter Island and Fogo. This study uses a combination of SfM 3D modelling and mechanical and hydraulic testing to further the understanding of each of the collapses and to characterise the features of the pre-collapse edifices that may have led to developing instabilities.

SfM modelling has been used to create 3D models of two exposed volcanic flank collapse scarps and has proved to be a valuable tool in their analysis. This is a particularly useful methodology when localities are remote or in hard-to-reach areas. For example, Ritter Island is a small remote island in Papua New Guinea and this model has improved the resolution of elevation and ortho images available for this island. At Fogo, the 3D model help as the almost-vertical scarp is up to 1000 m high and difficult to access in some regions. The SfM models generated were used in several ways to gain measurements for the collapse scars at Ritter and Fogo.

The 3D model created for Ritter Island produced outputs of a 5.53 cm/px orthomosaic and a 7.33 cm/px DEM. These were used to map the geology of Ritter as well as analyse the morphology and reconstruct the pre-collapse island to estimate a collapse volume of 3.7 km^3. This is 12% lower than the estimate from Day et al. (2015) of 4.2 km^3 and 42% higher than an estimate from Karstens et al. (2020) of 2.59 km^3. An accurate estimate of collapsed volume is critical to be able to run tsunami models of the event. The 3D model produced at Fogo for the Bordeira cliff produced orthomosaic and DEM outputs from resolutions of up to 2cm/px. This was used to map in detail 2070 dykes in the cliff. Reconstructions of pre-collapse topography has found differing results at Fogo and Ritter in terms of the position of post-collapse volcanism relative to the pre-collapse summit. At Ritter, the conduit feeding eruptions is inferred to remain in place whereas at Fogo, the position of the main eruptive vent has moved 2900 m in the direction of collapse due to the removal of confining pressures.

The measurements of rock hydraulic and mechanical properties including porosity, permeability, uniaxial compressive strength and Young's modulus, has allowed speculation of the relative strengths and weaknesses within edifice of both pre-collapse volcanoes. The trends from both islands show that with increasing porosity, the permeability increases, the Young's modulus decreases and the strength decreases which corroborates previously published datasets on other volcanic rocks.

In both Ritter Island and Fogo, the dykes are strong, impermeable and have low porosity. In both volcanoes the presence of fractures in the dykes plays an important role in their permeability. Closure of fractures under higher confining pressures suggests that they may have lower porosities and permeabilities at depth. Intrusion may result in pockets of pressurisation creating some unstable zones and leading to hydrothermal alteration to host rocks. At Ritter, host rocks porosities vary from 8 to 25% which is attributed to the presence of vesicles in most samples. Permeability increases with porosity, suggesting that the lavas allow fluid to flow through them, leading to wide regions of hydrothermal alteration.

At Ritter Island, altered host rock accounts for 13% of the cliff and is mainly distributed near the base of the cliff and surrounding intrusions. Results suggest that the presence of alteration in porous lavas can lead to a decrease of strength by almost 50% suggesting sulphate leaching argillic alteration. It is inferred that this alteration is present throughout the edifice and in higher proportions at depth with an increase of intrusion and groundwater interaction. Due to its distribution in the cliff face and evidence that it reduces compressive

strengths of edifice rocks, this alteration is suggested to be a key part of the instability in the Ritter Island volcano that led to collapse. This adds to the literature suggesting that the identification of the presence of alteration, its type and effect on compressive strengths of edifice rocks and its extent can be crucial to identifying unstable edifices.

Across all samples from Fogo, the rocks were generally stronger than those from Ritter Island, which may result from the samples being less porous reflecting the volcanic setting and eruptive style. The host rocks are more variable than at Ritter due to a sampling bias at Ritter and the more heterogeneous layering found at Fogo. In Fogo, these rocks can be either very weak, as in the case of the pyroclastic rocks, or very strong as in the case of the low porosity lavas. This means the edifice is built of alternating very strong and weak rocks. From this study, the inference is that the weaker clastic deposits form weak layers where the edifice may have begun to fail upon at depth.

Comparison of the two collapse scars show a similarity in scar morphology and pattern of dyke orientation. At both localities, radial dykes were present in the cliffs as well as a clustering of dykes in a central protruding cusp. At Ritter Island there are fewer radial dykes but at Fogo many more were mapped. Directions were extrapolated from the radial dykes at Fogo which has indicated the presence of one main eruptive centre and possibly two smaller centres along a N-S lineation west of the present-day Pico do Fogo. Also present at both volcanoes is a non-radial trend of dykes orientated perpendicularly to the direction of collapse. As suggested in previous literature for Fogo, this might represent a region of instability along this axis resulting from the gradual movement of the flank to the east. This study suggests this mechanism is also apparent at Ritter. At Ritter Island, these trending dykes are inferred to be of different compositions and age suggesting the movement of the flank may have been long lived relative to the age of the volcano. At Fogo, these dykes have a distinct ankaramitic composition that fed a series of lava flows preceding the collapse. The continued intrusions in this zone for both volcanoes, as a result of a developing instability, is likely to have pushed the edifice closer to collapse due to the outward magmatic pressure in the form of mechanical and thermal energy perpendicular to the dyke trend. This process has been inferred to be important in development of instability at both islands. These two examples highlight that monitoring dyke emplacement and flank movement is significant in identifying unstable edifices.

This project has highlighted the value of using SfM modelling to generate high resolution 3D models of collapse scars in this field of study. New 3D models for Ritter Island and the

Borderia Cliff on Fogo have improved the available datasets from both localities. This project has analysed these models to provide scar measurements and pre-collapse reconstructions which, alongside hydraulic and mechanical properties obtained, have allowed speculation on the pre-collapse structure of the islands and methods of generating instability that eventually led to their tsunamigenic collapse. This has implications for hazard assessment where vulnerable edifices to collapse could be identified by assessing the flank for a change in emplacement pattern or emplacements causing an acceleration of a flank's movement. This would be useful in monitoring these situations in terms of observing flank movement and acceleration.

To conclude, the main knowledge advances from this project can be summarised as:

- Drone imagery and SfM modelling are powerful tools for investigating volcanic collapse scars. Methodologies presented in this research can be replicated for other similar investigations to generate high-resolution elevation models and orthoimages which can be used to map scar morphology and geology and measure scar dimensions. This information can help deduce the evolution of an edifice, open up avenues for postulating potential weakening mechanisms and improve collapse volume estimates which can be used in tsunami modelling to estimate wave size and run-ups.
- Using this technique at Ritter has produced an improved estimate of a collapse volume at 3.7 km^3. Detailed mapping of the island has identified widespread areas of alteration and trends of dykes perpendicular to the direction of collapse. Reconstruction of the pre-collapse island also suggests the position of the eruptive centre remained unchanged since the collapse event in 1888. Mechanical experiments on Ritter Island samples suggest that this widespread alteration may have been a weakening mechanism throughout the edifice.
- Using this SfM technique at Fogo led to high resolution mapping of the complex dyke network in the Bordeira cliff. These trends indicated the location of the central volcanic centre and possibly 1 to 2 additional eruptive centres along a N-S axis. This showed the migration this past eruptive centre to the present main eruptive centre in the direction of collapse. A study into the distinct cross-cutting 'ankaramitic' dykes suggest a change in volcanic plumbing prior to the collapse event which may present evidence of the edifice weakening and also

provide a possible weakening mechanism as the emplacement new N-S trending dykes pushed the flank outwards.

- Notable similarities are apparent across Ritter Island and Fogo collapse scar morphology and geology, despite their distinct geological context and size. This suggests common processes that may have occurred at both and therefore potentially at other volcanic collapses. In particular, the intrusions perpendicular to collapse orientation are evident across both collapse scars. This may be used as evidence in identifying flanks vulnerable to collapse in the future and hence is a key process to monitor for improved hazard assessments.

Appendices

Appendix 1: Table summarising accounts of Ritter Island from Ray (2017).

1700	William Dampier described an eruption of the Island lasting for a day with frequent paroxysms followed by strombolian fountaining and lava flows. Clear weather allowed him to sketch the island depicting a conical shape with a slight bulge to the North west and no indication of vegetation with a plume of ash being emitted from its summit (Figure 3.14a).
1793	D'entercasteaux described Ritter during eruption with smoke and lavas as a possible strombolian type.
1830	Durmont d'Urville described Ritter during a period of quiescence. He described the steep sides and conical shape and some vegetation.
1835	Thomas Jefferson Jacobs observed steam from the summit of the island upon passing and noted that the slopes were unvegetated made of varied material and moulded by erosion. A sketch of the island by Jacobs was made from ESE orientation (Figure 3.14b).
1841	Hunter described the island in a state of quiescence
1848	Gregoire Villien reported the summit of Ritter was in 'flames' and had columns of smoke
1858	Ritter was described as always smoking and a possible seismic event. Its morphology described as very steep.
1862	Carl Salerio described it as constantly smoking high hill with a central vent slightly towards the south side. He also described small seismic events occurring two or three times a month
1871	Findlay found the island in a period of quiescence, also describing a steep-sided cone
1885	Chalmers reported a thick heavy smoke emitting from Ritter in January. Later that year two reports from Eicksteadt and Finsch from a passing ship found the island inactive describing it as 'a simple pointed cone' with 'an extinct crater, mountainous with bald slopes'.

1887	Father Reina described Ritter as a very steep hill that smoked constantly. He also described a seismic event which is likely to have been a regional event rather than associated with Ritter

Appendix 2 – list of 3D models: sketchfab links
The models are password protected where the Ritter models password is: **ritter** and the Fogo models password is: **fogo**

Island	Model	Link
Ritter	whole	https://sketchfab.com/3d-models/ritter-island-3-701e10c7a2a144eaa9fd6214e7288bfa
Ritter	Central cusp	https://sketchfab.com/3d-models/ritter-middle-74fa2ffbd8994316953755b8f15dadd6
Ritter	volume calculations	https://sketchfab.com/3d-models/collapsed-materail-volumes-0f3124beb49344419d2c2edbf0242a21
Ritter	slope analysis	https://sketchfab.com/3d-models/ritter-island-slope-analysis-806e48eb476c44a3a2ba4732e3694eea
Ritter	data gap	https://sketchfab.com/3d-models/ritter-island-inferred-data-gap-9d36bf4cb6c84e17bad51a8368644b7d
Fogo	Whole Bordeira cliff	https://sketchfab.com/3d-models/fogo-bordeira-cliff-model-a4bc147fec8b4378a64d8bb799cf5b7e
Fogo	Bordeira cliff - north	https://sketchfab.com/3d-models/bordeira-cliff-north-b73f6d777b6b427796c284891edd457f
Fogo	Bordeira cliff - south sample area	https://sketchfab.com/3d-models/southcliff-samplearea-f8da0b668f0d46a4a0ae176369c7535e
Fogo	Bordeira cliff - south cusp	https://sketchfab.com/3d-models/bordeira-cliff-southern-cusp-b726200ffe1e470fac22f1c2ae4ceb5d
Fogo	Bordeira cliff - south	https://sketchfab.com/3d-models/bordeira-cliff-south-ae894fc728d84e8895992cb5867e3fc7
Fogo	Bordeira cliff - middle	https://sketchfab.com/3d-models/bordeira-cliff-mid-section-c6d565a6d538436c88c4c1cadba51424
Fogo	Monte Amarelo - dykes	https://sketchfab.com/3d-models/monte-amerelo-dykes-40c9850434624573b519a559f9e6408e
Fogo	Bordeira cliff - middle: feeder dyke	https://sketchfab.com/3d-models/bordeira-cliff-feeder-dyke-19771f7364d64b3f8e63b496b6cc6307

ID	Longitude	Latitude	Altitude	Class	Shape	Colour	Strike	Dip	trend	Average Thickness	tip?	Length	Low	High	Elevation range	notes
1	148.114186	-5.514226	13.92367	Dyke	Straight	mid grey	120	87	ESE-WNW	2.81		15.1	0	16.3	16.3	protrudes from north of island - uncertain bit of model
2	148.11412	-5.514525	8.412256	Dyke	Straight	mid grey	85	90	E-W	2.56		21.4	0	5.369	5.369	from base - doesn't extend up cliff very far - unclear extent
3	148.114277	-5.514717	25.853539	Dyke	Sinuous	pale grey	111	83	ESE-WNW	2.59		26.7	14.9	24.3	9.4	clear in cliff but looks like it tapers towards the dip in the cliff
4	148.1144	-5.515686	17.59258	Dyke	Sinuous	mid-pale grey	110.5	77.5	ESE-WNW	2.51		45.9	3.08	34.1	31.02	looks like dipping to NE
5	148.114406	-5.5160409	7.504039	Dyke	Sinuous	dark grey	85	83	E-W	1.49	y	31.7	0	34.7	34.7	
6	148.114482	-5.516498	11.797127	Both	Sinuous	mid grey	162.7	84	SSE-NNW	2.19	y	60.4	2.5	24.2	21.7	possible steely dipping into cliff, moves towards more vertical towards tip
7	148.114497	-5.5169721	8.426811	Dyke	Straight	mid grey	21.48	83.3	NNE-SSW	2.70	?	41.9	2.95	32.3	29.35	dipping intocliff butmore towards south
8	148.114717	-5.5174986	32.09396	Dyke	Straight	mid-pale grey	107.7	65	ESE-WNW	2.38	?	55.9	0.27	40.9	40.63	interpretted as extending across talus in gully
9	148.114789	-5.5174622	36.23948	Dyke	Straight	mid-pale grey	138.5	59.5	SE-NW	1.39		31.1	26.9	36.6	9.7	interpretted as extending across talus in gully
10	148.114584	-5.5179411	15.095421	Both	Sinuous	pale grey	170.33	75.67	S-N	3.61	y	86	14.1	33.5	19.4	steeply dipping into cliff but outcrops horiontal - possible different to 11 due to change in colour
11	148.114455	-5.519308	94.3409	Dyke	Straight	mid grey	124.75	70.28	SE-NW	3.57		142	18.9	103.3	84.4	steeply dipping into cliff but outcrops horiontal but darker than above, protrudes all the way to the eastern cliff - outdrops nicely to show dip
14	148.114345	-5.5187033	6.780864	Dyke	Straight	mid-dark grey	120	83	ESE-WNW	1.16	y	28.7	0	36.5	36.5	goes up into cliff and is cross cut by 11 (unclear as under veg)
15	148.113893	-5.5191584	12.546866	Dyke	Fingering	mid grey	161	78.2	SSE-NNW	3.55		27.8	7.57	54.3	46.73	has some spurs coming off dyke and goes under vegetation
16	148.113975	-5.5192156	36.88251	Dyke	Straight	mid-pale grey	119	80.6	ESE-WNW	1.03		3.09	34.1	40.6	6.5	small dyke in cliff - covered by vegetation
17	148.113629	-5.5192684	32.169216	Dyke	Fingering	mid grey	25	49	NNE-SSW	2.37	y?	33.9	18.8	43.9	25.1	dyke on north side of cental cusp with inclusions of host rock
18	148.113578	-5.5192791	26.123592	Dyke	Straight	mid dark grey	164	61	SSE-NNW	2.31		35.4	0	45.1	45.1	dyke might join onto 19 but separated on central cusp
19	148.11357	-5.519687	70.57516	Dyke	Straight	mid-dark grey	144	69	SE-NW	2.64		76.5	36.2	71.3	35.1	dyke that may continue from 18 wraps around central cusp and protrudes from cliff
20	148.11353	-5.5193102	16.384663	Dyke	Sinuous	mid-pale grey	18	69	NNE-SSW	3.87		55.4	0	35.6	35.6	dyke that protrudes out in sea, changes a lot in width- dissapears under vegetation
21	148.113571	-5.5191793	2.093225	Dyke	Straight	dark gery	5	76	N-S	2.17		21	0	8.23	8.23	protrudes out to sea - gets cross-cut by 20?
22	148.113548	-5.5192483	2.243599	Dyke	Straight	brown/grey	9	69.5	N-S	1.23		11.3	1	6.4	5.4	small brown/grey dyke seen alongside 21
23	148.113368	-5.519459	39.885143	Dyke	Fingering	pale grey	151.7	44.67	SSE-NNW	3.66		80.4	0	41.97	41.97	Starts discrete in north of cusp but joins big fingered intrusion on front of cusp - probably is also part of 24 or may be individual
24	148.113368	-5.519459	39.885143	Dyke	Straight	pale grey	7.5	81.5	N-S	4.50	y	51.7	0	29.27	29.27	protrudes a bit out to sea on north of cusp, looks like is dipping steeply into cliff - could be part of dyke 23 but looks like different dip
25	148.113323	-5.519572	22.497772	Dyke	Straight	green grey				1.32		6.54	7.64	22.35	14.71	one of a group of vertical greenish dykes in central cusp cross cut by 23 and 24
26	148.113311	-5.519626	17.644041	Dyke	Straight	green grey				1.26		4.46	7.52	24.46	16.94	one of a group of vertical greenish dykes in central cusp cross cut by 23 and 24
27	148.113351	-5.519804	12.475694	Dyke	Straight	green grey				4.49		11.6	5.16	25.5	20.34	greenish dyke looksvertical but may actually strike more to SE dipping into cliff - cross cut by 23
28	148.114367	-5.519752	100.01081	Dyke	Straight	mid grey				1.32		48.8	80.4	102.1	21.7	two outcrops higher up in cliff at central cusp - difficult to make out eneath vegetation - may join onto 15?
29	148.113779	-5.519694	67.81919	Sill	Straight	pale grey				3.815		28.7	55.8	76.4	20.6	pale sill seenon south side of top central cusp
30	148.113686	-5.519917	25.135986	Dyke	Straight	mid-pale grey	38	68	NE-SW	2.31	y	34.5	18.4	44.85	26.45	dyke with tip on south side of central cusp - base obscured by talus
31	148.113989	-5.520095	47.538475	Dyke	Straight	mid-pale grey	0	85	N-S	4.85		58.1	27.9	51.4	23.5	striking NE dipping to SE
32	148.114275	-5.52022	71.91217	Dyke	Sinuous	mid-pale grey	155	71.5	SSE-NNW	2.23		121	60.6	90.7	30.1	long dyke crossing across gully, quite sinuous,steeply dipping
33	148.114292	-5.520599	59.92691	Dyke	Straight	pale grey				3.46		36.4	52	63	11	pale dyke quite large on cliff but looks like striking NS ish
34	148.114142	-5.52088	41.1365395	Sill	Sinuous	pale grey				2.80		132	30.4	40.46	10.06	long dyke across cliff, varies in thickness ,changes direction slightly to the south
35	148.114049	-5.52129	12.2933664	Dyke	Straight	mid-pale grey	165.5	74.5	SSE-NNW	3.84		126	0	45.6	45.6	protrudes at the base of cliff - seems to be dipping into cliff steeply - maybe changes direction as it thins upwards
36	148.114364	-5.52187	47.3575821	Dyke	Straight	mid-pale grey				1.35		5.35	51	58.7	7.7	small dyke sub parallel to 35
37	148.111968	-5.52446	5.44267797	Dyke	Straight	mid/dark grey	152	80	SSE-NNW	1.79		27.4	0	34	34	clear dyke on point of south cliff, cross cuts clearly across lavas
38	148.11196	-5.52451	1.56120801	Dyke	Straight	pale yellowish				0.90		12.6	0	31.35	31.35	small pale dyke next to 27 as described by previous fieldwork as clastic
39	148.112242	-5.52439	10.56915	Dyke	Sinuous	mid-dark grey						28.9	0	31.647	31.647	hard to see dyke - looks like it appears at the top of the cliff as well after thinning out
41	148.11196	-5.52451	1.56120801	Dyke	Straight	pale yellowish						12.3	0	12.765	12.765	next to prominent dyke
42	148.11459	-5.51805	17.3648663	Sill	Straight	pale grey				3.345		33	0	8.4	8.4	sill at base of cliff - as described by saunders and kudon - Rit 7 sample
43	148.112629	-5.51909	8.02520466	Dyke	Straight	mid										dyke cutting accros central islet as described by simon day

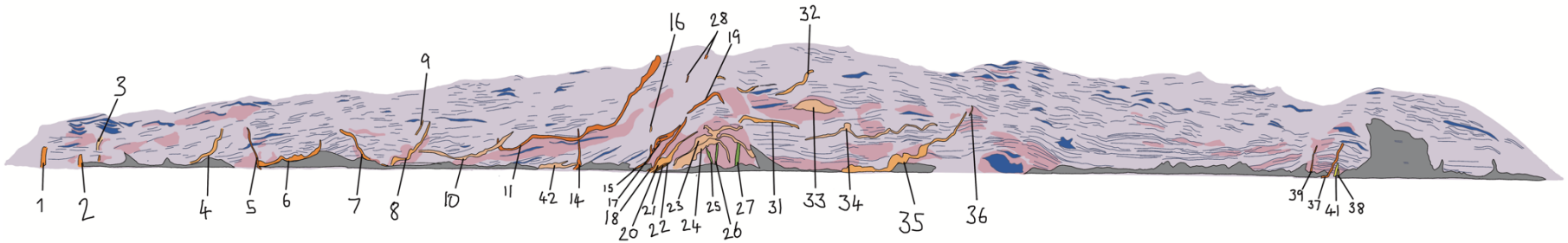

Appendix 3: Table of intrusion measurements and notes from mapping with a diagram highlighting the intrusion ID.

Bibliography

ACOCELLA, V. 2005. Modes of sector collapse of volcanic cones: Insights from analogue experiments. *Journal of Geophysical Research: Solid Earth,* 110.

AMELUNG, F. & DAY, S. 2002. InSAR observations of the 1995 Fogo, Cape Verde, eruption: Implications for the effects of collapse events upon island volcanoes. *Geophysical Research Letters,* 29**,** 47-1-47-4.

ANDRADE, S. D. & DE VRIES, B. V. W. 2010. Structural analysis of the early stages of catastrophic stratovolcano flank-collapse using analogue models. *Bulletin of Volcanology,* 72**,** 771-789.

BAKKER, R. R., VIOLAY, M. E., BENSON, P. M. & VINCIGUERRA, S. C. 2015. Ductile flow in sub-volcanic carbonate basement as the main control for edifice stability: New experimental insights. *Earth and Planetary Science Letters,* 430**,** 533-541.

BALDWIN, S. L., FITZGERALD, P. G. & WEBB, L. E. 2012. Tectonics of the New Guinea region. *Annual Review of Earth and Planetary Sciences,* 40.

BARRETT, R., LEBAS, E., RAMALHO, R., KLAUCKE, I., KUTTEROLF, S., KLÜGEL, A., LINDHORST, K., GROSS, F. & KRASTEL, S. 2020. Revisiting the tsunamigenic volcanic flank collapse of Fogo Island in the Cape Verdes, offshore West Africa. *Geological Society, London, Special Publications,* 500**,** 13-26.

BATTAGLIA, M., DI BARI, M., ACOCELLA, V. & NERI, M. 2011. Dike emplacement and flank instability at Mount Etna: constraints from a poro-elastic-model of flank collapse. *Journal of volcanology and geothermal research,* 199**,** 153-164.

BENSON, P. M., MEREDITH, P. G., PLATZMAN, E. S. & WHITE, R. E. 2005. Pore fabric shape anisotropy in porous sandstones and its relation to elastic wave velocity and permeability anisotropy under hydrostatic pressure. *International Journal of Rock Mechanics and Mining Sciences,* 42**,** 890-899.

BENZ, H. M., HERMAN, M., TARR, A. C., HAYES, G. P., FURLONG, K. P., VILLASEÑOR, A., DART, R. L. & RHEA, S. 2011. Seismicity of the Earth 1900-2010 New Guinea and vicinity. US Geological Survey.

BERNARD, B., TAKARADA, S., ANDRADE, S. D. & DUFRESNE, A. 2021. Terminology and strategy to describe large volcanic landslides and debris avalanches. *Volcanic debris avalanches: From collapse to hazard***,** 51-73.

BERNDT, C., MUFF, S., KLAUCKE, I., WATT, S., BÖTTNER, C., SCHRAMM, B., VÖLSCH, A., BENNECKE, S., ELGER, J. & CHI, W.-C. 2017. RV SONNE 252 Cruise Report/Fahrtbericht, Yokohama: 05.11. 2016-Nouméa: 18.12. 2016. SO252: RITTER ISLAND Tsunami potential of volcanic flank collapses.

BLAHŮT, J., BALEK, J., KLIMEŠ, J., ROWBERRY, M., KUSÁK, M. & KALINA, J. 2019. A comprehensive global database of giant landslides on volcanic islands. *Landslides,* 16**,** 2045-2052.

BLAHUT, J., KLIMEŠ, J., ROWBERRY, M. & KUSÁK, M. 2018. Database of giant landslides on volcanic islands—first results from the Atlantic Ocean. *Landslides,* 15**,** 823-827.

BONALI, F. L., TIBALDI, A., MARCHESE, F., FALLATI, L., RUSSO, E., CORSELLI, C. & SAVINI, A. 2019. UAV-based surveying in volcano-tectonics: An example from the Iceland rift. *Journal of Structural Geology,* 121**,** 46-64.

BORGIA, A. 1994. Dynamic basis of volcanic spreading. *Journal of Geophysical Research: Solid Earth,* 99**,** 17791-17804.
BROWNING, J., DRYMONI, K. & GUDMUNDSSON, A. 2015. Forecasting magma-chamber rupture at Santorini volcano, Greece. *Scientific reports,* 5**,** 15785.
BRUM DA SILVEIRA, A., MADEIRA, J. & SERRALHEIRO, A. 1997. *A erupção vulcânica de 1995, na Ilha do Fogo, Cabo Verde*, Ministério da Ciência et da Tecnologia, Instituto de Investigação Científica ….
CALVARI, S., INTRIERI, E., DI TRAGLIA, F., BONACCORSO, A., CASAGLI, N. & CRISTALDI, A. 2016. Monitoring crater-wall collapse at active volcanoes: A study of the 12 January 2013 event at Stromboli. *Bulletin of volcanology,* 78**,** 1-16.
CARRACEDO, J., DAY, S., GUILLOU, H., RODRIGUEZ-BADIOLA, E., CANAS, J. A. & PEREZ-TORRADO, F.-J. 1997. Geochronological, structural and morphological constrains in the genesis and evolution of the Canary Islands.
CARVALHO, J., SILVEIRA, G., DUMONT, S. & RAMALHO, R. 2022. 3D-ambient noise surface wave tomography of Fogo volcano, Cape Verde. *Journal of Volcanology and Geothermal Research,* 432**,** 107702.
CASTAGNA, A., OUGIER-SIMONIN, A., BENSON, P., BROWNING, J., WALKER, R. J., FAZIO, M. & VINCIGUERRA, S. 2018. Thermal damage and pore pressure effects of the Brittle-Ductile transition in comiso limestone. *Journal of Geophysical Research: Solid Earth,* 123**,** 7644-7660.
CLARE, M. A., LE BAS, T., PRICE, D. M., HUNT, J. E., SEAR, D., CARTIGNY, M. J., VELLINGA, A., SYMONS, W., FIRTH, C. & CRONIN, S. 2018. Complex and cascading triggering of submarine landslides and turbidity currents at volcanic islands revealed from integration of high-resolution onshore and offshore surveys. *Frontiers in Earth Science,* 6**,** 223.
COOKE, R. J. 1981. Eruptive history of the volcano at Ritter Island. *Geol Surv Papua New Guinea Mem,* 10**,** 115-123.
CORNU, M.-N. 2017. *Evolution magmatique d'un volcan bouclier océanique avant et après une déstabilisation massive de ses flancs: Fogo, Cap Vert et Tenerife, Canaries.* Université Clermont Auvergne(2017-2020).
CORNU, M.-N., PARIS, R., DOUCELANCE, R., BACHÈLERY, P., BOSQ, C., AUCLAIR, D., BENBAKKAR, M., GANNOUN, A.-M. & GUILLOU, H. 2021. Exploring the links between volcano flank collapse and the magmatic evolution of an ocean island volcano: Fogo, Cape Verde. *Scientific Reports,* 11**,** 1-12.
COULOMB, C. 1776. Essai sur une application des règles des maximis et minimis à quelques problèmes de statique relatifs à l'architecture, vol. 7. *Paris: Mém Math Phys Acad Roy Sci par divers Savants*.
DAY, S. 1996. Hydrothermal pore fluid pressure and the stability of porous, permeable volcanoes. *Geological Society, London, Special Publications,* 110**,** 77-93.
DAY, S., CARRACEDO, J. & GUILLOU, H. 1997. Age and geometry of an aborted rift flank collapse: the San Andres fault system, El Hierro, Canary Islands. *Geological Magazine,* 134**,** 523-537.
DAY, S., DA SILVA, S. H. & FONSECA, J. 1999. A past giant lateral collapse and present-day flank instability of Fogo, Cape Verde Islands. *Journal of Volcanology and Geothermal Research,* 94**,** 191-218.

DAY, S., LLANES, P., SILVER, E., HOFFMANN, G., WARD, S. & DRISCOLL, N. 2015. Submarine landslide deposits of the historical lateral collapse of Ritter Island, Papua New Guinea. *Marine and Petroleum Geology,* 67**,** 419-438.

DE BENI, E., CANTARERO, M. & MESSINA, A. 2019. UAVs for volcano monitoring: A new approach applied on an active lava flow on Mt. Etna (Italy), during the 27 February–02 March 2017 eruption. *Journal of Volcanology and Geothermal Research,* 369**,** 250-262.

DEL POTRO, R. & HÜRLIMANN, M. 2009. The decrease in the shear strength of volcanic materials with argillic hydrothermal alteration, insights from the summit region of Teide stratovolcano, Tenerife. *Engineering Geology,* 104**,** 135-143.

DELANEY, P. T. 1982. Rapid intrusion of magma into wet rock: groundwater flow due to pore pressure increases. *Journal of Geophysical Research: Solid Earth,* 87**,** 7739-7756.

DI TRAGLIA, F., DE LUCA, C., MANZO, M., NOLESINI, T., CASAGLI, N., LANARI, R. & CASU, F. 2021. Joint exploitation of space-borne and ground-based multitemporal InSAR measurements for volcano monitoring: The Stromboli volcano case study. *Remote Sensing of Environment,* 260**,** 112441.

DINÇER, I., ACAR, A., ÇOBANOĞLU, I. & URAS, Y. 2004. Correlation between Schmidt hardness, uniaxial compressive strength and Young's modulus for andesites, basalts and tuffs. *Bulletin of Engineering Geology and the Environment,* 63**,** 141-148.

DUFRESNE, A., SIEBERT, L. & BERNARD, B. 2021. Distribution and geometric parameters of volcanic debris avalanche deposits. *Volcanic Debris Avalanches: From Collapse to Hazard***,** 75-90.

EGGERTSSON, G., LAVALLÉE, Y., KENDRICK, J. & MARKÚSSON, S. 2020. Improving fluid flow in geothermal reservoirs by thermal and mechanical stimulation: The case of Krafla volcano, Iceland. *Journal of Volcanology and Geothermal Research,* 391**,** 106351.

ELSWORTH, D. & VOIGHT, B. 1996. Evaluation of volcano flank instability triggered by dyke intrusion. *Geological Society, London, Special Publications,* 110**,** 45-53.

ELTNER, A. & SOFIA, G. 2020. Structure from motion photogrammetric technique. *Developments in Earth surface processes.* Elsevier.

ENGVIK, A. K., BERTRAM, A., KALTHOFF, J. F., STÖCKHERT, B., AUSTRHEIM, H. & ELVEVOLD, S. 2005. Magma-driven hydraulic fracturing and infiltration of fluids into the damaged host rock, an example from Dronning Maud Land, Antarctica. *Journal of Structural Geology,* 27**,** 839-854.

FAN, T., WANG, Y., XU, Z., SUN, L., WANG, P. & HOU, J. 2024. A Review of Historical Volcanic Tsunamis: A New Scheme for a Volcanic Tsunami Monitoring System. *Journal of Marine Science and Engineering,* 12**,** 278.

FISKE, R. & JACKSON, E. 1972. Orientation and growth of Hawaiian volcanic rifts: the effect of regional structure and gravitational stresses. *Proceedings of the Royal Society of London. A. Mathematical and Physical Sciences,* 329**,** 299-326.

FOEKEN, J. P., DAY, S. & STUART, F. M. 2009. Cosmogenic 3He exposure dating of the Quaternary basalts from Fogo, Cape Verdes: implications for rift zone and magmatic reorganisation. *Quaternary Geochronology,* 4**,** 37-49.

FOSSEN, H. 2016. *Structural geology*, Cambridge University Press.

GESHI, N., BROWNING, J. & KUSUMOTO, S. 2020. Magmatic overpressures, volatile exsolution and potential explosivity of fissure eruptions inferred via dike aspect ratios. *Scientific reports,* 10**,** 9406.

GESHI, N., KUSUMOTO, S. & GUDMUNDSSON, A. 2010. Geometric difference between non-feeder and feeder dikes. *Geology,* 38**,** 195-198.
GLICKEN, H. 1996. Rockslide-debris avalanche of May 18, 1980, Mount St. Helens volcano, Washington. US Geological Survey.
GONZÁLEZ, P. J., BAGNARDI, M., HOOPER, A. J., LARSEN, Y., MARINKOVIC, P., SAMSONOV, S. V. & WRIGHT, T. J. 2015. The 2014–2015 eruption of Fogo volcano: Geodetic modeling of Sentinel-1 TOPS interferometry. *Geophysical research letters,* 42**,** 9239-9246.
GONZALEZ-SANTANA, J., WAUTHIER, C., TUNG, S. & MASTERLARK, T. 2023. The effect of edifice slope, detachment fault geometry, and magmatic triggers on the development of volcanic flank instability. *Authorea Preprints*.
GRILLI, S. T., TAPPIN, D. R., CAREY, S., WATT, S. F., WARD, S. N., GRILLI, A. R., ENGWELL, S. L., ZHANG, C., KIRBY, J. T. & SCHAMBACH, L. 2019. Modelling of the tsunami from the December 22, 2018 lateral collapse of Anak Krakatau volcano in the Sunda Straits, Indonesia. *Scientific reports,* 9**,** 1-13.
HAWKES, I. & MELLOR, M. 1970. Uniaxial testing in rock mechanics laboratories. *Engineering Geology,* 4**,** 179-285.
HEAP, M., REUSCHLÉ, T., FARQUHARSON, J. & BAUD, P. 2018. Permeability of volcanic rocks to gas and water. *Journal of Volcanology and Geothermal Research,* 354**,** 29-38.
HEAP, M. J., BAUMANN, T., GILG, H. A., KOLZENBURG, S., RYAN, A. G., VILLENEUVE, M., RUSSELL, J. K., KENNEDY, L. A., ROSAS-CARBAJAL, M. & CLYNNE, M. A. 2021a. Hydrothermal alteration can result in pore pressurization and volcano instability. *Geology,* 49**,** 1348-1352.
HEAP, M. J., BAUMANN, T. S., ROSAS-CARBAJAL, M., KOMOROWSKI, J. C., GILG, H. A., VILLENEUVE, M., MORETTI, R., BAUD, P., CARBILLET, L. & HARNETT, C. 2021b. Alteration-Induced Volcano Instability at La Soufrière de Guadeloupe (Eastern Caribbean). *Journal of Geophysical Research: Solid Earth,* 126**,** e2021JB022514.
HEAP, M. J. & KENNEDY, B. M. 2016. Exploring the scale-dependent permeability of fractured andesite. *Earth and Planetary Science Letters,* 447**,** 139-150.
HEAP, M. J., KENNEDY, B. M., PERNIN, N., JACQUEMARD, L., BAUD, P., FARQUHARSON, J. I., SCHEU, B., LAVALLÉE, Y., GILG, H. A. & LETHAM-BRAKE, M. 2015. Mechanical behaviour and failure modes in the Whakaari (White Island volcano) hydrothermal system, New Zealand. *Journal of Volcanology and Geothermal Research,* 295**,** 26-42.
HEAP, M. J., TROLL, V. R., KUSHNIR, A. R., GILG, H. A., COLLINSON, A. S., DEEGAN, F. M., DARMAWAN, H., SERAPHINE, N., NEUBERG, J. & WALTER, T. R. 2019. Hydrothermal alteration of andesitic lava domes can lead to explosive volcanic behaviour. *Nature communications,* 10**,** 1-10.
HEAP, M. J. & VIOLAY, M. E. 2021. The mechanical behaviour and failure modes of volcanic rocks: a review. *Bulletin of Volcanology,* 83**,** 33.
HEAP, M. J., XU, T. & CHEN, C.-F. 2014. The influence of porosity and vesicle size on the brittle strength of volcanic rocks and magma. *Bulletin of Volcanology,* 76**,** 1-15.
HUANG, H., LONG, J., YI, W., YI, Q., ZHANG, G. & LEI, B. 2017. A method for using unmanned aerial vehicles for emergency investigation of single geo-hazards and sample applications of this method. *Natural Hazards and Earth System Sciences,* 17**,** 1961-1979.

HUBBERT, M. & RUBEY, W. W. 1959. Role of fluid pressure in mechanics of overthrust faulting: I. Mechanics of fluid-filled porous solids and its application to overthrust faulting. *Geological Society of America Bulletin,* 70**,** 115-166.

IVERSON, R. M. 1995. Can magma-injection and groundwater forces cause massive landslides on Hawaiian volcanoes? *Journal of Volcanology and Geothermal Research,* 66**,** 295-308.

JOHNSON, R. 1987. Large-scale volcanic cone collapse: the 1888 slope failure of Ritter volcano, and other examples from Papua New Guinea. *Bulletin of Volcanology,* 49**,** 669-679.

KARSTENS, J., BERNDT, C., URLAUB, M., WATT, S. F., MICALLEF, A., RAY, M., KLAUCKE, I., MUFF, S., KLAESCHEN, D. & KÜHN, M. 2019. From gradual spreading to catastrophic collapse–Reconstruction of the 1888 Ritter Island volcanic sector collapse from high-resolution 3D seismic data. *Earth and Planetary Science Letters,* 517**,** 1-13.

KARSTENS, J., KELFOUN, K., WATT, S. F. & BERNDT, C. 2020. Combining 3D seismics, eyewitness accounts and numerical simulations to reconstruct the 1888 Ritter Island sector collapse and tsunami. *International Journal of Earth Sciences,* 109**,** 2659-2677.

LACHENBRUCH, A. H. 1980. Frictional heating, fluid pressure, and the resistance to fault motion. *Journal of Geophysical Research: Solid Earth,* 85**,** 6097-6112.

LATTER, J. 1981. Tsunamis of volcanic origin: summary of causes, with particular reference to Krakatoa, 1883. *Bulletin volcanologique,* 44**,** 467-490.

LAUTZE, N. C. & HOUGHTON, B. F. 2007. Linking variable explosion style and magma textures during 2002 at Stromboli volcano, Italy. *Bulletin of Volcanology,* 69**,** 445-460.

LE CORVEC, N. & MCGOVERN, P. J. 2018. The effect of ocean loading on the growth of basaltic ocean island volcanoes and their magmatic plumbing system. *Frontiers in Earth Science,* 6**,** 119.

LÓPEZ, D. L. & WILLIAMS, S. N. 1993. Catastrophic volcanic collapse: relation to hydrothermal processes. *Science,* 260**,** 1794-1796.

MACKENZIE, W. S., ADAMS, A. E. & BRODIE, K. H. 2017. *Rocks and minerals in thin section: A colour atlas*, CRC Press.

MAGRAMO, K. 2024. *Indonesia issues tsunami alert after volcano erupts on remote island* [Online]. CNN. Available: https://edition.cnn.com/2024/04/17/asia/indonesia-mount-ruang-volcano-eruption-intl-hnk [Accessed].

MARQUES, F., HILDENBRAND, A., VICTÓRIA, S., CUNHA, C. & DIAS, P. 2019. Caldera or flank collapse in the Fogo volcano? What age? Consequences for risk assessment in volcanic islands. *Journal of Volcanology and Geothermal Research,* 388**,** 106686.

MARTÍ, J. 2019. Las Cañadas caldera, Tenerife, Canary Islands: A review, or the end of a long volcanological controversy. *Earth-Science Reviews,* 196**,** 102889.

MARTÍNEZ-MORENO, F., SANTOS, F. M., MADEIRA, J., POUS, J., BERNARDO, I., SOARES, A., ESTEVES, M., ADÃO, F., RIBEIRO, J. & MATA, J. 2018. Investigating collapse structures in oceanic islands using magnetotelluric surveys: The case of Fogo Island in Cape Verde. *Journal of Volcanology and Geothermal Research,* 357**,** 152-162.

MASSON, D., LE BAS, T., GREVEMEYER, I. & WEINREBE, W. 2008. Flank collapse and large-scale landsliding in the Cape Verde Islands, off West Africa. *Geochemistry, Geophysics, Geosystems,* 9.

MCGUIRE, W., HOWARTH, R. J., FIRTH, C. R., SOLOW, A. R., PULLEN, A., SAUNDERS, S., STEWART, I. S. & VITA-FINZI, C. 1997. Correlation between rate of sea-level change and frequency of explosive volcanism in the Mediterranean. *Nature,* 389**,** 473-476.

MCGUIRE, W. J. 1996. Volcano instability: a review of contemporary themes. *Geological Society, London, Special Publications,* 110**,** 1-23.
MCMURTRY, G., WATTS, P., FRYER, G., SMITH, J. & IMAMURA, F. 2004. Giant landslides, mega-tsunamis, and paleo-sea level in the Hawaiian Islands. *Marine Geology,* 203**,** 219-233.
MOORE, G. W. & MOORE, J. G. 1988. Large-scale bedforms in boulder gravel produced by giant waves in Hawaii. *GSA Special Papers,* 229**,** 101-110.
MOORE, J. G., CLAGUE, D. A., HOLCOMB, R., LIPMAN, P. W., NORMARK, W. R. & TORRESAN, M. E. 1989. Prodigious submarine landslides on the Hawaiian Ridge. *Journal of Geophysical Research: Solid Earth,* 94**,** 17465-17484.
MOSBRUCKER, A. R., MAJOR, J. J., SPICER, K. R. & PITLICK, J. 2017. Camera system considerations for geomorphic applications of SfM photogrammetry. *Earth Surface Processes and Landforms,* 42**,** 969-986.
PARIS, R., GIACHETTI, T., CHEVALIER, J., GUILLOU, H. & FRANK, N. 2011. Tsunami deposits in Santiago Island (Cape Verde archipelago) as possible evidence of a massive flank failure of Fogos volcano. *Sedimentary Geology,* 239**,** 129-145.
PARIS, R., SWITZER, A. D., BELOUSOVA, M., BELOUSOV, A., ONTOWIRJO, B., WHELLEY, P. L. & ULVROVA, M. 2014. Volcanic tsunami: a review of source mechanisms, past events and hazards in Southeast Asia (Indonesia, Philippines, Papua New Guinea). *Natural Hazards,* 70**,** 447-470.
PATERSON, M. S. & WONG, T.-F. 2005. *Experimental rock deformation: the brittle field*, Springer.
POLAND, M. P., PELTIER, A., BONFORTE, A. & PUGLISI, G. 2017. The spectrum of persistent volcanic flank instability: A review and proposed framework based on Kīlauea, Piton de la Fournaise, and Etna. *Journal of Volcanology and Geothermal Research,* 339**,** 63-80.
RAMALHO, R. S., WINCKLER, G., MADEIRA, J., HELFFRICH, G. R., HIPÓLITO, A., QUARTAU, R., ADENA, K. & SCHAEFER, J. M. 2015. Hazard potential of volcanic flank collapses raised by new megatsunami evidence. *Science advances,* 1**,** e1500456.
RAY, M. J. 2017. Unpublished MPhil Thesis, Birkbeck
REID, M. E. 2004. Massive collapse of volcano edifices triggered by hydrothermal pressurization. *Geology,* 32**,** 373-376.
ROLFE-BETTS, B., DAY, S. J., DOWNES, H., MILLAR, I. & PALUBICKI, K. 2024. Compositional variations in shield-stage volcanism in Fogo, Cape Verde islands. *Journal of Volcanology and Geothermal Research***,** 107996.
ROMERO, J. E., POLACCI, M., WATT, S., KITAMURA, S., TORMEY, D., SIELFELD, G., ARZILLI, F., LA SPINA, G., FRANCO, L. & BURTON, M. 2021. Volcanic lateral collapse processes in mafic arc edifices: A review of their driving processes, types and consequences. *Frontiers in Earth Science,* 9**,** 639825.
SAUNDERS, S. & KUDUON, J. 2009. The June 2009 Investigation of Ritter Volcano, with a Brief Discussion on its Current Nature. *Papua New Guinea Department of Mineral Policy and Geohazards Management, Open File Report,* 3**,** 2009.
SCHAEFER, L. N., KENDRICK, J. E., OOMMEN, T., LAVALLÉE, Y. & CHIGNA, G. 2015. Geomechanical rock properties of a basaltic volcano. *Frontiers in Earth Science,* 3**,** 29.
SCHONBERGER, J. L. & FRAHM, J.-M. Structure-from-motion revisited. Proceedings of the IEEE conference on computer vision and pattern recognition, 2016. 4104-4113.

SHEA, T., HOUGHTON, B. F., GURIOLI, L., CASHMAN, K. V., HAMMER, J. E. & HOBDEN, B. J. 2010. Textural studies of vesicles in volcanic rocks: an integrated methodology. *Journal of Volcanology and Geothermal Research,* 190**,** 271-289.

SIEBERT, L. 1984. Large volcanic debris avalanches: characteristics of source areas, deposits, and associated eruptions. *Journal of volcanology and geothermal research,* 22**,** 163-197.

SIEBERT, L. & ROVERATO, M. 2021. A historical perspective on lateral collapse and volcanic debris avalanches. *Volcanic Debris Avalanches.* Springer.

SIGURDSSON, H., CAREY, S., ALEXANDRI, M., VOUGIOUKALAKIS, G., CROFF, K., ROMAN, C., SAKELLARIOU, D., ANAGNOSTOU, C., ROUSAKIS, G. & IOAKIM, C. 2006. Marine investigations of Greece's Santorini volcanic field. *EOS, Transactions American Geophysical Union,* 87**,** 337-342.

SILVER, E., DAY, S., WARD, S., HOFFMANN, G., LLANES, P., DRISCOLL, N., APPELGATE, B. & SAUNDERS, S. 2009. Volcano collapse and tsunami generation in the Bismarck volcanic arc, Papua New Guinea. *Journal of Volcanology and Geothermal Research,* 186**,** 210-222.

SMITH, J. R. & WESSEL, P. 2000. Isostatic consequences of giant landslides on the Hawaiian Ridge. *Pure and Applied Geophysics,* 157**,** 1097-1114.

TAPPIN, D., WATTS, P., MCMURTRY, G., LAFOY, Y. & MATSUMOTO, T. 2001. The Sissano, Papua New Guinea tsunami of July 1998—offshore evidence on the source mechanism. *Marine Geology,* 175**,** 1-23.

TOLLAN, P. M. E., DALE, C., HERMANN, J., DAVIDSON, J. & ARCULUS, R. 2017. Generation and modification of the mantle wedge and lithosphere beneath the West Bismarck island arc: melting, metasomatism and thermal history of peridotite xenoliths from Ritter island. *Journal of petrology,* 58**,** 1475-1510.

TOST, M., CRONIN, S., PROCTER, J., SMITH, I., NEALL, V. & PRICE, R. 2015. Impacts of catastrophic volcanic collapse on the erosion and morphology of a distal fluvial landscape: Hautapu River, Mount Ruapehu, New Zealand. *Bulletin,* 127**,** 266-280.

VIDAL, N. & MERLE, O. 2000. Reactivation of basement faults beneath volcanoes: a new model of flank collapse. *Journal of Volcanology and Geothermal Research,* 99**,** 9-26.

VOIGHT, B., LIPMAN, P. & MULLINEAUX, D. 1981. Time scale for the first moments of the May 18 eruption. *US Geol. Surv. Prof. Pap,* 1250**,** 69-86.

WALLACE, L. M., STEVENS, C., SILVER, E., MCCAFFREY, R., LORATUNG, W., HASIATA, S., STANAWAY, R., CURLEY, R., ROSA, R. & TAUGALOIDI, J. 2004. GPS and seismological constraints on active tectonics and arc-continent collision in Papua New Guinea: Implications for mechanics of microplate rotations in a plate boundary zone. *Journal of Geophysical Research: Solid Earth,* 109.

WALTER, T. R., HAGHSHENAS HAGHIGHI, M., SCHNEIDER, F. M., COPPOLA, D., MOTAGH, M., SAUL, J., BABEYKO, A., DAHM, T., TROLL, V. R. & TILMANN, F. 2019. Complex hazard cascade culminating in the Anak Krakatau sector collapse. *Nature communications,* 10**,** 4339.

WALTER, T. R. & TROLL, V. R. 2003. Experiments on rift zone evolution in unstable volcanic edifices. *Journal of Volcanology and Geothermal Research,* 127**,** 107-120.

WARD, S. N. & DAY, S. 2003. Ritter Island Volcano—lateral collapse and the tsunami of 1888. *Geophysical Journal International,* 154**,** 891-902.

WATT, S. F. 2019. The evolution of volcanic systems following sector collapse. *Journal of Volcanology and Geothermal Research*.

WATT, S. F., KARSTENS, J. & BERNDT, C. 2021. Volcanic-island lateral collapses and their submarine deposits. *Volcanic Debris Avalanches: From Collapse to Hazard***,** 255-279.
WATT, S. F., KARSTENS, J., MICALLEF, A., BERNDT, C., URLAUB, M., RAY, M., DESAI, A., SAMMARTINI, M., KLAUCKE, I. & BÖTTNER, C. 2019. From catastrophic collapse to multi-phase deposition: Flow transformation, seafloor interaction and triggered eruption following a volcanic-island landslide. *Earth and Planetary Science Letters,* 517**,** 135-147.
WIBBERLEY, C. A., YIELDING, G. & DI TORO, G. 2008. Recent advances in the understanding of fault zone internal structure: a review. *Geological Society, London, Special Publications,* 299**,** 5-33.
WITHAM, C. S. 2005. Volcanic disasters and incidents: A new database. *Journal of Volcanology and Geothermal Research,* 148**,** 191-233.
WOODHEAD, J., HERGT, J., SANDIFORD, M. & JOHNSON, W. 2010. The big crunch: Physical and chemical expressions of arc/continent collision in the Western Bismarck arc. *Journal of Volcanology and Geothermal Research,* 190**,** 11-24.
WORSLEY, P. 2015. Physical geology of the Fogo volcano (Cape Verde Islands) and its 2014–2015 eruption. *Geology Today,* 31**,** 153-159.
WRIGHT, H. M., CASHMAN, K. V., GOTTESFELD, E. H. & ROBERTS, J. J. 2009. Pore structure of volcanic clasts: measurements of permeability and electrical conductivity. *Earth and Planetary Science Letters,* 280**,** 93-104.
ZERNACK, A. V. & PROCTER, J. N. 2021. Cyclic growth and destruction of volcanoes. *Volcanic Debris Avalanches: From collapse to hazard***,** 311-355.
ZORN, E. U., VASSILEVA, M., WALTER, T. R., DARMAWAN, H., RÖHLER, L. & AMELUNG, F. 2023. Interactions of magmatic intrusions with the multiyear flank instability at Anak Krakatau volcano, Indonesia: Insights from InSAR and analogue modeling. *Geology,* 51**,** 340-344.